

FREDERIKE BENSCH

---

# **MOLECULAR IMAGING ON THE MOVE**

From feasibility to contribution in clinical questions

Printing of this thesis was financially supported by the Dutch Cancer Society and the Stichting Werkgroep Interne Oncologie, UMCG.

**Cover** Joke Schepers | [www.jokeschepers.exto.nl](http://www.jokeschepers.exto.nl)  
**Layout** Renate Siebes | [Proefschrift.nu](http://Proefschrift.nu)  
**Printed by** [Proefschriftmaken.nl](http://Proefschriftmaken.nl)  
**ISBN** 978-94-90791-68-1

© 2018 **Frederike Bensch**

All rights reserved. No part of this publication may be reproduced, stored in a retrieval system, or transmitted, in any form or by any means, electronically, mechanically, by photo-copying, recording or otherwise, without the prior written permission of the author.



university of  
 groningen

# **Molecular imaging on the move**

From feasibility to contribution in clinical questions

## **Proefschrift**

ter verkrijging van de graad van doctor aan de  
 Rijksuniversiteit Groningen  
 op gezag van de  
 rector magnificus prof. dr. E. Sterken  
 en volgens besluit van het College voor Promoties.

De openbare verdediging zal plaatsvinden op

maandag 18 maart 2019 om 12.45 uur

door

**Frederike Bensch**

geboren op 26 augustus 1985  
 te Hagenow, Duitsland

**Promotor**

Prof. dr. E.G.E. de Vries

**Copromotor**

Dr. C.P. Schröder

**Beoordelingscommissie**

Prof. dr. G.M. van Dam

Prof. dr. H.W. Nijman

Prof. dr. O. Boerman

**Paranimfen**

Titia Lamberts

Niek Westerink



*Für Papa*



# CONTENTS

<b>Chapter 1</b>	General introduction and outline of the thesis	7
<b>Chapter 2</b>	Suspicion of acute anterior circulation stroke, but posterior circulation infarct as the final diagnosis Submitted	17
<b>Chapter 3</b>	Additional diagnostic value of CT-perfusion for detection of acute ischemic stroke in the posterior circulation Stroke. 2015;46:1113-1115	31
<b>Chapter 4</b>	Collateral flow predicts outcome after basilar artery occlusion: the posterior circulation collateral score Int J Stroke. 2016;11:768-775	41
<b>Chapter 5</b>	Clot length predicts recanalisation but not outcome after basilar artery occlusion Eur Stroke J. 2016;1:330-336	55
<b>Chapter 6</b>	Vertebral artery stenosis in the Basilar Artery International Cooperation Study (BASICS): prevalence and outcome J Neurol. 2015;262:410-417	69
<b>Chapter 7</b>	The Basilar Artery International Cooperation Study (BASICS): study protocol for a randomised controlled trial Trials. 2013;14:200	87
<b>Chapter 8</b>	General discussion	105
	Summary	123



# Chapter 1

**General introduction**

---

## BACKGROUND

1

During early cancer drug development, detailed information on drug pharmacokinetics, including normal organ distribution, target expression at baseline and target kinetics over time are of great interest to increase insight in the mechanism of action, and to potentially optimize treatment schedule and patient selection. Furthermore, in the current era of immunotherapy, also information on the immune system and its changes over time is of potential relevance in order to incorporate obtained knowledge for future drug development, as well as for design of combination therapies. However, whole body information of normal organ drug distribution and target expression in humans is usually not available, as current pharmacokinetic and pharmacodynamic analyses are based on blood and/or tumor sampling. Assumptions with regard to pharmacokinetics are mainly based on empirical models, which are a simplified approximations of reality.<sup>1</sup> Moreover, knowledge from preclinical models are of limited value when studying whole body drug effects as animal models do not completely reflect the situation in men. Furthermore, pharmacodynamic analysis in humans can be hampered by the invasiveness of biopsy procedures or by the limited amount of available tumor material as lesions may not be accessible for a biopsy. As a consequence, target expression, as well as potential heterogeneity within and between metastatic sites, at baseline and over time are disregarded.

A well-known therapeutically relevant receptor in breast cancer is the human epidermal growth factor receptor 2 (HER2). Administration of trastuzumab, the anti-HER2 monoclonal antibody, improved overall survival in women with HER2-positive disease at various disease stages.<sup>2-4</sup> Other members of the HER-family, *e.g.* HER3, and growth factors such as the transforming growth factor- $\beta$  (TGF- $\beta$ ) have been evaluated as potential drug target in several tumor types.<sup>5-7</sup> But the most successful novel approach in cancer treatment is the activation of the immune system by immune checkpoint inhibition, which is less dependent on tumor characteristics such as driver mutations. Molecules of the programmed death-1 (PD-1) receptor/programmed death-ligand 1 (PD-L1) axis promote attenuation of T-cell activation, which subsequently suppresses the immune response and enables the tumor to evade the host's immune system.<sup>8-12</sup> PD-1/PD-L1 checkpoint inhibitors, such as nivolumab, pembrolizumab and atezolizumab, overcome this functional unresponsiveness and can induce impressive and durable responses, which led to registration of these drugs across several tumor types.<sup>8</sup> In certain settings, PD-L1 expression is currently being used as biomarker for patient selection. Identifying patients likely to benefit, however, remains challenging, as response is also observed in a substantial number of patients without high tumor PD-L1 expression. A macroscopic, non-invasive molecular imaging readout for an immune checkpoint like PD-L1 might provide new insights by assessing the expression status in normal tissues and in tumor lesions throughout

the whole body, potentially at multiple time points, capturing information about the tumor immune infiltrate and changes over time.

Molecular imaging with positron emission tomography (PET) is a non-invasive technique which can make use of monoclonal antibodies labeled with a radionuclide to assess their biodistribution and target expression at the whole body level. Depending on the characteristics of the molecule, a radionuclide with either a relatively short half-life (e.g. fluorine-18,  $^{18}\text{F}$ , with 110 minutes) or a longer half-life (e.g. zirconium-89,  $^{89}\text{Zr}$ , with 78.4 hours) can be chosen.<sup>13, 14</sup>  $^{89}\text{Zr}$ , thereby, has increasingly been used for labeling of monoclonal antibodies due to its favorable characteristics for PET imaging: i)  $^{89}\text{Zr}$  remains in cells after internalization of the antibody-target complex leading to high tumor image contrast via accumulation, and ii)  $^{89}\text{Zr}$ 's half-life allows target binding over a longer period of time and therefore properly matches the long half-life of monoclonal antibodies.<sup>14</sup> Until now over 20 therapeutic antibodies have been labeled with  $^{89}\text{Zr}$  and tested in clinical trials to assess biodistribution and target expression.<sup>13</sup> Performing serial PET scans before and during treatment, furthermore, allows investigation of target accessibility during treatment and may therefore be used to determine whether target saturation has been achieved. Multiple imaging trials in cancer patients have delivered detailed information on target distribution and dynamics, but data is not comparable due to different analysis approaches. With analysis of new targets and comparative analysis of already gathered data, PET could support understanding of working mechanisms, as well as development of future therapies, and improve patient selection.

## AIM OF THIS THESIS

The aim of this thesis is to investigate the role of molecular imaging with monoclonal antibodies to increase knowledge of whole body pharmacokinetics and pharmacodynamics, and to evaluate the contribution of molecular imaging to therapy decision making and to response prediction.

## OUTLINE OF THE THESIS

**Chapter 2** provides a literature overview of the potential role of molecular imaging in breast cancer. To this end, we performed a search of the current literature on molecular imaging of the two general tumor processes, proliferation and glucose metabolism, of the for breast cancer relevant receptors, the hormone receptors and the growth factor receptors, as well as molecular imaging of the tumor micro-environment. We thereby focused on the ability of molecular imaging to predict and monitor treatment response in this patient population.

**Chapter 3** describes the study performed to determine tumor target expression before and during treatment, as well as the normal organ distribution of the anti-HER3 monoclonal antibody lumretuzumab. To this end, lumretuzumab was labeled with  $^{89}\text{Zr}$  and serial PET imaging in patients with HER3-positive solid tumors was performed, at baseline and after the first antibody dose. Patients enrolled in the phase I drug dose finding trial were also eligible for participation in the imaging trial: after administration of 37 MBq  $^{89}\text{Zr}$ -lumretuzumab, initially only at baseline and later also after the first pharmacodynamic-active dose, up to 3 PET scans (2, 4 and 7 days after injection) were performed. Blood samples were collected during the imaging series to determine  $^{89}\text{Zr}$  and lumretuzumab pharmacokinetics. Normal organ distribution and tumor tracer uptake at baseline and after the first dose were evaluated by calculating the standardized uptake value.

In **chapter 4** we aimed to investigate  $^{89}\text{Zr}$ -fresolimumab uptake, an antibody against TGF- $\beta$ , in patients with recurrent high-grade glioma and to evaluate tumor response to fresolimumab treatment. Before fresolimumab treatment, patients received 37 MBq  $^{89}\text{Zr}$ -fresolimumab intravenously and underwent a PET scan of the brain 4 days after tracer injection. A second scan already 2 days after injection was additionally performed in some patients to assess the tumor tracer accumulation over time. Moreover, to assess normal organ distribution of  $^{89}\text{Zr}$ -fresolimumab a whole body PET instead of a brain only scan was performed in part of the enrolled patient population. Tumor tracer uptake was assessed by calculation of the standardized uptake value and treatment response was evaluated by magnetic resonance imaging of the brain. Blood samples were collected to assess fresolimumab and  $^{89}\text{Zr}$ -fresolimumab pharmacokinetics, next to amount of TGF- $\beta$ 1 in plasma. In addition to standard of care immunohistochemistry, p-SMAD2 was analyzed in archival paraffin embedded primary tumor tissue as readout for TGF- $\beta$  signalling.

In the past, multiple imaging trials with different  $^{89}\text{Zr}$ -labeled antibodies have been performed. Data comparison, however, was hampered by the lack of a harmonization protocol with regard to the performance of the PET scan including the reconstruction method and a standard delineation protocol. In **chapter 5**, the first comparative biodistribution analysis of four of our  $^{89}\text{Zr}$ -labeled monoclonal antibodies was performed. PET scans of nine patients per tracer were selected when the administered tracer activity was 37 MBq ( $\pm$  10%), the PET scan was performed 4 days after tracer injection together with a low-dose computed tomography (CT) and the tracer was complemented with the previously determined optimal unlabeled imaging protein dose. The scans were reconstructed based on the recently published  $^{89}\text{Zr}$ -harmonization protocol and analyzed according to our standardized delineation protocol for  $^{89}\text{Zr}$ -tracers using the software A Medical Imaging Data Examiner (AMIDE version 0.9.1; Stanford University). Normal tissue distribution of all four tracers, calculated as percentage injected dose per kilogram tissue normalized to the calibrated dose of the  $^{89}\text{Zr}$ -tracer and corrected for decay at the time of scanning, was compared and influence of tumor load, body weight and fat percentage were assessed.

The clinical trial, which is described in **chapter 6**, aimed to study the uptake of the  $^{89}\text{Zr}$ -labeled PD-L1 antibody atezolizumab in primary and metastatic tumor lesions and normal organ drug distribution in patients with non-small cell lung cancer, triple negative breast cancer or bladder cancer prior to treatment with atezolizumab. At baseline, eligible patients received  $^{89}\text{Zr}$ -atezolizumab including 10 mg unlabeled antibody followed by up to four PET scans 1 hour, 2, 4 and 7 days after tracer injection. During the PET imaging series, blood samples were collected for determination of tracer amount in the peripheral blood, peripheral blood mononuclear cell fraction and atezolizumab serum concentration. After the last PET scan a tumor biopsy was obtained for immunohistochemistry and RNA sequencing, and patients received atezolizumab monotherapy until disease progression. Response to treatment was monitored every 6 weeks by a diagnostic CT scan. PET image analysis was performed with the Accurate tool for volume-of-interest-based lesion and background analysis, and correlated to PD-L1 immunohistochemistry and RNA expression data from the tumor biopsies, as well as treatment response. Additionally, we studied PD-L1 and CD8 immunohistochemistry in normal lymph node and spleen tissue, and internalization of  $^{89}\text{Zr}$ -atezolizumab *in vitro* in the human lung mucoepidermoid pulmonary H292 and the bronchioalveolar H358 tumor cell line, as well as in peripheral blood mononuclear cells pooled from healthy volunteers.

In metastatic breast cancer management, up-to-date information of HER2 status is essential, due to variable expression during the course of the disease. This information, however, cannot always be obtained as lesions might not be accessible, due to patient- or tumor related factors, resulting in a dilemma with regard to treatment decisions. In the trial described in **chapter 7** we aimed to assess the clinical value of a  $^{89}\text{Zr}$ -trastuzumab PET in patients with metastatic breast cancer and a known history of HER2-positive disease, in whom standard work-up, including a bone scan, a  $^{18}\text{F}$ -fluorodeoxyglucose PET, a CT and if feasible a biopsy, failed to clarify HER2 status of their disease. We performed a  $^{89}\text{Zr}$ -trastuzumab PET scan in 20 patients presenting with such a clinical dilemma, next to central pathology revision of archival tumor material, and assessed HER2 status of circulating tumor cells. The referring clinicians completed three questionnaires to rate the clinical value of the additional PET scan in terms of diagnostic understanding and treatment decision. HER2 status of circulating tumor cells was correlated to treatment decision and  $^{89}\text{Zr}$ -trastuzumab PET result.

Finally, results of this thesis are summarized and future perspectives are given in **chapter 8**. The summaries in Dutch and German are provided in **chapters 9 and 10**.

## REFERENCES

1. Charnick, S. B. *et al.* Perspectives in pharmacokinetics. Physiologically based pharmacokinetic modeling as a tool for drug development. *J. Pharmacokinet. Biopharm.* 23, 217-229 (1995).
2. Perez, E. A. *et al.* Four-year follow-up of trastuzumab plus adjuvant chemotherapy for operable human epidermal growth factor receptor 2-positive breast cancer: joint analysis of data from NCCTG N9831 and NSABP B-31. *J. Clin. Oncol.* 29, 3366-3373 (2011).
3. Swain, S. M. *et al.* Pertuzumab, trastuzumab, and docetaxel for HER2-positive metastatic breast cancer (CLEOPATRA study): overall survival results from a randomised, double-blind, placebo-controlled, phase 3 study. *Lancet Oncol.* 14, 461-471 (2013).
4. Gianni, L. *et al.* Neoadjuvant and adjuvant trastuzumab in patients with HER2-positive locally advanced breast cancer (NOAH): follow-up of a randomised controlled superiority trial with a parallel HER2-negative cohort. *Lancet Oncol.* 15, 640-647 (2014).
5. Kol, A. *et al.* HER3, serious partner in crime: therapeutic approaches and potential biomarkers for effect of HER3-targeting. *Pharmacol. Ther.* 143, 1-11 (2014).
6. Meulendijks, D. *et al.* First-in-human phase I study of lumretuzumab, a glycoengineered humanized anti-HER3 monoclonal antibody, in patients with metastatic or advanced HER3-positive solid tumors. *Clin. Cancer Res.* 22, 877-885 (2016).
7. Eichhorn, P. J. *et al.* USP15 stabilizes TGF- $\beta$  receptor I and promotes oncogenesis through the activation of TGF- $\beta$  signaling in glioblastoma. *Nat. Med.* 18, 429-435 (2012).
8. Freeman, G. J. Structures of PD-1 with its ligands: sideways and dancing cheek to cheek. *Proc. Natl. Acad. Sci. USA* 105, 10275-10276 (2008).
9. Butte, M. J., Keir, M. E., Phamduy, T. B., Sharpe, A. H. & Freeman, G. J. Programmed death-1 ligand 1 interacts specifically with the B7-1 costimulatory molecule to inhibit T cell responses. *Immunity* 27, 111-122 (2007).
10. Frey, A. B. & Monu, N. Signaling defects in anti-tumor T cells. *Immunol. Rev.* 222, 192-205 (2008).
11. Greenwald, R. J., Freeman, G. J. & Sharpe, A. H. The B7 family revisited. *Annu. Rev. Immunol.* 23, 515-548 (2005).
12. Paterson, A. M. *et al.* The programmed death-1 ligand 1:B7-1 pathway restrains diabetogenic effector T cells in vivo. *J. Immunol.* 187, 1097-1105 (2011).
13. Lamberts, L. E. *et al.* Antibody positron emission tomography imaging in anticancer drug development. *J. Clin. Oncol.* 33, 1491-1504 (2015).
14. Verel, I. *et al.*  $^{89}\text{Zr}$  immuno-PET: comprehensive procedures for the production of  $^{89}\text{Zr}$ -labeled monoclonal antibodies. *J. Nucl. Med.* 44, 1271-1281 (2003).





# Chapter 2

## **Molecular imaging for monitoring treatment response in breast cancer patients**

---

Frederike Bensch<sup>1</sup>, Michel van Kruchten<sup>1</sup>, Laetitia E. Lamberts<sup>1</sup>, Carolien P. Schröder<sup>1</sup>, Geke A.P. Hospers<sup>1</sup>, Adrienne H. Brouwers<sup>2</sup>, Marcel A.T.M. van Vugt<sup>1</sup>, Elisabeth G.E. de Vries<sup>1</sup>

<sup>1</sup>Department of Medical Oncology, <sup>2</sup>Department of Nuclear Medicine and Molecular Imaging, University of Groningen, University Medical Centre Groningen, Groningen, The Netherlands.

## ABSTRACT

2

Currently, tumor response following drug treatment is based on measurement of anatomical size changes. This is often done according to Response Evaluation Criteria in Solid Tumors (RECIST) and is generally performed every 2-3 cycles. Bone metastases, being the most common site of distant metastases in breast cancer, are not measurable by RECIST. The standard response measurement provides no insight in changes of molecular characteristics. In the era of targeted medicine, knowledge of specific molecular tumor characteristics becomes more important. A potential way to assess this is by means of molecular imaging. Molecular imaging can visualize general tumor processes, such as glucose metabolism with  $^{18}\text{F}$ -fluorodeoxyglucose ( $^{18}\text{F}$ -FDG) and DNA synthesis with  $^{18}\text{F}$ -fluorodeoxythymidine ( $^{18}\text{F}$ -FLT). In addition, an increasing number of more specific targets, such as hormone receptors, growth factor receptors, and growth factors can be visualized. In the future molecular imaging may thus be of value for personalized treatment-selection by providing insight in the expression of these drug targets. Additionally, when molecular changes can be detected early during therapy, this may serve as early predictor of response. However, in order to define clinical utility of this approach results from (ongoing) clinical trials is required.

In this review we summarize the potential role of molecular imaging of general tumor processes as well as hormone receptors, growth factor receptors, and tumor micro-environment for predicting and monitoring treatment response in breast cancer patients.

## 1. INTRODUCTION

Treatment decision-making in locally advanced and metastatic breast cancer is currently based on the extent and sites of disease, and the expression of hormone receptors as well as the human epidermal growth factor receptor 2 (HER2). To assess the effect of the initiated therapy, response monitoring is performed. The European Society of Medical Oncology (ESMO) and National Comprehensive Cancer Network (NCCN) guidelines therefore advise serial conventional radiography, with chest X-ray, computed tomography (CT) or magnetic resonance imaging (MRI).<sup>1,2</sup>

The most commonly used criteria for defining response are provided in the Response Evaluation Criteria for Solid Tumors (RECIST v1.1).<sup>3</sup> These criteria use anatomical measurements and are based on a warehouse filled with data from chemotherapy trials. Objective tumor response with tumor shrinkage of  $\geq 30\%$  and progression with tumor growth of  $\geq 20\%$  or new lesions, are widely applied endpoints in clinical trials. The only exception of non-anatomical imaging in RECIST criteria is new metastases detected on  $^{18}\text{F}$ -fluorodeoxyglucose positron emission tomography ( $^{18}\text{F}$ -FDG PET).

With the rising number of targeted drugs for breast cancer treatment, there is an increasing need for reliable predictive biomarkers to select the most suitable therapy for the individual patient. For targeted therapies, the precise value of RECIST criteria is not yet known. Especially in case of targeted agents, visualization of distinct molecular targets or drug behavior may also be of interest.

Anatomical imaging determines response by evaluating measurable lesions. This approach excludes many breast cancer patients from response evaluation according to RECIST, as bone metastases are the most common site of distant metastases. They occur in  $\sim 70\%$  of the patients and are in 17-34% of the patients the only site of presentation at the initial diagnosis of metastatic disease.<sup>4</sup> Currently bone scintigraphy is the standard staging method to detect bone metastases. However, for response evaluation bone scintigraphy is not valuable, since it takes 6 months or longer to reliably detect a response.<sup>5</sup> Therefore patients with bone-only disease are often excluded from clinical trials. This is undesirable as bone metastases apart from being frequently occurring, can cause symptoms.<sup>6</sup> It would therefore be valuable to have a tool that allows also response evaluation in bone metastases.

Finally, response monitoring by conventional methods is recommended after 2-3 months for endocrine therapy and 2-3 cycles of chemotherapy.<sup>1</sup> This period is needed since size changes often occur at a modest pace. It would clearly be a big advantage when before or early during treatment anti-tumor efficacy could be predicted. Similarly, patients with locally-advanced breast cancer receiving neo-adjuvant chemotherapy may benefit from early response monitoring, since ineffective treatment could be timely replaced.

In breast cancer, estrogen receptor (ER) and HER2 expression, in general measured immunohistochemically, are proven biomarkers. Presence of these receptors is predictive for respectively response to endocrine and HER2-targeted therapy.<sup>7</sup> Recent guidelines advise re-evaluation of receptor status in metastatic patients, since discordances between primary tumor and metastases can occur in up to 40% of the patients.<sup>8,9</sup> Therefore ESMO and NCCN guidelines advise that histology and receptor expression should be repeated at relapse.<sup>1,2</sup> A biopsy can however not always be obtained, and tumor characteristics can be heterogeneously expressed within and across metastases. It might therefore well be valuable to obtain whole-body information about the expression of relevant drug targets in all tumor lesions within an individual patient.

A potential novel way of response monitoring is by molecular imaging with single photon emission computed tomography (SPECT) or PET imaging with radio-labeled tracers. This allows serial measurements of general tumor processes such as glucose metabolism with <sup>18</sup>F-FDG PET or DNA synthesis with <sup>18</sup>F-fluorodeoxy-L-thymidine (<sup>18</sup>F-FLT PET). Increasingly, also relevant drug targets can be visualized such as hormone receptors, growth factor receptors, and growth factors. Molecular imaging of drug-specific targets can in the future potentially support selection of patients for certain therapies and measure early treatment-specific changes in tumors. The recently developed multimodality scanners, such as PET/CT and PET/MRI, combine anatomical and molecular information (Fig. 1). In this review, we summarize the available literature on PET imaging of general tumor processes, hormone receptors, growth factor receptors, and tumor micro-environment, for predicting and monitoring treatment response in breast cancer.

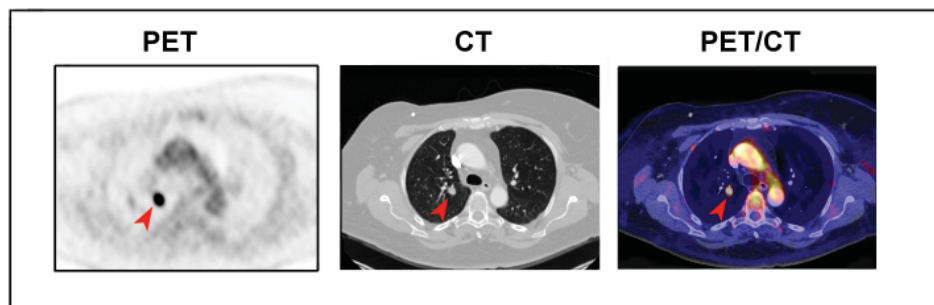


**Figure 1** PET imaging (left) can acquire molecular information, while on CT scan (middle) anatomical information can be obtained. Fusion of both techniques (right) allows simultaneous visualization of molecular and anatomical information. In this example of a patient with metastatic breast cancer, areas with increased <sup>18</sup>F-FDG uptake can be observed in a right axillary lymph node, sternum, and chest wall metastasis.

## 2. $^{18}\text{F}$ -FDG PET

The possibility to visualize glucose metabolism and thereby metabolic activity of malignancies with  $^{18}\text{F}$ -FDG PET has led to a wide range of studies evaluating it for primary tumor detection, diagnosis, (re)staging and monitoring therapy response.  $^{18}\text{F}$ -FDG PET is currently not recommended for primary breast cancer staging. The resolution of the PET-camera does not permit detection of small primary lesions as well as nodal sites, and tracer uptake characteristics vary within different (breast) cancers.<sup>10-12</sup> To limit overuse of  $^{18}\text{F}$ -FDG PET in primary staging and follow-up it is included as 2 of the 5 don'ts of the American Society of Clinical Oncology in the American Board of Internal Medicine Foundation's Choosing Wisely® campaign.<sup>13</sup> NCCN and ESMO guidelines advise to consider  $^{18}\text{F}$ -FDG PET as additional work up in locally advanced, inflammatory, recurrent or metastatic disease, especially when standard imaging remains equivocal or suspicious, and if lesions are inaccessible for biopsy.<sup>1,2</sup>

Several trials studied  $^{18}\text{F}$ -FDG PET to monitor treatment response (Table 1). In 1999, the European Organization for Research and Treatment of Cancer (EORTC) PET study group developed criteria to measure lesions at baseline and to objectify treatment response using  $^{18}\text{F}$ -FDG PET, based on hypothetical considerations as well as literature review with limited published and unpublished data available.<sup>14</sup> The change in standardized uptake value (SUV) within the tumor lesion compared to a previous scan is used for the assessment. Complete metabolic response is defined as complete resolution of the lesion's  $^{18}\text{F}$ -FDG signal against its surrounding tissue, partial metabolic response as a reduction of  $\geq 15\%$  SUV after one cycle or  $\geq 25\%$  after 2 or more cycles. It is emphasized that also standardized imaging protocols are required to be able to evaluate response. Another attempt to introduce a standard method for PET interpretation is formulated in the PERCIST criteria.<sup>15</sup> After an extensive literature review, response criteria were proposed and conclusions were obtained using a Delphi-like approach. The PERCIST criteria advise to correct the SUV for lean body mass (SUL). Here partial metabolic response is defined as a SUL peak reduction of  $\geq 30\%$ . Furthermore, signal of the target lesion must be less than mean liver activity and indistinguishable from surrounding blood-pool levels to be evaluated as complete metabolic response.

Several studies evaluated response by measuring metabolic activity with  $^{18}\text{F}$ -FDG PET. In a meta-analysis, 19 mainly prospective ( $n = 17$ ) studies with in total 786 breast cancer patients who received neo-adjuvant treatment were included.<sup>16</sup> In 15 studies  $^{18}\text{F}$ -FDG PET scan was performed before and at different moments during chemotherapy. The pooled analysis showed that  $^{18}\text{F}$ -FDG PET with a sensitivity of 84%, a negative predictive value of 91% and a diagnostic odds ratio (DOR) of 11.9 has a beneficial value to forecast pathological response after neo-adjuvant chemotherapy. However, because of relatively low specificity (66%) and positive predictive value (50%)  $^{18}\text{F}$ -FDG PET has to be interpreted carefully in the clinic. In a subgroup analysis  $^{18}\text{F}$ -FDG

**Table 1** <sup>18</sup>F-FDG PET studies aiming to predict and monitor treatment response in metastatic breast cancer

Ref #	Treatment	No. pts	Clinical endpoint	PET endpoints	PPV/NPV
26	Tamoxifen	40	CR+PR+SD	≥ 10% increase in <sup>18</sup> F-FDG-uptake 7-10 days after therapy initiation <sup>a</sup>	91%/94%
28	AI (n = 40) FUL (n = 11)	51	CR+PR+SD	≥ 12% increase in <sup>18</sup> F-FDG-uptake 1 day after 30 mg oestradiol <sup>a</sup>	100%/94%
29	Estradiol 6 mg or 30 mg	46	CR or PR or SD according to RECIST after 24 weeks	≥ 12% increase in <sup>18</sup> F-FDG-uptake 1 day after therapy initiation	80%/87%
30	Anti-hormonal (various)	22	PFS	PFS 28 months in metabolic responders and stable disease vs. PFS 6 months in metabolic non-responders (EORTC criteria)	NA
18	TAG vs. AT	9	CR or PR according to WHO criteria, after 6 cycles	> 10% decrease in <sup>18</sup> F-FDG-uptake after the 1 <sup>st</sup> cycle of chemotherapy <sup>a</sup>	100%/100%
20	AC vs. AT	11	CR or PR or SD according to WHO criteria, after 6 cycles	≥ 20% decrease in <sup>18</sup> F-FDG uptake after the 1 <sup>st</sup> cycle of chemotherapy <sup>a</sup>	86%/71%
21	A (n = 4) and T (n = 16)	20	CR or PR according to RECIST and/or clinical assessment, after 6 cycles	EORTC criteria (≥ 15% decrease in <sup>18</sup> F-FDG uptake) after the 1 <sup>st</sup> cycle of chemotherapy  EORTC criteria (> 25% decrease in <sup>18</sup> F-FDG uptake) after the 3 <sup>rd</sup> cycle of chemotherapy	75%/75%  63%/75%

<sup>a</sup> Retrospectively defined optimal threshold. CR, complete response; PR, partial response; SD, stable disease; PPV, positive predictive value; NPV, negative predictive value; AI, aromatase inhibitor; FUL, fulvestrant; G, gemcitabine; A, anthracycline; T, taxane; C, cyclophosphamide; NA, not available.

PET after 1-2 cycles of neo-adjuvant treatment had a better DOR (21.8), sensitivity (88%) and specificity (70%) than PET scanning after 3 cycles or later (DOR 5.1, sensitivity 81%, specificity 61%). In this data set, complete response defined by a SUV decrease of ≥ 55-65% would predict response to neo-adjuvant therapy in primary breast cancer more accurately.

In metastatic breast cancer <sup>18</sup>F-FDG PET has been evaluated for its ability to predict (early) response and survival. In several prospective studies with in total 61 locally advanced or metastatic breast cancer patients receiving chemotherapy, <sup>18</sup>F-FDG uptake decreased in almost all responding lesions already after the first cycle.<sup>17-21</sup> Analysis of 11 patients showed a SUV

decrease of  $38\% \pm 21\%$  in responding and  $6\% \pm 19\%$  in non-responding lesions after the first course.<sup>20</sup> After the second and third course 31 patients in two studies experienced a SUV decrease in responders of  $46\% \pm 16\%$  in one and 52-56% in the other study and in non-responders  $21\% \pm 9\%$  and 16-26%, respectively.<sup>20,21</sup> The ability to predict survival was evaluated prospective and retrospective in 4 studies in a total of 306 patients.<sup>22-25</sup> The second  $^{18}\text{F}$ -FDG PET scan was done as mid-therapy scan or at the end of treatment. About half of the patients had bone dominant or bony disease and all patients received different systemic therapies. Whereas  $^{18}\text{F}$ -FDG PET was predictive for survival in all four data sets, just in two studies this ability remained present in a multivariate analysis.<sup>24,25</sup>

The main focus for the role of  $^{18}\text{F}$ -FDG PET during hormonal treatment has been on the metabolic flare phenomenon as measured by an initial increase in tumor  $^{18}\text{F}$ -FDG uptake. This phenomenon can already be observed 24 h after therapy initiation. In two studies in a total of 40 metastatic breast cancer patients,  $^{18}\text{F}$ -FDG PET was performed prior to and 7-10 days after start of tamoxifen. Response was based on a combination of RECIST and clinical assessment. While in the responding patients (complete or partial response, or stable disease  $\geq 6$  months) a higher tumor  $^{18}\text{F}$ -FDG uptake was noted 7-10 days after the initiation of tamoxifen, in the non-responding patients tumor  $^{18}\text{F}$ -FDG uptake decreased ( $28 \pm 23\%$  vs.  $10 \pm 16\%$ ,  $P = 0.0002$ ).<sup>26,27</sup> An arbitrary 10% increase in tumor  $^{18}\text{F}$ -FDG uptake would have resulted in a 91% positive predictive value and 94% negative predictive value for response to tamoxifen.

In another study in 51 postmenopausal metastatic breast cancer patients,  $^{18}\text{F}$ -FDG PET was performed prior to and 1 day after 30 mg estradiol orally. Thereafter the patients received an aromatase inhibitor ( $n = 40$ ) or fulvestrant ( $n = 11$ ).  $^{18}\text{F}$ -FDG tumor uptake (SUVmax) increased in patients that subsequently responded to endocrine therapy compared to a slight decrease in non-responding patients ( $21 \pm 24\%$  vs.  $-4 \pm 11\%$ ;  $P < 0.0001$ ). Receiver-operating-characteristic (ROC) analysis revealed an optimal threshold of 12% increase in  $^{18}\text{F}$ -FDG uptake to differentiate between responders and non-responders.<sup>28</sup> Finally, this threshold was prospectively evaluated in 66 metastatic patients randomized to estradiol 6 mg or 30 mg daily. Forty-six patients underwent serial  $^{18}\text{F}$ -FDG PET. The prospectively defined 12% increase in tumor  $^{18}\text{F}$ -FDG uptake, 1 day after initiation of the assigned dose of estradiol, positively predicted response in 80% (12 of 15 such patients responded), and negatively predicted response in 87% (27 of 31 such patients did not respond,  $P < 0.001$ ).<sup>29</sup>

A few small studies evaluated  $^{18}\text{F}$ -FDG PET after a longer period of endocrine therapy. In 22 ER-positive metastatic breast cancer patients on various endocrine drugs,  $^{18}\text{F}$ -FDG PET was performed within 7 days prior to therapy initiation and at a mean of  $10 \pm 4$  weeks later. Mean progression free survival (PFS) was 27.5 months in the group with metabolic response or stable metabolic disease, compared to 5.8 months in patients with progressive metabolic disease ( $P < 0.0001$ ) according to EORTC criteria.<sup>30</sup> In a neo-adjuvant study in 11 patients with ER-positive

breast tumors,  $^{18}\text{F}$ -FDG PET was performed prior to and 4 weeks after start of letrozole, followed by surgery at 12 weeks.<sup>31</sup> Metabolic response, defined as > 40% decrease in tumor  $^{18}\text{F}$ -FDG uptake (SUVmax), did not correlate with morphologic and pathologic response. Metabolic responders did however have a clear decrease in Ki-67 labeling index ( $91\% \pm 11\%$  relative decrease) compared to non-responders.

Few clinical and preclinical studies addressed response evaluation with  $^{18}\text{F}$ -FDG PET after administration of HER2-targeting drugs in breast cancer. In patients with advanced malignancies, SUV decreased > 25% after 1 month of lapatinib treatment in 4 out of 8 patients (breast cancer  $n = 1$ ), one of whom had partial response, while the other 3 had stable ( $n = 2$ ) or progressive disease.<sup>32</sup>

A number of preclinical studies evaluated effects of targeted drugs on  $^{18}\text{F}$ -FDG PET. However, studies evaluating  $^{18}\text{F}$ -FDG PET in mouse models need to be interpreted cautiously. Biodistribution in mice is dependent on dietary status, ambient temperature and muscle activity, and tumor uptake often seems low because of high background uptake of normal tissue.<sup>33</sup>

Mice with HER2-over-expressing or with low HER2-expressing human xenografts were treated with trastuzumab or phosphate-buffered saline (PBS) on day 1, 2, 7 and 14.<sup>34</sup>  $^{18}\text{F}$ -FDG uptake was lower in trastuzumab treated HER2-over-expressing mice than in the PBS treated control group after 16, but not after 2 or 9 days. Tracer uptake was not influenced in trastuzumab and PBS treated mice with low HER2-expression. In another study, mice with tumors transplanted from MMTV/HER2 transgenic mice or with BT474 human xenografts were treated and imaged twice weekly for 3 weeks with trastuzumab or PBS.<sup>35</sup> In contrast to the former study, independent of tumor response  $^{18}\text{F}$ -FDG uptake did not change. Heat shock protein 90 (HSP90) inhibitors, such as 17-AAG and NVP-AUY922 have mostly been tested combined with  $^{18}\text{F}$ -FLT PET in preclinical studies (see section 3). In a BT474 human xenograft mouse model treated with 17-AAG once, there was no change in  $^{18}\text{F}$ -FDG uptake during the first 22 days thereafter.<sup>36</sup>

In conclusion, FGD PET can be of value in case of advanced stage and problematic staging of breast cancer. For response monitoring several studies suggest a potential role in (metastatic) breast cancer. But given several unsolved issues, it is not yet part of standard tumor response measurement guidelines.

### 3. $^{18}\text{F}$ -FLT PET

Uptake of  $^{18}\text{F}$ -FLT is determined by the activity of the enzyme thymidine kinase, which is involved in DNA synthesis and reflects therefore indirectly the proliferative state of cells. This was confirmed in a meta-analysis where  $^{18}\text{F}$ -FLT uptake correlated with Ki-67 staining with sufficient data available for at least brain, lung and breast cancer.<sup>37</sup> Over the last years small studies evaluated the ability of this tracer to monitor response in breast cancer. Fourteen patients

with metastatic breast cancer, treated by chemotherapy ( $n = 9$ ) or hormonal therapy ( $n = 5$ ) underwent  $^{18}\text{F}$ -FLT PET scans at baseline, 2 weeks after the first and 2 weeks after the last course of therapy or maximal 1 year after the initial scan.<sup>38</sup> Here,  $^{18}\text{F}$ -FLT uptake correlated with overall response, based on change in tumor marker (CA27.29;  $r = 0.79$ ) and tumor size measured on CT ( $r = 0.74$ ). In another prospective study  $^{18}\text{F}$ -FLT PET and response was analyzed in 12 breast cancer patients.<sup>39</sup> Scans were performed at baseline and one week after the first administration of 5-fluoruracil, epirubicin and cyclophosphamide (FEC). Tumors were assessed according to the RECIST criteria and proliferation was scored as response when  $^{18}\text{F}$ -FLT SUV decreased at least 18%. With these prospectively defined criteria,  $^{18}\text{F}$ -FLT PET showed response in 12 out of 17 lesions. In these lesions, mean SUV change 1 week after the first course of chemotherapy was higher than in non-responding lesions (-41.3% vs. +3.1%). The 6 clinically responding patients were identified correctly by  $^{18}\text{F}$ -FLT PET. Response assessment in another 18 patients after the first or second cycles of docetaxel has been performed.<sup>40</sup> Response criteria were prospectively defined either according to RECIST in case of conventional imaging or a SUV change of  $\geq 20\%$ . Change of the  $^{18}\text{F}$ -FLT signal after 1-2 cycles correlated with the size of the lesion after the third cycle ( $r = 0.64$ ). Eleven out of 13 responders and 4 out of 5 non-responders were correctly identified with  $^{18}\text{F}$ -FLT PET. Sensitivity of  $^{18}\text{F}$ -FLT PET was 85% with a specificity of 80%.<sup>40</sup> Six patients with locally advanced or metastatic breast cancer treated with capecitabine were scanned 2-10 days before and 1 hour after the first drug administration.<sup>41</sup> Interestingly, tracer uptake increased 3.4%-84.5% in 9 out of 10 lesions. Other parameters like blood flow and  $^{18}\text{F}$ -FLT delivery variables were largely unchanged. Increased influx of nucleosides due to redistribution of nucleoside transporters and increased activity of thymidine kinase 1 induced by thymidylate synthase inhibition may explain this flare phenomenon.<sup>41,42</sup>

Preclinical studies addressed response evaluation on targeted agents with  $^{18}\text{F}$ -FLT PET, mainly in comparison to  $^{18}\text{F}$ -FDG PET.  $^{18}\text{F}$ -FLT, but not  $^{18}\text{F}$ -FDG, 3 days after pulse treatment with NVP-AUY922 in BT474 multilayer spheroids showed, in accordance with growth inhibition, a dose-dependent decrease in tracer uptake.<sup>43</sup> A second study confirmed this positive correlation between changes in  $^{18}\text{F}$ -FLT uptake and growth inhibition in BT474, MCF-7, U87MG and HCT116 cell spheroids.<sup>44</sup>  $^{18}\text{F}$ -FDG uptake only correlated highly in BT474 spheroids and poorly in MCF-7 cells. Trastuzumab treatment in mice with BT474 human xenografts reduced  $^{18}\text{F}$ -FLT tumor uptake, whereas uptake was not changed in mice with tumors transplanted from MMTV/HER2 transgenic mice after treatment.<sup>35</sup>

Moreover, it is important to take into account that  $^{18}\text{F}$ -FLT uptake in rodents is influenced by a higher thymidine plasma level as compared to humans. Competition of endogenous thymidine and  $^{18}\text{F}$ -FLT can be neutralized by administration of thymidine phosphorylase right before tracer injection, leading to increased tracer accumulation in the tumor.<sup>45</sup> If neutralization was no part of the imaging protocol, interpretation of  $^{18}\text{F}$ -FLT uptake in rodents must be done carefully. However, in the latter study it is not reported that thymidine neutralization was done.

**Table 2 (Ongoing) clinical trials with <sup>18</sup>F-FDG PET and <sup>18</sup>F-FLT PET for determination of predictive value before and/or during breast cancer therapy**

Tracer	Therapy	Scan planning	Planned no. of pts	Aim of the study	Clin. Trial ID (NCT#)
<sup>18</sup> F-FDG	Trastuzumab-DM1	After cycle 1 and 3 palliative trastuzumab-DM1	60	Negative predictive value of the early <sup>18</sup> F-FDG PET for response on trastuzumab-DM1 therapy	01565200
<sup>18</sup> F-FDG	NAC	Before start, 15 days after 1 cycle	80	Value of <sup>18</sup> F-FDG PET after 1 course of NAC in prediction of pathological response	01038258
<sup>18</sup> F-FDG/ <sup>18</sup> F-FLT	NAC	Before start, after cycle 1 and just before cycle 2	30	Value of changes in the SUV as a predictor of complete pathologic response	01222416
<sup>18</sup> F-FDG	NAC	Before start of therapy and after cycle 1 and 6	50	Efficacy of multi-parametric MRI, <sup>18</sup> F-FDG PET, and PET-MR fusion imaging in the prediction and monitoring response to NA	01190566
<sup>18</sup> F-FDG PEM	NAC	Bilateral and axillary PEM and MRI at baseline, after 1-2 weeks and after 3-4 weeks of NAC	50	Response to NAC	01012440
<sup>18</sup> F-FDG	HER2-targeted or hormonal therapy	Before and 2 weeks after neo-adjuvant or palliative therapy	40	Correlation between the % change in <sup>18</sup> F-FDG PET SUV and % change in cell proliferation (assessed in tumor biopsy)	00362973
<sup>18</sup> F-FDG/ <sup>18</sup> F-FLT	NAC	Prior to and after completion of NAC before definitive surgery	20	Sensitivity and specificity of <sup>18</sup> F-FLT PET compared to <sup>18</sup> F-FDG PET. Correlation between PET and % Ki-67.	01018251
<sup>18</sup> F-FLT	NAC	Before start, after 1 cycle, and at the end of NAC	45	Correlation between change in tumor <sup>18</sup> F-FLT uptake and % Ki-67	01015131
<sup>18</sup> F-FLT/ <sup>18</sup> F-FDG/MRI	NAC	At initial staging, 3 times during NAC and prior to surgery	60	Sensitivity and specificity of the three imaging modalities for prediction of response to NAC	00236275
<sup>18</sup> F-FLT	NAC	Before start, mid-treatment, and prior to surgery	36	Predictive value of <sup>18</sup> F-FLT PET for response to NAC	00572728
<sup>18</sup> F-FLT	NAC	Before start, before cycle 2 and prior to surgery	100	Predictive value of <sup>18</sup> F-FLT PET for response to NAC according to Sataloff criteria <sup>94</sup>	00534274
<sup>18</sup> F-FDG	Hormonal therapy	Before start	100	Predictive value of <sup>18</sup> F-FDG PET for response to hormonal therapy	00358098

NAC, neo-adjuvant chemotherapy; PEM, positron emission mammography; PET, positron emission tomography; SUV, standardized uptake value; <sup>18</sup>F-FDG, <sup>18</sup>F-fluorodeoxyglucose; <sup>18</sup>F-FLT, <sup>18</sup>F-fluorodeoxythymidine.

There is currently no role for  $^{18}\text{F}$ -FLT PET in standard clinical breast cancer care. More information is expected from 6 ongoing trials in over 250 patients. In these trials results are compared between  $^{18}\text{F}$ -FLT PET and  $^{18}\text{F}$ -FDG PET, MRI and CT as well as to histological parameters like Ki-67, grade and tumor type in the neo-adjuvant setting (Table 2).

## 4. HORMONE RECEPTOR IMAGING

### Estrogen receptor

The most relevant hormone receptor in breast cancer is the ER. It is expressed in ~ 75% of the patients. For the patients with an ER-positive tumor, endocrine therapy can be an important treatment option.

A novel way to evaluate ER expression is by  $^{18}\text{F}$ -fluoroestradiol ( $^{18}\text{F}$ -FES) PET.  $^{18}\text{F}$ -FES PET measures tumor ER-expression with a 69-100% sensitivity and 80-100% specificity when compared to *in vitro* assays.<sup>46-49</sup> These results support future trials to examine  $^{18}\text{F}$ -FES PET to re-evaluate ER-expression non-invasively in patients that cannot be biopsied, and thus may support treatment decision-making.<sup>50</sup>

$^{18}\text{F}$ -FES PET has been evaluated as biomarker to predict response in four relatively small studies.<sup>26-28, 51</sup> Here, the positive predictive value of increased  $^{18}\text{F}$ -FES uptake at baseline was limited and ranged 34-79%, while the negative predictive value of low  $^{18}\text{F}$ -FES uptake was relatively good (81-100%). Although these results show the potential of  $^{18}\text{F}$ -FES PET to guide therapy decisions, still many aspects are unresolved. Most importantly, aforementioned studies have used different, often retrospectively defined, thresholds to dichotomize  $^{18}\text{F}$ -FES PET results.

Serial  $^{18}\text{F}$ -FES PET imaging was studied to measure effect of endocrine therapy in two small studies. A retrospective study in 30 metastatic breast cancer patients evaluated  $^{18}\text{F}$ -FES uptake prior to and 1-18 weeks after endocrine therapy initiation.<sup>52</sup> Drugs that competitively bind the ER (tamoxifen and fulvestrant) blocked tumor  $^{18}\text{F}$ -FES uptake, although partially with an average decrease of 54%. Aromatase inhibitors, which affect circulating estrogen levels, hardly affected tumor  $^{18}\text{F}$ -FES uptake (< 15% decrease).<sup>52</sup> Correlation between changes in  $^{18}\text{F}$ -FES uptake and clinical outcome was not evaluated. In a prospective study in 40 metastatic breast cancer patients,  $^{18}\text{F}$ -FES PET was performed prior to and 7-10 days after the initiation of tamoxifen. Response was defined as objective tumor response or stable disease (< 50% decrease and < 25% increase in lesion diameter)  $\geq$  6 months.<sup>26</sup> Responders had a larger decrease in  $^{18}\text{F}$ -FES uptake than non-responders (-55% vs. -19%,  $P = 0.0003$ ). However, the threshold to optimally differentiate between responders and non-responders, as well as the corresponding positive and negative predictive value, is still to be elucidated.

### Androgen receptor

The androgen receptor (AR) is a key target in prostate cancer patients and various anti-androgens are available in the clinic. The AR is expressed in ~ 70% of all breast cancer patients, and 12-40% of the so-called triple-negative patients.<sup>53, 54</sup> Therefore, the AR is currently also being explored as a potential therapeutic target in breast cancer.<sup>55-57</sup> The AR can be imaged by <sup>18</sup>F-fluorodihydrotestosterone (FDHT) PET. Currently no information is available on FDHT PET in breast cancer patients. In metastatic prostate cancer patients, <sup>18</sup>F-FDHT uptake occurs in the majority of metastases.<sup>58</sup> This uptake can be blocked by the AR antagonists flutamide and MDV3100, illustrating the specificity of <sup>18</sup>F-FDHT for the AR.<sup>59, 60</sup> With the emerging interest for anti-androgen therapy in breast cancer patients, this PET tracer may well show its value in the near future.

### Progesterone receptor

The progesterone receptor (PR), although not a direct target of endocrine therapy in breast cancer itself, is a predictive marker for response to anti-estrogen therapy. Several attempts have been made to develop a PR-specific PET tracer, although with limited success. The best tracer available to date is 21-<sup>18</sup>F-fluoro-16 $\alpha$ ,17 $\alpha$ -[[(R)-1'- $\alpha$ -furylmethylidene)dioxy]-19-norpregn-4-ene-3,20-dione (<sup>18</sup>F-FFNP). In 22 patients <sup>18</sup>F-FFNP PET showed visually increased uptake in 15 of 16 PR-positive primary breast tumors, while <sup>18</sup>F-FFNP uptake was moderate-low in 5 of 6 PR-negative primary breast tumors.<sup>61</sup> However, no correlation between quantitative <sup>18</sup>F-FFNP uptake and PR status determined by immunohistochemistry was observed nor did <sup>18</sup>F-FFNP uptake differ in PR-positive compared to PR-negative tumor lesions (SUV<sub>max</sub> 2.5  $\pm$  0.9 vs. 2.0  $\pm$  1.3). The prognostic and predictive value of <sup>18</sup>F-FFNP PET, and the use of <sup>18</sup>F-FFNP PET to monitor treatment response, has not been evaluated in the clinic. In a preclinical study, however, in mice with ER/PR-positive murine mammary adenocarcinomas the ER-antagonist fulvestrant decreased <sup>18</sup>F-FES-uptake in both fulvestrant-sensitive and fulvestrant-resistant tumors, while tumor <sup>18</sup>F-FFNP-uptake only decreased in the fulvestrant-sensitive tumors. These early results suggest that serial <sup>18</sup>F-FFNP PET may be a good read-out and predictor of endocrine therapy efficacy.<sup>62</sup>

## 5. GROWTH FACTOR RECEPTOR IMAGING

Amplification of the HER2 gene results in over-expression of the HER2 protein, which occurs in 20-25% of primary breast cancers.<sup>63, 64</sup> HER2 is a member of the cell surface receptor HER family with tyrosine kinase activity, involved in transmission of signals controlling cell growth and proliferation. HER2-over-expression, when left untreated, is associated with aggressive growth and poor prognosis.<sup>65, 66</sup> The anti-HER2 monoclonal antibody trastuzumab, which targets the

extracellular domain of HER2, is part of treatment in the adjuvant as well as in the metastatic setting of HER2-positive breast cancer.<sup>67,68</sup>

We used radio-labeled trastuzumab for molecular imaging of the HER2 status in breast cancer patients with SPECT and PET. First the SPECT tracer <sup>111</sup>In-trastuzumab was developed for clinical use. Subsequently in 15 HER2-expressing metastatic breast cancer patients, specific uptake of <sup>111</sup>In-trastuzumab was shown in HER2-positive tumor lesions. In addition, new HER2-positive lesions were identified in 13 of 15 patients.<sup>69</sup> The next step in HER2 imaging was labeling of trastuzumab with the radioisotope <sup>89</sup>Zr for PET imaging of HER2 (Fig. 2).<sup>70,71</sup> PET imaging reaches higher spatial resolution than SPECT and tumor uptake of the tracer is easier to quantify. <sup>89</sup>Zr has a half-life of 78.4 hours, which is compatible with the relative long biological half-life of the trastuzumab antibody. In the first clinical trial with <sup>89</sup>Zr-trastuzumab 14 metastatic breast cancer

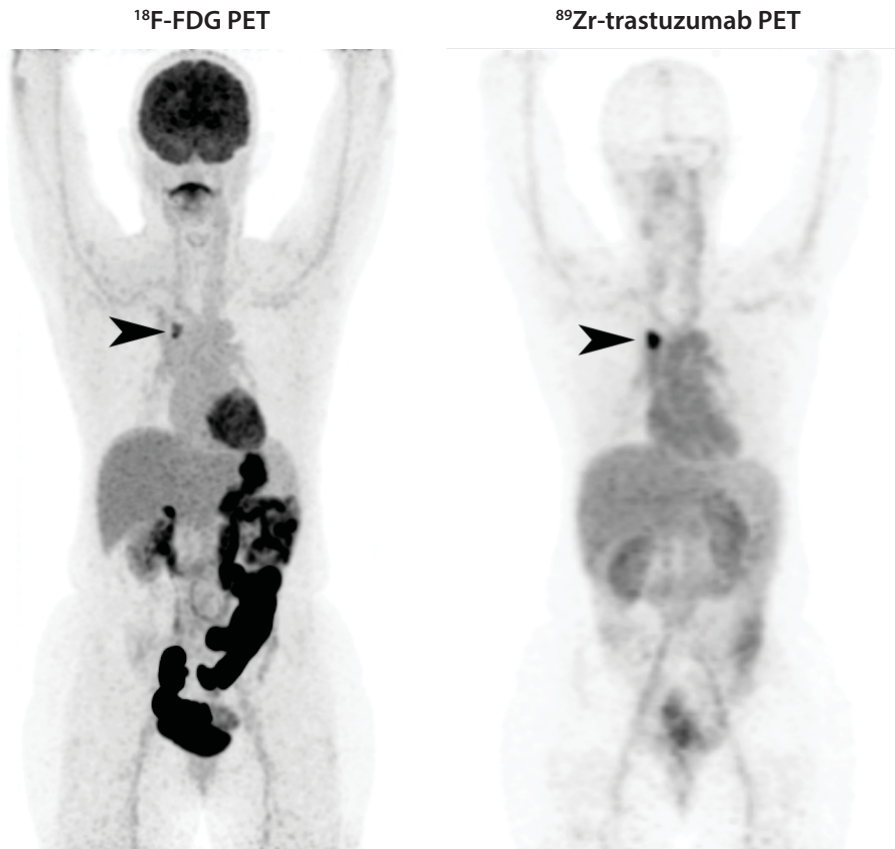


**Figure 2** Molecular imaging can provide information on glucose metabolism by <sup>18</sup>F-FDG PET (left) and HER2-status by <sup>89</sup>Zr-trastuzumab PET (right). Arrow heads indicate a mediastinal lesion with increased <sup>18</sup>F-FDG and <sup>89</sup>Zr-trastuzumab uptake in this patient with HER2-positive metastatic breast cancer. Note the differences in physiological uptake as a result of distribution, metabolism and excretion of both tracers.

patients with HER2-positive tumors received 37 MBq  $^{89}\text{Zr}$ -trastuzumab. Optimal PET scanning results were found at 4–5 days after tracer injection, with sufficient tumor uptake, less background signal and sufficient count-statistics. Most lesions were detected with excellent tumor uptake and visualization. Moreover, unknown brain metastases were detected in two patients, showing that trastuzumab can penetrate the brain in case of brain metastases.<sup>70</sup> In a patient with both a HER2-positive and a HER2-negative breast cancer who developed metastases, standard work up failed to determine HER2 status. The  $^{89}\text{Zr}$ -trastuzumab PET scan showed uptake of  $^{89}\text{Zr}$ -trastuzumab in the metastases, leading to initiation of anti-HER2 therapy.<sup>72</sup> The predictive value of the  $^{89}\text{Zr}$ -trastuzumab PET scan still deserves further studies.

Another role of imaging may be to determine the negative predictive value of  $^{89}\text{Zr}$ -trastuzumab PET in HER2-positive metastatic breast cancer patients who receive the antibody drug conjugate trastuzumab-DM1 (T-DM1). This is part of an ongoing trial (NCT 01565200). T-DM1 was recently assessed in a phase III trial in patients with HER2-positive advanced breast cancer. T-DM1 improved progression free survival as well as overall survival compared to lapatinib and capecitabine, with less toxicity.<sup>73</sup>

Trastuzumab was also labeled to  $^{64}\text{Cu}$  for PET imaging. The half-life of  $^{64}\text{Cu}$  is 12.7 hours. This leads to less radiation exposure compared to  $^{89}\text{Zr}$  imaging, but may also have a relatively low physical half-life compared to the long biological half-life of trastuzumab.  $^{64}\text{Cu}$ -DOTA-trastuzumab PET detected primary breast cancer, lymph node and lung metastases in 15 HER2-positive breast cancer patients on trastuzumab therapy.<sup>74</sup> Currently two clinical trials are ongoing investigating  $^{64}\text{Cu}$ -DOTA-trastuzumab in HER2-positive metastatic breast cancer patients to determine the optimal imaging dose and biodistribution and to assess the correlation of tumor tracer uptake with HER2 expression by immunohistochemistry (NCT01093612; NCT00605397). There is as yet no head to head comparison available between  $^{64}\text{Cu}$ -trastuzumab and  $^{89}\text{Zr}$ -trastuzumab PET.

Besides a more intensive role of non-invasive PET imaging with  $^{89}\text{Zr}$ -trastuzumab for selecting the most suitable patients for anti-HER2 therapy, this technique might also be able to facilitate early response measurement of targeted therapy in breast cancer. HER2 is degraded upon HSP90 inhibition and is therefore a rational candidate for treatment monitoring during HSP90 inhibition. One study used a  $^{68}\text{Ga}$  labeled  $\text{F(ab)'}_2$  fragment of trastuzumab in HER2 expressing breast cancer xenografts before and during therapy with the HSP90 inhibitor 17-AAG. HER2 expression lowered 80% 24 h after treatment, and increased to 50% of the initial expression 2 to 7 days after treatment.<sup>75</sup> The other study was performed with  $^{89}\text{Zr}$ -trastuzumab in HER2-over-expressing tumor bearing mice treated with the HSP90 inhibitor NVP-AUY922.  $^{89}\text{Zr}$ -trastuzumab tumor uptake was reduced 41% after three doses of NVP-AUY922.<sup>76,77</sup> These results led to the initiation of a clinical study investigating the role of  $^{89}\text{Zr}$ -trastuzumab PET to monitor treatment effects of the HSP90 inhibitor NVP-AUY922 in metastatic breast cancer patients with HER2 positive tumors (NCT01081600).<sup>78</sup>

## 6. IMAGING OF TUMOR MICRO-ENVIRONMENT

Not only tumor cell membrane receptors and proteins, but also soluble tumor specific targets present in the tumor micro-environment can be visualized with molecular imaging. Vascular endothelial growth factor (VEGF) and transforming growth factor beta (TGF $\beta$ ) are such targets. VEGF is an important factor involved in tumor angiogenesis.<sup>79</sup> VEGF is produced by tumor cells and over-expression is present in many human tumor types, making it a rational target for anti-angiogenic therapy.<sup>80,81</sup> VEGF signaling can be blocked with neutralizing antibodies, inhibiting VEGF-receptor tyrosine kinases on endothelial cells and by inhibiting cellular tumor signaling pathways. Bevacizumab is a humanized monoclonal antibody that binds and inactivates VEGF-A, thereby inhibiting VEGF-mediated angiogenesis. Multiple randomized phase 3 trials with bevacizumab were conducted in metastatic breast cancer patients. They demonstrated modest improvements in PFS for bevacizumab combined with chemotherapy, without improvement in overall survival.<sup>82,83</sup> The addition of bevacizumab in a phase 3 randomized trial to neo-adjuvant chemotherapy increased the rate of complete pathological response only in a subpopulation of triple negative patients.<sup>84,85</sup> A complete pathological response rate of 34.5% following the addition of bevacizumab to standard chemotherapy in HER2-negative breast cancer patients vs. 28.2% without bevacizumab was shown in another study.<sup>86</sup> Proper selection of patients who might benefit of bevacizumab would be very helpful. However, robust, predictive, biologic or clinical markers for bevacizumab are currently lacking.

Bevacizumab has been radio-labeled for non-invasive tumor monitoring with <sup>111</sup>In for SPECT imaging and with <sup>89</sup>Zr for PET. Specific tumor accumulation occurred with both tracers. <sup>89</sup>Zr-bevacizumab uptake could be quantified in VEGF expressing tumor bearing mice.<sup>87</sup> This was translated to a study in primary breast cancer patients. Twenty-three patients with 26 tumors received 37 MBq <sup>89</sup>Zr-bevacizumab at a protein dose of 5 mg followed by PET 4 days later, before surgery. Twenty-five of 26 tumors were detectable. VEGF expression was measured with ELISA after resection in 17 tumors and VEGF-A levels were higher in tumors than in normal breast tissue from the same patients.<sup>88</sup>

<sup>89</sup>Zr-bevacizumab PET was used as a so called *effect sensor* to monitor treatment effects with the HSP90 inhibitor NVP-AUY922 in mice bearing ovarian cancer xenografts.<sup>89</sup> Tumor uptake of <sup>89</sup>Zr-bevacizumab decreased 44% after treatment with NVP-AUY922 measured with PET scans 144 h after tracer injection. The extent of the change in tracer uptake during treatment was related to the down-regulation of VEGF levels measured by quantitative ELISA.<sup>90</sup> A study evaluating <sup>89</sup>Zr-bevacizumab PET in ER-positive metastatic breast cancer patients treated with NVP-AUY922 is currently ongoing (NCT01081613).

The role of <sup>89</sup>Zr-bevacizumab PET imaging as a biomarker of angiogenic changes during treatment with sunitinib or bevacizumab/interferon was determined in metastatic renal cell

cancer patients. Tracer uptake decreased 47% during bevacizumab, and only 15% during sunitinib.<sup>91</sup>

## 7. DISCUSSION

This review shows that molecular imaging might support treatment decision making in the future. Especially PET imaging with tumor specific tracers like <sup>89</sup>Zr-trastuzumab or <sup>18</sup>F-FES has the potential to select the most suitable therapy for each individual patient. Furthermore, serial imaging of general tumor process with tracers such as <sup>18</sup>F-FDG and <sup>18</sup>F-FLT may provide early prediction of anti-tumor efficacy (Fig. 3). Up-front or early detection of non-responding patients can avoid unnecessary toxicities and reduce health care costs. However, studies performed until now are (too) small and mainly have retrospectively determined end points. Uptake characteristics for different breast cancer subtypes, as well as for different chemotherapy and/or targeted therapy regimens remain unclear. The optimal moment of scanning, the quantification method and validation of PET with conventional imaging and histology are issues, which further need to be dealt with. For PET to be implemented in the clinic robust and properly powered trials with clearly defined patient populations, standardized PET protocols and prospectively set endpoints need to be performed to prove its clinical utility.

Next to these future trials, more novel tracers are being developed for molecular imaging in breast cancer. Apart for patient selection, these tracers might also have an important role in response measurement. However, not for all molecular-targeted therapies it is clear which tracers can be used to measure response to treatment. It is therefore recommended to investigate which tumor characteristic correlates with therapeutic response and thus may be suitable as a starting point to develop tracers against.<sup>89</sup>

New targeted therapies are designed with tyrosine kinase inhibitors, HSP90 inhibitors and phosphoinositide 3-kinase (PI3K) inhibitors. Moreover a new group of drugs are developed; the antibody-drug conjugates (ADCs). ADCs are monoclonal antibodies conjugated with a highly toxic component that is specifically delivered to the tumor since it is only released after intracellular tumor uptake. To determine the amount of toxin delivered to the tumor, PET might be used to calculate the targeting of the compound to the tumor by labeling the 'naked' antibody with <sup>89</sup>Zr.

The knowledge obtained with nuclear molecular imaging of tumor lesions with SPECT and PET is currently translated to optical molecular imaging. With optical imaging, no radioactivity is administered to patients, creating a more important role of imaging in the diagnostic and intra-operative setting. Recently the near infrared fluorescent IRDye 800CW was labeled to the therapeutic monoclonal antibodies bevacizumab and trastuzumab targeting VEGF and HER2 respectively. *In vivo* both bevacizumab-800CW and trastuzumab-800CW showed specific tumor

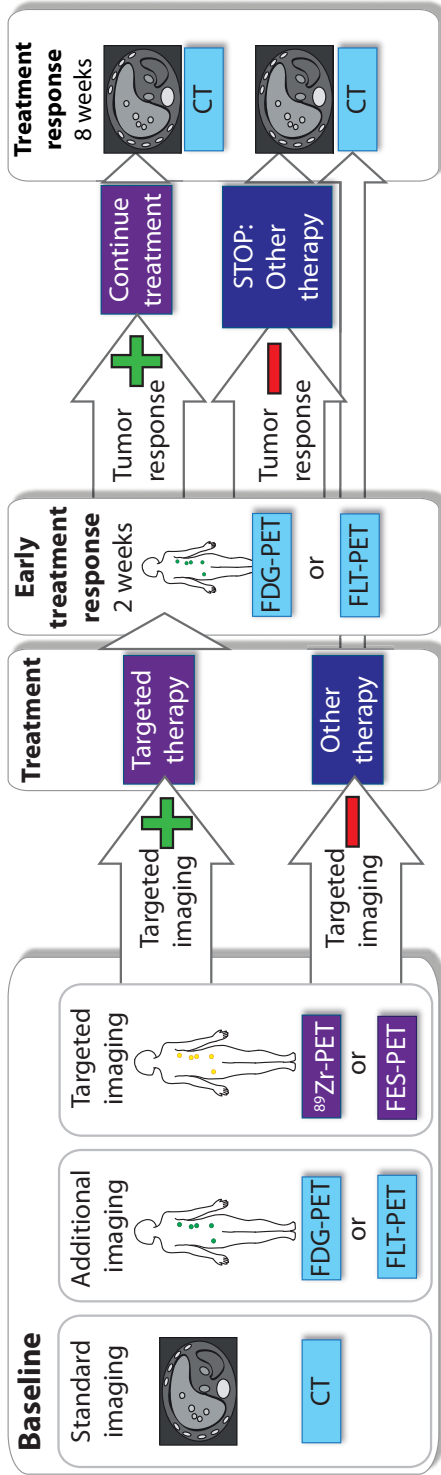


**Figure 3** Next to standard imaging with CT scan, also additional imaging of general tumor processes with  $^{18}\text{F}$ -FDG or  $^{18}\text{F}$ -FLT PET, and molecular imaging of relevant drug targets (such as the ER or HER2 using  $^{18}\text{F}$ -FES or  $^{89}\text{Zr}$ -trastuzumab) before therapy initiation might aid to select the right patients for targeted therapies at an early time point.

detection in tumor-bearing mice using the real-time intra-operative clinical prototype camera system.<sup>92</sup> Clinical testing with the fluorescent labeled antibodies has started based on a similar procedure as used for the radio-labeled antibodies (NCT01508572). Potentially the uptake of this tracer could be quantified serially with a handheld probe or endoscope measuring fluorescence in accessible tumor lesions.<sup>89</sup> Furthermore the anti-EGFR nanobody 7D12 was labeled with IDRYe800CW and showed high tumor uptake with optical imaging in human tumor xenografts as early as 30 minutes after injection.<sup>93</sup>

### **Acknowledgements**

This research was supported by the Center for Translational Molecular Medicine – Mammary Carcinoma Molecular Imaging for Diagnosis and Therapeutics (CTMM - MAMMOTH) Project. We thank Esther van Straten for her assistance with designing Fig. 3.

### **Authors disclosures of potential conflicts of interest**

Geke A.P. Hospers received a research grant from AstraZeneca, Elisabeth G.E. de Vries of Roche and Novartis.

## REFERENCES

1. Cardoso, F. *et al.* Locally recurrent or metastatic breast cancer: ESMO clinical practice guidelines for diagnosis, treatment and follow-up. *Ann. Oncol.* 21, suppl 5, abstr v15-9 (2010).
2. National Comprehensive Cancer Network (NCCN). NCCN clinical practice guidelines in oncology (NCCN guidelines); Breast Cancer version 1, NCCN (2012).
3. Eisenhauer, E. A. *et al.* New response evaluation criteria in solid tumours: revised RECIST guideline (version 1.1). *Eur. J. Cancer* 45, 228-247 (2009).
4. Niikura, N. *et al.* Retrospective analysis of antitumor effects of zoledronic acid in breast cancer patients with bone-only metastases. *Cancer* 118, 2039-2047 (2012).
5. Hamaoka, T. *et al.* Tumour response interpretation with new tumour response criteria versus the World Health Organisation criteria in patients with bone-only metastatic breast cancer. *Br. J. Cancer* 102, 651-657 (2010).
6. Sihto, H. *et al.* Breast cancer biological subtypes and protein expression predict for the preferential distant metastasis sites: a nationwide cohort study. *Breast Cancer Res.* 13, R87 (2011).
7. Early Breast Cancer Trialists' Collaborative Group (EBCTCG) *et al.* Relevance of breast cancer hormone receptors and other factors to the efficacy of adjuvant tamoxifen: patient-level meta-analysis of randomised trials. *Lancet* 378, 771-784 (2011).
8. Simmons, C. *et al.* Does confirmatory tumor biopsy alter the management of breast cancer patients with distant metastases? *Ann. Oncol.* 20, 1499-1504 (2009).
9. Amir, E. *et al.* Prospective study evaluating the impact of tissue confirmation of metastatic disease in patients with breast cancer. *J. Clin. Oncol.* 30, 587-592 (2012).
10. Rosen, E. L., Eubank, W. B. & Mankoff, D. A. FDG PET, PET/CT, and breast cancer imaging. *Radiographics* 27, suppl 1, abstr S215-29 (2007).
11. Lim, H. S. *et al.* FDG PET/CT for the detection and evaluation of breast diseases: usefulness and limitations. *Radiographics* 27, suppl 1, abstr S197-213 (2007).
12. Gennari, A. *et al.* Whither the PET scan? The role of PET imaging in the staging and treatment of breast cancer. *Curr. Oncol. Rep.* 14, 20-26 (2012).
13. Schnipper, L. E. *et al.* American Society of Clinical Oncology identifies five key opportunities to improve care and reduce costs: the top five list for oncology. *J. Clin. Oncol.* 30, 1715-1724 (2012).
14. Young, H. *et al.* Measurement of clinical and subclinical tumour response using <sup>18</sup>F-fluorodeoxyglucose and positron emission tomography: review and 1999 EORTC recommendations. European Organization for Research and Treatment of Cancer (EORTC) PET Study Group. *Eur. J. Cancer* 35, 1773-1782 (1999).
15. Wahl, R. L., Jacene, H., Kasamon, Y. & Lodge, M. A. From RECIST to PERCIST: Evolving considerations for PET response criteria in solid tumors. *J. Nucl. Med.* 50, suppl 1, abstr 122S-50S (2009).
16. Wang, Y., Zhang, C., Liu, J. & Huang, G. Is <sup>18</sup>F-FDG PET accurate to predict neoadjuvant therapy response in breast cancer? A meta-analysis. *Breast Cancer Res. Treat.* 131, 357-369 (2012).
17. Jansson, T. *et al.* Positron emission tomography studies in patients with locally advanced and/or metastatic breast cancer: a method for early therapy evaluation? *J. Clin. Oncol.* 13, 1470-1477 (1995).
18. Gennari, A. *et al.* Role of <sup>2-18</sup>F-fluorodeoxyglucose (FDG) positron emission tomography (PET) in the early assessment of response to chemotherapy in metastatic breast cancer patients. *Clin. Breast Cancer.* 1, 156-61; discussion 162-3 (2000).
19. Mariani, G. *et al.* Early Assessment by PET with FDG of response to first-line chemotherapy of metastatic breast cancer. *Clin. Positron Imaging* 2, 342 (1999).
20. Dose Schwarz, J. *et al.* Early prediction of response to chemotherapy in metastatic breast cancer using sequential <sup>18</sup>F-FDG PET. *J. Nucl. Med.* 46, 1144-1150 (2005).
21. Couturier, O., Jerusalem, G., N'Guyen, J. M. & Hustinx, R. Sequential positron emission tomography using <sup>18</sup>F-fluorodeoxyglucose for monitoring response to chemotherapy in metastatic breast cancer. *Clin. Cancer Res.* 12, 6437-6443 (2006).

22. De Giorgi, U. *et al.*  $^{18}\text{F}$ -FDG PET/CT findings and circulating tumor cell counts in the monitoring of systemic therapies for bone metastases from breast cancer. *J. Nucl. Med.* 51, 1213-1218 (2010).
23. De Giorgi, U. *et al.* Circulating tumor cells and  $^{18}\text{F}$ -fluorodeoxyglucose positron emission tomography/computed tomography for outcome prediction in metastatic breast cancer. *J. Clin. Oncol.* 27, 3303-3311 (2009).
24. Tateishi, U. *et al.* Bone metastases in patients with metastatic breast cancer: morphologic and metabolic monitoring of response to systemic therapy with integrated PET/CT. *Radiology* 247, 189-196 (2008).
25. Cachin, F., Prince, H. M., Hogg, A., Ware, R. E. & Hicks, R. J. Powerful prognostic stratification by  $^{18}\text{F}$ -fluorodeoxyglucose positron emission tomography in patients with metastatic breast cancer treated with high-dose chemotherapy. *J. Clin. Oncol.* 24, 3026-3031 (2006).
26. Mortimer, J. E. *et al.* Metabolic flare: indicator of hormone responsiveness in advanced breast cancer. *J. Clin. Oncol.* 19, 2797-2803 (2001).
27. Dehdashti, F. *et al.* Positron emission tomographic assessment of "metabolic flare" to predict response of metastatic breast cancer to antiestrogen therapy. *Eur. J. Nucl. Med.* 26, 51-56 (1999).
28. Dehdashti, F. *et al.* PET-based estradiol challenge as a predictive biomarker of response to endocrine therapy in women with estrogen-receptor-positive breast cancer. *Breast Cancer Res. Treat.* 113, 509-517 (2009).
29. Ellis, M. J. *et al.* Lower-dose versus high-dose oral estradiol therapy of hormone receptor-positive, aromatase inhibitor-resistant advanced breast cancer: a phase 2 randomized study. *JAMA* 302, 774-780 (2009).
30. Mortazavi-Jehanno, N. *et al.* Assessment of response to endocrine therapy using FDG PET/CT in metastatic breast cancer: a pilot study. *Eur. J. Nucl. Med. Mol. Imaging* 39, 450-460 (2012).
31. Ueda, S. *et al.* Early metabolic response to neoadjuvant letrozole, measured by FDG PET/CT, is correlated with a decrease in the Ki67 labeling index in patients with hormone receptor-positive primary breast cancer: a pilot study. *Breast Cancer* 18, 299-308 (2011).
32. Kawada, K. *et al.* Prospective study of positron emission tomography for evaluation of the activity of lapatinib, a dual inhibitor of the ErbB1 and ErbB2 tyrosine kinases, in patients with advanced tumors. *Jpn. J. Clin. Oncol.* 37, 44-48 (2007).
33. Fueger, B. J. *et al.* Impact of animal handling on the results of  $^{18}\text{F}$ -FDG PET studies in mice. *J. Nucl. Med.* 47, 999-1006 (2006).
34. McLarty, K. *et al.*  $^{18}\text{F}$ -FDG small-animal PET/CT differentiates trastuzumab-responsive from unresponsive human breast cancer xenografts in athymic mice. *J. Nucl. Med.* 50, 1848-1856 (2009).
35. Shah, C. *et al.* Imaging biomarkers predict response to anti-HER2 (ErbB2) therapy in preclinical models of breast cancer. *Clin. Cancer Res.* 15, 4712-4721 (2009).
36. Smith-Jones, P. M., Solit, D., Afroze, F., Rosen, N. & Larson, S. M. Early tumor response to Hsp90 therapy using HER2 PET: comparison with  $^{18}\text{F}$ -FDG PET. *J. Nucl. Med.* 47, 793-796 (2006).
37. Chalkidou, A. *et al.* Correlation between Ki-67 immunohistochemistry and  $^{18}\text{F}$ -fluorothymidine uptake in patients with cancer: A systematic review and meta-analysis. *Eur. J. Cancer* 48, 3499-3513 (2012).
38. Pio, B. S. *et al.* Usefulness of  $3'\text{-}^{18}\text{F}$ -fluoro- $3'$ -deoxythymidine with positron emission tomography in predicting breast cancer response to therapy. *Mol. Imaging Biol.* 8, 36-42 (2006).
39. Kenny, L. *et al.* Imaging early changes in proliferation at 1 week post chemotherapy: a pilot study in breast cancer patients with  $3'$ -deoxy- $3'\text{-}^{18}\text{F}$ -fluorothymidine positron emission tomography. *Eur. J. Nucl. Med. Mol. Imaging* 34, 1339-1347 (2007).
40. Contractor, K. B. *et al.*  $^{18}\text{F}$ - $3'$ -Deoxy- $3'$ -fluorothymidine positron emission tomography and breast cancer response to docetaxel. *Clin. Cancer Res.* 17, 7664-7672 (2011).
41. Kenny, L. M. *et al.* Altered tissue  $3'$ -deoxy- $3'\text{-}^{18}\text{F}$ -fluorothymidine pharmacokinetics in human breast cancer following capecitabine treatment detected by positron emission tomography. *Clin. Cancer Res.* 15, 6649-6657 (2009).
42. Lee, S. J. *et al.* Induction of thymidine kinase 1 after 5-fluorouracil as a mechanism for  $3'$ -deoxy- $3'\text{-}^{18}\text{F}$ -fluorothymidine flare. *Biochem. Pharmacol.* 80, 1528-1536 (2010).
43. Bergstrom, M. *et al.* Modeling spheroid growth, PET tracer uptake, and treatment effects of the Hsp90 inhibitor NVP-AUY922. *J. Nucl. Med.* 49, 1204-1210 (2008).

44. Monazzam, A. *et al.* Evaluation of the Hsp90 inhibitor NVP-AUY922 in multicellular tumour spheroids with respect to effects on growth and PET tracer uptake. *Nucl. Med. Biol.* 36, 335-342 (2009).
45. van Waarde, A. *et al.* Selectivity of  $^{18}\text{F}$ -FLT and  $^{18}\text{F}$ -FDG for differentiating tumor from inflammation in a rodent model. *J. Nucl. Med.* 45, 695-700 (2004).
46. Mintun, M. A. *et al.* Breast cancer: PET imaging of estrogen receptors. *Radiology* 169, 45-48 (1988).
47. Dehdashti, F. *et al.* Positron tomographic assessment of estrogen receptors in breast cancer: comparison with FDG-PET and in vitro receptor assays. *J. Nucl. Med.* 36, 1766-1774 (1995).
48. Mortimer, J. E. *et al.* Positron emission tomography with 2- $^{18}\text{F}$ -fluoro-2-deoxy-D-glucose and 16 $\alpha$ - $^{18}\text{F}$ -fluoro-17 $\beta$ -estradiol in breast cancer: correlation with estrogen receptor status and response to systemic therapy. *Clin. Cancer Res.* 2, 933-939 (1996).
49. Peterson, L. M. *et al.* Quantitative imaging of estrogen receptor expression in breast cancer with PET and  $^{18}\text{F}$ -fluoroestradiol. *J. Nucl. Med.* 49, 367-374 (2008).
50. van Kruchten, M. *et al.* PET imaging of estrogen receptors as a diagnostic tool for breast cancer patients presenting with a clinical dilemma. *J. Nucl. Med.* 53, 182-190 (2012).
51. Linden, H. M. *et al.* Quantitative fluoroestradiol positron emission tomography imaging predicts response to endocrine treatment in breast cancer. *J. Clin. Oncol.* 24, 2793-2799 (2006).
52. Linden, H. M. *et al.* Fluoroestradiol positron emission tomography reveals differences in pharmacodynamics of aromatase inhibitors, tamoxifen, and fulvestrant in patients with metastatic breast cancer. *Clin. Cancer Res.* 17, 4799-4805 (2011).
53. Ogawa, Y. *et al.* Androgen receptor expression in breast cancer: relationship with clinicopathological factors and biomarkers. *Int. J. Clin. Oncol.* 13, 431-435 (2008).
54. Collins, L. C. *et al.* Androgen receptor expression in breast cancer in relation to molecular phenotype: results from the Nurses' Health Study. *Mod. Pathol.* 24, 924-931 (2011).
55. Elias, A. D. *et al.* Effect of MDV3100, an androgen receptor signaling inhibitor, on tumor growth of estrogen and androgen receptor-positive (ER+/AR+) breast cancer xenografts. *J. Clin. Oncol.* 30, suppl, abstr 564 (2012).
56. Elias, A. D. *et al.* MDV3100-08: A phase I open-label, dose-escalation study evaluating the safety, tolerability, and pharmacokinetics of MDV3100 in women with incurable breast cancer. *J. Clin. Oncol.* 30, suppl, abstr TPS668 (2012).
57. Gucalp, A. *et al.* Targeting the androgen receptor (AR) in women with AR+ ER-/PR- metastatic breast cancer (MBC). *J. Clin. Oncol.* 30, suppl, abstr 1006 (2012).
58. Larson, S. M. *et al.* Tumor localization of 16 $\beta$ - $^{18}\text{F}$ -fluoro-5 $\alpha$ -dihydrotestosterone versus  $^{18}\text{F}$ -FDG in patients with progressive, metastatic prostate cancer. *J. Nucl. Med.* 45, 366-373 (2004).
59. Scher, H. I. *et al.* Antitumour activity of MDV3100 in castration-resistant prostate cancer: a phase 1-2 study. *Lancet* 375, 1437-1446 (2010).
60. Dehdashti, F. *et al.* Positron tomographic assessment of androgen receptors in prostatic carcinoma. *Eur. J. Nucl. Med. Mol. Imaging* 32, 344-350 (2005).
61. Dehdashti, F. *et al.* Assessment of progesterone receptors in breast carcinoma by PET with 21- $^{18}\text{F}$ -fluoro-16 $\alpha$ ,17 $\alpha$ -[(R)-(1'- $\alpha$ -furylmethylidene)dioxy]-19-norpregn-4-ene-3,20-dione. *J. Nucl. Med.* 53, 363-370 (2012).
62. Fowler, A. M. *et al.* Small-animal PET of steroid hormone receptors predicts tumor response to endocrine therapy using a preclinical model of breast cancer. *J. Nucl. Med.* 53, 1119-1126 (2012).
63. Slamon, D. J. *et al.* Human breast cancer: correlation of relapse and survival with amplification of the HER-2/neu oncogene. *Science* 235, 177-182 (1987).
64. Slamon, D. J. *et al.* Studies of the HER-2/neu proto-oncogene in human breast and ovarian cancer. *Science* 244, 707-712 (1989).
65. Ross, J. S. *et al.* The HER-2 receptor and breast cancer: ten years of targeted anti-HER-2 therapy and personalized medicine. *Oncologist* 14, 320-368 (2009).
66. Moasser, M. M. The oncogene HER2: its signaling and transforming functions and its role in human cancer pathogenesis. *Oncogene* 26, 6469-6487 (2007).

67. Vogel, C. L. *et al.* Efficacy and safety of trastuzumab as a single agent in first-line treatment of HER2-overexpressing metastatic breast cancer. *J. Clin. Oncol.* 20, 719-726 (2002).
68. Slamon, D. *et al.* Adjuvant trastuzumab in HER2-positive breast cancer. *N. Engl. J. Med.* 365, 1273-1283 (2011).
69. Perik, P. J. *et al.* Indium-111-labeled trastuzumab scintigraphy in patients with human epidermal growth factor receptor 2-positive metastatic breast cancer. *J. Clin. Oncol.* 24, 2276-2282 (2006).
70. Dijkers, E. C. *et al.* Biodistribution of <sup>89</sup>Zr-trastuzumab and PET imaging of HER2-positive lesions in patients with metastatic breast cancer. *Clin. Pharmacol. Ther.* 87, 586-592 (2010).
71. Dijkers, E. C. *et al.* Development and characterization of clinical-grade <sup>89</sup>Zr-trastuzumab for HER2/neu immunoPET imaging. *J. Nucl. Med.* 50, 974-981 (2009).
72. Gaykema, S. B. *et al.* Zirconium-89-trastuzumab positron emission tomography as a tool to solve a clinical dilemma in a patient with breast cancer. *J. Clin. Oncol.* 30, e74-5 (2012).
73. Verma, S. *et al.* Trastuzumab emtansine for HER2-positive advanced breast cancer. *N. Engl. J. Med.* 367, 1783-1791 (2012).
74. Tamura, K. *et al.* <sup>64</sup>Cu-DOTA-trastuzumab-PET imaging in patients with HER2-positive breast cancer. *J. Clin. Oncol.* 30, suppl, abstr 10519 (2012).
75. Smith-Jones, P. M. *et al.* Imaging the pharmacodynamics of HER2 degradation in response to Hsp90 inhibitors. *Nat. Biotechnol.* 22, 701-706 (2004).
76. Oude Munnink, T. H. *et al.* Trastuzumab pharmacokinetics influenced by extent human epidermal growth factor receptor 2-positive tumor load. *J. Clin. Oncol.* 28, e355 (2010).
77. Oude Munnink, T. H. *et al.* Molecular imaging of breast cancer. *Breast* 18, suppl 3, abstr S66-73 (2009).
78. Schroder, C. P. *et al.* Use of biomarkers and imaging to evaluate the treatment effect of AU922, an HSP90 inhibitor, in patients with HER2+ or ER+ metastatic breast cancer. *J. Clin. Oncol.* 29, suppl, abstr 15 (2011).
79. Hanahan, D. & Weinberg, R. A. Hallmarks of cancer: the next generation. *Cell* 144, 646-674 (2011).
80. Ferrara, N. Vascular endothelial growth factor: basic science and clinical progress. *Endocr. Rev.* 25, 581-611 (2004).
81. Dvorak, H. F. Vascular permeability factor/vascular endothelial growth factor: a critical cytokine in tumor angiogenesis and a potential target for diagnosis and therapy. *J. Clin. Oncol.* 20, 4368-4380 (2002).
82. Mackey, J. R. *et al.* Controlling angiogenesis in breast cancer: a systematic review of anti-angiogenic trials. *Cancer Treat. Rev.* 38, 673-688 (2012).
83. Stevenson, C. E. *et al.* Bevacizumab and breast cancer: what does the future hold? *Future Oncol.* 8, 403-414 (2012).
84. von Minckwitz, G. *et al.* Integrating bevacizumab, everolimus, and lapatinib into current neoadjuvant chemotherapy regimen for primary breast cancer. Safety results of the GeparQuinto trial. *Ann. Oncol.* 22, 301-306 (2011).
85. von Minckwitz, G. *et al.* Neoadjuvant chemotherapy and bevacizumab for HER2-negative breast cancer. *N. Engl. J. Med.* 366, 299-309 (2012).
86. Bear, H. D. *et al.* Bevacizumab added to neoadjuvant chemotherapy for breast cancer. *N. Engl. J. Med.* 366, 310-320 (2012).
87. Nagengast, W. B. *et al.* In vivo VEGF imaging with radiolabeled bevacizumab in a human ovarian tumor xenograft. *J. Nucl. Med.* 48, 1313-1319 (2007).
88. Gaykema, S. B. M. *et al.* <sup>89</sup>Zr-bevacizumab PET imaging in primary breast cancer. *Ann. Oncol.* 23, suppl 2, abstr ii32 (2012).
89. de Vries, E. G., Oude Munnink, T. H., van Vugt, M. A. & Nagengast, W. B. Toward molecular imaging-driven drug development in oncology. *Cancer Discov.* 1, 25-28 (2011).
90. Nagengast, W. B. *et al.* <sup>89</sup>Zr-bevacizumab PET of early antiangiogenic tumor response to treatment with HSP90 inhibitor NVP-AUY922. *J. Nucl. Med.* 51, 761-767 (2010).
91. Oosting, S. *et al.* <sup>89</sup>Zr-bevacizumab PET imaging in metastatic renal cell carcinoma patients before and during antiangiogenic treatment. *J. Clin. Oncol.* 30, suppl, abstr 10581 (2012).

92. Terwisscha van Scheltinga, A. G. *et al.* Intraoperative near-infrared fluorescence tumor imaging with vascular endothelial growth factor and human epidermal growth factor receptor 2 targeting antibodies. *J. Nucl. Med.* 52, 1778-1785 (2011).
93. Oliveira, S. *et al.* Rapid visualization of human tumor xenografts through optical imaging with a near-infrared fluorescent anti-epidermal growth factor receptor nanobody. *Mol. Imaging* 11, 33-46 (2012).
94. Sataloff, D. M. *et al.* Pathologic response to induction chemotherapy in locally advanced carcinoma of the breast: a determinant of outcome. *J. Am. Coll. Surg.* 180, 297-306 (1995).



# Chapter 3

## **<sup>89</sup>Zr-lumretuzumab PET imaging before and during HER3 antibody lumretuzumab treatment in patients with solid tumors**

Frederike Bensch<sup>1\*</sup>, Laetitia E. Lamberts<sup>1\*</sup>, Michaël M. Smeenk<sup>1</sup>, Annelies Jorritsma-Smit<sup>2</sup>, Marjolijn N. Lub-de Hooge<sup>2,3</sup>, Anton G.T. Terwisscha van Scheltinga<sup>2</sup>, Johan R. de Jong<sup>3</sup>, Jourik A. Gietema<sup>1</sup>, Carolien P. Schröder<sup>1</sup>, Marlene Thomas<sup>4</sup>, Wolfgang Jacob<sup>4</sup>, Keelara Abiraj<sup>5</sup>, Celine Adessi<sup>5</sup>, Georgina Meneses-Lorente<sup>6</sup>, Ian James<sup>7</sup>, Martin Weisser<sup>4</sup>, Adrienne H. Brouwers<sup>3</sup>, Elisabeth G.E. de Vries<sup>1</sup>

\* These authors contributed equally to this manuscript

Departments of Medical Oncology<sup>1</sup>, Clinical Pharmacy and Pharmacology<sup>2</sup>, Nuclear Medicine and Molecular Imaging<sup>3</sup>, University of Groningen, University Medical Center Groningen, the Netherlands. Pharma Research and Early Development, Roche Innovation Center Munich, Penzberg, Germany<sup>4</sup>. Pharma Research and Early Development, Roche Innovation Center Basel, Basel, Switzerland<sup>5</sup>. Pharma Research and Early Development, Roche Innovation Center Welwyn, Welwyn, UK<sup>6</sup>. A4P Consulting Ltd, Sandwich, UK<sup>7</sup>.

## ABSTRACT

**Purpose:** We evaluated biodistribution and tumor targeting of  $^{89}\text{Zr}$ -lumretuzumab before and during treatment with lumretuzumab, a human epidermal growth factor receptor 3 (HER3)-targeting monoclonal antibody.

**Experimental design:** 20 patients with histologically confirmed HER3-expressing tumors received  $^{89}\text{Zr}$ -lumretuzumab and underwent Positron Emission Tomography (PET). In Part A,  $^{89}\text{Zr}$ -lumretuzumab was given with additional, escalating doses of unlabeled lumretuzumab and scans were performed 2, 4 and 7 days postinjection to determine optimal imaging conditions. In Part B, patients were scanned following tracer injection before (baseline) and after a pharmacodynamic (PD)-active lumretuzumab dose for saturation analysis. HER3 expression was determined immunohistochemically in skin biopsies. Tracer uptake was calculated as standardized uptake value (SUV).

**Results:** Optimal PET conditions were found to be 4 and 7 days after administration of  $^{89}\text{Zr}$ -lumretuzumab with 100 mg unlabeled lumretuzumab. At baseline using 100 mg unlabeled lumretuzumab, the tumor SUVmax was 3.4 ( $\pm$  1.9) at 4 days postinjection. SUVmean for normal blood, liver, lung and brain tissues were 4.9, 6.4, 0.9 and 0.2, respectively. Saturation analysis ( $n = 7$ ) showed that 4 days after lumretuzumab administration, tumor uptake decreased by 11.9% ( $\pm$  8.2), 10.0% ( $\pm$  16.5) and 24.6% ( $\pm$  20.9) at PD-active doses of 400, 800 and 1600 mg, respectively, when compared to baseline. Membranous HER3 was completely downregulated in paired skin biopsies already at and above 400 mg lumretuzumab.

**Conclusions:** PET imaging showed biodistribution and tumor specific  $^{89}\text{Zr}$ -lumretuzumab uptake. Although, PD-active lumretuzumab doses decreased  $^{89}\text{Zr}$ -lumretuzumab uptake, there was no clear evidence of tumor saturation by PET imaging as the tumor SUV did not plateau with increasing doses.

## TRANSLATIONAL RELEVANCE

The human epidermal growth factor receptor 3 (HER3) plays an important role in tumor growth, proliferation and progression. The humanized, HER3-targeting monoclonal, glycoengineered antibody lumretuzumab is in development for treatment of patients with HER3-positive solid tumors. Challenges in drug development include obtaining information concerning drug biodistribution, target occupancy and intra- and interpatient tumor heterogeneity. In this study assessment of biodistribution and visualization of tumor lesions was feasible with  $^{89}\text{Zr}$ -lumretuzumab PET. Highest uptake in normal tissues was observed in the liver. Tumor tracer uptake varied between and within patients possibly reflecting inpatient heterogeneity. Serial imaging at baseline and after the first pharmacodynamically-active lumretuzumab dose showed decreased tumor uptake already after 400 mg, however, without plateauing. This study supports serial antibody PET-imaging during early clinical development to determine biodistribution and obtain insight in effects of different antibody doses on tumor targeting.

## INTRODUCTION

The members of the human epidermal growth factor receptor (HER) family play a critical role in tumor growth, proliferation and progression in multiple epithelial malignancies.<sup>1</sup> Due to its lack of intrinsic tyrosine kinase activity and its need for dimerization partners, the role of HER3 in cancer, however, has long been unclear. HER3 is physiologically expressed in normal human tissues, such as the gastrointestinal, urinary, respiratory and reproductive tract and skin.<sup>2</sup> In multiple cancer types, HER3 overexpression has been linked with poor prognosis which increased interest in HER3 as potential target in cancer therapy.<sup>3-9</sup>

Lumretuzumab (RG7116, RO5479599) is a glycoengineered humanized monoclonal antibody directed against the extracellular domain of HER3, displacing its ligand and inhibiting heterodimerization and downstream signaling. Furthermore, the antibody can cause direct cell death through antibody-dependent cellular cytotoxicity.<sup>10</sup> A phase I study in patients with HER3-positive solid tumors of epithelial origin showed that lumretuzumab monotherapy was well tolerated and signs of clinical activity were reported.<sup>11</sup>

Several challenges hamper early clinical development of novel molecular tumor-targeting agents. Firstly, intra- and intertumor heterogeneity with regard to target expression is likely an important contributor to treatment failure.<sup>12-19</sup> Secondly, finding the optimal dose and dosing schedule of antibodies in a dose escalation study with a limited number of (heterogeneous) patients is challenging given potentially high intra- and interindividual variance in blood pharmacokinetics (PK). Due to limited or no side effects even at high doses, traditional approaches focusing on dose-limiting toxicities do not provide sufficient guidance.<sup>20</sup> Finally, assumptions concerning the biodistribution of new drugs are often only based on blood PK while information concerning the antibody level in the tumor lesions and target saturation at different doses are lacking.

By labeling antibodies with zirconium-89 (<sup>89</sup>Zr) positron emission tomography (PET) can be performed. This technique can assess target expression non-invasively at a whole body level and determine the biodistribution of the administered antibody.<sup>21</sup> Over 15 therapeutic antibodies have already been labeled with <sup>89</sup>Zr and tested in clinical trials.<sup>21-29</sup> Performing serial PET scans before and during treatment allows investigation of target accessibility during treatment and may therefore be used to assess whether target saturation has been achieved. Based on antibody characteristics, radioactive decay and dose of <sup>89</sup>Zr, a second tracer injection followed by a series PET scans can be performed 14 days after the first.<sup>24, 26</sup>

First we labeled the anti-HER3-antibody lumretuzumab with <sup>89</sup>Zr with high specific activity and radiochemical purity. Subsequently, in human tumor-bearing mice we showed that <sup>89</sup>Zr-lumretuzumab specifically accumulated in HER3-expressing tumors related to HER3 expression levels.<sup>30</sup>

This resulted in the clinical trial in which we determined the biodistribution and tumor targeting characteristics of  $^{89}\text{Zr}$ -lumretuzumab before and during lumretuzumab treatment, including assessment of target saturation, and comparing these to serum PK and skin biopsies to evaluate pharmacodynamic (PD) effects.

## PATIENTS AND METHODS

### Patient population

Patients with histologically confirmed locally advanced or metastatic HER3-expressing solid tumors of epithelial origin for whom no standard therapy existed were eligible for this study. Other eligibility criteria included age  $\geq 18$  years, written informed consent, Eastern Cooperative Oncology Group (ECOG) performance status of 0-2 and adequate hematological (neutrophil count  $\geq 1.5 \times 10^9/\text{L}$ , platelet count  $\geq 100 \times 10^9/\text{L}$ , hemoglobin  $\geq 10$  g/dL), liver (bilirubin  $\leq 1.5 \times$  upper limit of normal [ULN], aspartate aminotransferase/alanine aminotransferase  $\leq 2.5 \times$  ULN, in case of liver metastases  $\leq 5 \times$  ULN) and renal function (serum creatinine  $\leq 1.5 \times$  ULN). Patients with significant concomitant diseases, active infections, current high doses of systemic corticosteroids or symptomatic central nervous system primary tumors or metastases, were excluded. Patients with previously unknown, asymptomatic brain metastases, which were detected on  $^{89}\text{Zr}$ -lumretuzumab PET, were allowed to remain on the study according to the investigator's judgment unless radiotherapy for brain metastases was indicated.

This study was centrally approved by the Medical Ethical Committee of the Netherlands Cancer Institute and the Central Committee on Research Involving Human Subjects. All patients provided written informed consent. It was registered as part of the phase I study (ClinicalTrials.gov identifier NCT01482377).

### HER3 expression in archival and freshly obtained tumor and skin samples

HER3 membrane expression was assessed centrally in biopsies from metastases to confirm patient eligibility for entry into the study and in skin biopsies at baseline and after the first PD-active dose using a validated immunohistochemistry (IHC) assay (Ventana Benchmark XT platform, primary antibody HER3 monoclonal antibody clone 7.3.8, Source Bioscience Ltd). HER3 positivity was defined as any positive membrane staining with a minimum of 100 neoplastic cells being evaluated. IHC was assessed semi-quantitatively using an immunoreactive score (IRS) according to:  $\text{IRS} = \text{staining intensity (SI)} \times \text{percent tumor cells stained (PS)}$ , where  $\text{SI} = 1 \times \text{"+" score} + 2 \times \text{"++" score} + 3 \times \text{"+++"} \text{ score} / 100$  and  $\text{PS} = (\text{"+" score} + \text{"++" score} + \text{"+++"} \text{ score}) / 100$ .

## Study design

This single-center, open-label, imaging study was performed at the University Medical Center Groningen (UMCG), the Netherlands.

Clinical grade <sup>89</sup>Zr-lumretuzumab was produced at UMCG essentially as described previously.<sup>30,31</sup> In Part A, the optimal imaging dose and schedule for <sup>89</sup>Zr-lumretuzumab PET imaging were assessed, and in Part B, patients underwent two series of <sup>89</sup>Zr-lumretuzumab PET to analyze the biodistribution of <sup>89</sup>Zr-lumretuzumab and to determine the dose of unlabeled PD-active lumretuzumab required to achieve maximal or optimal tumor saturation.

In Part A, a fixed dose of 37 MBq <sup>89</sup>Zr-lumretuzumab (~ 1 mg) was given with additional, escalating doses of unlabeled lumretuzumab in cohorts of 2 to 3 patients. The unlabeled lumretuzumab was administered over 15 minutes via an intravenous infusion, before <sup>89</sup>Zr-lumretuzumab bolus injection. After tracer injection patients were observed for 4 hours for infusion-related reactions (IRRs). PET scans in combination with low dose CT scans for attenuation correction and anatomic reference were performed at 2, 4 and 7 days postinjection with a Biograph mCT 64-slice PET/CT camera (Siemens).

As often, an additional dose of unlabeled antibody was required for imaging to guarantee sufficient circulating labeled antibody and thereby to improve tumor visualization.<sup>23,26,29,32</sup> We first verified the tracer biodistribution with escalating doses of 10, 50 and 100 mg of unlabeled lumretuzumab. We considered the unlabeled antibody dose to be sufficient when the circulation was adequately visualized 7 days post tracer injection. The optimal time point for PET scanning was determined by analyzing tumor tracer uptake serially at 2, 4 and 7 days postinjection and available amount of tracer in the circulation.

In Part B, patients underwent two series of <sup>89</sup>Zr-lumretuzumab PET imaging. The first series (baseline) was performed using the optimal imaging dose and schedule determined in Part A (~ 1 mg <sup>89</sup>Zr-lumretuzumab along with 100 mg unlabeled lumretuzumab followed by PET scans at days 4 and 7 postinjection). Fourteen days after the first tracer injection a second tracer injection was administered and imaging repeated at optimal schedule. During the second series (on-treatment), <sup>89</sup>Zr-lumretuzumab was dosed with increasing PD-active doses of unlabeled lumretuzumab (400, 800 or 1600 mg) in subsequent patient cohorts. These lumretuzumab doses had been cleared for safety in the phase I study and all resulted in a downregulation of membranous HER3 protein measured by IHC in 35/38 tumor and skin biopsies 14 days after the first lumretuzumab administration compared to baseline.<sup>11</sup>

After the last PET scan, patients continued with lumretuzumab monotherapy on a 2-weekly schedule and at the highest safe dose determined in the phase I study. Diagnostic CT scans were performed within 28 days before the first tracer injection and every 8 weeks (± 7 days) after start of lumretuzumab treatment or if clinically indicated.

### **<sup>89</sup>Zr-lumretuzumab PET analysis**

PET scans were reconstructed (iterative reconstruction method: 28 matrix, 2 iterations, 8 subsets and 10 mm filter) and analyzed by a single dedicated nuclear medicine physician. All tumor lesions on the baseline diagnostic CT scan were recorded, including measurability according to RECIST 1.1.<sup>33</sup> Tumor lesions with visible tracer uptake on the <sup>89</sup>Zr-lumretuzumab PET were considered quantifiable when the tumor size was at least 10 mm and measurement of tumor tracer uptake was considered not to be influenced by surrounding tissue (e.g. by the aorta or the liver). With the AMIDE (A Medical Image Data Examiner) software (version 0.9.3, Stanford University), radioactivity was quantified by manually drawing three dimensional volumes of interest (VOI) around tumor lesions and in the left ventricle (reflecting blood pool), liver, spleen, kidney, intestine, lung, brain, compact bone and muscle to assess <sup>89</sup>Zr-lumretuzumab normal organ distribution.<sup>34</sup> Standardized uptake values (SUV) were calculated using the amount of injected activity, bodyweight and the amount of radioactivity within a VOI. We report the SUVmax (the maximum voxel intensity in the VOI) for tumor lesions and SUVmean (the mean voxel intensity of all voxels in the VOI) for normal organ tracer uptake. Furthermore, the tumor-to-blood ratio (TBR) was calculated for all tumor lesions. In Part B, baseline tumor tracer uptake, assessed during the first PET imaging series, was compared to tumor tracer uptake after the PD-active lumretuzumab dose during the second PET imaging series. In both series the tumor tracer uptake was calculated as TBR to increase comparability and the change in TBR with escalating PD-active doses of lumretuzumab served as a read out for target saturation.

Additionally, the liver was delineated on all PET scans and its volume and the radioactivity present were calculated. The activity of the liver was compared to the injected dose and the remaining dose in the body (VOI: head to tuber ischiadicum) on the respective PET scan and expressed as percent of injected (%ID) and percent of remaining dose (%RD), respectively.

### **Safety assessments**

The National Cancer Institute (NCI) Common Terminology Criteria for Adverse Events version 4.03 were used to evaluate side effects.<sup>35</sup> Patients were assessed for adverse events at each clinical visit and if necessary throughout the study.

### **Pharmacokinetic assessments**

Blood samples were collected for determination of labeled and free <sup>89</sup>Zr and lumretuzumab PK before, directly after, as well as 2 and 4 hours following tracer injection and on the days of PET scans (2, 4 and 7 days post tracer injection) during the baseline scan series (Part A and B). After the second tracer injection (Part B only) blood samples only for lumretuzumab PK were collected before, directly after, 2, 5 hours and 2, 4 and 7 days postinjection.

Lumretuzumab concentration (in µg/mL) was determined in human serum using a validated ELISA method. Biotinylated ectodomain of human HER3, lumretuzumab reference standard or diluted samples and anti-lumretuzumab detection antibody labeled with digoxigenin were bound to streptavidin-coated plates. The immobilized immune complexes were detected by anti-digoxigenin antibody conjugated to horseradish peroxidase. 3,3',5,5'-Tetramethylbenzidine substrate was used to produce a colorimetric signal photometrically determined at 450 nm (690 nm reference wave length) which is proportional to the lumretuzumab amount in the sample. The calibration was 10.0 ng/mL to 1000 ng/mL for lumretuzumab in 100% human serum. The lower limit of quantification was 15.0 ng/mL in native human serum.

Activity (in counts per minute) of <sup>89</sup>Zr was measured in 1 mL serum and in 1 mL whole blood using a calibrated well-type γ-counter (LKB Instruments), followed by conversion to radioactivity concentration (Bq/mL). The radioactivity concentrations of serum and whole blood samples were then compared to the activity in the blood pool (Bq/mL) on PET scans, and to the measured lumretuzumab serum concentrations.

### Statistical analyses

Statistical analyses were performed using SPSS Version 22. Significant differences between two groups were calculated either using independent sample Student's t-test or Mann-Whitney U test depending on normality of distribution as assessed by the Shapiro-Wilk test. In case of three or more groups with normally distributed data, significant differences were calculated using a one-way ANOVA with either posthoc Gabriel or Games-Howell test depending on homogeneity of variances as assessed by Levene's test. If data was not normally distributed, groups were compared using a Kruskal-Wallis followed by a Mann-Whitney U test.  $P \leq 0.05$  was considered to be a significant difference. All analyses were 2-sided. Bivariate correlations were performed using Pearson (for continuous variables) or Spearman (for ordinal variables) correlation coefficients. Data are presented as mean ± standard deviation (SD), unless otherwise stated.

## RESULTS

### Patient characteristics

Twenty patients were enrolled from December 2012 until November 2014, 7 in Part A and 13 in Part B. Patient characteristics are summarized in Table 1 and Supplementary Fig. 1.

Eighteen of 20 patients received one or more infusions of lumretuzumab (range 0 to 8, median 4) after baseline <sup>89</sup>Zr-lumretuzumab PET.

**Table 1 Patient characteristics**

Characteristic	All patients (n = 20)
Age, median years (range)	62.5 (45-72)
Sex	
Male, n (%)	10 (50)
Female, n (%)	10 (50)
ECOG PS	
0, n (%)	12 (60)
1, n (%)	5 (25)
2, n (%)	3 (15)
Tumor type, n (%)	
Rectal cancer	7 (35)
Colon cancer	4 (20)
Head and neck cancer	2 (10)
Cancer of unknown primary <sup>a</sup>	2 (10)
Ovarian cancer	1 (5)
Esophageal cancer	1 (5)
Breast cancer	1 (5)
Cancer of the ampulla of Vater	1 (5)
Vulvar cancer	1 (5)
Prior systemic palliative therapies, n	
0	5 (25)
1	3 (15)
2	4 (20)
> 2 (3-7)	8 (40)

<sup>a</sup> Tumor cells were considered of epithelial origin based on positive staining of at least one epithelial marker (cytokeratins, EMA and EpCAM).

### <sup>89</sup>Zr-lumretuzumab PET

#### *Optimal imaging dose and schedule*

The optimal imaging dose was assessed in 7 patients across 3 cohorts. Patients in the first two cohorts (n = 2 each) received ~ 1 mg <sup>89</sup>Zr-lumretuzumab with either 10 or 50 mg additional unlabeled lumretuzumab. At both doses, the amount of tracer left in the circulation 7 days postinjection was too low for adequate tumor visualization (SUV<sub>mean</sub> in blood 7 days postinjection 0.5 ± 0.2 with 10 mg, 2.3 ± 1.5 with 50 mg unlabeled lumretuzumab). Therefore, another 3 patients received <sup>89</sup>Zr-lumretuzumab together with 100 mg of unlabeled lumretuzumab, which resulted in sufficient tracer present in the circulation 7 days postinjection (SUV<sub>mean</sub> in blood of 3.6 ± 1.1) to allow adequate tumor visualization. Improved blood tracer availability over time resulted in superior imaging results compared to the 10 and 50 mg dose cohorts. Mean tumor tracer uptake increased from SUV<sub>max</sub> 1.8 ± 1.1 assessed in 25 tumor lesions (10 mg) to 4.2 ± 2.4 assessed in 18 lesions (100 mg; P < 0.05). The PET scan 2 days

postinjection was omitted in Part B, as it did not add information to the PET scans performed 4 and 7 days postinjection.

**Organ distribution**

Normal organ distribution was evaluated in all 16 patients who received 100 mg unlabeled lumretuzumab together with the tracer followed by at least two baseline PET scans 4 and 7 days postinjection (Part A *n* = 3, Part B *n* = 13). On day 4 postinjection the highest tracer uptake was seen in the liver with SUVmean of  $6.4 \pm 1.1$  (Fig. 1). Furthermore, relatively high tracer levels

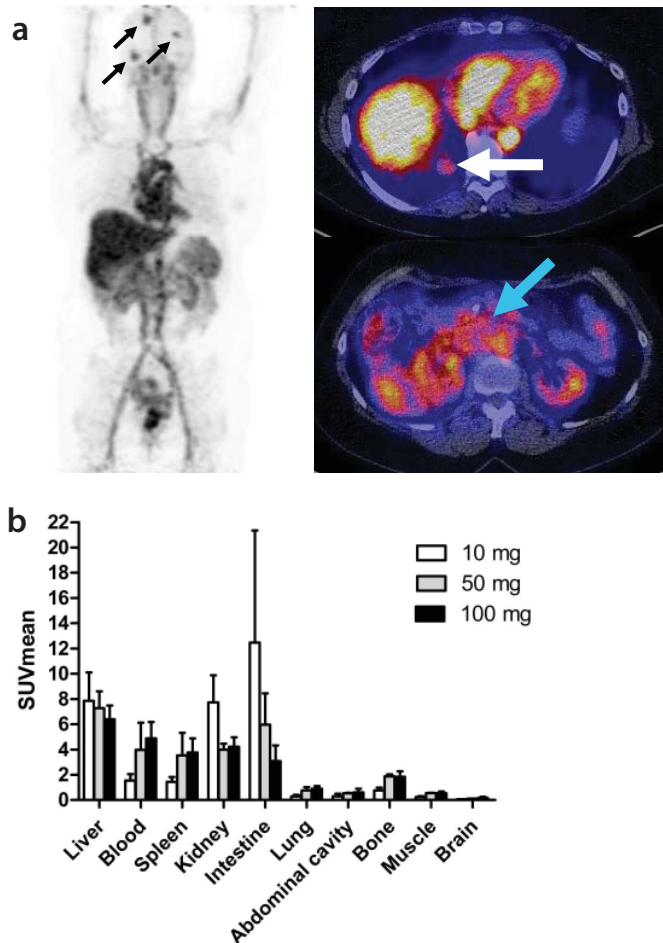


**Figure 1 (a)** <sup>89</sup>Zr-lumretuzumab PET scan with 100 mg unlabeled lumretuzumab 4 days post injection with representative whole body tracer distribution and tracer uptake in multiple brain metastases (black arrows), one lung metastasis behind the liver (white arrow) and the primary tumor (Cancer of the ampulla of Vater, blue arrow). **(b)** <sup>89</sup>Zr-lumretuzumab organ biodistribution 4 days post injection for different doses of unlabeled lumretuzumab; 10 mg unlabeled lumretuzumab in white bars (*n* = 2), 50 mg unlabeled lumretuzumab in grey bars (*n* = 2), 100 mg unlabeled lumretuzumab in black bars (*n* = 16).

were seen in the circulation ( $4.9 \pm 1.3$ ), the kidneys ( $4.2 \pm 0.8$ ), spleen ( $3.8 \pm 1.1$ ) and intestine ( $3.1 \pm 1.2$ ). Tracer uptake was much lower in brain, muscle, bone, abdominal cavity and lung (SUV<sub>mean</sub>  $0.2 \pm 0.1$ ,  $0.5 \pm 0.2$ ,  $0.6 \pm 0.2$ ,  $0.6 \pm 0.3$  and  $0.9 \pm 0.2$ , respectively). Comparable tracer distributions were seen on day 7 postinjection, and in the patients who received 10 or 50 mg unlabeled lumretuzumab in Part A.

Relatively high tracer uptake was observed in healthy liver tissue, which was comparable across dose levels at baseline and after the first lumretuzumab dose ( $P > 0.05$ ; Fig. 1 and Supplementary Fig. 2). When compared to injected imaging dose, liver uptake decreased over time from 10.2 %ID ( $\pm 2.7$ ) on day 2 to 3.4 %ID ( $\pm 2.9$ ) on day 7 (Supplementary Fig. 2a) during the baseline scan series and were comparable after the first PD-active dose ( $P > 0.05$ ). After correcting for the amount of radioactivity remaining in the body assessed on the PET scan, the liver uptake for all dose cohorts did not differ ( $P > 0.05$ ) with a mean liver uptake of 14.6% ( $\pm 0.8$ ) of the remaining dose (%RD; Supplementary Fig. 2b).

### **Tracer uptake in tumor lesions**

Overall, a total of 598 tumor lesions (median number of lesions per patient: 18, range 3-159) from 20 patients were recorded based on the diagnostic CT scans (Supplementary Table 1). Of these, 382 lesions were  $< 10$  mm. Of the 216 lesions  $\geq 10$  mm, 146 lesions (67.6%) were visible on  $^{89}\text{Zr}$ -lumretuzumab PET, of which 115 (53.2%) had quantifiable  $^{89}\text{Zr}$ -lumretuzumab tracer uptake. In all but one patient, tracer uptake was observed in at least one lesion. A median of 5 (range 0-20) lesions per patient were quantifiable for  $^{89}\text{Zr}$ -lumretuzumab tracer uptake. Seventy of the 216 lesions (32.4%) with a diameter  $\geq 10$  mm were not visible on  $^{89}\text{Zr}$ -lumretuzumab PET. Of these 70 lesions, 19 were liver metastases where visible tracer uptake was precluded by the relatively higher tracer uptake of surrounding normal liver tissue. The remaining 51 non-visible lesions in 17 patients were located outside the liver.

Using 10 mg of unlabeled lumretuzumab SUV<sub>max</sub> was 2.7 ( $\pm 1.1$ ), 2.2 ( $\pm 1.0$ ) and 1.8 ( $\pm 1.1$ ) in 25 quantifiable tumor lesions in two patients on 2, 4 and 7 days postinjection, respectively. At 50 mg SUV<sub>max</sub> was comparable ( $n = 2$  patients with 13 lesions). At 100 mg of unlabeled lumretuzumab, SUV<sub>max</sub> increased to 4.0 ( $\pm 2.1$ ) 2 days postinjection ( $n = 3$  patients with 18 lesions, Part A), 3.4 ( $\pm 1.9$ ) 4 days postinjection and 3.4 ( $\pm 2.1$ ) 7 days postinjection (both 4 and 7 days postinjection  $n = 16$  patients with 77 lesions, Part A and B) and the TBR increased over time (Supplementary Fig. 3). The highest SUV<sub>max</sub> at the 100 mg dose level was seen in 8 abdominal lesions (adrenal gland, intestine and ovaries, and other unspecified abdominal tissue lesions) with 6.0 ( $\pm 1.9$ ) and 6.0 ( $\pm 2.2$ ) 4 and 7 days postinjection, respectively (Table 2). Furthermore, tumor uptake was also high in head and neck lesions, lymph nodes, brain lesions and a previously unknown bone metastasis, but lower in pulmonary and subcutaneous lesions. Ascites and/or pleural effusion present in three patients were also visible on all PET scans.

**Table 2** <sup>89</sup>Zr-lumretuzumab tumor uptake at the 100 mg unlabeled lumretuzumab dose level

Tumor lesion, organ (n)	SUVmax (SD) 4 days pi	SUVmax (SD) 7 days pi
Solid quantifiable lesions (77) <sup>a</sup>		
Abdominal lesions (8) <sup>b</sup>	6.0 (1.9)	6.0 (2.2)
Lymph node (11)	5.1 (1.4)	4.8 (1.9)
Head and neck (4)	4.9 (0.9)	3.8 (0.9)
Bone (1) <sup>c</sup>	4.5	5.4
Brain (5)	3.9 (1.7)	4.9 (2.1)
Lung (43)	2.4 (1.2)	2.4 (1.5)
Subcutaneous lesion (5)	2.1 (0.4)	1.9 (0.3)
Malignant fluids (5) <sup>d</sup>		
Ascites (2)	6.4 (0.4)	5.4 (3.)
Pleural effusion (3)	3.0 (1.6)	2.6 (1.1)

<sup>a</sup> Seventy-seven lesions assessed in 16 patients who received 100 mg unlabeled lumretuzumab in addition to the tracer. <sup>b</sup> Abdominal lesions include lesions in the adrenal gland, the intestine, ovaries and other unspecified abdominal tissue. <sup>c</sup> The detected bone metastases was previously unknown and confirmed by MRI after the <sup>89</sup>Zr-lumretuzumab PET. <sup>d</sup> Malignant fluids were found in three patients, one having both ascites and pleural effusion. Pi, postinjection.

<sup>89</sup>Zr-lumretuzumab tracer uptake was shown in at least one tumor lesion in 19/20 patients. In the patient without tumor tracer uptake all 5 lesions visible on the CT scan were located in the liver. Here, <sup>89</sup>Zr-lumretuzumab uptake was lower than in the surrounding liver tissue and therefore not reliably quantifiable (Fig. 2).

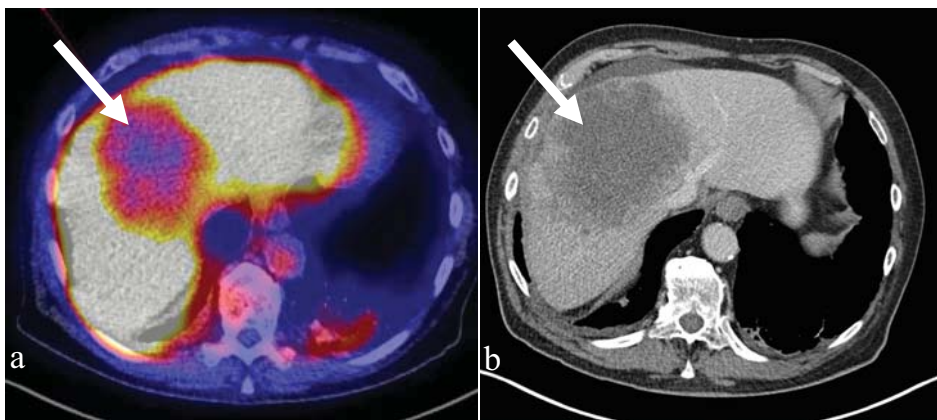


**Figure 2** <sup>89</sup>Zr-lumretuzumab PET (**a**) and diagnostic CT scan (**b**) of the liver of patient 4. The liver metastasis (white arrow) is visually cold on the <sup>89</sup>Zr-lumretuzumab PET scan 7 days after injection of the tracer with additional 50 mg unlabeled lumretuzumab.

### *Tumor<sup>89</sup>Zr-lumretuzumab tracer uptake after the first PD-active dose of lumretuzumab compared to baseline*

Fourteen days after the first tracer injection (~ 1 mg <sup>89</sup>Zr-lumretuzumab together with 100 mg unlabeled lumretuzumab), patients in Part B ( $n = 13$ ) received a second tracer injection with 400, 800 or 1600 mg lumretuzumab followed by a scan 4 and 7 days postinjection to evaluate the decrease in tracer uptake and potential target saturation. Differences in tracer uptake were evaluable in 7 of the 13 patients. In the remaining six patients this failed due to absence of tumor lesions (repeatedly) quantifiable for tracer uptake ( $n = 2$ ), obesity (body mass index of 45 in 1 patient), high liver uptake during the second scan series exceeding baseline liver uptake influencing normal tracer biodistribution ( $n = 1$ ), technical problems ( $n = 1$ ) and no second series due to progressive disease ( $n = 1$ ).

Six lesions in the 400 mg cohort, 9 lesions in the 800 mg cohort and 8 lesions in the 1600 mg cohort were quantifiable (Supplementary Table 2). A decrease in tumor tracer uptake at day 4 after the first PD-active dose and the corresponding baseline PET was seen in all 6 lesions at the 400 mg dose level, in 6 out of 9 lesions at 800 mg and in 7 out of 8 lesions at 1600 mg (Fig. 3 and Supplementary Table 3). In the 800 mg cohort, the 3 lesions without a decrease in tracer uptake were located in the lung, whereas the one at 1600 mg without a decrease in uptake was an abdominal lesion.

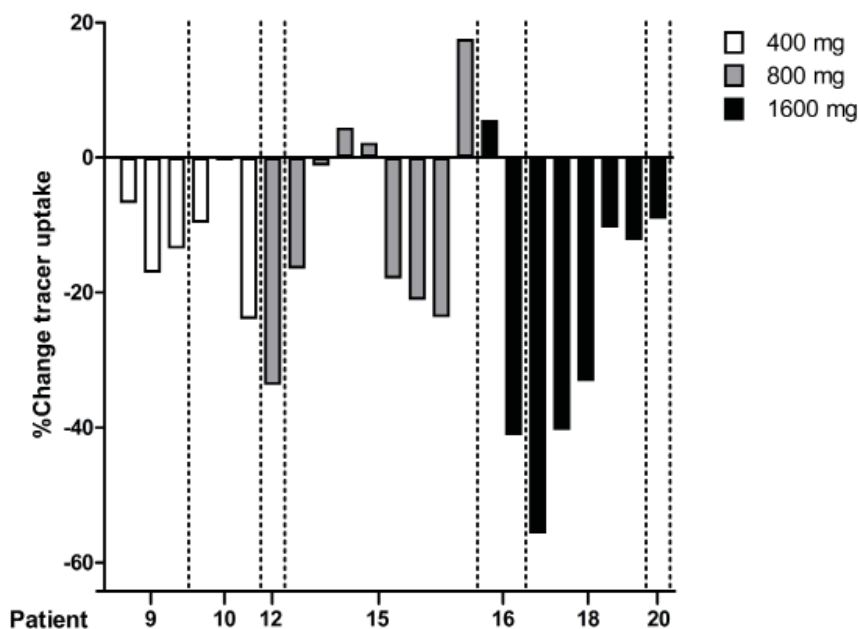


**Figure 3** Percentage change of tracer uptake (as tumor-to-blood ratio) after the first PD-active dose of lumretuzumab (400, 800 or 1600 mg) vs. baseline (100 mg unlabeled lumretuzumab) in 23 quantifiable lesions ( $n = 7$  patients) 4 days postinjection.

The tumor tracer uptake (as percentage change in TBR) in the quantifiable lesions decreased 4 days postinjection by 11.9% ( $\pm$  8.2%) at 400 mg, 10.0% ( $\pm$  16.5%) at 800 mg and 24.6% ( $\pm$  20.9%) at 1600 mg compared to the baseline PET scan with 100 mg of unlabeled lumretuzumab, whilst at 7 days postinjection, the decrease in tumor uptake was 1.5% ( $\pm$  14.0%) at 400 mg, 16.9% ( $\pm$  12.4%) at 800 mg and 11.8% ( $\pm$  28.2%) at 1600 mg compared to baseline (Supplementary Fig. 4).

### Lumretuzumab and <sup>89</sup>Zr pharmacokinetics

The PK of lumretuzumab was non-linear from 10 mg up to 100 mg. Both  $C_{\text{max}}$  and  $AUC_{\text{last}}$  showed a greater than dose proportional increase, accompanied by a decline in clearance over the same dose range, indicating that the elimination of lumretuzumab across this dose range was predominantly target-mediated. Overall, systemic exposure ( $AUC_{\text{last}}$ ) during the first cycle in patients treated with 400, 800 and 1600 mg increased dose proportional with comparable total clearance. PK variability was observed among cohorts and within cohorts.

Activity of <sup>89</sup>Zr assessed in serum and whole blood samples and lumretuzumab serum concentration correlated strongly with blood pool activity assessed on PET scans at baseline (Supplementary Fig. 5).

### HER3 expression

HER3 tumor expression was seen in all 20 patients at baseline (Supplementary Fig. 6). In 11 of 12 biopsied non-hepatic tumor lesions tracer uptake was visible on <sup>89</sup>Zr-lumretuzumab PET. The one metastasis without visible tracer uptake was an abdominal lesion. Tracer uptake at either day 4 or day 7 did not correlate with baseline HER3 tumor expression (Spearman's correlation coefficient = 0.049 ( $P$  = 0.89) and 0.049 ( $P$  = 0.89), respectively,  $n$  = 10, Table 3).

Membranous HER3, assessed in paired skin biopsies ( $n$  = 8 patients in Part B), was completely downregulated 14 days after the first PD-active lumretuzumab dose compared to baseline (HER3 IHC as median IRS: pre 0.69, post 0;  $P$  < 0.0001), which is in line with previously published data.<sup>11</sup>

### Efficacy and safety of lumretuzumab monotherapy

After the baseline <sup>89</sup>Zr-lumretuzumab PET scans, the first patient in Part A received lumretuzumab at a dose of 1600 mg for further treatment. All following patients received 2000 mg lumretuzumab. Patients received lumretuzumab for a median of 4 cycles (range 0 to 8 cycles) or a median duration of 57 days (range 1 to 120 days). Five patients (25%) had as best response stable disease. Patients were discontinued from the study due to progressive disease according to RECIST 1.1 ( $n$  = 17), clinical progression ( $n$  = 2) or death ( $n$  = 1).

**Table 3 Tumor HER3 expression and <sup>89</sup>Zr-lumretuzumab tumor tracer uptake**

Patient	Unlabeled lumretuzumab (mg)	Tumor lesion, organ	HER3 expression (IRS)	<sup>89</sup> Zr-lumretuzumab uptake (SUVmax)	
				4 days pi	7 days pi
1 <sup>f</sup>	10	Lung	2.90	2.37	1.52
2	10	Lymph node	2.90	- <sup>e</sup>	- <sup>e</sup>
3	50	Lung	1.62	2.12	2.29
4 <sup>f</sup>	50	Liver <sup>a</sup>	2.50	-	-
5 <sup>f</sup>	100	Lung	0.078	2.39	1.86
6	100	Subcutaneous lesion	2.40	2.29	2.14
7 <sup>f</sup>	100	Liver <sup>a</sup>	2.25	-	-
8	100	Liver <sup>a</sup>	2.50	-	-
9	100	Head and neck	1.35	5.98	4.89
10	100	Liver <sup>a</sup>	0.0035	-	-
11	100	Head and neck	0.16	5.63	3.89
12	100	Liver <sup>a</sup>	2.43	-	-
13	100	Lung	1.71	1.65	1.64
14 <sup>f</sup>	100	Liver <sup>a</sup>	2.57	-	-
15	100	Lung	2.71	3.88	4.23
16	100	Abdominal lesion <sup>b</sup>	3.0	7.93	7.54
17 <sup>f</sup>	100	Abdominal lesion <sup>b,d</sup>	1.62	2.14 <sup>d</sup>	2.35 <sup>d</sup>
18 <sup>f</sup>	100	Liver <sup>a</sup>	1.13	-	-
19	100	Liver <sup>a</sup>	2.25	-	-
20	100	Ascites <sup>c</sup>	NA	6.68	7.75

<sup>a</sup> Tracer uptake in hepatic lesions is not visible and not quantifiable on <sup>89</sup>Zr-lumretuzumab PET due to high tracer uptake of surrounding normal liver tissue. <sup>b</sup> Abdominal lesions include metastasis in the intestine and ovaries. <sup>c</sup> For IHC, tumor cells were obtained from malignant cell-rich ascites. <sup>d</sup> The abdominal mass of patient 17 was visually negative on <sup>89</sup>Zr-lumretuzumab PET, the lesion was quantified for correlation analysis. <sup>e</sup> Lesion was visible on <sup>89</sup>Zr-lumretuzumab PET but tracer uptake was not reliably quantifiable due to adjacent vessels with high blood activity. <sup>f</sup> Patients who received EGFR-targeted therapy in any line prior to inclusion in this study. IRS, immunoreactive score; NA, not available; pi, postinjection.

Baseline <sup>89</sup>Zr-lumretuzumab tracer uptake in individual target lesions did not correlate with size change on CT during first or second response assessment ( $n = 14$  patients with 31 lesions and  $n = 4$  patients with 6 lesions, respectively).

The <sup>89</sup>Zr-lumretuzumab tracer and lumretuzumab monotherapy up to 2000 mg per cycle were well tolerated (Supplementary Table 4).

## DISCUSSION

In this study we were able to characterize the biodistribution of <sup>89</sup>Zr-lumretuzumab and tumor uptake by serial imaging with the <sup>89</sup>Zr-labeled therapeutic antibody lumretuzumab before and during treatment in patients with advanced or metastatic HER3-positive solid tumors. Although PD-active lumretuzumab doses decreased <sup>89</sup>Zr-lumretuzumab uptake, there was no clear evidence of tumor saturation by PET imaging as the tumor SUV did not plateau with increasing doses.

Development of therapeutic HER3 antibodies is still in an early phase. Results of first trials with these HER3 antibodies indicate that further application of these drugs will focus on biomarker-enriched populations, as well as on combination with other treatments targeting other HER family members.<sup>11</sup> This makes insight in biodistribution, information on intra- and interpatient target heterogeneity and target accessibility, as well as target occupation or even saturation of utmost importance. First attempts to label an HER3 antibody were made in a small study with Copper-64-tetra-azacyclododecanetetra-acetic acid (<sup>64</sup>Cu-DOTA)-patritumab and feasibility was shown.<sup>36</sup> We preferred <sup>89</sup>Zr over <sup>64</sup>Cu as its longer half-life of 78.4 hours compared with 12.7 hours for <sup>64</sup>Cu better matches the half-life of lumretuzumab.<sup>30,37</sup> Furthermore, the target saturation for different PD-active doses of lumretuzumab was analyzed in the current study.

All but one patient, who had liver metastases only, showed quantifiable tracer tumor uptake in at least one metastasis. Tumor uptake of <sup>89</sup>Zr-lumretuzumab varied within and between patients, with tumor SUV<sub>max</sub> ranging from 0.5 up to 8.9 with up to a 6-fold difference in mean tumor tracer uptake between patients. Lesions with a diameter ≥ 10 mm were <sup>89</sup>Zr-lumretuzumab PET-negative in 32.4%. Although testing positive for HER3 by IHC, the PET-negative lesions and the observed variance in <sup>89</sup>Zr-lumretuzumab tumor uptake may be a result of intratumor and inpatient target heterogeneity. In addition it may well be that lesions with low tracer uptake or PET-negative lesions have other characteristics than PET-positive lesions causing lack of tracer permeability within those lesions. Contributing factors might be the vascularization, tissue permeability and retention, as well as the size of the lesion.<sup>38</sup> These factors together with low target expression could have generated insufficient signal to be picked up adequately by PET imaging on the late scan moments with the used scan time and administered dose of radioactivity.

Similar results on heterogeneity of tumor tracer uptake were reported for the ZEPHIR trial, where one third of HER2-positive metastatic breast cancer patients were considered <sup>89</sup>Zr-trastuzumab PET-negative before start of treatment with trastuzumab-emtansine.<sup>39</sup> Another trial assessing the biodistribution and PD of the Indium-111-labeled, anti-human death receptor 5 (DR5) monoclonal antibody tigatuzumab, seven out of 19 patients (37%) with metastatic colorectal cancer also had no SPECT-positive lesions and tumor tracer uptake did not correlate

with DR5 expression or tumor response.<sup>40</sup> In both trials, target heterogeneity and tissue-dependent properties were proposed factors to influence general tracer availability and tumor tracer uptake. To conclude, all these studies suggest that we most likely underestimate other factors which may influence penetration of drugs and local drug concentration in the tumor, next to heterogeneity in target expression.

<sup>89</sup>Zr-lumretuzumab uptake in liver metastases was always considered negative on PET imaging given relatively higher <sup>89</sup>Zr-lumretuzumab background activity in healthy liver tissue. The background liver tracer uptake even exceeded tumor lesions with the highest uptake outside the liver. This is clearly different from <sup>89</sup>Zr-trastuzumab uptake in liver metastases, which was almost 2-fold higher compared to surrounding healthy liver tissue in HER2-positive metastatic breast cancer patients.<sup>23</sup> The high tracer accumulation in healthy liver tissue might be due to uptake and metabolism of (<sup>89</sup>Zr-labeled) lumretuzumab by healthy liver nonparenchymal Kupffer cells due to glycosylation of lumretuzumab. Especially glycosylation with mannose increases blood clearance of the antibody and enhances Antibody-dependent cell-mediated cytotoxicity (ADCC) against tumor cells.<sup>41</sup> As the liver is a key organ in antibody clearance and attracting the immune system for ADCC, it might explain the relatively higher tracer uptake in healthy liver tissue compared to liver metastases. This, however, did not result in specific liver toxicity or higher efficacy in liver metastases.<sup>11</sup> On the other hand, the target receptor density, which is generally lower in HER3-positive tumor lesions compared to HER2-positive lesions, might also explain the PET-negative liver lesions.

For optimal imaging results, an additional dose of 100 mg of unlabeled lumretuzumab was required, as lower doses did not result in sufficient tracer in the circulation for adequate tumor visualization. For imaging of a number of antibodies without dose-dependent PK, such as bevacizumab, fresolimumab or the mesothelin-targeting antibody MMOT0530A, a dose of 5 or 10 mg unlabeled antibody was already sufficient for optimal PET imaging.<sup>24,29,32,42</sup> However, for HER2 imaging with <sup>89</sup>Zr-trastuzumab, an antibody with clear dose-dependent PK, an additional dose of 50 mg unlabeled trastuzumab is needed for optimal imaging.<sup>43,44</sup> As described previously, we showed that lumretuzumab has also dose-dependent PK with declining clearance up to 400 mg dose, which at least in part explains the need of additional 100 mg unlabeled antibody for optimal imaging.<sup>11</sup>

The organ biodistribution of <sup>89</sup>Zr-lumretuzumab was largely comparable to the distribution of other <sup>89</sup>Zr-labeled antibodies.<sup>23-25</sup> The highest uptake was observed in the liver (14.6% of the remaining dose) and intestine, representing locations of antibody metabolism and excretion without showing clear signs of organ-specific drug-mediated toxicity.

In the absence of side effects therapeutic antibodies may easily be dosed above the maximum tumor saturation.<sup>45</sup> In this study there was a dose proportional increase of systemic exposure from 400 mg to 1600 mg lumretuzumab. A decrease in tumor tracer uptake between PET assessments after administration of the first PD-active dose compared to baseline was

detectable. The decrease in tumor tracer uptake at 4 days postinjection compared to baseline was the highest at the highest tested lumretuzumab dose of 1600 mg, confirming PD activity but without showing a plateau. Immunohistochemical analyses of skin samples showed receptor saturation at and above lumretuzumab doses of 400 mg 14 days following the first PD-active dose. Regrettably, the resolution of PET does not allow visualizing the skin as a separate organ and therefore precludes comparison with tumor saturation. Furthermore, we performed PET imaging only up to 7 days after the first PD-active lumretuzumab administration, which might have been too early to visualize the full effect of the dose.

Based on assumptions from classic saturation analysis, the dose at which no additional decrease in tumor drug uptake is seen would confirm target saturation and would identify the maximum required drug dose.<sup>46</sup> However, receptor expression and related processes are dynamic and novel ways of analysis might be helpful to take receptor dynamics into account. From preclinical assessments it is known that HER3 membrane expression is highly dynamic and expression is influenced by internalization, degradation and relocation to the membrane of formerly internalized receptors.<sup>47</sup> Furthermore, internalization might even be increased by activation of endocytosis due to antibody treatment further increasing receptor internalization.<sup>48-50</sup> With molecular imaging of <sup>89</sup>Zr-tracers, more than with other techniques, such dynamic processes might influence the outcome. Thereby, PET visualizes a combination of membrane-bound activity, as well as the intracellular fraction as the relatively long-living radionuclide <sup>89</sup>Zr residualizes in tumor cells after internalization. This information differs from the HER3 expression measured serially in (skin) biopsies in this trial by scoring membrane staining only.<sup>37</sup> Other factors influencing tumor tracer uptake might be the effect of enhanced permeability and retention in tumor lesions and (unspecific) tracer uptake *e.g.* due to the effect of Fc gamma receptor engagement within the tumor environment possibly differing between tumor types. To correct for variance in tracer blood levels, the tumor-to-blood ratios were used to assess the difference in uptake after administration of the PD-active dose and baseline imaging. Furthermore, in HER2-positive breast cancer patients, <sup>111</sup>In-trastuzumab scintigraphy showed a decrease in tumor uptake of only 20% during steady state following three therapeutic doses of trastuzumab.<sup>42</sup> Data from this and our trial might also suggest that it might be impossible to completely saturate these receptors due to its constant renewal and relocation. To obtain additional insight in tracer accumulation and behavior on a cellular level, however, additional microscopic fluorescence imaging using fluorescent tracers might be considered in future trials. Furthermore, when HER3 antibodies get a firmer place in the clinic, a broader role for this tracer including assessment of the ability to predict tumor response to treatment can be foreseen.

In conclusion, we demonstrated <sup>89</sup>Zr-lumretuzumab biodistribution and specific tumor tracer uptake in patients with HER3-positive epithelial tumors and observed inter- and intra-patient heterogeneity in lesions across the body apart from the liver. Serial imaging after the first PD-

active dose with HER3 downregulation in skin biopsies at and above 400 mg lumretuzumab showed reduced tumor tracer uptake compared to baseline, confirming PD activity. In contrast to the phase I PD data, there was no clear evidence of tumor saturation by PET imaging as the tumor SUV did not plateau with increasing doses. This suggests highly dynamic receptor processes, but could also be influenced by technical limitations, variable expression levels of the target, as well as variable saturation kinetics.

### **Acknowledgments**

We thank Linda Pot and Rianne Bakker for technical support for the labeling procedures and Paul van Snick, Johan Wiegers and Eelco Severs for their assistance with PET data transfer.

### **Disclosure of potential conflicts of interest**

W. Jacob holds ownership interest (including patents) in Roche stock. M. Weisser holds ownership interest (including patents) in Roche shares. No potential conflicts of interest were disclosed by the other authors.

### **Grant support**

The ERC-advanced grant OnQview was provided to E.G.E. de Vries, and financial support for the study was provided by F. Hoffmann–La Roche Ltd to the UMCG.

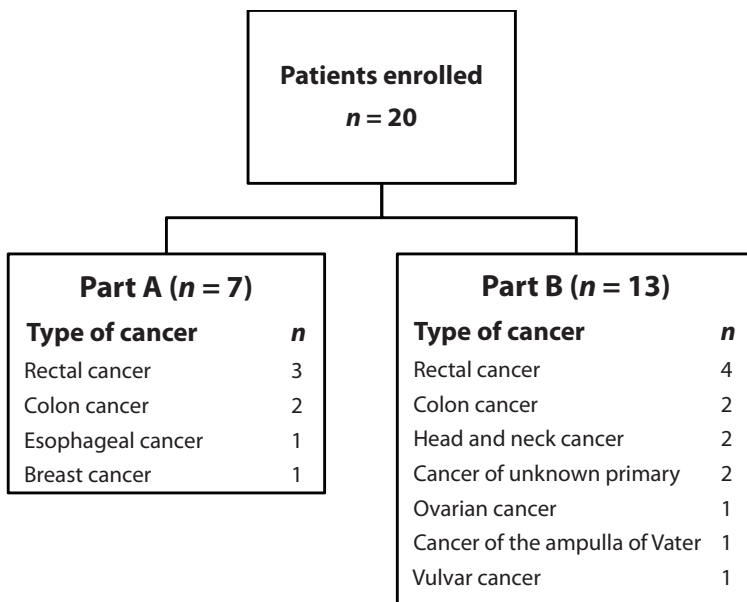
## REFERENCES

1. Campbell, M. R., Amin, D. & Moasser, M. M. HER3 comes of age: new insights into its functions and role in signaling, tumor biology, and cancer therapy. *Clin. Cancer Res.* 16, 1373-1383 (2010).
2. Prigent, S. A. *et al.* Expression of the c-erbB-3 protein in normal human adult and fetal tissues. *Oncogene* 7, 1273-1278 (1992).
3. Hayashi, M. *et al.* High expression of HER3 is associated with a decreased survival in gastric cancer. *Clin. Cancer Res.* 14, 7843-7849 (2008).
4. Cao, G. D., Chen, K., Xiong, M. M. & Chen, B. HER3, but not HER4, plays an essential role in the clinicopathology and prognosis of gastric cancer: A meta-analysis. *PLoS One* 11, e0161219 (2016).
5. Debska-Szmich, S. *et al.* Prognostic value of HER3, PTEN and p-HER2 expression in patients with HER2-positive breast cancer. *Postepy Hig. Med. Dosw. (Online)* 69, 586-597 (2015).
6. Tanner, B. *et al.* ErbB-3 predicts survival in ovarian cancer. *J. Clin. Oncol.* 24, 4317-4323 (2006).
7. Hirakawa, T. *et al.* HER3 overexpression as an independent indicator of poor prognosis for patients with curatively resected pancreatic cancer. *Oncology* 81, 192-198 (2011).
8. Sithanandam, G. & Anderson, L. M. The ERBB3 receptor in cancer and cancer gene therapy. *Cancer Gene Ther.* 15, 413-448 (2008).
9. Ocana, A. *et al.* HER3 overexpression and survival in solid tumors: a meta-analysis. *J. Natl. Cancer Inst.* 105, 266-273 (2013).
10. Mirschberger, C. *et al.* RG7116, a therapeutic antibody that binds the inactive HER3 receptor and is optimized for immune effector activation. *Cancer Res.* 73, 5183-5194 (2013).
11. Meulendijks, D. *et al.* First-in-human phase I study of lumretuzumab, a glycoengineered humanized anti-HER3 monoclonal antibody, in patients with metastatic or advanced HER3-positive solid tumors. *Clin. Cancer Res.* 22, 877-885 (2016).
12. Burrell, R. A. & Swanton, C. Tumour heterogeneity and the evolution of polyclonal drug resistance. *Mol. Oncol.* 8, 1095-1111 (2014).
13. Heitz, F. *et al.* Differences in the receptor status between primary and recurrent breast cancer—the frequency of and the reasons for discordance. *Oncology* 84, 319-325 (2013).
14. Moussa, O., Purdie, C., Vinnicombe, S. & Thompson, A. M. Biomarker discordance: prospective and retrospective evidence that biopsy of recurrent disease is of clinical utility. *Cancer. Biomark* 12, 231-239 (2012).
15. Houssami, N., Macaskill, P., Balleine, R. L., Bilous, M. & Pegram, M. D. HER2 discordance between primary breast cancer and its paired metastasis: tumor biology or test artefact? Insights through meta-analysis. *Breast Cancer Res. Treat.* 129, 659-674 (2011).
16. Siyar Ekinci, A. *et al.* KRAS discordance between primary and metastatic tumor in patients with metastatic colorectal carcinoma. *J. BUON.* 20, 128-135 (2015).
17. Amir, E. *et al.* Discordance between receptor status in primary and metastatic breast cancer: an exploratory study of bone and bone marrow biopsies. *Clin. Oncol. (R. Coll. Radiol)* 20, 763-768 (2008).
18. Lower, E. E., Glass, E., Blau, R. & Harman, S. HER2/neu expression in primary and metastatic breast cancer. *Breast Cancer Res. Treat.* 113, 301-306 (2009).
19. Curigliano, G. *et al.* Should liver metastases of breast cancer be biopsied to improve treatment choice? *Ann. Oncol.* 22, 2227-2233 (2011).
20. Tosi, D. *et al.* Clinical development strategies and outcomes in first-in-human trials of monoclonal antibodies. *J. Clin. Oncol.* 33, 2158-2165 (2015).
21. Lamberts, L. E. *et al.* Antibody positron emission tomography imaging in anticancer drug development. *J. Clin. Oncol.* 33, 1491-1504 (2015).
22. van Dongen, G. A., Poot, A. J. & Vugts, D. J. PET imaging with radiolabeled antibodies and tyrosine kinase inhibitors: immuno-PET and TKI-PET. *Tumour Biol.* 33, 607-615 (2012).
23. Dijkers, E. C. *et al.* Biodistribution of <sup>89</sup>Zr-trastuzumab and PET imaging of HER2-positive lesions in patients with metastatic breast cancer. *Clin. Pharmacol. Ther.* 87, 586-592 (2010).

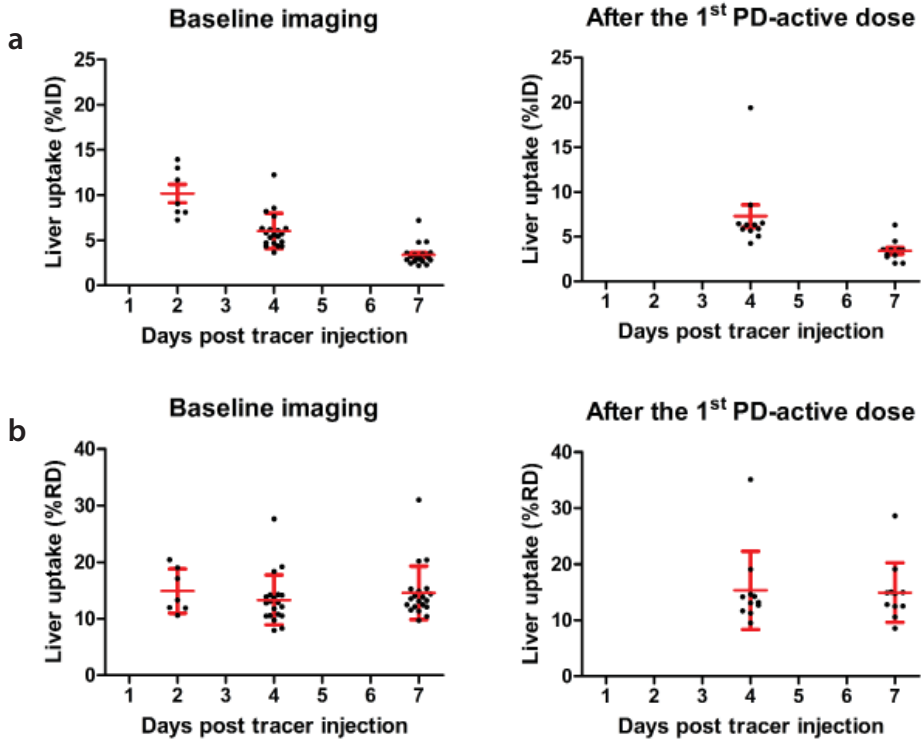
24. Oosting, S. F. *et al.*  $^{89}\text{Zr}$ -bevacizumab PET visualizes heterogeneous tracer accumulation in tumor lesions of renal cell carcinoma patients and differential effects of antiangiogenic treatment. *J. Nucl. Med.* 56, 63-69 (2015).
25. Gaykema, S. B. *et al.*  $^{89}\text{Zr}$ -bevacizumab PET imaging in primary breast cancer. *J. Nucl. Med.* 54, 1014-1018 (2013).
26. Gaykema, S. B. *et al.*  $^{89}\text{Zr}$ -trastuzumab and  $^{89}\text{Zr}$ -bevacizumab PET to evaluate the effect of the HSP90 inhibitor NVP-AUY922 in metastatic breast cancer patients. *Clin. Cancer Res.* 20, 3945-3954 (2014).
27. Borjesson, P. K. *et al.* Performance of immuno-positron emission tomography with zirconium-89-labeled chimeric monoclonal antibody U36 in the detection of lymph node metastases in head and neck cancer patients. *Clin. Cancer Res.* 12, 2133-2140 (2006).
28. Rizvi, S. N. *et al.* Biodistribution, radiation dosimetry and scouting of  $^{90}\text{Y}$ -ibratumomab tiuxetan therapy in patients with relapsed B-cell non-Hodgkin's lymphoma using  $^{89}\text{Zr}$ -ibratumomab tiuxetan and PET. *Eur. J. Nucl. Med. Mol. Imaging* 39, 512-520 (2012).
29. den Hollander, M. W. *et al.* TGF- $\beta$  antibody uptake in recurrent high-grade glioma imaged with  $^{89}\text{Zr}$ -fresolimumab PET. *J. Nucl. Med.* 56, 1310-1314 (2015).
30. Terwisscha van Scheltinga, A. G. *et al.* ImmunoPET and biodistribution with human epidermal growth factor receptor 3 targeting antibody  $^{89}\text{Zr}$ -RG7116. *MAbs* 6, 1051-1058 (2014).
31. Verel, I. *et al.*  $^{89}\text{Zr}$  immuno-PET: comprehensive procedures for the production of  $^{89}\text{Zr}$ -labeled monoclonal antibodies. *J. Nucl. Med.* 44, 1271-1281 (2003).
32. Lamberts, T. E. *et al.* ImmunoPET with anti-mesothelin antibody in patients with pancreatic and ovarian cancer before anti-mesothelin antibody-drug conjugate treatment. *Clin. Cancer Res.* 22, 1642-1652 (2016).
33. Eisenhauer, E. A. *et al.* New response evaluation criteria in solid tumours: revised RECIST guideline (version 1.1). *Eur. J. Cancer* 45, 228-247 (2009).
34. Loening, A. M. & Gambhir, S. S. AMIDE: a free software tool for multimodality medical image analysis. *Mol. Imaging* 2, 131-137 (2003).
35. National Cancer Institute. Common terminology criteria for adverse events v4.0. *NCI, NIH, DHHS.*, NIH publication # 09-7473. (2009).
36. Lockhart, A. C. *et al.* Phase 1 evaluation of  $^{64}\text{Cu}$ -DOTA-patritumab to assess dosimetry, apparent receptor occupancy, and safety in subjects with advanced solid tumors. *Mol. Imaging Biol.* 18, 446-453 (2016).
37. Perk, L. R. *et al.*  $^{89}\text{Zr}$  as a PET surrogate radioisotope for scouting biodistribution of the therapeutic radiometals  $^{90}\text{Y}$  and  $^{177}\text{Lu}$  in tumor-bearing nude mice after coupling to the internalizing antibody cetuximab. *J. Nucl. Med.* 46, 1898-1906 (2005).
38. Baban, D. F. & Seymour, L. W. Control of tumour vascular permeability. *Adv. Drug Deliv. Rev.* 34, 109-119 (1998).
39. Gebhart, G. *et al.* Molecular imaging as a tool to investigate heterogeneity of advanced HER2-positive breast cancer and to predict patient outcome under trastuzumab emtansine (T-DM1): the ZEPHIR Trial. *Ann Oncol.* 27, 619-624 (2016).
40. Ciprotti, M. *et al.* Phase I imaging and pharmacodynamic trial of CS-1008 in patients with metastatic colorectal cancer. *J. Clin. Oncol.* 33, 2609-2616 (2015).
41. Liu, L. Antibody glycosylation and its impact on the pharmacokinetics and pharmacodynamics of monoclonal antibodies and Fc-fusion proteins. *J. Pharm. Sci.* 104, 1866-1884 (2015).
42. Gaykema, S. B. *et al.*  $^{111}\text{In}$ -trastuzumab scintigraphy in HER2-positive metastatic breast cancer patients remains feasible during trastuzumab treatment. *Mol. Imaging* 13 (2014).
43. Oude Munnink, T. H. *et al.* Trastuzumab pharmacokinetics influenced by extent human epidermal growth factor receptor 2-positive tumor load. *J. Clin. Oncol.* 28, e355 (2010).
44. Bruno, R. *et al.* Population pharmacokinetics of trastuzumab in patients with HER2-positive metastatic breast cancer. *Cancer Chemother. Pharmacol.* 56, 361-369 (2005).
45. Weissleder, R., Ross, B., Rehemtulla, A. & Gambhir, S. in *Molecular imaging principles and practice*. 1161-1178 (Shelton, Connecticut, USA: People's Medical Publishing House, 2010).
46. Hulme, E. C. & Trevethick, M. A. Ligand binding assays at equilibrium: validation and interpretation. *Br. J. Pharmacol.* 161, 1219-1237 (2010).

47. Kol, A. *et al.* HER3, serious partner in crime: therapeutic approaches and potential biomarkers for effect of HER3-targeting. *Pharmacol. Ther.* 143, 1-11 (2014).
48. Jaramillo, M. L. *et al.* Effect of the anti-receptor ligand-blocking 225 monoclonal antibody on EGF receptor endocytosis and sorting. *Exp. Cell Res.* 312, 2778-2790 (2006).
49. Sunada, H., Magun, B. E., Mendelsohn, J. & MacLeod, C. L. Monoclonal antibody against epidermal growth factor receptor is internalized without stimulating receptor phosphorylation. *Proc. Natl. Acad. Sci. USA.* 83, 3825-3829 (1986).
50. Austin, C. D. *et al.* Endocytosis and sorting of ErbB2 and the site of action of cancer therapeutics trastuzumab and geldanamycin. *Mol. Biol. Cell* 15, 5268-5282 (2004).

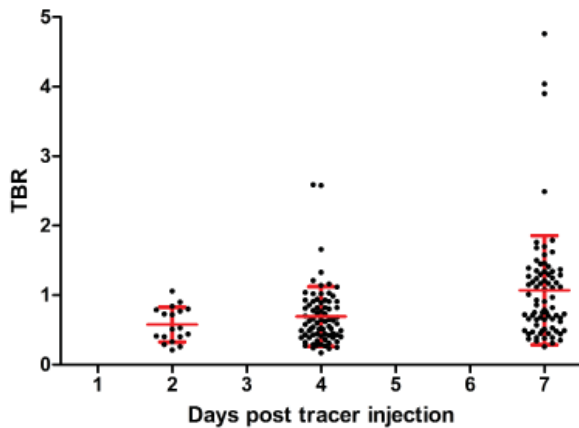
## SUPPLEMENTARY MATERIAL



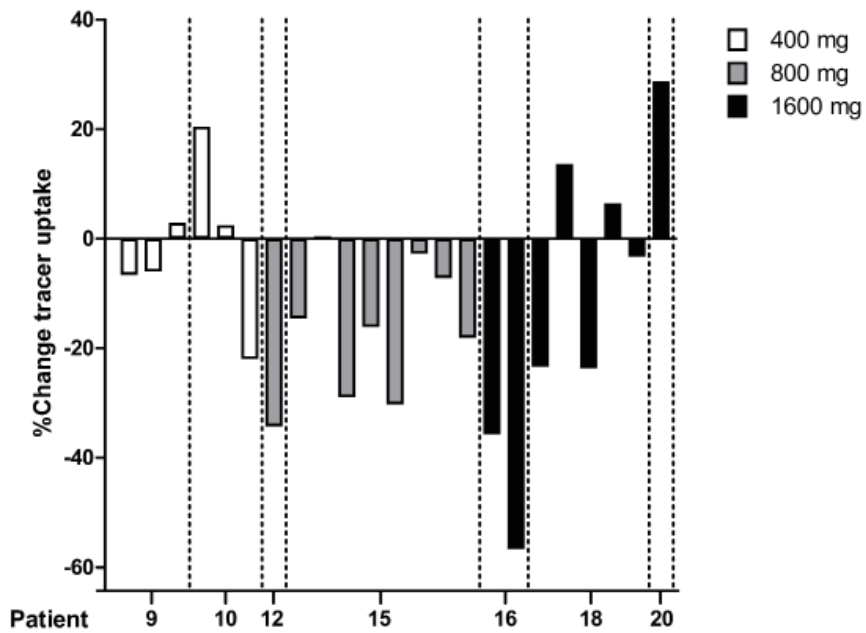
Supplementary Figure 1 Cancer types per study part.



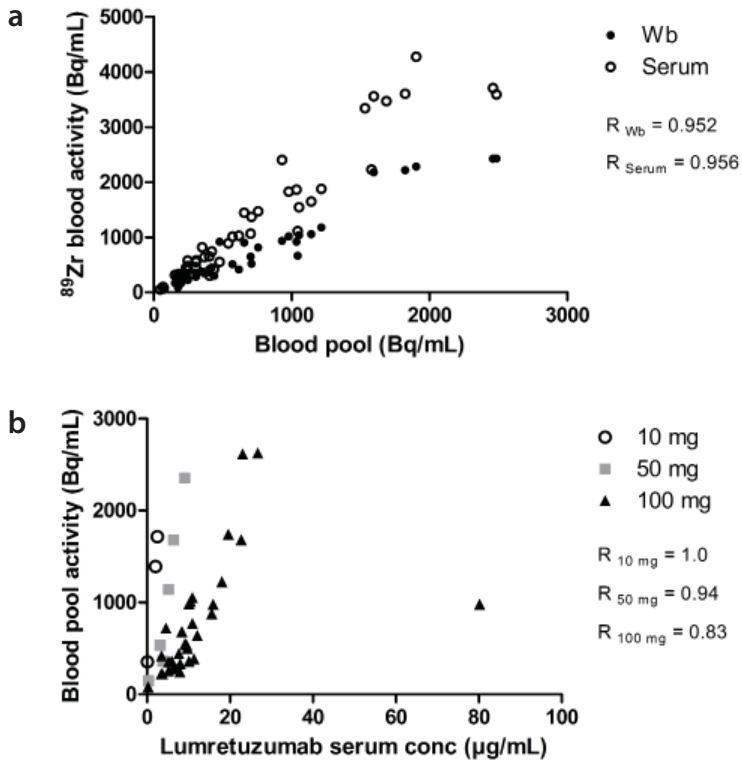
**Supplementary Figure 2** Mean ( $\pm$  SD) <sup>89</sup>Zr-lumretuzumab liver uptake at baseline imaging and after the first PD-active dose assessed on PET scan and expressed as percentage of injected tracer dose (%ID, **a**) or as percentage of at this moment remaining tracer dose (%RD, **b**).



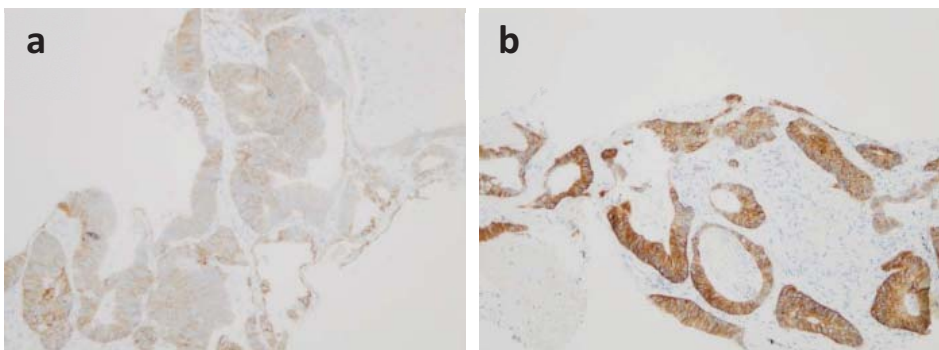
**Supplementary Figure 3** Tumor-to-blood ratio (TBR) on day 2 ( $n = 3$  patients with 18 lesions), day 4 and day 7 ( $n = 16$  patients with 77 lesions) after administration of <sup>89</sup>Zr-lumretuzumab accompanied by 100 mg unlabeled lumretuzumab (baseline).



**Supplementary Figure 4** Percentage change of tracer uptake (as tumor-to-blood ratio) after the first PD-active dose of lumretuzumab (400, 800 or 1600 mg) vs. baseline (100 mg unlabeled lumretuzumab) in 23 quantifiable lesions ( $n = 7$  patients) 7 days postinjection.



**Supplementary Figure 5** (a) <sup>89</sup>Zr-blood activity (counts per minute of serum or whole blood (wb) converted to SUV) vs. blood pool activity on PET scans (SUVmean) at baseline. (b) Lumretuzumab serum concentration (µg/mL) vs. blood pool activity on PET (Bq/mL) at baseline.



**Supplementary Figure 6** HER3 staining of two cases: patient 5 with low IRS (0.078, a) and patient 1 with high IRS (2.90, b).

**Supplementary Table 1 Lesion counts based on conventional CT and <sup>89</sup>Zr-lumretuzumab PET**

Category	Number (%)
Total number of lesions determined on diagnostic CT:	598
Lesions with diameter < 10 mm	382 (63.9) *
Lesions with diameter ≥ 10 mm	216 (36.1) *
Lesions ≥ 10 mm and visible on <sup>89</sup> Zr-lumretuzumab PET	146 (67.6) **
Lesions ≥ 10 mm and quantifiable on <sup>89</sup> Zr-lumretuzumab PET	115 (53.2) **
10 mg unlabeled lumretuzumab	25
50 mg unlabeled lumretuzumab	13
100 mg unlabeled lumretuzumab	77
Lesions ≥ 10 mm and without visible <sup>89</sup> Zr-lumretuzumab uptake	70 (32.4) **
Hepatic metastases <sup>a</sup>	19
Non-hepatic lesions <sup>b</sup>	51
Lung	27
Lymph node	11
Bone	6
Abdominal soft tissue	3
Kidney	2
Spleen	1
Subcutaneous lesion	1

<sup>a</sup> Tracer uptake in all hepatic lesions is considered not visible and not quantifiable. <sup>b</sup> On <sup>89</sup>Zr-lumretuzumab PET non-hepatic lesions without visible tracer uptake with a diameter of ≥ 10 mm were recorded in 17/20 patients. \* Percentage of all lesions; \*\* Percentage of all lesions with diameter ≥ 10 mm.

**Supplementary Table 2 Location of tumor lesions repeatedly quantifiable on <sup>89</sup>Zr-lumretuzumab PET scans**

Unlabeled lumretuzumab (mg)	Number of patients	Tumor lesion, organ (n)
400	2	Lung (3) Lymph nodes (3)
800	2	Lung (8) Intestine (1)
1600	3	Lung (5) Abdominal soft tissue (3) <sup>a</sup>

<sup>a</sup> Two of three abdominal soft tissue lesions derived from ovarian cancer.

**Supplementary Table 3 SUV of blood pool and quantifiable lesions per patient over time**

Patient	Lesion	Blood pool (SUVmean)				Tumor uptake (SUVmax)			
		Baseline		1 <sup>st</sup> PD-active dose		Baseline		1 <sup>st</sup> PD-active dose	
		Day 4	Day 7	Day 4	Day 7	Day 4	Day 7	Day 4	Day 7
9	1	5.84	4.05	7.48	5.14	4.78	3.91	5.70	4.64
	2					5.98	4.89	6.34	5.84
	3					3.80	2.86	4.21	3.74
10	1	5.64	3.50	4.74	4.37	2.97	2.48	2.25	3.72
	2					3.74	3.53	3.13	4.52
	3					5.03	4.54	3.21	4.42
12	1	3.93	2.57	4.44	2.82	3.17	3.05	2.37	2.19
15	1	4.26	3.08	5.76	4.29	2.32	2.63	2.62	3.13
	2					1.84	2.03	2.46	2.84
	3					2.50	2.85	3.52	2.82
	4					3.40	3.60	4.69	4.20
	5					3.28	4.46	3.64	4.33
	6					3.87	3.32	4.13	4.50
	7					3.88	4.23	4.00	5.46
	8					1.93	2.20	3.06	2.51
16	1	3.08	1.87	4.66	2.93	7.93	7.54	12.68	7.61
	2					7.96	8.90	7.09	6.04
18	1	4.12	3.35	6.78	3.92	2.79	2.21	2.03	1.99
	2					2.24	1.77	2.19	2.36
	3					2.64	2.65	2.90	2.37
	4					1.77	1.63	2.61	2.04
	5					1.61	1.52	2.32	1.72
20	1	4.82	3.36	5.90	3.34	5.51	5.91	6.12	7.57

**Supplementary Table 4 Most frequent adverse events (reported for at least 3 patients)**

Event <sup>a</sup>	Number of patients (%)	Number of patients with Grade 3 events (%) <sup>b</sup>
Diarrhea	9 (45)	-
Infusion-related reaction	5 (25)	-
Abdominal pain	4 (20)	-
Upper respiratory tract infection	4 (20)	-
Urinary tract infection	3 (15)	-
Fatigue	3 (15)	2 (10)
Pyrexia	3 (15)	-

<sup>a</sup> A total of 101 adverse events were experienced by 20 patients. 33 events were considered related and reported for 14 patients (70%). <sup>b</sup> A total of six Grade 3 events were reported in 4 patients. Next to fatigue, hypokalemia and pruritus were observed in a single patient each (5%). No events with Grade 4 or higher were observed.





# Chapter 4

## **TGF- $\beta$ antibody uptake in recurrent high grade glioma imaged with $^{89}\text{Zr}$ -fresolimumab PET**

---

Martha W. den Hollander<sup>1</sup>, Frederike Bensch<sup>1</sup>, Andor W.J.M. Glaudemans<sup>2</sup>,  
Thijs H. Oude Munnink<sup>1</sup>, Roelien H. Enting<sup>3</sup>, Wilfred F.A. den Dunnen<sup>4</sup>, Mart A.A.M. Heesters<sup>5</sup>,  
Frank A.E. Kruyt<sup>1</sup>, Marjolijn N. Lub-de Hooge<sup>2,7</sup>, Jan Cees de Groot<sup>8</sup>, Joseph Pearlberg<sup>9</sup>,  
Jourik A. Gietema<sup>1</sup>, Elisabeth G.E. de Vries<sup>1</sup>, Annemiek M.E. Walenkamp<sup>1</sup>

Departments of Medical Oncology<sup>1</sup>, Nuclear Medicine and Molecular Imaging<sup>2</sup>, Neurology<sup>3</sup>,  
Pathology<sup>4</sup>, Radiotherapy<sup>5</sup>, Neurosurgery<sup>6</sup>, Clinical Pharmacy and Pharmacology<sup>7</sup>, Radiology<sup>8</sup>,  
University of Groningen, University Medical Center Groningen, Groningen, The Netherlands,  
Sanofi-Aventis Oncology<sup>9</sup>, Cambridge, MA, USA.

## ABSTRACT

Transforming growth factor- $\beta$  (TGF- $\beta$ ) signaling is involved in glioma development. The monoclonal antibody fresolimumab (GC1008) can neutralize all mammalian isoforms of TGF- $\beta$ , and tumor uptake can be visualized and quantified with  $^{89}\text{Zr}$ -fresolimumab PET in mice. The aim of this study was to investigate the fresolimumab uptake in recurrent high-grade gliomas using  $^{89}\text{Zr}$ -fresolimumab PET and to assess treatment outcome in patients with recurrent high-grade glioma treated with fresolimumab.

**Patients and methods:** Patients with recurrent glioma were eligible. After intravenous administration of 37 MBq (5 mg) of  $^{89}\text{Zr}$ -fresolimumab, PET scans were acquired on day 2 or day 4 after tracer injection. Thereafter, patients were treated with 5 mg of fresolimumab per kilogram intravenously every 3 weeks.  $^{89}\text{Zr}$ -fresolimumab tumor uptake was quantified as maximum standardized uptake value (SUVmax). MR imaging for response evaluation was performed after 3 infusions or as clinically indicated.

**Results:** Twelve patients with recurrent high-grade glioma were included: 10 glioblastomas, 1 anaplastic oligodendroglioma, and 1 anaplastic astrocytoma. All patients underwent  $^{89}\text{Zr}$ -fresolimumab PET 4 d after injection. In 4 patients, an additional PET scan was obtained on day 2 after injection. SUVmax on day 4 in tumor lesions was 4.6 (range 1.5-13.9) vs. a median SUVmean of 0.3 (range 0.2-0.5) in normal brain tissue. All patients showed clinical or radiologic progression after 1-3 infusions of fresolimumab. Median progression-free survival was 61 d (range 25-80), and median overall survival was 106 d (range 37-417).

**Conclusion:**  $^{89}\text{Zr}$ -fresolimumab penetrated recurrent high grade gliomas very well but did not result in clinical benefit.

## INTRODUCTION

High grade gliomas are rapidly progressive brain tumors that are divided into anaplastic gliomas and glioblastomas multiforme (GBM) on the basis of their histopathologic features. The 5-year survival rates for anaplastic oligodendroglioma, anaplastic astrocytoma and GBM are 49%, 25% and 5%, respectively.<sup>1</sup> In addition to surgery, the standard treatment of gliomas is currently based on tumor cell death induction by radiotherapy and chemotherapy. As a result of the modest treatment results, novel strategies for the treatment of malignant glioma are needed.

Transforming growth factor- $\beta$  (TGF- $\beta$ ) acts as a tumor promoter in advanced tumors, where it induces proliferation and metastasis and suppresses the immune response.<sup>2</sup> TGF- $\beta$  and its receptors are overexpressed in GBM, and TGF- $\beta$  signaling is involved in multiple steps of GBM development and invasion.<sup>3-5</sup> Plasma TGF- $\beta$  levels are elevated in GBM patients and decrease after surgical tumor resection.<sup>6</sup> In addition, progression-free survival (PFS) and overall survival are decreased in glioma patients with high levels of phosphorylated SMAD2 (p-SMAD2), the substrate of the TGF- $\beta$  receptor I, compared with glioma patients with low levels of p-SMAD2.<sup>7</sup> These features make TGF- $\beta$  a promising target molecule for therapeutic approaches in recurrent glioma; therefore, several TGF- $\beta$ -inhibitors are under investigation in this setting.<sup>8</sup>

Fresolimumab (GC1008) is a monoclonal antibody capable of neutralizing all mammalian isoforms of TGF- $\beta$  (*i.e.* 1, 2, and 3).<sup>9</sup> In a phase 1 study with fresolimumab in patients with melanoma and renal cell carcinoma, 6 patients achieved stable disease and one patient had a partial response.<sup>10</sup> In a phase 2 study in 13 mesothelioma patients stable disease was seen in 3 patients at 3 months.<sup>11</sup>

Current standard-of-care and experimental treatment results in patients with recurrent high-grade glioma are disappointing. It is often suggested that this is because of the impermeability of the blood–brain barrier, which may prevent drugs from reaching the tumor.<sup>12</sup> For therapeutic success in brain tumors, it is essential for a monoclonal antibody such as fresolimumab to reach the target site in the brain. In tumor xenograft models, tumor uptake could be visualized and quantified with <sup>89</sup>Zr-fresolimumab PET.<sup>13</sup> Therefore, the aim of this study was to visualize and quantify fresolimumab uptake in recurrent high-grade glioma using <sup>89</sup>Zr-fresolimumab PET. In addition, we evaluated the effect of treatment with fresolimumab in patients with recurrent high-grade glioma.

## MATERIAL AND METHODS

### Patients

Adult patients who had recurrent glioma with one or more contrast-enhancing lesions of at least 20 mm on MR imaging were eligible. The main additional inclusion criteria were a

World Health Organization performance score of 0-2; adequate bone marrow; coagulation; kidney and liver function; and negative tests for hepatitis B, C, and HIV. Previous surgery, radiotherapy, chemotherapy, or investigational agents should have been more than 4 weeks before inclusion (> 6 weeks for nitrosourea or monoclonal antibodies), and patients must have recovered from previous treatment. Main exclusion criteria were a history of ascites or pleural effusions, active hypercoagulability states or use of anticoagulants, hypercalcemia, pregnancy or nursing, diagnosis with other malignancies (unless curatively treated), organ transplants, immunosuppressive therapy, active infection, autoimmune disease, and other significant uncontrolled medical illnesses.

This study has been approved by the local medical ethical committee and registered in a clinical trial register (trial registration ID, NCT01472731). All patients gave written informed consent. A data safety monitoring board reviewed progress and safety during the study.

## Treatment

Patients were treated with a 5 mg/kg dose of fresolimumab (Genzyme; Sanofi-Aventis Oncology) intravenously every 3 weeks until the occurrence of radiologic or clinical progression or unacceptable toxicity. Fresolimumab was administered over 90 min for the first infusion, then over 60 min, and finally over 30 min if no infusion-related reactions occurred. Within 30 min before infusion, patients received acetaminophen (500 mg) and clemastine (2 mg) as premedication. All adverse events were recorded and graded according to the Common Terminology Criteria for Adverse Events, version 4. PFS and overall survival were calculated from date of informed consent to date of disease progression on MR imaging, clinical progression, or death.

## Imaging

Conjugation and radio labeling of fresolimumab were performed under good manufacturing conditions as previously described.<sup>13</sup> Before the start of treatment with fresolimumab, patients were injected with 37 MBq (5 mg) of <sup>89</sup>Zr-fresolimumab. The radioactive dose of 37 MBq and the protein dose of 5 mg result in a specific activity of 7.4 MBq/mg. Thereafter, patients were observed for 2 h for possible infusion-related reactions.

<sup>89</sup>Zr-fresolimumab PET scans were acquired on day 4 after injection. To assess the tumor accumulation of <sup>89</sup>Zr-fresolimumab over time, an additional scan was acquired on day 2 after injection in some patients. Normal organ distribution of <sup>89</sup>Zr-fresolimumab was assessed using whole-body PET scans. The images were acquired using 2 PET camera systems (ECAT HR1 [Siemens Medical Systems] and mCT Biograph [Siemens Medical Systems]). Acquisition time for the ECAT HR1 PET camera was 10 min per bed position on day 2 after injection (of which 20% is transmission time). On day 4 after injection, imaging time was prolonged to 12 min per

bed position to correct for decay time. For the mCT camera, imaging time was shorter (5 min per bed position). All scans were reviewed and analyzed by a nuclear medicine physician and an investigator. All attenuation-corrected PET images and MR imaging series (gadolinium-enhanced T1-weighted imaging, performed within 4 weeks before the start of the study) were retrospectively fused using a commercially available software program (esoft, 3D fusion; Siemens Medical Solutions) on a Siemens workstation (syngo MMWP; Siemens Medical Solutions) to identify tumor lesions. The 2 datasets were aligned on the basis of mutual information using the anatomic contours of the loaded datasets. Regions of interest were drawn around the tumor lesions on the PET scans. In normal organs, regions of interest were drawn in the same area of the organs for all patients. <sup>89</sup>Zr-fresolimumab uptake was quantified using AMIDE Medical Image Data Examiner software, version 0.9.2 (Stanford University), to calculate the standardized uptake value (SUV).<sup>14</sup> The SUVmax of the tumor lesions and the SUVmean of normal organs, including blood (measured in the sinus confluens and the iliac artery), were calculated. Follow-up brain MR imaging (1.5 T using T1-, T2-, and contrast-enhanced 3D T1-weighted gradient-echo sequences) was performed after every 3 treatment cycles (every 9 weeks) or as clinically indicated. MR imaging data for this study were assessed by a neuroradiologist using the criteria of Macdonald et al. for tumor response evaluation.<sup>15</sup>

### Plasma pharmacokinetics and biomarkers

Heparin plasma samples for <sup>89</sup>Zr-fresolimumab pharmacokinetics were collected from patients 1 h after injection and at the time of PET scanning. Plasma samples were counted in a gamma counter, and the tracer concentration in plasma was calculated using a calibration graph. Before the start of fresolimumab treatment, citrate plasma samples were collected. Blood samples were drawn without a tourniquet when possible, immediately placed on ice, and centrifuged at 2,500g for 30 min at 4°C with the brake turned off. Plasma samples were stored at -70°C. In these samples, total TGF-β1 was analyzed using a human TGF-β1 immunoassay (Quantikine; R&D Systems).

An analysis of p-SMAD2 as a readout of TGF-β signaling was performed in archival paraffin-embedded primary tumor tissue for all patients. Formalin-fixed, paraffin-embedded 3-mm tissue sections were mounted on microscope slides and dried overnight at 55°C. Tissue sections were dewaxed in xylene and rehydrated in a graded series of ethanol. Sections were subjected to microwave pretreatment with pH 6.0 citrate buffer for staining of p-SMAD2 (catalog no. 3101; Cell Signaling Technology, Inc.). Subsequently, sections were treated with 0.3% H<sub>2</sub>O<sub>2</sub> for 30 min, blocked for 1 h with 2% bovine serum albumin to reduce nonspecific antibody binding, and incubated with primary antibody. All antibody solutions were made in phosphate-buffered saline with 1% bovine serum albumin and 0.1% TritonX-100 (The Dow Chemical Co.). Incubation

at 4°C overnight was followed by incubation with goat anti-rabbit antibody conjugated to peroxidase (Dako) and subsequently with rabbit anti-goat antibody conjugated to peroxidase (Dako). Staining was visualized by 3,39-diaminobenzidine, and sections were counterstained with hematoxylin and mounted. As a negative control, primary antibody was omitted and incubations were performed as described previously.

### Statistical analysis

In the protocol, 2 stopping rules were defined. The study would be terminated after the inclusion of 6 patients if no <sup>89</sup>Zr-fresolimumab uptake was seen on the PET scan, and after the inclusion of 12 patients if treatment with fresolimumab showed no clinical benefit. If a clinical benefit was seen, a maximum of 20 patients could be included. Statistical analyses were performed using the Pearson correlation test and the Mann–Whitney U test using SPSS statistics 20 (IBM). Data are presented as median with range unless stated otherwise. Two-sided *P*-values of 0.05 or less were considered to indicate significance. Graphs were made using Prism, version 5.00 (GraphPad), for Windows (Microsoft).

## RESULTS

### Patients and treatment

Twelve patients with recurrent high-grade glioma (9 primary GBM, 1 secondary GBM [World Health Organization grade IV], 1 secondary anaplastic oligodendroglioma, and 1 secondary anaplastic astrocytoma [grade III]) were enrolled in this study (Table 1). Patients were previously treated with 2 (range 1-8) lines of treatment.

Two patients received 1 infusion of fresolimumab, 5 patients received 2 infusions, and 5 patients received 3 infusions. All patients showed clinical progressive disease during treatment or progressive disease on the first MR imaging scan obtained during treatment. PFS was 61 d (range 25-80), and overall survival was 106 d (range 37-417). In the absence of clinical benefit, the study was closed after the first 12 patients.

No adverse events were related to tracer injection. In 12 patients, 69 nonhematologic adverse events, mostly grade 1 or 2 and mostly related to progression of the disease, were observed during the study. Thirteen hematologic grade 1 adverse events were registered. The most common adverse events were neurologic deterioration, headache, skin disorders, nausea, and fatigue (Table 2). Adverse events that were considered as possibly related to fresolimumab were acneiform rash (grade 1, 1 patient), dry skin (grade 1, 1 patient), fatigue (grade 2, 2 patients), thrombocytopenia (grade 1, 1 patient), and epistaxis (grade 1, 1 patient). Four serious adverse events were recorded, of which 3 were neurologic worsening related to progressive disease and

**Table 1 Patient characteristics**

Characteristic	<i>n</i>
No. of patients	12
Age, (y)	
Median	51
Range	32-68
Sex	
Male	6
Female	6
Tumor type	
GBM	10
Anaplastic astrocytoma	1
Anaplastic oligodendroglioma	1
No. of previous treatments	
Median	2
Range	1-8
Previous treatment	
Surgery	11
Radiotherapy + temozolomide	9
Radiotherapy	2
Repeated resection	5
Reirradiation	4
Temozolomide	3
Lomustine	2
Bevacizumab	1

1 was pain related to an osteoporotic vertebra fracture, all of which were assessed as unrelated to fresolimumab.

In 4 patients, no MR imaging after treatment was performed because of clinical deterioration. In 2 patients, suspected dispersed hemorrhagic spots were seen in the tumor on MR imaging after treatment. A relationship with fresolimumab could not be excluded, although one of these patients also had a second course of radiotherapy before entrance into the study.

## Imaging

All 12 patients underwent at least a brain-only PET scan on day 4 after injection. Seven patients underwent a whole-body scan. Four patients underwent a whole-body scan on both day 2 and day 4 after injection. The mean interval between date of consent and injection of the PET tracer was 7 d (range 0-15).

**Table 2 Hematologic adverse events and most common non-hematologic adverse events**

Adverse event	No. of cases	Grade 1	Grade 2	Grade 3
Neurologic deterioration	16	3	8	5
Headache	12	7	3	2
Skin disorders	8	7	1	
Nausea	7	3	3	1
Fatigue	6	2	4	
Thrombocytopenia	6	6		
Anemia	5	5		
Leucopenia	2	2		

In all patients, uptake of  $^{89}\text{Zr}$ -fresolimumab was seen in tumor lesions (n 5 16). The mean SUVmax in tumor lesions on day 4 was 4.6 (range 1.5-13.9), which was higher than the SUVmean of normal brain tissue (0.3, range 0.2-0.5) ( $P < 0.01$ ). The SUVmean was 3.0 (range 2.0-6.2) in the blood of the sinus confluens. In patients who had a whole-body scan, the SUVmean of normal organs was the highest in the heart (8.3 [range 6.4-8.9]), followed by the liver (7.1, range 5.4-11.2) and the kidneys (5.5, range 3.4-6.6) (Fig. 1). In 8 patients, not all tumor lesions showed  $^{89}\text{Zr}$ -fresolimumab uptake. Most tumor lesions that did not show uptake were small ( $< 10$  mm on MR imaging). In 3 patients, no uptake was seen in larger gadolinium-enhanced lesions of

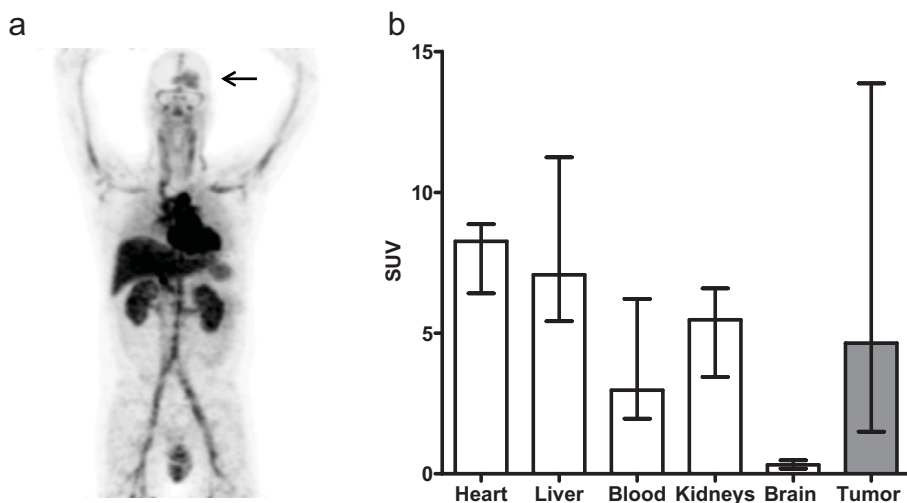


**Figure 1** (a) Representative example of  $^{89}\text{Zr}$ -fresolimumab PET on day 4 and uptake in brain tumor (arrow). (b) Uptake of  $^{89}\text{Zr}$ -fresolimumab in different organs (SUVmean) and tumor (SUVmax) on day 4 after tracer injection. Blood pool uptake was measured in the sinus confluens. Blood pool uptake was measured in sinus confluens. Blood, brain, and tumor values were measured in 12 patients, other organs in 7 patients.

13, 18, and 12 mm. The latter 2 lesions were found in previously irradiated areas, and one of these was not visible on the follow-up MR imaging (Fig. 2). In all 4 patients who underwent a PET scan on both day 2 and day 4 after injection, the tumor-to-blood ratio (measured in the sinus confluens) increased from day 2 to day 4 after injection (Fig. 2). There was no correlation between tumor uptake and PFS or overall survival.

### Plasma pharmacokinetics and biomarkers

The mean plasma concentrations of <sup>89</sup>Zr-fresolimumab at 1 h, 2 d, and 4 d after injection were 1.87 mg/mL (range 1.20-2.30), 1.31 mg/mL (range 0.96-1.76), and 1.06 mg/mL (range 0.72-1.38), respectively. When corrected for the injected dose, the extrapolated maximum concentration per dose was 0.37 mg/mL/mg (range 0.23-0.41) (*n* = 10). Pretreatment plasma TGF-β1 levels were 2,058 pg/mL (range 837-3,444) and correlated with mean SUVmax in the tumor lesions 4

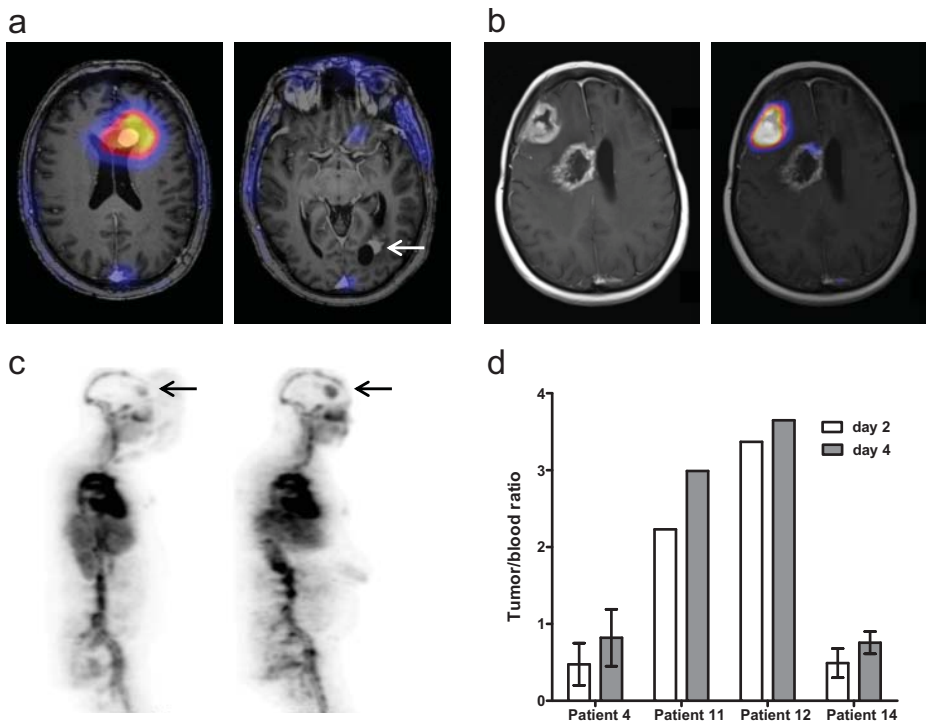


**Figure 2** (a) PET/MR images of a patient with 2 contrast-enhancing lesions. High uptake is visible in frontal lesion (left) but not in the previously irradiated occipital lesion (right). (b) PET/MR images of a patient with 2 contrast-enhancing lesions. SUVmax was 5.5 in progressive right frontal lesion and 2.1 in the previously irradiated right paraventricular lesion. (c) Whole-body PET scans on days 2 (left) and 4 (right) showing increase in SUVmax from 4.0 to 5.5 in frontal brain lesion (arrows). Tumor-to-blood ratio increased from 0.8 to 1.2. (d) Tumor-to-blood ratios on <sup>89</sup>Zr-fresolimumab PET in 4 patients on days 2 and 4.

d after injection ( $r = 0.61, P = 0.04$ ) (Fig. 3). Staining in primary tumor tissue with p-SMAD2 was positive for all tumors but also for normal brain tissue (Fig. 4).

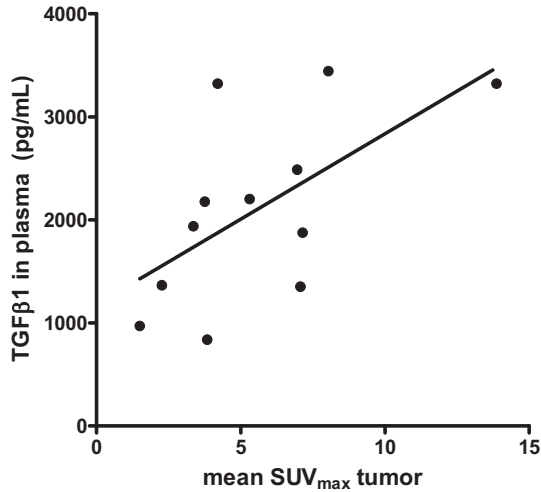


**Figure 3** Correlation between TGF- $\beta$ 1 in plasma and mean SUV<sub>max</sub> of  $^{89}\text{Zr}$ -fresolimumab in brain tumor lesions on day 4 after injection ( $r = 0.61, P = 0.04$ ).

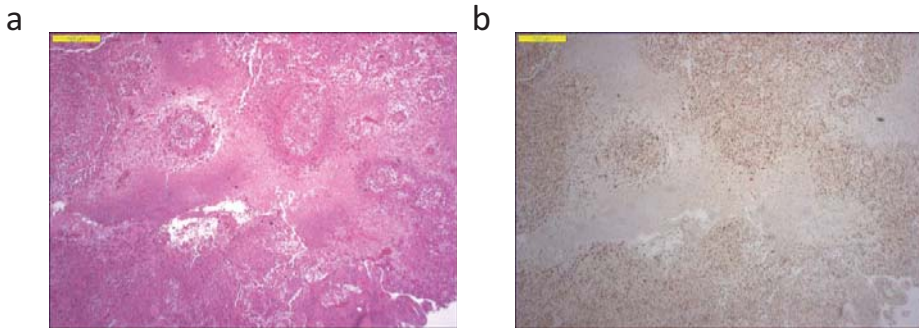


**Figure 4** (a) GBM with central necrosis on hematoxylin and eosin and (b) p-SMAD2 staining of the same area.

## DISCUSSION

To our knowledge, this was the first study to show tumor uptake of a radiolabeled antibody in patients with recurrent high-grade gliomas, indicating that fresolimumab does reach its target destination in the brain. Unfortunately, monotherapy with fresolimumab did not result in an antitumor effect.

The median SUV<sub>max</sub> of 4.6 found in the gliomas is comparable to the SUV<sub>max</sub> of 5.8 (range 1.7-15.1) found with  $^{89}\text{Zr}$ -bevacizumab PET in metastatic lesions in patients with neuroendocrine

tumors.<sup>16</sup> The maximum concentration per dose of <sup>89</sup>Zr-fresolimumab 1 h after injection of 0.37 mg/mL/mg is comparable to the pharmacokinetic results of an earlier study with fresolimumab.<sup>17</sup> This indicates that the radiolabeled antibody has a maximum concentration similar to that found for fresolimumab in other studies. Three contrast-enhancing lesions larger than 10 mm did not take up <sup>89</sup>Zr-fresolimumab. Two were found in previously irradiated areas, and one of these disappeared on follow-up MR imaging. These lesions are suspected to represent radionecrosis instead of viable tumor tissue, which might be the reason for the lack of TGF- $\beta$  and uptake of <sup>89</sup>Zr-fresolimumab. In all patients who underwent a whole-body PET scan on both day 2 and day 4 after injection, the tumor-to-blood ratio increased. This increase in ratio supports the notion of tumor-specific uptake. This pattern of tumor accumulation and increasing tumor-to-blood ratios over time was also seen in our preclinical study with <sup>89</sup>Zr-fresolimumab and in brain metastases in a clinical study with <sup>89</sup>Zr-trastuzumab in patients with metastatic breast cancer.<sup>13,18</sup> Taken together, these findings suggest that <sup>89</sup>Zr-fresolimumab uptake not only was a reflection of antibody leakage due to a damaged blood–brain barrier but was tumor-specific and TGF- $\beta$ -driven.

In earlier studies, the uptake of gemcitabine and GRN1005 in patients with recurrent glioma was shown by analyzing tumor tissue obtained during surgery.<sup>19,20</sup> However, performing tumor biopsies is often not feasible in this patient group, and tumor characteristics may change over time. PET scanning can be a noninvasive alternative for exploring potential targets that may be influenced by drugs and showing tumor penetration of drugs.

Treatment with fresolimumab was generally well tolerated, without infusion-related reactions. Most adverse events were grade 1 or grade 2 and related to progression of the disease. Unfortunately, no clinical benefit was observed in this small and often extensively pretreated patient group in which only one dose of fresolimumab was tested. Possible effects of this treatment in higher doses can therefore not be excluded. The median PFS was 61 d, which is comparable to the PFS of the physician-choice chemotherapy arm in recurrent GBM in a recently conducted randomized phase 3 trial.<sup>21</sup>

In all archival tumor samples, p-SMAD2 was positive, indicating that the TGF- $\beta$  pathway was active in the tumors. In gliomas, multiple signaling pathways are activated, and inhibition of just one pathway might be insufficient for a response.<sup>22</sup> Recently, other clinical studies using TGF- $\beta$  inhibition in glioma patients have been published. Trabectedin is an antisense oligodeoxynucleotide that inhibits TGF- $\beta$ 2. In a randomized grade 2B study, trabectedin was administered intratumorally by convection-enhanced delivery and compared with standard chemotherapy in patients with recurrent or refractory high-grade glioma. Six-month tumor control rates did not significantly differ among the entire study population (anaplastic astrocytoma and GBM). A prespecified anaplastic astrocytoma subgroup analysis showed a significant benefit regarding the 14-months tumor control rate for trabectedin vs.

chemotherapy.<sup>23</sup> A phase 1 study with LY2157299 (a TGF- $\beta$ 1 receptor kinase inhibitor) showed confirmed responses in treatment-refractory gliomas in 3 of 28 patients.<sup>24</sup> Therefore, TGF- $\beta$  remains a potential interesting target in glioma patients, and more combination studies are welcomed.

## **Conclusion**

This study proved that an antibody against TGF- $\beta$  reaches recurrent high-grade gliomas. Although no treatment benefit was seen, this finding could be exploited for further development of recurrent high-grade glioma treatment with antibodies or antibody–drug conjugates.

## **Disclosure**

The costs of publication of this article were defrayed in part by the payment of page charges. Therefore, and solely to indicate this fact, this article is hereby marked “advertisement” in accordance with 18 USC section 1734. This work was supported by Genzyme (Sanofi-Aventis Oncology), including a grant for PET scans that was made available to the UMCG. Joseph Pearlberg was employed by Sanofi Aventis Oncology, Cambridge, MA. He is currently working at Infinity Pharmaceuticals, Cambridge, MA. No other potential conflict of interest relevant to this article was reported.

## **Funding**

This work was supported by Genzyme (Sanofi-Aventis Oncology). Grant of Genzyme (Sanofi-Aventis Oncology) for PET scans to EGE de Vries was made available to the UMCG.

## REFERENCES

1. Dolecek, T. A., Propp, J. M., Stroup, N. E. & Kruchko, C. CBTRUS statistical report: primary brain and central nervous system tumors diagnosed in the United States in 2005-2009. *Neuro Oncol.* 14 Suppl 5, v1-49 (2012).
2. Massague, J. TGF-beta in Cancer. *Cell* 134, 215-230 (2008).
3. Eichhorn, P. J. *et al.* USP15 stabilizes TGF-beta receptor I and promotes oncogenesis through the activation of TGF-beta signaling in glioblastoma. *Nat. Med.* 18, 429-435 (2012).
4. Wesolowska, A. *et al.* Microglia-derived TGF-beta as an important regulator of glioblastoma invasion--an inhibition of TGF-beta-dependent effects by shRNA against human TGF-beta type II receptor. *Oncogene* 27, 918-930 (2008).
5. Kjellman, C. *et al.* Expression of TGF-beta isoforms, TGF-beta receptors, and SMAD molecules at different stages of human glioma. *Int. J. Cancer* 89, 251-258 (2000).
6. Schneider, T., Sailer, M., Ansorge, S., Firsching, R. & Reinhold, D. Increased concentrations of transforming growth factor beta1 and beta2 in the plasma of patients with glioblastoma. *J. Neurooncol.* 79, 61-65 (2006).
7. Bruna, A. *et al.* High TGF-beta-Smad activity confers poor prognosis in glioma patients and promotes cell proliferation depending on the methylation of the PDGF-B gene. *Cancer. Cell.* 11, 147-160 (2007).
8. Arjaans, M. *et al.* Transforming growth factor (TGF)-beta expression and activation mechanisms as potential targets for anti-tumor therapy and tumor imaging. *Pharmacol. Ther.* 135, 123-132 (2012).
9. Lonning, S., Mannick, J. & McPherson, J. M. Antibody targeting of TGF-beta in cancer patients. *Curr. Pharm. Biotechnol.* 12, 2176-2189 (2011).
10. Morris, J. C. *et al.* Phase I study of GC1008 (fresolimumab): a human anti-transforming growth factor-beta (TGF-beta) monoclonal antibody in patients with advanced malignant melanoma or renal cell carcinoma. *PLoS One* 9, e90353 (2014).
11. Stevenson, J. P. *et al.* Immunological effects of the TGF-beta-blocking antibody GC1008 in malignant pleural mesothelioma patients. *Oncoimmunology* 2, e26218 (2013).
12. Lampson, L. A. Monoclonal antibodies in neuro-oncology: Getting past the blood-brain barrier. *MAbs* 3, 153-160 (2011).
13. Oude Munnink, T. H. *et al.* PET with the <sup>89</sup>Zr-labeled transforming growth factor-beta antibody fresolimumab in tumor models. *J. Nucl. Med.* 52, 2001-2008 (2011).
14. Loening, A. M. & Gambhir, S. S. AMIDE: a free software tool for multimodality medical image analysis. *Mol. Imaging.* 2, 131-137 (2003).
15. Macdonald, D. R., Cascino, T. L., Schold, S. C., Jr & Cairncross, J. G. Response criteria for phase II studies of supratentorial malignant glioma. *J. Clin. Oncol.* 8, 1277-1280 (1990).
16. van Asselt, S. J. *et al.* Everolimus reduces <sup>89</sup>Zr-bevacizumab tumor uptake in patients with neuroendocrine tumors. *J. Nucl. Med.* 55, 1087-1092 (2014).
17. Trachtman, H. *et al.* A phase 1, single-dose study of fresolimumab, an anti-TGF-beta antibody, in treatment-resistant primary focal segmental glomerulosclerosis. *Kidney Int.* 79, 1236-1243 (2011).
18. Dijkers, E. C. *et al.* Biodistribution of <sup>89</sup>Zr-trastuzumab and PET imaging of HER2-positive lesions in patients with metastatic breast cancer. *Clin. Pharmacol. Ther.* 87, 586-592 (2010).
19. Drappatz, J. *et al.* Phase I study of GRN1005 in recurrent malignant glioma. *Clin. Cancer Res.* 19, 1567-1576 (2013).
20. Sigmond, J. *et al.* Gemcitabine uptake in glioblastoma multiforme: potential as a radiosensitizer. *Ann. Oncol.* 20, 182-187 (2009).
21. Stupp, R. *et al.* NovoTTF-100A versus physician's choice chemotherapy in recurrent glioblastoma: a randomised phase III trial of a novel treatment modality. *Eur. J. Cancer* 48, 2192-2202 (2012).
22. Stommel, J. M. *et al.* Coactivation of receptor tyrosine kinases affects the response of tumor cells to targeted therapies. *Science* 318, 287-290 (2007).
23. Bogdahn, U. *et al.* Targeted therapy for high-grade glioma with the TGF-beta2 inhibitor trabedersen: results of a randomized and controlled phase IIb study. *Neuro Oncol.* 13, 132-142 (2011).
24. Rodon, J. *et al.* First-in-human dose study of the novel transforming growth factor-beta receptor I kinase inhibitor LY2157299 monohydrate in patients with advanced cancer and glioma. *Clin. Cancer Res.* 21, 553-560 (2015).



# Chapter 5

## **Comparative biodistribution analysis across four different $^{89}\text{Zr}$ -monoclonal antibody tracers – The first step towards an imaging warehouse**

---

Frederike Bensch<sup>1</sup>, Michaël M. Smeenk<sup>1</sup>, Suzanne C. van Es<sup>1</sup>, Johan R. de Jong<sup>3</sup>, Carolina P. Schröder<sup>1</sup>, Sjoukje F. Oosting<sup>1</sup>, Marjolijn N. Lub-de Hooge<sup>2,3</sup>, C. Willemien Menke-van der Houven van Oordt<sup>4</sup>, Adrienne H. Brouwers<sup>3</sup>, Ronald Boellaard<sup>3</sup>, Elisabeth G.E. de Vries<sup>1</sup>

Departments of Medical Oncology<sup>1</sup>, Clinical Pharmacy and Pharmacology<sup>2</sup>, Nuclear Medicine and Molecular Imaging<sup>3</sup>, University of Groningen, University Medical Center Groningen, the Netherlands. Department of Medical Oncology<sup>4</sup>, Cancer Center Amsterdam, VU University Medical Center, Amsterdam, the Netherlands.

## ABSTRACT

**Rationale:** Knowledge on monoclonal antibody biodistribution in healthy tissues in humans can support clinical drug development. Molecular imaging with positron emission tomography can yield information in this setting. However, recent imaging studies have analyzed the behavior of single antibodies only, neglecting comparison across different antibodies.

**Methods:** We compared the distribution of four  $^{89}\text{Zr}$ -labeled antibodies in healthy tissue in a retrospective analysis based on the recently published harmonization protocol for  $^{89}\text{Zr}$ -tracers and our delineation protocol.

**Results:** The biodistribution patterns of  $^{89}\text{Zr}$ -lumretuzumab,  $^{89}\text{Zr}$ -MMOT0530A,  $^{89}\text{Zr}$ -bevacizumab and  $^{89}\text{Zr}$ -trastuzumab on day 4 after tracer injection were largely similar. The highest tracer concentration was seen in healthy liver, spleen, kidney and intestines. About one-third of the injected tracer dose was found in the circulation, up to 15% in the liver and only 4% in the spleen and kidney. Lower tracer concentration was seen in bone marrow, lung, compact bone, muscle, fat and the brain. Despite low tracer accumulation per gram of tissue, large-volume tissues, especially fat, can influence overall distribution: On average, 5-7% of the injected tracer dose accumulated in fat, with a peak of 19% in a patient with morbid obesity.

**Conclusion:** The similar biodistribution of the four antibodies is probably based on their similar molecular structure, binding characteristics and similar metabolic pathways. These data provide a basis for a prospectively growing, online accessible warehouse of molecular imaging data, which enables researchers to increase and exchange knowledge on whole body drug distribution and potentially supports drug development decisions.

## INTRODUCTION

In the last two decades, 28 monoclonal antibodies (mAb), an important class of targeted anti-cancer therapeutics, have been approved by the FDA and EMA for cancer therapy.<sup>1-4</sup> The majority of these drugs were engineered to bind to a specific target. In addition, two antibody drug conjugates—mAbs loaded with a cytotoxic agent to specifically bring its cargo to cancer cells—are currently approved for use in patients. During the next decade much cancer drug development is expected to focus on antibodies or constructs based on antibodies, like antibody-drug conjugates, antibody fragments and bispecific antibodies.<sup>5</sup> As a result, rational drug dosing choices for mAbs are a crucial focus of clinical research, especially because the maximum tolerated doses often cannot be established.

This research can be enhanced with molecular imaging, which enables whole body assessment of drug distribution in healthy and malignant tissue over time. Moreover, molecular imaging can potentially enhance understanding of drug pharmacokinetics and support dosing decisions in early clinical drug development.<sup>6</sup> At present, nearly 20 mAbs have been coupled to various radionuclides and evaluated in early clinical trials using positron emission tomography (PET).<sup>6</sup> Of the radionuclides currently available, zirconium-89 (<sup>89</sup>Zr) is increasingly being used to label mAbs. <sup>89</sup>Zr is advantageous because it remains in cells after internalization of the mAb-receptor complex, which leads to improved tumor image contrast via accumulation, and its half-life of about 78 hours allows target binding over a longer period of time, which better matches the long half-lives of mAbs.<sup>7</sup> A head-to-head comparison of Indium-111-trastuzumab and <sup>89</sup>Zr-trastuzumab in mice showed the favorable image quality of the <sup>89</sup>Zr-labeled tracer and a comparable normal organ distribution, with as the only difference a higher normal bone tracer uptake at the latest scan moment for <sup>89</sup>Zr-trastuzumab.<sup>8</sup>

Until now, imaging trials only focused on biodistribution analysis of single agents, neglecting comparison across different antibodies. The latter, however, might be of great value during drug development, especially in the era of immune checkpoint inhibitors, as those target lymphoid (effector) tissue exclusively or in combination with tumor tissue potentially resulting in a different distribution pattern. Drug dose decisions might be optimized based on deeper knowledge of distribution, the influence of the size and/or structure of the molecule itself or the target. To discern specifics in the biodistribution of single mAbs, general knowledge about mAb distribution is required. Thereby, the administered protein dose is of special interest, as monoclonal antibodies can show different pharmacokinetic and potentially target saturation might occur after administration of therapeutic doses. Furthermore, as also engineered antibodies and other constructs like bispecific antibodies or antibody fragments with potentially different kinetics and dynamics are introduced in the clinics, more detailed information on distribution in combination with long term experience in dosing, side effects and efficacy of

the currently used mAb might speed up gain of knowledge.<sup>9</sup> Finally, molecular PET imaging with <sup>89</sup>Zr-mAb tracers seems to have the potential to predict response to mAb drug treatment.<sup>10</sup>

Previous multicenter trials with fluorine-18 have shown the necessity of harmonization to reduce data variability and enable comparison of data between trials and sites, which led to development of the European Association of Nuclear medicine (EANM) guidelines and establishment of the EANM Research Ltd (EARL) accreditation.<sup>11, 12</sup> For <sup>89</sup>Zr, a comparable harmonization protocol has been developed only recently.<sup>13</sup> Before this harmonization protocol became available, it was not possible to compare the biodistribution of <sup>89</sup>Zr-labeled mAbs assessed by PET. Comparison between the biodistribution of antibodies was also hampered by the lack of a standard delineation protocol when performing the semi-quantitative analyses. Moreover, biodistribution of some mAbs assessed in clinical imaging studies was described as part of a detailed dosimetric analysis (*e.g.*,<sup>14</sup>), whereas other imaging trials used a standardized uptake value (SUV) based description of the biodistribution (*e.g.*,<sup>15-18</sup>). If we could make standardized comparisons, this would be an important step towards using molecular imaging data for optimizing rational drug development.

To support such inter-study comparisons, we decided to generate the basis of a prospectively growing mAb imaging data warehouse. To do so, we performed a comparative biodistribution analysis of four <sup>89</sup>Zr-labeled mAbs that we previously explored in clinical studies: the anti-human epidermal growth factor receptor (HER) 2 antibody trastuzumab, the anti-HER3 antibody lumretuzumab, the anti-vascular endothelial growth factor A (VEGF-A) antibody bevacizumab and the anti-mesothelin antibody MMOT0530A.<sup>15-18</sup> This analysis was based on the <sup>89</sup>Zr-harmonization protocol and was conducted according to the delineation protocol for <sup>89</sup>Zr-tracers, which we recently established. We then deposited this data in an online warehouse.

## METHODS

### PET scan selection

For this analysis, we selected PET scans of patients following injection of the mAb tracers <sup>89</sup>Zr-lumretuzumab, <sup>89</sup>Zr-MMOT0530A, <sup>89</sup>Zr-bevacizumab or <sup>89</sup>Zr-trastuzumab. These scans were obtained from clinical imaging trials (specified below) or from extended clinical work-ups and had been performed before start of treatment on patients with locally advanced or metastatic solid cancer. The inclusion criteria for the scans were as follows: administered tracer activity of 37 MBq ( $\pm$  10%), the PET scan had to be performed 4 days after tracer injection together with a low-dose computed tomography (LD CT) and the tracer had to be complemented with the previously determined optimal unlabeled imaging protein dose (100 mg lumretuzumab, 50 mg trastuzumab, 10 mg MMOT0530A or no unlabeled mAb in case of bevacizumab imaging).<sup>17-19</sup> The

optimal unlabeled imaging protein dose was defined as the dose required to ensure sufficient tracer in the circulation 4 days after tracer injection for adequate tumor visualization. Patients and their corresponding PET scans were excluded from the biodistribution analysis if patient-related and/or disease-related factors were identified that might have influenced the biodistribution, like recurrent pleural effusion needing continuous drainage or a history of hemihepatectomy. Patients' history, age, sex, weight and height were collected from their dossiers.

PET scans were performed in clinical imaging trials executed in the Department of Medical Oncology of the University Medical Center Groningen (UMCG, Groningen, the Netherlands) and of the VU University Medical Center (VUMC, Amsterdam, the Netherlands),<sup>17, 18</sup> or as part of an extended clinical work-up. All clinical trials were approved by the responsible Medical Ethics Committee, as well as the Central Committee on Research Involving Human Subjects, and registered individually or as part of the corresponding phase I trial (ClinicalTrials.gov identifiers NCT01482377, NCT01832116 and NCT01028638).

## PET imaging

PET acquisition at 4 days postinjection was carried out from head to upper thigh, in bed positions of 5 minutes per bed position with a PET/CT camera (Biograph mCT, Siemens [UMCG], and Gemini TF or Ingenuity TF, Philips [VUMC]). PET scans were accompanied by a LD CT scan for attenuation correction. All PET images were reconstructed using the harmonized reconstruction algorithm recommended for multicenter <sup>89</sup>Zr-mAb PET scan trials.<sup>13</sup>

## <sup>89</sup>Zr-mAb PET scan analysis

PET scans of all four tracers were analyzed using the software A Medical Imaging Data Examiner (AMIDE version 0.9.1; Stanford University,<sup>20</sup>), in a standardized manner according to our delineation protocol (Supplementary Table 1). Spherical volumes of interest (VOI) with predefined sizes were drawn in healthy tissue in the brain, lung, liver, muscle, spleen, kidney, bone marrow, compact bone, fat and the intestine. A VOI in the aorta was used as readout for blood pool activity. Furthermore, all tumor lesions visible on PET and/or diagnostic CT scan were delineated per patient to estimate total tumor volume. In patients without liver metastases, the whole liver was manually delineated using the LD CT for anatomic reference to assess whole organ tracer uptake. A whole body VOI was drawn from head to the tuber ischiadicum to estimate the total amount of tracer left in the patient (excluding the legs).

For all VOIs, the percentage injected dose per kilogram (%ID/kg), normalized to calibrated dose of the <sup>89</sup>Zr-tracer, corrected for decay at the time of scanning, was calculated (Supplementary Table 1). The total tumor volume was estimated by the sum of single tumor volumes calculated based on the SUV<sub>mean40</sub>.<sup>21</sup> The percentage body fat<sup>22</sup> multiplied by patient's weight, and the

results of the delineation of the whole liver were used to calculate the activity as percentage of the injected dose (%ID) in total fat and liver, respectively (Supplementary Table 1). To assess the activity (%ID) in the spleen, kidneys and total blood volume, the volumes of the spleen and the kidneys were estimated based on linear CT measurements,<sup>23,24</sup> and the total blood volume was calculated using Nadler's formula.<sup>25</sup>

## Statistics

Statistical analyses were performed using IBM SPSS Version 22. In case of normally distributed data, groups were compared using a one-way ANOVA with either post hoc Gabriel or Games-Howell test depending on homogeneity of variances as assessed by Levene's test. If results were not normally distributed, comparison was performed using a Kruskal-Wallis followed by a Mann-Whitney U test.  $P \leq 0.05$  was considered to be a significant difference. All analyses were 2-sided. Bivariate correlations were performed using Pearson correlation coefficients. Data are presented as mean  $\pm$  standard deviation (SD), unless otherwise stated.

## RESULTS

### Patient characteristics

For <sup>89</sup>Zr-lumretuzumab, <sup>89</sup>Zr-MMOT0530A, <sup>89</sup>Zr-bevacizumab and <sup>89</sup>Zr-trastuzumab, scans of eleven, nine, ten and nine patients, respectively, were eligible for comparative <sup>89</sup>Zr-tracer biodistribution analysis (Fig. 1). Per tracer, we analyzed the same number of scans ( $n = 9$ ). If

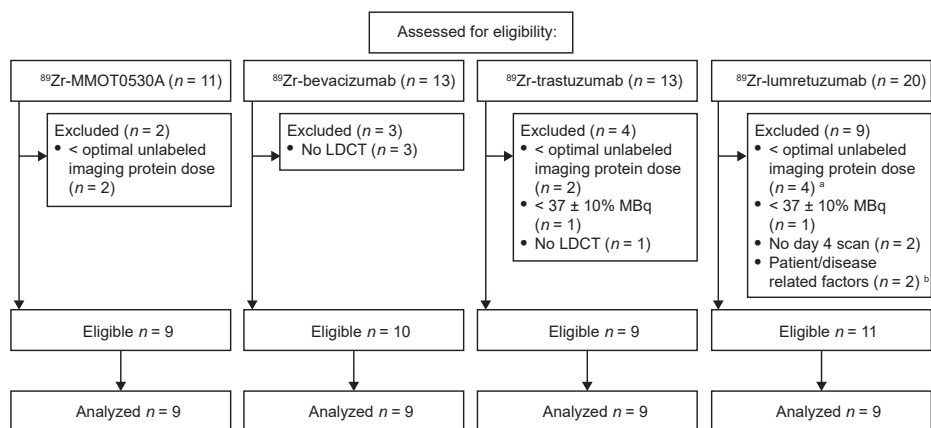


**Figure 1** Scan selection per tracer according to predefined eligibility criteria. <sup>a</sup> Optimal imaging dose of unlabeled lumretuzumab was considered 100 mg, scans with 10 and 50 mg were excluded. <sup>b</sup> The scans of patients with a history of a hemihepatectomy ( $n = 1$ ) and recurrent pleural effusion needing continuous drainage ( $n = 1$ ) were excluded.

more than 9 scans were available, the first 9 of all eligible PET scans were selected. Additional information on the mAbs and the respective <sup>89</sup>Zr-tracers are summarized in Supplementary Table 2. The analyzed PET scans were performed between November 2009 and August 2014. Included patients had locally advanced or metastatic cancer, the majority of the patients had multiple metastatic sites. Patient characteristics are summarized in Table 1.

**Table 1 Patient characteristics**

Characteristics	<sup>89</sup> Zr-lumretuzumab <sup>a</sup>	<sup>89</sup> Zr-MMOT0530A	<sup>89</sup> Zr-bevacizumab	<sup>89</sup> Zr-trastuzumab <sup>b</sup>
Age, median years (range)	59 (48-72)	62 (44-70)	64 (51-68)	47 (22-73)
Number of patients	9	9	9	9
Male	5 (56)	2 (22)	5 (56)	2 (22)
Female	4 (44)	7 (78)	4 (44)	7 (78)
Tumor type, <i>n</i> (%)				
Colorectal	5 (56)	-	-	1 (11)
Breast	1 (11)	-	-	8 (89)
Oropharyngeal	1 (11)	-	-	-
CUP	1 (11)	-	-	-
Vulvar	1 (11)	-	-	-
Ovarian	-	2 (22)	-	-
Pancreatic	-	7 (78)	-	-
Renal cell	-	-	9 (100)	-
Sites of tumor lesions, <i>n</i> <sup>c</sup>				
Adrenal gland	3	3	3	-
Bone	1	-	40	121
Brain	-	-	2	9
Breast	-	-	-	2
Intestine	2	-	2	1
Kidney	-	-	16	-
Lung	34	3	6	2
Liver	-	7	7	48
Lymph nodes	10	6	9	27
Pancreas	-	4	4	-
Pleura	2	-	3	-
Soft tissue <sup>d</sup>	10	6	29	6
Spleen	-	-	1	1
Thyroid gland	-	-	2	-
Uterus	-	2	-	-
Tumor load, mL (± SD)	41 (± 25)	42 (± 22)	116 (± 67)	99 (± 133)

<sup>a</sup> <sup>89</sup>Zr-lumretuzumab PET was performed in patients with HER3-positive disease according to study protocol (Meulendijks et al., CCR 2017). <sup>b</sup> <sup>89</sup>Zr-trastuzumab PET was performed in patients with HER2-positive disease as part of an extended clinical work-up. <sup>c</sup> Sites of tumor lesions comprise sites of primary tumors and sites of metastases at the time of PET imaging. <sup>d</sup> Soft tissue lesions include subcutaneous lesions not further specified, intramuscular lesions and abdominal soft tissue lesions. CUP, cancer of unknown primary.

### $^{89}\text{Zr}$ -mAb tracer distribution in healthy tissue

All tracers showed a comparable distribution pattern throughout the whole body with the highest tracer uptake (calculated as %ID/kg) in healthy liver tissue, as well as in the spleen, kidneys and intestines (Fig. 2). Generally, lower tracer concentration was observed in the bone marrow, lung, compact bone, muscle, fat tissue and the brain (Table 2).

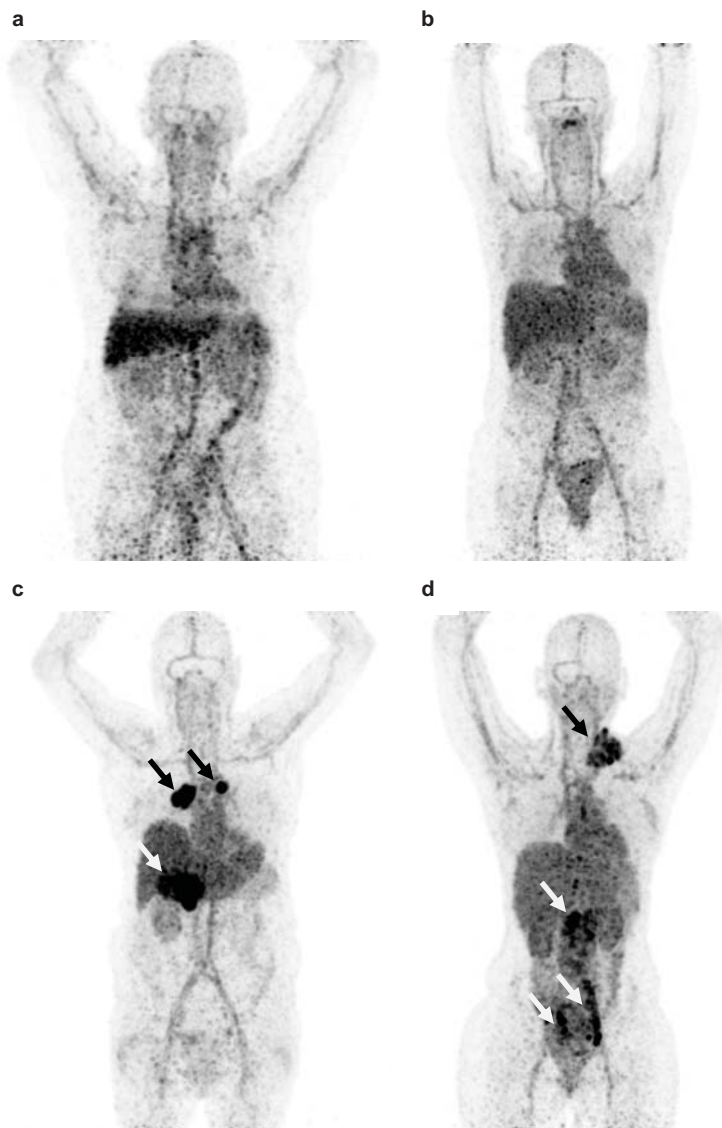


**Figure 2** Representative maximum intensity projection of a PET scan 4 days after injection with  $^{89}\text{Zr}$ -lumretuzumab (a),  $^{89}\text{Zr}$ -MMOT0530A (b),  $^{89}\text{Zr}$ -bevacizumab (c) and  $^{89}\text{Zr}$ -trastuzumab (d). The patients injected with  $^{89}\text{Zr}$ -bevacizumab (c) and  $^{89}\text{Zr}$ -trastuzumab (d) show clear tumor tracer uptake (black and white arrows), whereas tumor lesions on the  $^{89}\text{Zr}$ -lumretuzumab PET and  $^{89}\text{Zr}$ -MMOT0530A were visually negative.

**Table 2 Normal tissue tracer uptake as percent of injected dose per kilogram bodyweight per <sup>89</sup>Zr-monoconal antibody tracer 4 days post tracer injection**

Tissue	VOI (%ID/kg, ± SD)				ANOVA/ Kruskal-Wallis <i>P</i>
	<sup>89</sup> Zr- lumretuzumab	<sup>89</sup> Zr- MMOT0530A	<sup>89</sup> Zr- bevacizumab	<sup>89</sup> Zr- trastuzumab	
Aorta	6.2 (± 1.6)	7.5 (± 1.3)	7.1 (± 1.6)	7.7 (± 2.8)	0.35
Bone marrow	1.9 (± 0.6)	2.9 (± 0.5)	2.1 (± 0.7)	2.8 (± 1.0)	<b>0.02</b> <sup>a</sup>
Brain	0.1 (± 0.1)	0.3 (± 0.2)	0.2 (± 0.1)	0.3 (± 0.1)	0.09
Compact bone	0.9 (± 0.6)	1.2 (± 0.3)	0.6 (± 0.2)	0.8 (± 0.4)	<b>0.01</b> <sup>b</sup>
Fat tissue	0.2 (± 0.1)	0.2 (± 0.1)	0.2 (± 0.2)	0.3 (± 0.1)	0.26
Intestine	3.4 (± 1.5)	3.9 (± 1.5)	2.7 (± 1.5)	5.4 (± 2.4)	<b>0.02</b> <sup>c</sup>
Kidney	5.4 (± 0.6)	7.6 (± 1.6)	6.1 (± 1.1)	8.7 (± 1.5)	<b>&lt; 0.01</b> <sup>d</sup>
Liver	7.3 (± 1.3)	10.8 (± 3.6)	9.9 (± 1.4)	6.8 (± 1.6)	<b>&lt; 0.01</b> <sup>e</sup>
Lung	1.1 (± 0.1)	1.7 (± 0.7)	1.1 (± 0.2)	1.4 (± 0.4)	<b>0.02</b> <sup>a</sup>
Muscle	0.7 (± 0.2)	0.8 (± 0.2)	0.7 (± 0.2)	0.8 (± 0.3)	0.36
Spleen	5.0 (± 1.2)	5.8 (± 1.8)	4.6 (± 0.8)	5.1 (± 1.6)	0.32

<sup>a</sup> Post hoc analysis showed no significant difference between the four groups. <sup>b</sup> Significant difference between <sup>89</sup>Zr-MMOT0530A and <sup>89</sup>Zr-bevacizumab. <sup>c</sup> Significant difference between <sup>89</sup>Zr-bevacizumab and <sup>89</sup>Zr-trastuzumab. <sup>d</sup> Significant difference between <sup>89</sup>Zr-lumretuzumab and <sup>89</sup>Zr-MMOT0530A, <sup>89</sup>Zr-lumretuzumab and <sup>89</sup>Zr-trastuzumab, <sup>89</sup>Zr-bevacizumab and <sup>89</sup>Zr-trastuzumab, and <sup>89</sup>Zr-MMOT0530A. <sup>e</sup> Significant difference between <sup>89</sup>Zr-lumretuzumab and <sup>89</sup>Zr-bevacizumab, <sup>89</sup>Zr-bevacizumab and <sup>89</sup>Zr-trastuzumab, and <sup>89</sup>Zr-trastuzumab and <sup>89</sup>Zr-MMOT0530A. VOI, volume of interest.

Healthy lung tracer uptake was the highest for <sup>89</sup>Zr-MMOT0530A compared to the other tracers with a mean of 1.7 (± 0.7) %ID/kg (Fig. 3 and Table 2). Furthermore, lung uptake varied most between patients injected with <sup>89</sup>Zr-MMOT0530A (range 0.8-3.1 vs. 0.9-1.3, 0.7-1.4 and 0.5-2.0 for patients injected with <sup>89</sup>Zr-lumretuzumab, <sup>89</sup>Zr-bevacizumab and <sup>89</sup>Zr-trastuzumab, respectively). Also uptake in healthy liver tissue, compact bone and bone marrow was the highest for <sup>89</sup>Zr-MMOT0530A (10.8 ± 3.6, 1.2 ± 0.3 and 2.9 ± 0.5 %ID/kg). In the intestine, likely influenced by fecal content, as well as in healthy renal tissue, the highest activity, representing at least partially excretion, was observed for <sup>89</sup>Zr-trastuzumab (5.4 ± 2.4 and 8.7 ± 1.5 %ID/kg). For brain, spleen, muscle and fat tissue comparable uptake was observed between the four analyzed <sup>89</sup>Zr-mAb tracers. The remaining radioactivity present in the aorta (= readout for blood pool) was similar between all <sup>89</sup>Zr-mAb tracers as a result of the added unlabeled antibody imaging dose selected in earlier trials. Blood pool activity did not correlate with the tumor load for <sup>89</sup>Zr-lumretuzumab, <sup>89</sup>Zr-bevacizumab and <sup>89</sup>Zr-MMOT0530A, and only poorly for <sup>89</sup>Zr-trastuzumab ( $r^2 = 0.46$ , Supplementary Fig. 1).

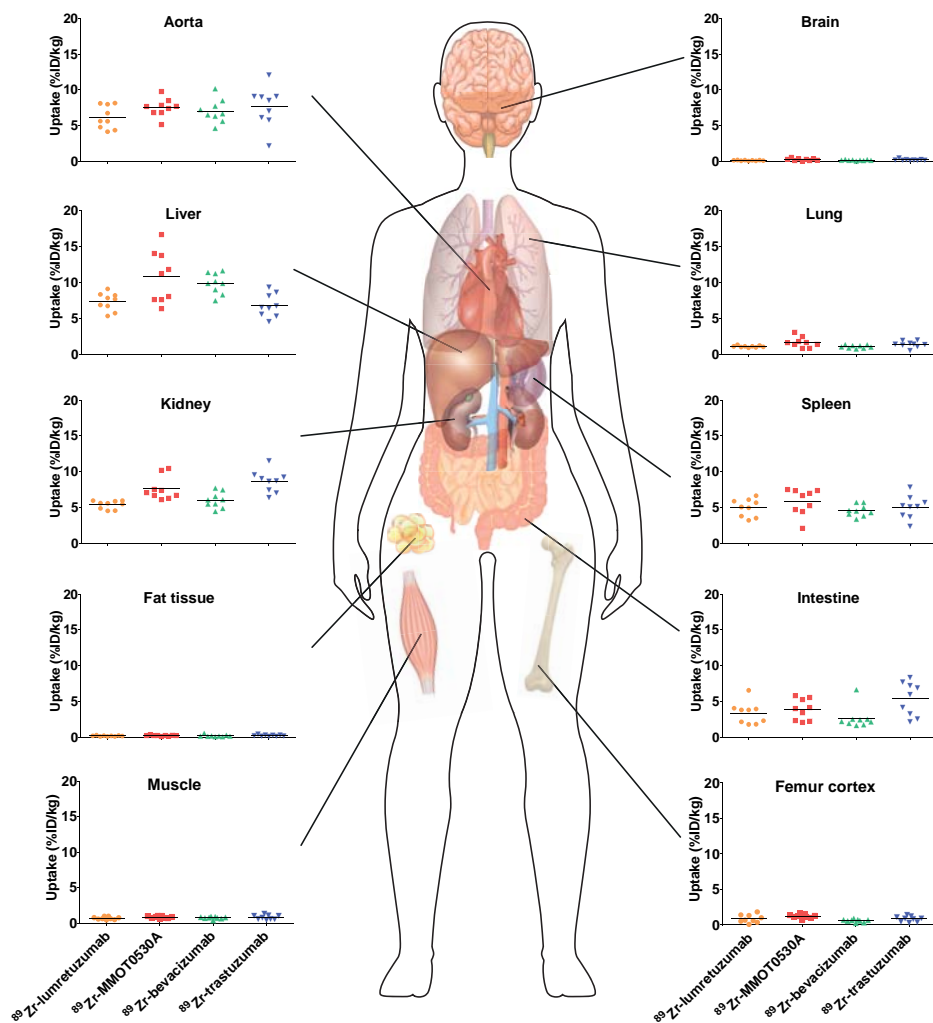


**Figure 3** Tracer uptake (%ID/kg) per healthy tissue and in blood for  $^{89}\text{Zr}$ -lumretuzumab,  $^{89}\text{Zr}$ -MMOT0530A,  $^{89}\text{Zr}$ -bevacizumab and  $^{89}\text{Zr}$ -trastuzumab (left to right) 4 days post tracer injection. Each dot represents an individual patient; mean is plotted per tracer.

### Amount of tracer in healthy tissue, as percentage of injected dose

There was no difference between the total amount of  $^{89}\text{Zr}$ -lumretuzumab,  $^{89}\text{Zr}$ -bevacizumab and  $^{89}\text{Zr}$ -trastuzumab remaining in the body on day 4 after tracer injection ( $69.5 \pm 7.1$ ,  $69.9 \pm 6.3$  and  $67.9 \pm 6.1$  %ID, respectively). The remaining activity in patients injected with  $^{89}\text{Zr}$ -MMOT0530A was higher compared to the other three tracers ( $85.8 \pm 8.5$  %ID) (Fig. 4).

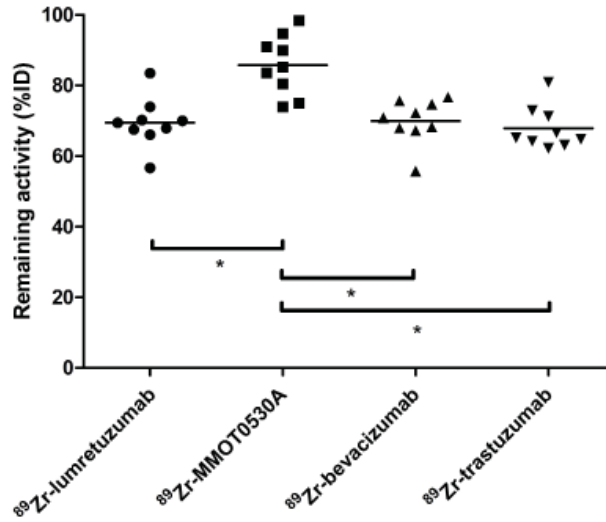


**Figure 4** Radioactivity as %ID left in the body (head to tuber ischiadicum) 4 days postinjection per tracer. Each dot represents individual patients and asterisk indicates differences between groups with  $P < 0.05$ .

A mean of  $34.5 (\pm 8.4)$ ,  $33.5 (\pm 3.7)$ ,  $34.0 (\pm 5.7)$  and  $30.9 (\pm 12.5)$  %ID was still circulating in the blood 4 days after administration of <sup>89</sup>Zr-lumretuzumab, <sup>89</sup>Zr-MMOT0530A, <sup>89</sup>Zr-bevacizumab and <sup>89</sup>Zr-trastuzumab, respectively (Table 3 and Fig. 5). In patients without liver metastases on average  $10.3 (\pm 1.2)$ , <sup>89</sup>Zr-trastuzumab %ID up to  $14.0 (\pm 0.7)$ , <sup>89</sup>Zr-MMOT0530A %ID accumulated in the liver 4 days post injection ( $n = 5, 3, 4$  and  $3$  patients who received, respectively, <sup>89</sup>Zr-lumretuzumab, <sup>89</sup>Zr-MMOT0530A, <sup>89</sup>Zr-bevacizumab and <sup>89</sup>Zr-trastuzumab). The total liver uptake ranged from  $8.5$  %ID to  $16.0$  %ID (Fig. 6). Despite the relatively high tracer concentration in the

**Table 3** Activity as part of the injected dose per <sup>89</sup>Zr-monoclonal antibody tracer 4 days post tracer injection

Tissue	VOI (%ID, $\pm$ SD)			
	<sup>89</sup> Zr-lumretuzumab	<sup>89</sup> Zr-MMOT0530A	<sup>89</sup> Zr-bevacizumab	<sup>89</sup> Zr-trastuzumab
Total blood pool	$34.5 (\pm 8.4)$	$33.5 (\pm 3.7)$	$34.0 (\pm 5.7)$	$30.9 (\pm 12.5)$
Liver	$11.7 (\pm 2.3)$	$14.2 (\pm 0.7)$	$13.5 (\pm 2.4)$	$10.3 (\pm 1.2)$
Spleen	$1.8 (\pm 1.0)$	$1.4 (\pm 0.5)$	$0.9 (\pm 0.2)$	$1.0 (\pm 0.1)$
Kidney	$1.0 (\pm 0.4)$	$1.1 (\pm 0.3)$	$1.6 (\pm 0.9)$	$1.1 (\pm 0.1)$
Fat tissue	$7.4 (\pm 5.1)$	$7.0 (\pm 2.2)$	$5.4 (\pm 2.4)$	$4.9 (\pm 2.7)$
Tumor	$0.1 (\pm 0.1)$	$0.4 (\pm 0.3)$	$0.3 (\pm 0.2)$	$0.9 (\pm 1.8)$

VOI, volume of interest.

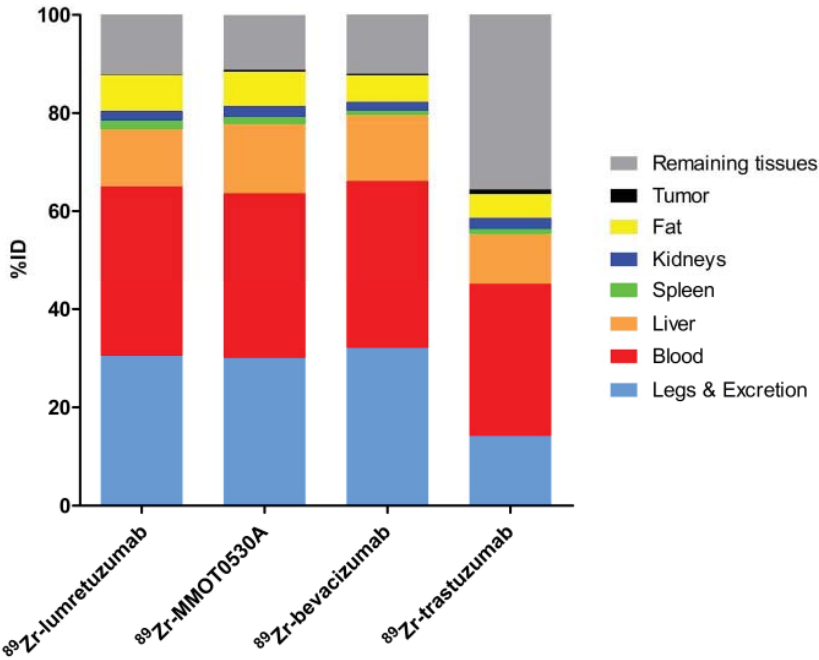


**Figure 5** Mean uptake as %ID per <sup>89</sup>Zr-monoclonal antibody tracer in blood, liver, spleen, kidney, fat, tumor, remaining tissues (including intestines), as well as excreted part and the legs.

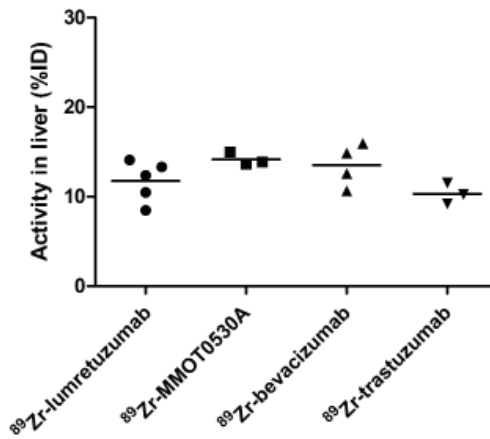


**Figure 6** Radioactivity as %ID in the liver without metastatic disease could be assessed in 5, 3, 4 and 3 patients injected with <sup>89</sup>Zr-lumretuzumab, <sup>89</sup>Zr-MMOT0530A, <sup>89</sup>Zr-bevacizumab and <sup>89</sup>Zr-trastuzumab, respectively.

spleen (up to  $5.8 \pm 1.8$  %ID/kg) and kidney (up to  $8.7 \pm 1.5$  %ID/kg), the absolute proportion of tracer accumulating in these organs was only 0.6 to 3.3 %ID for the spleen and 0.4 to 3.9 %ID for one kidney (Fig. 7). Tracer concentration in fat tissue, in contrast, was low compared to other healthy tissues:  $0.2 (\pm 0.1)$ ,  $0.2 (\pm 0.1)$ ,  $0.2 (\pm 0.2)$  and  $0.3 (\pm 0.1)$  %ID/kg for <sup>89</sup>Zr-lumretuzumab,

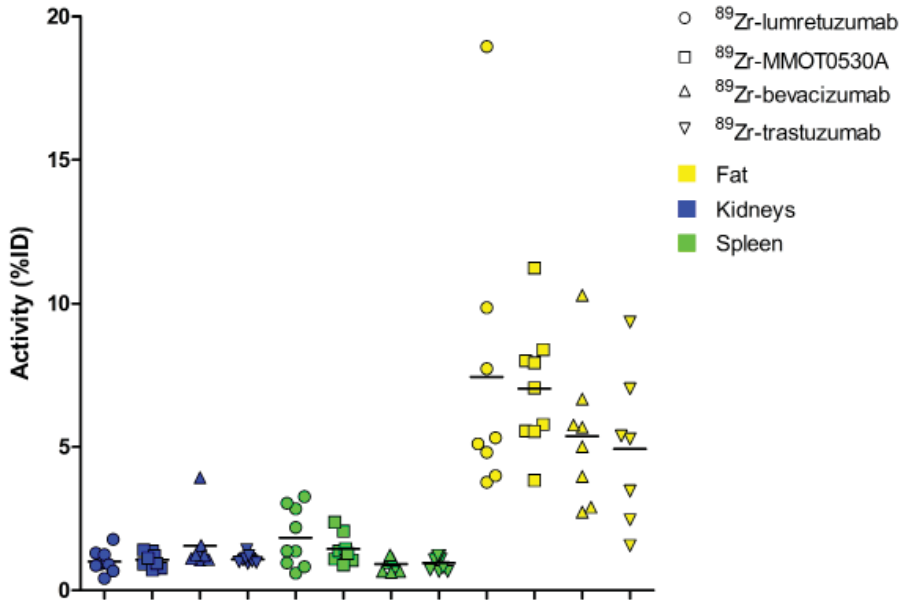


**Figure 7** Radioactivity as %ID per  $^{89}\text{Zr}$ -mono antibody tracer in kidney, spleen and fat per patient per tracer (mean).

$^{89}\text{Zr}$ -MMOT0530A,  $^{89}\text{Zr}$ -bevacizumab and  $^{89}\text{Zr}$ -trastuzumab, respectively. Despite this generally low tracer concentration in fat, when the total amount of fat tissue in the patient was considered, a substantial proportion of the injected tracer dose accumulated in fat tissue:  $7.4 (\pm 5.4)$ ,  $7.0 (\pm 2.2)$ ,  $5.4 (\pm 2.6)$  and  $4.9 (\pm 2.8)$  %ID of  $^{89}\text{Zr}$ -lumretuzumab,  $^{89}\text{Zr}$ -MMOT0530A,  $^{89}\text{Zr}$ -bevacizumab and  $^{89}\text{Zr}$ -trastuzumab, respectively; Fig. 5. The estimated total amount of tracer accumulated in fat tissue ranged between 1.56 %ID and 18.95 %ID depending on the physique of the patient (Fig. 7).

The median measurable tumor load was  $41 (\pm 25)$  mL,  $42 (\pm 22)$  mL,  $116 (\pm 67)$  mL and  $99 (\pm 133)$  mL for  $^{89}\text{Zr}$ -lumretuzumab,  $^{89}\text{Zr}$ -MMOT0530A,  $^{89}\text{Zr}$ -bevacizumab and  $^{89}\text{Zr}$ -trastuzumab, respectively (Table 1). In this dataset, on average per tracer less than 1 %ID accumulated in tumor lesions per patient (Table 3).

## DISCUSSION

We conducted the first comparative analysis of the healthy tissue distribution of four  $^{89}\text{Zr}$ -mAb tracers, based on the recently published harmonization protocol for  $^{89}\text{Zr}$  <sup>13</sup> and analyzed according to our delineation protocol for  $^{89}\text{Zr}$ -mAb tracers.

$^{89}\text{Zr}$ -lumretuzumab,  $^{89}\text{Zr}$ -MMOT0530A,  $^{89}\text{Zr}$ -bevacizumab and  $^{89}\text{Zr}$ -trastuzumab showed a similar healthy tissue distribution pattern, with highest uptake in the liver, spleen and kidneys

and lower uptake in the bone marrow, lung, compact bone, muscle, fat tissue and the brain. Tissues with generally low uptake can also be of interest with regards to distribution if the respective tissue comprises a larger volume, potentially influencing (optimal) tumor targeting. Fat tissue, for example, had one of the lowest uptake values in our dataset. However, depending on the physique of the patient, up to 19 %ID accumulated in fat. In comparison, the liver, which often is considered as sink organ by visual analysis due to its high tracer uptake per kg tissue, contained about 10-15 %ID and the spleen and one kidney account for a maximum of 4 %ID each, whereas less than 1 %ID accumulated in tumor lesions. The observed slight differences in healthy tissue distribution between the four analyzed  $^{89}\text{Zr}$ -mAb tracers might be the consequence of target specific uptake, non-specific tracer accumulation and/or clearance mechanisms specific for the certain mAb.

$^{89}\text{Zr}$ -MMT0530A uptake, compared to the other three tracers, was higher in the lung, which might partly be explained by the expression of mesothelin in mesothelial cells *e.g.* in the lining of the pleura,<sup>26,27</sup> whereas higher uptake in the liver, compact bone and bone marrow cannot be explained by the known protein expression profile. HER2 expression in and tracer excretion via the intestinal and urinary tract, in contrast, might have influenced  $^{89}\text{Zr}$ -trastuzumab uptake in the respective healthy tissues.<sup>28</sup> Different from studies on  $^{111}\text{In}$ -trastuzumab performed shortly after cardiotoxic anthracycline treatment, in the present study cardiac HER2 expression was not visualized by  $^{89}\text{Zr}$ -trastuzumab PET. This was probably due to a receptor expression level that was below the PET-detectable threshold in the unstressed heart of the imaged patient population.<sup>29,30</sup>

The location of the target itself, either in the cell membrane or in the surroundings of the tumor, did not seem to have much influence on the healthy tissue distribution of the four analyzed tracers;  $^{89}\text{Zr}$ -bevacizumab, which targets a non-membrane-bound growth factor, showed the same pattern as the other three mAbs that bind to membranous receptors. Besides tumor localized target, circulating target *e.g.*, as soluble receptor or expressed by circulating tumor cells could also influence tracer kinetics. For all four targets, circulating variants have been described, but the impact of this fraction on drug kinetics, however, is unclear.<sup>31-34</sup> Next to the ability of the analyzed mAbs to internalize in tumor cells, which was also indicated for bevacizumab,<sup>35</sup> the absolute amount of target expressed, which is largely influenced by overall tumor load, might affect mAb tracer kinetics. In our dataset, however, the proportion of tracer localized at tumor sites was quite low, probably due to the low mean tumor load of the selected patients. At least for trastuzumab, it has been shown previously that tumor load clearly influences tracer and drug kinetics.<sup>36</sup>

Tracer distribution in healthy organs might also be influenced by non-target specific factors, such as the amount of tracer available in the blood, as well as metabolism and excretion.<sup>37,38</sup> Together with the  $^{89}\text{Zr}$ -labeled mAb, a dose of unlabeled protein, which had been determined

in the previous imaging trials with the respective mAb, was injected. The unlabeled protein dose increases tracer availability over time, which is necessary with mAbs with dose-dependent kinetics like trastuzumab.<sup>36,39</sup> Per tracer, the optimal unlabeled protein dose for baseline imaging was selected to assure comparable activity concentration in the blood of all four tracers over time. However, with all analyzed tracers apart from <sup>89</sup>Zr-MMOT0530A, PET imaging has also been performed after administration of pharmacodynamics-active doses or the actual therapeutic dose.<sup>15, 16, 40</sup> Thereby, normal organ distribution was comparable between baseline imaging and on-treatment imaging, whereas tumor uptake changed over time. Next to the unlabeled protein dose, the amount of endogenous neonatal Fc receptor (FcRn) might also influence the circulation time of therapeutic immune globulin G (IgG) molecules by protecting them from fast degradation, resulting in a long half-life of more than 20 days.<sup>41,42</sup> All four mAbs are IgG1 molecules, so binding specifications to the FcRn are expected to be comparable, potentially explaining the similar biodistribution (Supplementary Table 2).

Due to their size, monoclonal antibodies like the ones studied here, are metabolized first to peptides and amino acids before being re-used for protein synthesis or excreted via the kidneys.<sup>42</sup> Several target and non-target specific mechanisms, as well as proteolysis by the liver and the reticuloendothelial system, contribute to mAb elimination. Advanced mAb engineering such as glycosylation can increase uptake and metabolism of mAbs by hepatic non-parenchymal Kupffer cells located in the liver, which might explain the relatively higher healthy liver tracer uptake.<sup>42,43</sup> After elimination, non-used remnants like the radionuclide can be excreted via the intestinal tract or potentially accumulate in compact bone or bone marrow, as visualized by PET. Furthermore, differences in tracer intactness over time might explain the differing uptake in compact bone.

The scientific community is becoming increasingly aware of the many benefits of data sharing.<sup>44</sup> An example of the usefulness of data sharing is provided by the RECIST criteria, which after development have been verified by a warehouse containing data from numerous trials.<sup>45</sup> With this first comparative analysis of four <sup>89</sup>Zr-labeled mAb we aimed to create a basis for a prospectively growing warehouse of molecular imaging data of antibody-based tracers that will enable researchers worldwide to enhance and share their knowledge on whole body drug distribution. Therefore, all researchers in the field of molecular imaging are encouraged to add data to this developing warehouse as only expansion of the available data is expected to deliver a valuable long-term gain of knowledge. A short description on how to share or request imaging data are provided in Supplementary Table 3. We aim to add data from ongoing and planned imaging trials assessing molecules belonging to another IgG subclass, with different molecule size or structure, will be added to this warehouse in the future. Potentially target saturation can occur with higher antibody doses than used for baseline imaging and changes in biodistribution might occur based on repeated therapeutic dosing. Therefore, addition and

comparison of biodistribution of the same antibody with varying unlabeled antibody doses for imaging will be of interest as well.

### **Abbreviations**

AMIDE: A medical imaging data examiner; (LD) CT: (Low dose) computed tomography; CUP: Cancer of unknown primary; EANM: European Association of Nuclear Medicine; EARL: EANM Research Ltd; FcRn: Neonatal Fc receptor; HER: Human epidermal growth factor receptor; ID: Injected dose; IgG: Immunoglobulin G; mAb: Monoclonal antibody; PET: Positron emission tomography; SD: Standard deviation; VEGF-A: Vascular endothelial growth factor A; VOI: Volume of interest; <sup>89</sup>Zr: Zirconium-89.

### **Grant support**

Supported by the ERC advanced grant OnQview to E.G.E. de Vries, a personnel grant from the Dutch Cancer Society to F. Bensch (RUG 2014-6625) and the Dutch Cancer Society IMPACT grant (RUG 2012-5565). Financial support for the conduct of the clinical imaging studies was provided by the Dutch Cancer Society, Genentech and F. Hoffmann–La Roche Ltd to the UMCG.

### **Acknowledgments**

We thank Paul van Snick, Johan Wieggers and Eelco Severs from the Department of Nuclear Medicine and Molecular Imaging, UMCG, for their assistance with PET data reconstruction.

### **Competing interests**

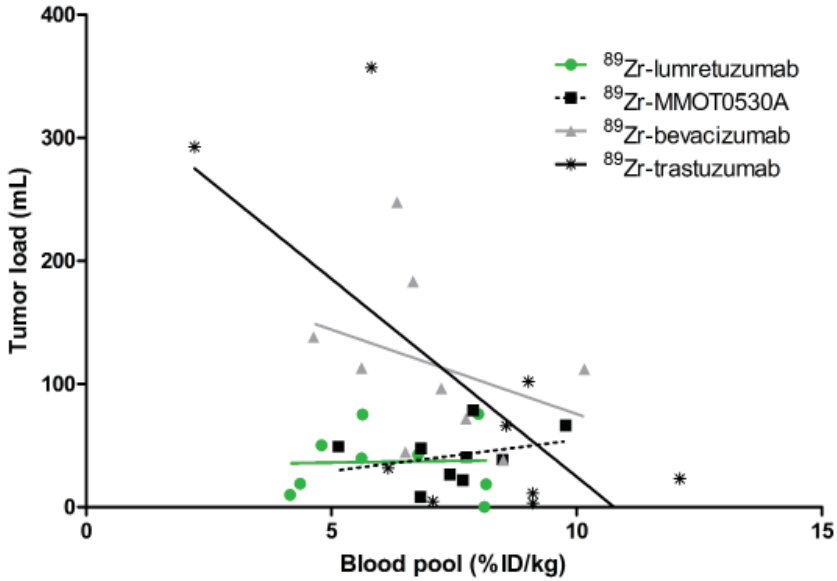
The UMCG received grants from Roche and Genentech for conduct of the imaging trials. All other authors declare no competing interests.

## REFERENCES

1. Reichert, J. M. Antibodies to watch in 2016. *MABs* 8, 197-204 (2016).
2. Reichert, J. M. Antibodies to watch in 2017. *MABs* 9, 167-181 (2017).
3. Reichert, J. M. Marketed therapeutic antibodies compendium. *MABs* 4, 413-415 (2012).
4. Ecker, D. M., Jones, S. D. & Levine, H. L. The therapeutic monoclonal antibody market. *MABs* 7, 9-14 (2015).
5. Long, G. The biopharmaceutical pipeline: Innovative therapies in clinical development. Analysis Group, Inc. (July 2017).
6. Lamberts, L. E. *et al.* Antibody positron emission tomography imaging in anticancer drug development. *J. Clin. Oncol.* 33, 1491-1504 (2015).
7. Verel, I. *et al.* <sup>89</sup>Zr immuno-PET: comprehensive procedures for the production of <sup>89</sup>Zr-labeled monoclonal antibodies. *J. Nucl. Med.* 44, 1271-1281 (2003).
8. Dijkers, E. C. *et al.* Development and characterization of clinical-grade <sup>89</sup>Zr-trastuzumab for HER2/neu immunoPET imaging. *J. Nucl. Med.* 50, 974-981 (2009).
9. Chen, D. S. & Mellman, I. Elements of cancer immunity and the cancer-immune set point. *Nature* 541, 321-330 (2017).
10. Bensch, F. *et al.* First-in-human PET imaging with the PD-L1 antibody <sup>89</sup>Zr-atezolizumab [abstract]. AACR Annual Meeting, Washington, D.C., USA (2017).
11. Gebhart, G. *et al.* Molecular imaging as a tool to investigate heterogeneity of advanced HER2-positive breast cancer and to predict patient outcome under trastuzumab emtansine (T-DM1): the ZEPHIR Trial. *Ann Oncol.* 27, 619-624 (2016).
12. Boellaard, R. *et al.* FDG PET/CT: EANM procedure guidelines for tumour imaging: version 2.0. *Eur. J. Nucl. Med. Mol. Imaging* 42, 328-354 (2015).
13. Makris, N. E. *et al.* Multicenter harmonization of <sup>89</sup>Zr PET/CT performance. *J. Nucl. Med.* 55, 264-267 (2014).
14. Borjesson, P. K. *et al.* Radiation dosimetry of <sup>89</sup>Zr-labeled chimeric monoclonal antibody U36 as used for immuno-PET in head and neck cancer patients. *J. Nucl. Med.* 50, 1828-1836 (2009).
15. Dijkers, E. C. *et al.* Biodistribution of <sup>89</sup>Zr-trastuzumab and PET imaging of HER2-positive lesions in patients with metastatic breast cancer. *Clin. Pharmacol. Ther.* 87, 586-592 (2010).
16. Oosting, S. F. *et al.* <sup>89</sup>Zr-bevacizumab PET visualizes heterogeneous tracer accumulation in tumor lesions of renal cell carcinoma patients and differential effects of antiangiogenic treatment. *J. Nucl. Med.* 56, 63-69 (2015).
17. Lamberts, T. E. *et al.* ImmunoPET with anti-mesothelin antibody in patients with pancreatic and ovarian cancer before anti-mesothelin antibody-drug conjugate treatment. *Clin. Cancer Res.* 22, 1642-1652 (2016).
18. Bensch, F. *et al.* <sup>89</sup>Zr-lumretuzumab PET imaging before and during HER3 antibody lumretuzumab treatment in patients with solid tumors. *Clin. Cancer Res.* 23, 6128-6137 (2017).
19. Gaykema, S. B. *et al.* <sup>89</sup>Zr-bevacizumab PET imaging in primary breast cancer. *J. Nucl. Med.* 54, 1014-1018 (2013).
20. Loening, A. M. & Gambhir, S. S. AMIDE: a free software tool for multimodality medical image analysis. *Mol. Imaging.* 2, 131-137 (2003).
21. Kruse, V. *et al.* Reproducibility of FDG PET based metabolic tumor volume measurements and of their FDG distribution within. *Q. J. Nucl. Med. Mol. Imaging* 59, 462-468 (2015).
22. Deurenberg, P., Weststrate, J. A. & Seidell, J. C. Body mass index as a measure of body fatness: age- and sex-specific prediction formulas. *Br. J. Nutr.* 65, 105-114 (1991).
23. Breaux, R. H. *et al.* A simple method to estimate renal volume from computed tomography. *Can. Urol. Assoc. J.* 7, 189-192 (2013).
24. Prassopoulos, P., Daskalogiannaki, M., Raissaki, M., Hatjidakis, A. & Gourtsoyiannis, N. Determination of normal splenic volume on computed tomography in relation to age, gender and body habitus. *Eur. Radiol.* 7, 246-248 (1997).
25. Nadler, S. B., Hidalgo, J. H. & Bloch, T. Prediction of blood volume in normal human adults. *Surgery* 51, 224-232 (1962).

26. Chang, K., Pastan, I. & Willingham, M. C. Isolation and characterization of a monoclonal antibody, K1, reactive with ovarian cancers and normal mesothelium. *Int. J. Cancer* 50, 373-381 (1992).
27. Hassan, R., Bera, T. & Pastan, I. Mesothelin: a new target for immunotherapy. *Clin. Cancer Res.* 10, 3937-3942 (2004).
28. Press, M. F., Cordon-Cardo, C. & Slamon, D. J. Expression of the HER-2/neu proto-oncogene in normal human adult and fetal tissues. *Oncogene* 5, 953-962 (1990).
29. Perik, P. J. *et al.* Indium-111-labeled trastuzumab scintigraphy in patients with human epidermal growth factor receptor 2-positive metastatic breast cancer. *J. Clin. Oncol.* 24, 2276-2282 (2006).
30. de Korte, M. A. *et al.* <sup>111</sup>In-diagnostic trastuzumab visualises myocardial human epidermal growth factor receptor 2 expression shortly after anthracycline treatment but not during heart failure: a clue to uncover the mechanisms of trastuzumab-related cardiotoxicity. *Eur. J. Cancer* 43, 2046-2051 (2007).
31. Willett, C. G. *et al.* Efficacy, safety, and biomarkers of neoadjuvant bevacizumab, radiation therapy, and fluorouracil in rectal cancer: a multidisciplinary phase II study. *J. Clin. Oncol.* 27, 3020-3026 (2009).
32. Moreno-Aspitia, A. *et al.* Soluble human epidermal growth factor receptor 2 (HER2) levels in patients with HER2-positive breast cancer receiving chemotherapy with or without trastuzumab: results from North Central Cancer Treatment Group adjuvant trial N9831. *Cancer* 119, 2675-2682 (2013).
33. Grigoriu, B. D. *et al.* Kinetics of soluble mesothelin in patients with malignant pleural mesothelioma during treatment. *Am. J. Respir. Crit. Care Med.* 179, 950-954 (2009).
34. Wakui, H. *et al.* Phase 1 and dose-finding study of patritumab (U3-1287), a human monoclonal antibody targeting HER3, in Japanese patients with advanced solid tumors. *Cancer Chemother. Pharmacol.* 73, 511-516 (2014).
35. Ashrafi, S. A., Hosseinimehr, S. J., Varmira, K. & Abedi, S. M. Radioimmunotherapy with <sup>131</sup>I-bevacizumab as a specific molecule for cells with overexpression of the vascular endothelial growth factor. *Cancer Biother. Radiopharm.* 27, 420-425 (2012).
36. Oude Munnink, T. H. *et al.* Trastuzumab pharmacokinetics influenced by extent human epidermal growth factor receptor 2-positive tumor load. *J. Clin. Oncol.* 28, e355-6;e357 (2010).
37. Kamath, A. V. Translational pharmacokinetics and pharmacodynamics of monoclonal antibodies. *Drug Discov. Today Technol.* 21, 75-83 (2016).
38. Ryman, J. T. & Meibohm, B. Pharmacokinetics of monoclonal antibodies. *CPT Pharmacometrics Syst. Pharmacol.* 6, 576-588 (2017).
39. Bruno, R. *et al.* Population pharmacokinetics of trastuzumab in patients with HER2+ metastatic breast cancer. *Cancer Chemother. Pharmacol.* 56, 361-369 (2005).
40. Gaykema, S. B. *et al.* <sup>111</sup>In-trastuzumab scintigraphy in HER2-positive metastatic breast cancer patients remains feasible during trastuzumab treatment. *Mol. Imaging* 13 (2014).
41. Ghetie, V. & Ward, E. S. Multiple roles for the major histocompatibility complex class I-related receptor FcRn. *Annu. Rev. Immunol.* 18, 739-766 (2000).
42. Keizer, R. J., Huitema, A. D., Schellens, J. H. & Beijnen, J. H. Clinical pharmacokinetics of therapeutic monoclonal antibodies. *Clin. Pharmacokinet.* 49, 493-507 (2010).
43. Liu, L. Antibody glycosylation and its impact on the pharmacokinetics and pharmacodynamics of monoclonal antibodies and Fc-fusion proteins. *J. Pharm. Sci.* 104, 1866-1884 (2015).
44. Rockhold, F., Nisen, P. & Freeman, A. Data sharing at a crossroads. *N. Engl. J. Med.* 375, 1115-1117 (2016).
45. Eisenhauer, E. A. *et al.* New response evaluation criteria in solid tumours: revised RECIST guideline (version 1.1). *Eur. J. Cancer* 45, 228-247 (2009).

## SUPPLEMENTARY MATERIALS



**Supplementary Figure 1** Correlation between activity in the aorta (%ID/kg) and tumor load (mL) for  $^{89}\text{Zr}$ -lumretuzumab ( $r^2 = 0.00$ ,  $P = 0.93$ ),  $^{89}\text{Zr}$ -MMOT0530A ( $r^2 = 0.09$ ,  $P = 0.44$ ),  $^{89}\text{Zr}$ -bevacizumab ( $r^2 = 0.11$ ,  $P = 0.38$ ) and  $^{89}\text{Zr}$ -trastuzumab ( $r^2 = 0.46$ ,  $P = 0.05$ ).

## Supplementary Table 1 Standard delineation protocol

### **1. Reconstruction method**

According to Makris et al.<sup>1</sup>

### **2. Analysis plan**

PET image analysis of scans performed 4 days post tracer injection.

Targets to select for PET quantification

- Tumor lesions
- Background regions (=healthy organs/tissue)
- Whole organs

PET quantification parameters

- Background regions: %ID/kg
- Tumor lesions: volume (mL)
- Whole organs: %ID/kg

Software

- A medical imaging data examiner (AMIDE, <sup>2</sup>)

### **Targets**

Lesions

- All visible lesions on PET and/or on diagnostic CT scan

Background regions

- For each background organ a background area should be quantified.
- Use an sphericalVOI (location and/or size ofVOI might be adapted in case of tumor locations) in at least 3 consecutive axial planes:
  - Brain 5 cm (left hemisphere, parietal)
  - Lung 5 cm (right upper lobe, mediolateral)
  - Aortic blood pool 2 cm (Aortic arch or thoracic aorta, highest region)
  - Muscle 5 cm (region right gluteus maximus/medius)
  - Spleen 5 cm (representative region; 4 cm if 5 cm VOI is too big) and 2 cm (highest region)
  - Liver 5 cm (representative region)
  - Kidney 2 cm (cortex of left kidney, highest region)
  - Bone marrow 2 cm (L4 or L5)
  - Bone cortex 1 cm (femur cortex, right)

- Intestine 2 cm (highest region)
- Fat tissue 2 cm (abdominal region)

#### Whole organ analysis

- Only assess organs when there is no metastatic disease located in this certain organ
- Organs of interest for whole organ analysis:
  - Liver

#### Calculations

AMIDE output (mean activity concentration in Bq/cc) was used to calculate the percentage injected dose per kilogram (%ID/kg) tissue of every VOI with the following formula:

$$\%ID/kg = \frac{\text{Activity concentration (Bq/kg)}}{\text{Injected activity (Bq)}} * 100\%$$

Injected activity was corrected for decay between moment of tracer injection and time of scanning (under the assumption of a tissue density of 1 kg/L).

Percentage organ and fat tissue tracer uptake was calculated using the following formula:

$$\text{Organ uptake (\%)} = \frac{\text{Activity concentration (Bq/gr)} * \text{Organ volume (gr)}}{\text{Injected activity (Bq)}} * 100\%$$

**Supplementary Table 2 Detailed information antibody and tracer characteristics**

	<sup>89</sup> Zr-lumretuzumab	<sup>89</sup> Zr-MMOT0530A	<sup>89</sup> Zr-bevacizumab	<sup>89</sup> Zr-trastuzumab
Pharmacokinetic parameters of monoclonal antibody				
Monoclonal antibody	Lumretuzumab	MMOT0530A	Bevacizumab	Trastuzumab
IgG class	Humanized glycoengineered IgG1k	Humanized IgG1	Humanized IgG1	Humanized IgG1
Target	HER3	Mesothelin	VEGF	HER2
Molecular weight (kDa)	150	150	150	150
Linear kinetics	Elimination of lumretuzumab across dose range 100-400 mg is predominantly target mediated; PK approached linearity at 400-2000 mg	Modest degree of target mediated clearance at doses < 1 mg/kg; linear clearance across tested dose range of 0.2 to 2.8 mg/kg for the q3w schedule	Linear pharmacokinetics for doses 1-10 mg/kg	Non-linear elimination
Clearance	1.04 L/d (100 mg); 0.264 L/d (> 2000 mg)	27 mL/d/kg	0.188 L/d - 0.220 L/d	0.111 L/d
Volume of distribution	3.64 L (100 mg); 4.4 L (> 2000 mg)	V <sub>ss</sub> = 68 mL/kg	2.73-3.28 L	2.91 L
Elimination half-life time	2.4 d (100 mg); 12 d (> 400 mg)	2.1-3.7 d	18-20 d	28.5 d
Reference	Meulendijks et al. <sup>3</sup>	Weekes et al. <sup>4</sup>	European public assessment report of Herceptin <sup>5</sup>	European public assessment report of Avastin <sup>6</sup>

Information on the <sup>89</sup> Zr-labeled antibodies			
Chelator	TFP-N-sucDf	TFP-N-sucDf	TFP-N-sucDf
Chelator:mAb conjugation ratio	1.5 ± 0.1	1.5 ± 0.1	1.5 ± 0.1
<i>In vitro</i> serum stability	Stable in serum; < 5% decrease in radiochemical purity (rcp) after 168 h	2% decrease in rcp after 168 h in normal saline at 20°C	6% decrease rcp after 168 h in serum 0.39 ± 0.02% decrease in rcp/day in serum
Radiochemical purity (%)	> 98	> 98	> 98
pH	4-7	5-8	6-7
Immunoreactivity (%)	Preserved	> 70	> 60
Appearance	Colorless to light yellow	Colorless to light yellow liquid	Colorless
Bacterial endotoxins (EU/mL)	< 2.5	< 2.5	< 1.0
Aggregates (%)	< 5	< 5	< 3
Sterility	Sterile	Sterile	Sterile

<sup>89</sup>Zr, zirconium-89; IgG, immunoglobulin gamma; HER, human epidermal growth factor receptor; mAb, monoclonal antibody; rcp, radiochemical purity; TFP-N-sucDf, tetrafluorophenol-N-succinyldester; VEGF, vascular endothelial growth factor receptor; Vss, steady state volume of distribution.

### Supplementary Table 3 Details on deposited data and curation process

#### **Data deposit**

An overview over the deposited datasets including details on the dataset, contact information, information on requesting and depositing data can be found online under [www.imagingwarehouse.eu](http://www.imagingwarehouse.eu).

#### **Deposited data**

Information on the individual subject and imaging data per individual subject will be deposited.

Specification of the deposited data for the four  $^{89}\text{Zr}$ -mAb tracers analyzed in the current manuscript:

##### **Patient related information:**

Weight, height, total tumor load (PET based, mL), injected [netto] dose, time between tracer injection and start of PET scan, activity on the day of tracer injection.

##### **PET imaging data per individual patient:**

AMIDE output and SUV calculations for blood and normal organ VOI's: aorta, liver, kidney, fat tissue, muscle, brain, lung, spleen, intestine, femur cortex and bone marrow.

AMIDE output per VOI includes median, mean, variance, standard deviation, minimum, maximum and size ( $\text{mm}^3$ ).

SUV calculations include SUVmean and SUVmax.

Data to be deposited by external parties should include at least above mentioned patient related information and PET related information. Thereby, the administered radiation dose is not restricted to 37 MBq, as the dose can vary. Information on the used analysis tool and/or algorithm should also be deposited. Throughout time, requirements on which data to be deposited might change, therefore, it is recommended to consult the website for further instructions ([www.imagingwarehouse.eu](http://www.imagingwarehouse.eu)).

#### **Data request**

All data will be provided upon request. Requests can be send by email to the imaging warehouse group ([imagingwarehouse@onco.umcg.nl](mailto:imagingwarehouse@onco.umcg.nl)). Data can be requested by health care professionals and all scientific personnel. Data is provided for research purpose only.

Re-processing of imaging data with other reconstruction protocols and additional information can be requested. Whether requested data can be provided, will be decided by the for the dataset responsible researcher or delegates (e.g. based on privacy laws).

### **Request format**

All requests need to contain a specification of the requested data set, information on the requesting person or group including name of the responsible investigator, function and institution. Furthermore, a short description of the intended aim/research question is preferred.

### **Public disclosure and publication policy**

Provenance of the data must be stated and data needs to be referenced to in all publications in written form, oral presentation or publication in any other form.

## REFERENCES

1. Makris, N. E. *et al.* Multicenter harmonization of  $^{89}\text{Zr}$  PET/CT performance. *J. Nucl. Med.* 55, 264-267 (2014).
2. Loening, A. M. & Gambhir, S. S. AMIDE: a free software tool for multimodality medical image analysis. *Mol. Imaging.* 2, 131-137 (2003).
3. Meulendijks, D. *et al.* First-in-human phase I study of lumretuzumab, a glycoengineered humanized anti-HER3 monoclonal antibody, in patients with metastatic or advanced HER3-positive solid tumors. *Clin. Cancer Res.* 22, 877-885 (2016).
4. Weekes, C. D. *et al.* Phase I study of DMOT4039A, an antibody-drug conjugate targeting mesothelin in patients with unresectable pancreatic or platinum-resistant ovarian cancer. *Mol. Cancer. Ther.* 15, 439-447 (2016).
5. European Medicines Agency, European public assessment report of Herceptin. Revised 13/12/2017. [http://www.ema.europa.eu/ema/index.jsp?curl=pages\\_/medicines/human/medicines/000278/human\\_med\\_000818.jsp&mid=WC0b01ac058001d124](http://www.ema.europa.eu/ema/index.jsp?curl=pages_/medicines/human/medicines/000278/human_med_000818.jsp&mid=WC0b01ac058001d124)
6. European Medicines Agency, European public assessment report of Avastin. Revised 15/12/2017. [http://www.ema.europa.eu/ema/index.jsp?curl=pages\\_/medicines/human/medicines/000582/human\\_med\\_000663.jsp&mid=WC0b01ac058001d124](http://www.ema.europa.eu/ema/index.jsp?curl=pages_/medicines/human/medicines/000582/human_med_000663.jsp&mid=WC0b01ac058001d124)





# Chapter 6

## **<sup>89</sup>Zr-atezolizumab imaging as non-invasive approach to assess clinical response to PD-L1 blockade in cancer**

Frederike Bensch<sup>1</sup>, Elly L. van der Veen<sup>1</sup>, Marjolijn N. Lub-de Hooge<sup>2,3</sup>, Annelies Jorritsma-Smit<sup>2</sup>, Ronald Boellaard<sup>3</sup>, Iris C. Kok<sup>1</sup>, Sjoukje F. Oosting<sup>1</sup>, Carolina P. Schröder<sup>1</sup>, T. Jeroen N. Hiltermann<sup>4</sup>, Anthonie J. van der Wekken<sup>4</sup>, Harry J.M. Groen<sup>4</sup>, Thomas C. Kwee<sup>3</sup>, Sjoerd G. Elias<sup>5</sup>, Jourik A. Gietema<sup>1</sup>, Sandra Sanabria Bohorquez<sup>6</sup>, Alex de Crespigny<sup>6</sup>, Simon-Peter Williams<sup>6</sup>, Christoph Mancao<sup>7</sup>, Adrienne H. Brouwers<sup>3</sup>, Bernard M. Fine<sup>6</sup>, Elisabeth G.E. de Vries<sup>1</sup>

Department of Medical Oncology<sup>1</sup>, University Medical Center Groningen, University of Groningen, the Netherlands. Clinical Pharmacy and Pharmacology<sup>2</sup>, University Medical Center Groningen, University of Groningen, the Netherlands. Medical Imaging Center<sup>3</sup>, University Medical Center Groningen, University of Groningen, the Netherlands. Pulmonary Oncology<sup>4</sup>, University Medical Center Groningen, University of Groningen, the Netherlands. Department of Epidemiology<sup>5</sup>, Julius Center for Health Sciences and Primary Care, University Medical Center Utrecht, Utrecht University, the Netherlands. Genentech<sup>6</sup>, San Francisco, CA, USA. Genentech Inc.<sup>7</sup>, Basel, Switzerland.

Programmed cell death protein-1/ligand-1 (PD-1/PD-L1) blockade is effective in a subset of patients with several tumor types, but predicting patient benefit using approved diagnostics is inexact as also some patients with PD-L1-negative tumors show clinical benefit.<sup>1,2</sup> Moreover, all biopsy-based tests are subject to the errors and limitations of invasive tissue collection.<sup>3-11</sup> Preclinical studies of PET imaging with PD-L1 antibodies suggested that this imaging approach might be an approach to selecting patients.<sup>12,13</sup> Such a technique, however, requires significant clinical development and validation; here we present the initial results from a first-in-human study to assess feasibility of imaging with zirconium-89 labeled atezolizumab (anti-PD-L1) including biodistribution, and secondly test its potential to predict response to PD-L1 blockade (ClinicalTrials.gov Identifiers NCT02453984 and NCT02478099). We imaged 22 patients across three tumor types prior to atezolizumab therapy. The PET signal, a function of tracer exposure and target expression, was high in lymphoid tissues and at sites of inflammation. In tumors uptake was generally high but heterogeneous, varying within and between lesions, patients, and tumor types. Intriguingly, clinical responses in our patients were better correlated with pre-treatment PET signal than with immunohistochemistry- or RNA sequencing-based predictive biomarkers, encouraging further development of molecular PET imaging for assessment of PD-L1 status and clinical response prediction.

Excitement about durable responses in cancer patients has spurred clinical investigations and marketing approvals for immunotherapies based on checkpoint blockade of PD-1 and its ligand PD-L1. Identifying patients likely to benefit from these therapies, however, remains challenging. Two diagnostic tests based on PD-L1 immunohistochemistry (IHC) have been approved to predict patient benefit. However, not all patients with high tumor PD-L1 benefit from treatment with checkpoint inhibitors, and some with no PD-L1 staining also show benefit.<sup>1, 2</sup> At present, it is unclear if this is primarily due to artifacts related to limited tissue sampling or under-appreciated facets of PD-L1 biology, including spatial and temporal heterogeneity.<sup>14-20</sup> Other predictive biopsy-based biomarkers have been evaluated, but are also subject to errors and limitations of invasive tissue collection.<sup>3-11</sup> As suggested by preclinical reports, a macroscopic, non-invasive molecular imaging readout for PD-L1 could provide new insights by assessing the PD-L1 status throughout the whole body, potentially at multiple time points, thus capturing information about the tumor immune infiltrate and its response to therapy.<sup>12, 13</sup> Such insights may be important in optimizing the use of existing treatments and in developing new immunotherapeutic agents and combinations.

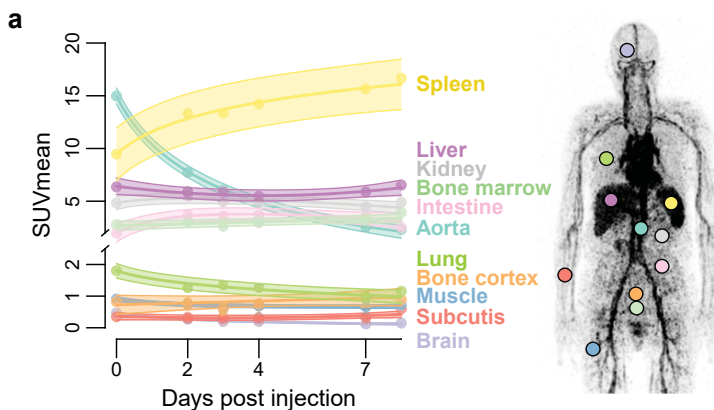
Here we present results from the first-in-human imaging study with <sup>89</sup>Zr-labeled atezolizumab (anti-PD-L1). We enrolled 25 patients with locally advanced or metastatic bladder cancer, non-small cell lung cancer (NSCLC), or triple-negative breast cancer (TNBC) between March and November 2016 (Supplementary Table 1). Three patients discontinued prematurely due to disease progression, before tracer injection or during imaging procedures. Twenty-two patients completed the full imaging series of up to four PET scans and were subsequently treated with atezolizumab until progressive disease (PD).

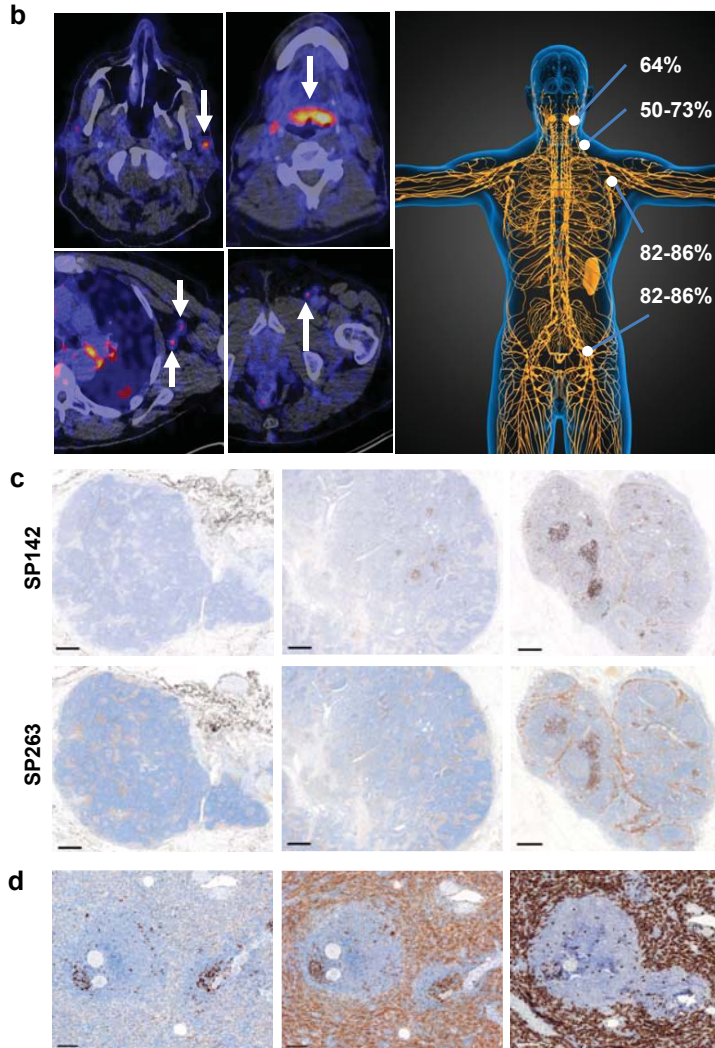
<sup>89</sup>Zr-atezolizumab injection was safe with only one related low-grade adverse event (Supplementary Table 2). The side effects of atezolizumab monotherapy were comparable with previous reports, except for the higher incidence of mainly low-grade infusion-related reactions ( $n = 4$ , including one grade 3 event).<sup>4, 8, 21</sup>

We added 10 mg unlabeled atezolizumab to the tracer to prevent rapid clearance during imaging. Pharmacokinetic analysis showed good correlation with activity of the blood pool on PET and confirmed that the circulating tracer dose corresponded with a serum atezolizumab concentration reached with 0.1-0.3 mg/kg atezolizumab, which is almost 100-fold lower than that reached with the recommended atezolizumab treatment dose (Supplementary Fig. 1a-b).<sup>22</sup> As day 4 blood pool, liver, and kidney <sup>89</sup>Zr-atezolizumab uptake was comparable with results of other <sup>89</sup>Zr-antibody tracers with well-known kinetics over time<sup>23-26</sup> and tumor lesions were visualized satisfactorily, we considered this unlabeled antibody dose to be sufficient. Since PET scans on days 0 and 2 did not add valuable information in the first ten patients, we decided to continue with scans on days 4 and 7 only.

First, we assessed  $^{89}\text{Zr}$ -atezolizumab biodistribution. We observed low uptake in healthy brain, subcutaneous tissue, muscle, compact bone, and lung, and higher uptake over time in the intestines, kidney, and liver; these last three probably reflecting antibody metabolism and elimination (Fig. 1a and Supplementary Fig. 2).  $^{89}\text{Zr}$ -atezolizumab uptake also increased slightly in bone marrow over time. This uptake was considered specific and not due to accumulation of free  $^{89}\text{Zr}$ , as uptake in compact bone was low and stable over time and the tracer remained intact in serum (Fig. 1a and Supplementary Fig. 3a-b). Non-malignant lymph nodes were also visualized with  $^{89}\text{Zr}$ -atezolizumab PET in the majority of patients on days 4 and 7 (Fig. 1b). In contrast to reports about  $^{89}\text{Zr}$ -antibody tumor cell and growth factor targeting tracers<sup>23-26</sup>, we observed increasing high and variable  $^{89}\text{Zr}$ -atezolizumab uptake in the spleen, compatible with target-specific binding (Fig. 1a). PD-L1 IHC showed variable expression in non-malignant lymph nodes and prominent expression in the spleen, the latter coinciding with CD8 expression (Fig. 1c-d). Based on morphology this is mainly attributed to endothelial littoral cells, which line the venous sinusoids (Fig. 1d). These cells are CD8 $\alpha$ - and PD-L1-positive and stain for CD68, a protein highly expressed by macrophages, suggesting a relationship between these two cell types (data not shown).<sup>27</sup> Overall, the observed  $^{89}\text{Zr}$ -atezolizumab uptake in lymphoid tissue might serve as a surrogate for the activation state of the body's immune system or as a measure for abundant PD-L1 expression. Finally, sites of clinically observed inflammation in individual patients were identified on  $^{89}\text{Zr}$ -atezolizumab PET (Supplementary Fig. 4). At these sites, depending on the phase of inflammation, different PD-L1-expressing immune cells can be found<sup>28</sup>, which might be visualized with PET.

Furthermore, we were able to visualize lesions at all main metastatic sites (Fig. 2a-b). As patients with central nervous system metastases were excluded from the study, it is unknown whether these metastases could also be visualized. Maximum standardized uptake value (SUVmax) of tumor lesions (overall and according to tumor type), tumor-to-background ratio for lung and bone metastases, and tumor-to-blood ratio increased over time, with the first two

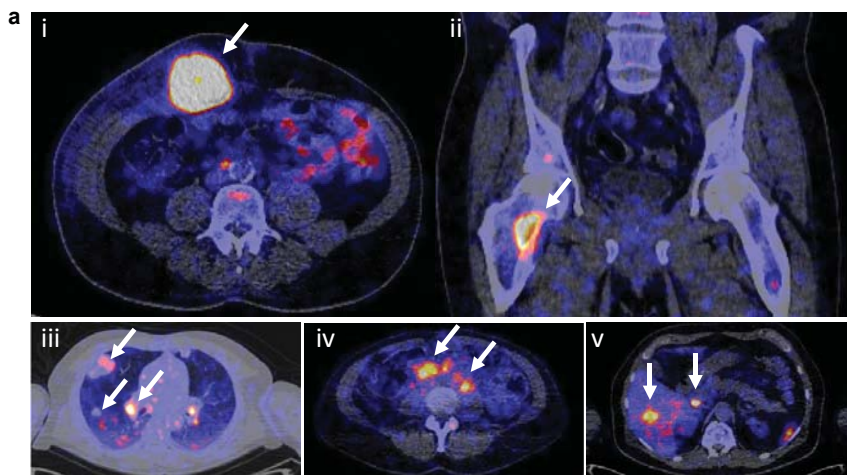




**Figure 1** <sup>89</sup>Zr-atezolizumab biodistribution and PD-L1 IHC in healthy tissue. **(a)** Tracer uptake as mean SUV<sub>mean</sub> (95% CI) per time point in healthy tissue and blood 1 h after tracer injection (day 0) and on days 2, 4, and 7 postinjection ( $\pm 1$  day); measured in ten patients on days 0 and 2 ( $\pm 1$  day) and in all 22 patients on days 4 and 7 ( $\pm 1$  day); fitted regression lines with 95% CI based on linear mixed effect models (764 data points from 12 localizations (liver uptake was measured in two regions per patient per time point) in 22 patients; 4 missing data points). Representative maximum intensity projection of an <sup>89</sup>Zr-atezolizumab PET scan on the right indicates location of measured healthy tissue. **(b)** Percentage of patients ( $n = 22$ ) with <sup>89</sup>Zr-atezolizumab uptake in healthy lymphoid tissue on day 7 (right) and examples of <sup>89</sup>Zr-atezolizumab uptake in the Waldeyer's tonsillar ring (upper middle) and small normal lymph nodes in the neck (upper left), axillary region (lower left) and inguinal region (lower middle) on day 7 postinjection (PET scans were performed once per patient and time point). **(c)** Examples of three normal non-malignant lymph nodes with PD-L1 IHC (SP142, upper panel; lower panel SP263) illustrating heterogeneous PD-L1 staining within and between samples (spare tissue, not obtained from study population) (scale bars, 500  $\mu$ m; IHC was performed once). **(d)** Healthy spleen with a lymphoid follicle surrounded by endothelial littoral cells with intense PD-L1 (SP142, left; SP263, middle) and high CD8 (right) staining (scale bars, 100  $\mu$ m; IHC was performed once).

stabilizing at day 7 postinjection (Supplementary Fig. 5a-c). We further report day 7 uptake data, as SUVmax of days 4 and 7 were highly correlated (Supplementary Fig. 5d) and tumor-to-blood ratio was the most favorable on the latest scan moment. Tumor  $^{89}\text{Zr}$ -atezolizumab uptake was generally high (Fig. 2b), with an overall geometric mean SUVmax of 10.4 (95% confidence interval (CI) 8.5-12.7; range 1.6-46.1). We observed major within-patient SUVmax heterogeneity in the 20 patients with more than one lesion with a median fold difference of 2.2 (range 1.0-9.4) and a median coefficient of variation of 12.2% (range 0.7-39.3%). Tumor tracer uptake differed per tumor type ( $P = 0.016$ ), with TNBC showing on average 50% (95% CI 17-70%) less uptake than bladder cancer (Fig. 2c). Moreover, tracer uptake varied per site of metastases ( $P = 2.2e^{-07}$ ): in sites with at least ten observations, liver metastases had the highest uptake and lung metastases the lowest (Fig. 2d). We also observed heterogeneous intra-tumor tracer distribution in several lesions of multiple patients (Fig. 2e). Autoradiography of two tumor samples showed heterogeneous tracer distribution, and PD-L1 as well as CD8 IHC showed heterogeneous staining, partly corresponding with regions of high tracer uptake (Fig. 3).

Given the high  $^{89}\text{Zr}$ -atezolizumab tumor uptake, the known property of  $^{89}\text{Zr}$  to remain in cells, and the potential role of atezolizumab internalization contributing to this signal, we determined the internalization of  $^{89}\text{Zr}$ -atezolizumab *in vitro* in two tumor cell lines and in healthy volunteers' peripheral blood mononuclear cells (PBMCs) and in T cells. We observed high internalization rates in the tumor cell lines, and lower rates in human PBMCs and T cells (Supplementary Fig. 6a,b). Analyses of the PBMC fraction isolated from blood obtained from participating patients confirmed that only, respectively, 0.3% and 0.4% of the tracer dose on day 4 ( $n = 2$ ) and 0.6% on day 7 ( $n = 1$ ), was bound to and/or internalized by PBMCs. The lower internalization rates observed in PBMCs and T cells relative to the tumor lines are assumed to be primarily dependent on the lower PD-L1 expression of these cells.



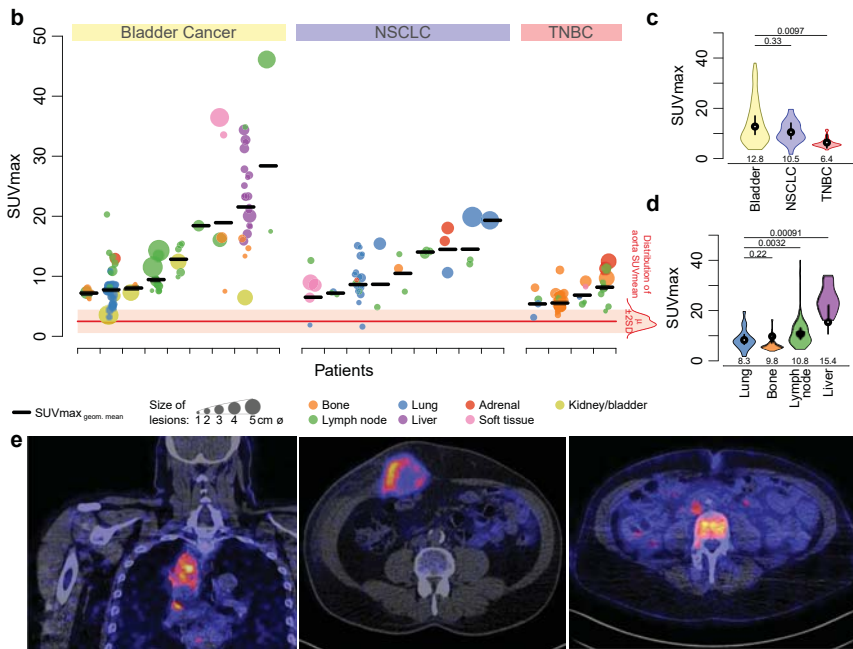


**Figure 2** <sup>89</sup>Zr-atezolizumab tumor uptake. **(a)** Examples of PET/CT images of four patients illustrating <sup>89</sup>Zr-atezolizumab tumor uptake in five different locations on day 7 postinjection (white arrows indicate tumor lesions; PET scans were performed once per patient and time point). Images (i) and (ii) are from the same patient, whereas images (iii), (iv) and (v) are from a separate patient each. **(b)** Overview of <sup>89</sup>Zr-atezolizumab uptake as SUVmax at day 7 postinjection in 196 tumor lesions with a diameter > 2 cm grouped per tumor type and ordered by increasing geometric mean SUVmax per patient, visualizing tumor size and site, and with blood pool background uptake as reference. Horizontal bars indicate geometric mean SUVmax per patient. **(c)** Violin plot of SUVmax in lesions per tumor type with bottom and top 1% of SUVmax values truncated (1<sup>st</sup>, 50<sup>th</sup>, and 99<sup>th</sup> SUVmax percentile: 3.6, 10.9, 38.0 for bladder; 1.7, 9.7, 19.6 for NSCLC; 3.4, 5.6, 11.7 for TNBC); black vertical lines are 95% CIs of geometric mean SUVmax, white dots within black lines and values below the violin plot are the actual geometric means, all based on a linear mixed regression model with two-sided Wald *P*-values using Satterthwaite approximations to degrees of freedom under restricted maximum likelihood shown above the graph;  $n_{\text{bladder}} = 85$  in nine patients,  $n_{\text{NSCLC}} = 43$  in nine patients,  $n_{\text{TNBC}} = 68$  in four patients. **(d)** Violin plot of actual distribution of SUVmax in lesions per site of lesion with bottom and top 1% of SUVmax values truncated (1<sup>st</sup>, 50<sup>th</sup>, and 99<sup>th</sup> SUVmax percentile: 1.7, 7.9, 19.6 for lung; 3.9, 5.6, 16.4 for bone; 4.6, 9.7, 40.1 for lymph node; 16.1, 23.3, 34.1 for liver); black vertical lines are 95% CIs of geometric mean SUVmax, white dots within black lines and values below the violin plot are the actual geometric means, all based on a linear mixed regression model with two-sided Wald *P*-values using Satterthwaite approximations to degrees of freedom under restricted maximum likelihood shown above the graph;  $n_{\text{lung}} = 44$  in ten patients,  $n_{\text{bone}} = 62$  in nine patients,  $n_{\text{lymph node}} = 54$  in 20 patients,  $n_{\text{liver}} = 19$  in one patient. **(e)** PET/CT images of lesions of three patients with heterogeneous intralesional <sup>89</sup>Zr-atezolizumab uptake on day 7 postinjection (PET scans were performed once per patient and time point). Mediastinal lesion of a NSCLC patient (SUVmax 19.9) (left), an abdominal wall metastases of a bladder cancer patient (SUVmax 36.4) (middle), and a bone metastasis of a TNBC patient (SUVmax 7.1) (right).

To help explain why some patients respond to checkpoint inhibitors despite low or absent PD-L1 expression, we compared PD-L1 expression and immune phenotypes based on IHC and RNA sequencing of post-tracer biopsies with tumor tracer uptake.

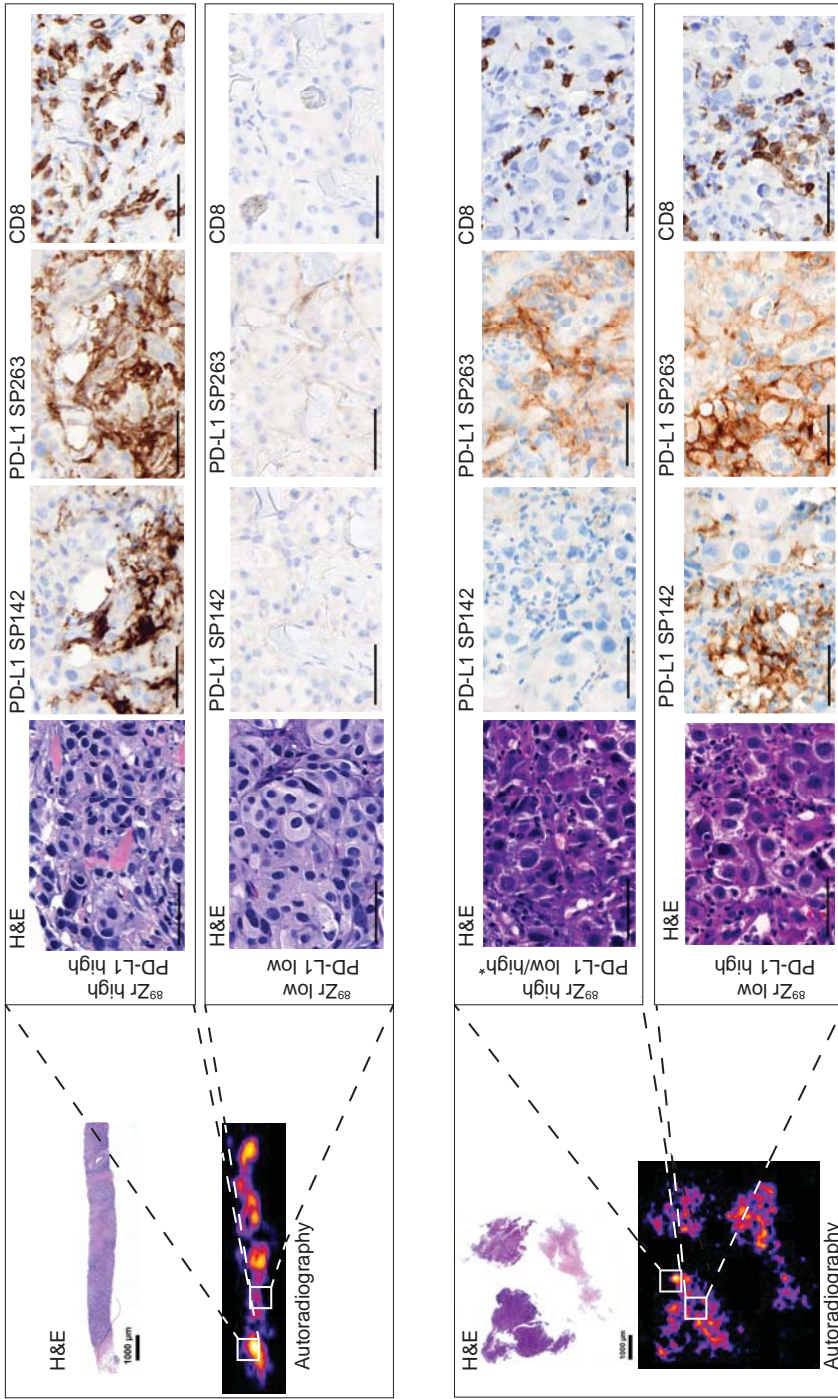


**Figure 3** Autoradiography and IHC of postimaging tumor biopsy, PD-L1 IHC (SP142 and SP263), as well as CD8 IHC of TNBC (upper panels). PD-L1 IHC (SP142 and SP263), as well as CD8 IHC of bladder cancer biopsy samples (lower panels). Scale bars, 50  $\mu$ m; autoradiography and all IHC were performed once per sample.

As expected, based on a prior study<sup>17</sup>, the two IHC assays generated conflicting results in 8 of 19 samples (kappa 0.17, 95% CI -0.23 to 0.57; Supplementary Fig. 7a). <sup>89</sup>Zr-atezolizumab uptake of the biopsied tumor lesions increased with PD-L1 IHC scores for SP142 (Supplementary Fig. 7b), but not for SP263 (Supplementary Fig. 7c). Furthermore, tracer uptake did not differ between IHC-based immune phenotypes ( $n = 16$ ; Supplementary Fig. 7d). Correlation of PD-L1 and T effector gene expression levels (CD8, granzyme B, interferon  $\gamma$ , chemokine ligand 9, and combined T effector signature) with <sup>89</sup>Zr-atezolizumab ranged between 0.51 and 0.76 (Pearson), and 0.46 and 0.62 (Spearman), respectively (Supplementary Fig. 7e-j). Similar to the IHC results, this could partly explain the generally high tumor tracer uptake.

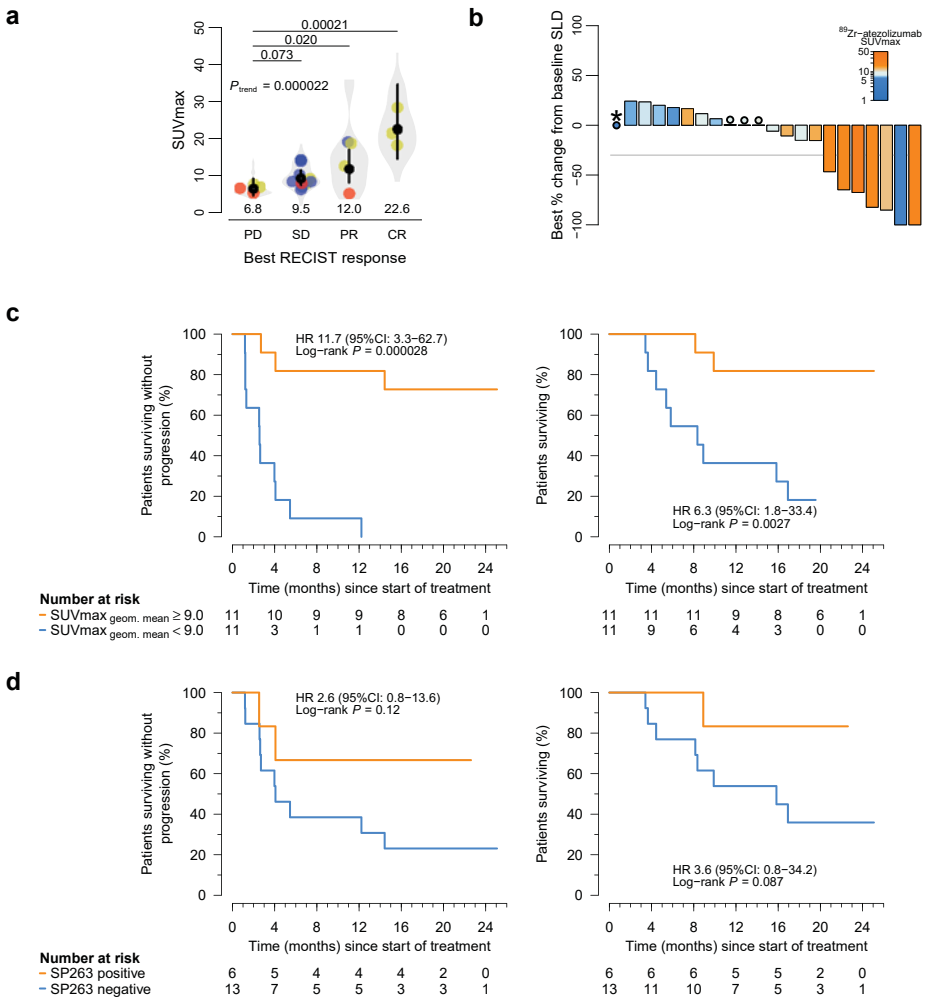
With a data cutoff date of 1 June 2018, seven patients were still in follow-up (median follow-up 21.9 months, range 16.7-25.1). Four of them were still on treatment, two were discontinued after two years of treatment and ongoing response, and one patient stopped atezolizumab due to side effects. Complete response (CR) was observed in three patients and partial response (PR) in four. Eleven patients showed stable disease (SD) as best response, and four patients progressed at the first CT evaluation (6 weeks; Supplementary Fig. 8a-b). The objective response rate was 56% for bladder cancer, 11% for NSCLC, and 25% for TNBC (Supplementary Table 3). Earlier reports described objective response rates of 26% for unselected urothelial carcinoma patients<sup>8,29</sup> while we included only patients with bladder cancer, 21-23% for NSCLC patients<sup>30,31</sup> and 24% for PD-L1-positive TNBC patients.<sup>32</sup> The median progression free survival (PFS) was 4.8 months (95% CI 2.7 to  $\infty$ ) for all patients and 13.3 months (95% CI 4.1 to  $\infty$ ) for those with SD, PR, or CR as best response.

At patient level, <sup>89</sup>Zr-atezolizumab tumor uptake increased with increasing best tumor response category (Fig. 4a; log-linear trend) and was related to target lesion size change (Fig. 4b): patients with CR as best response had a 235% higher SUVmax (95% CI 98 to 467%;  $P = 0.00021$ ) than patients who immediately progressed, and a twofold increase in geometric mean SUVmax per patient was associated with a best change in target lesion size from baseline of -35% on average (95% CI -61 to -9%;  $P = 0.010$ ). Furthermore, the geometric mean SUVmax per patient was strongly related to PFS (14 events) and overall survival (OS; 11 events): those with below median uptake were more likely to progress or die than those with above median uptake (Fig. 4c). These relationships between <sup>89</sup>Zr-atezolizumab uptake and patient outcome did not change and remained significant following adjustment for tumor type and tumor load (Supplementary Table 4), and when analyzed continuously (Supplementary Table 5). In our patient population, which lacked patients with a SP142 PD-L1 IHC score of 3, higher PD-L1 IHC expression was not related to better outcome (relationship with best tumor response: Fisher's exact  $P = 0.71$  and 0.80,  $n = 19$ ; relationship with best target lesion size change: t-test  $P = 0.46$  and 0.42 for SP263 and SP142, respectively,  $n = 18$ ; Fig. 4d-e shows relationship with survival). A patient's geometric mean <sup>89</sup>Zr-atezolizumab uptake discriminated effectively between patients with and without

PR/CR as best tumor response, and between those with long and short time to progression or time to death (Supplementary Table 6). Both PD-L1 IHC assays, in contrast, showed moderate to poor discrimination for patient outcome (Supplementary Table 6).

At lesion level, <sup>89</sup>Zr-atezolizumab uptake was also related to change in size during treatment (Supplementary Fig. 9a-c). A multilevel linear mixed model – taking into account the repeated treatment response measurements during treatment per lesion and the clustering of lesions within patients (651 measurements from 107 metastases in 21 patients) – showed that response of an individual lesion was strongly related to baseline SUVmax, with higher uptake indicating better response (interaction [time since start treatment]x[SUVmax]:  $P = 5.1 \times 10^{-13}$ ; Supplementary Fig. 10).

In conclusion, in this first-in-human assessment of <sup>89</sup>Zr-atezolizumab, we show that the imaging signal corresponds with PD-L1 expression at sites of inflammation and in various normal



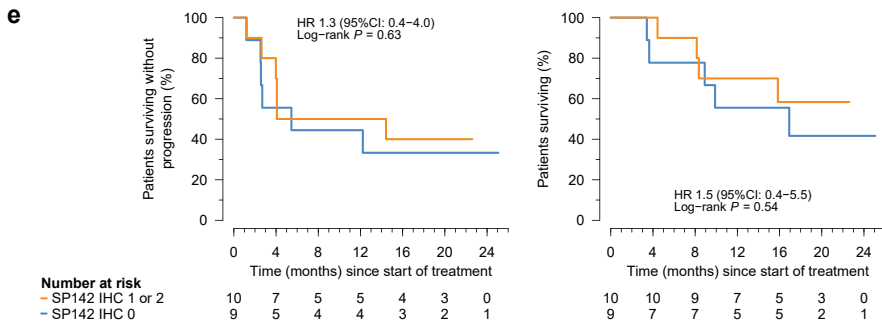


**Figure 4** <sup>89</sup>Zr-atezolizumab tumor uptake as predictor for response. **(a)** Relationship between <sup>89</sup>Zr-atezolizumab tumor uptake as geometric mean SUVmax and best RECIST response: gray violin plot areas show actual distribution of SUVmax at the metastasis level per best RECIST response category with bottom and top 1% values truncated (1<sup>st</sup>, 50<sup>th</sup>, and 99<sup>th</sup> SUVmax percentile: 3.5, 5.9, 14.7 for PD; 1.8, 90, 18.7 for SD; 3.5, 13.5, 36.0 for PR; 8.3,23,2,43.2 for CR); points show geometric mean uptake per patient with colors indicating tumor type (red, TNBC; blue, NSCLC; yellow, bladder cancer; black vertical lines are 95% CIs of geometric mean SUVmax, white dots within black lines and values below the violin plot are the actual geometric means; all based on a linear mixed regression model with two-sided Wald *P*-values using Satterthwaite approximations to degrees of freedom under restricted maximum likelihood shown above the graph, and a two-sided *P* for trend based on a likelihood-ratio test under maximum likelihood;  $n_{PD} = 88$  in four patients,  $n_{SD} = 65$  in 11 patients,  $n_{PR} = 16$  in four patients,  $n_{CR} = 27$  in three patients). **(b)** Waterfall plots depicting best percentage change from baseline SLD (measured on CT) with color scale indicating geometric mean SUVmax of tumor lesions per patient; circles show geometric SUVmax for patients with minimal change; \*, patient who was immediately progressive, no SLD change available. **(c)** PFS and OS according to the geometric mean SUVmax per patient (orange, above-median geometric mean uptake; blue, below-median geometric mean uptake;  $n = 22$  patients; two-sided log-rank test). **(d)** PFS and OS based on PD-L1 IHC (SP263; orange, IHC positive; blue, IHC negative;  $n = 19$  patients; two-sided log-rank test). **(e)** PFS and OS based on PD-L1 IHC (SP142; orange, IHC positive; blue, IHC negative;  $n = 19$  patients; two-sided log-rank test).

lymphoid tissues. Furthermore, in our study (with a small patient population and no tumor biopsies that were immunohistochemically highly PD-L1-positive) tracer uptake appeared to be a strong predictor for response to atezolizumab treatment, including PFS and OS. Future clinical studies are needed to confirm our findings in a larger patient population, to comprehensively assess different <sup>89</sup>Zr-atezolizumab uptake features in combination with other clinical data to optimize therapy response prediction, and to evaluate whether <sup>89</sup>Zr-atezolizumab PET could also be used as a response predictor for treatment with other monoclonal antibodies targeting the PD-1/PD-L1 axis.

## Acknowledgments

We thank patients and their families for participating in this study. This work was supported by the Dutch Cancer Society grant RUG 2016-10034 (POINTING) and the ERC Advanced grant OnQview ERC 293445, both awarded to E.G.E.d.V., a personal Dutch Cancer Society fellowship

RUG 2014-6625 awarded to F.B., and a research grant from Hoffmann-La Roche/Genentech, which was made available to the UMCG.

### **Author contributions**

F.B., E.G.E.d.V., B.M.F., A.d.C. designed the study; F.B., E.L.v.d.V., M.N.L.-d.H., A.J.-S., R.B., S.G.E., B.M.F., C.M., A.d.C. developed the methodology; Acquisition of data was performed by F.B., C.M., T.C.K., E.L.v.d.V., I.C.K., S.F.O., C.P.S., T.J.N.H., A.J.v.d.W., H.J.M.G., J.A.G., A.H.B., S.S.B.; S.G.E., F.B., C. M., E.L.v.d.V., S.-P.W. conducted statistical analyses and preclinical experiments; A.H.B. and E.G.E.d.V. supervised the study; F.B., E.G.E.d.V., B.M.F., S.-P.W., S.S.B., C.M. and S.G.E. wrote the manuscript. Results were discussed by all authors, who also commented on the manuscript.

### **Competing interests statement**

The authors declare the following as competing financial interests: H.J.M.G. received research support from Hoffmann-La Roche (payment to the institution) and has an advisory role for Roche Netherlands; B.M.F., C.M., S.S.B., A.d.C. and S.-P.W. are employed by Hoffman-La Roche/Genentech and own stock in Hoffman-La Roche/Genentech; E.G.E.d.V. received research support from Hoffman-La Roche/Genentech (payment to the institution) and is a member of the ESMO Magnitude of Clinical Benefit Scale.

### **Data availability**

The RNA sequencing data set presented in this manuscript is available through NCBI GEO (series accession number GSE115594). The data is annotated with a short summary and a description of the study design and can freely be downloaded via the GEO website (<https://www.ncbi.nlm.nih.gov/geo/>). Clinical details of the cases and laboratorial data, restricted to non-identifying data due to privacy concerns, can be requested by email from the corresponding author, who will handle all requests.

### **Reporting summary**

Further information on research design is described in the Nature Research Reporting Summary linked to this article.

## REFERENCES

1. Balar, A. V. *et al.* Atezolizumab as first-line treatment in cisplatin-ineligible patients with locally advanced and metastatic urothelial carcinoma: a single-arm, multicentre, phase 2 trial. *Lancet* 389, 67-76 (2017).
2. Daud, A. I. *et al.* Programmed death-ligand 1 expression and response to the anti-programmed death 1 antibody pembrolizumab in melanoma. *J. Clin. Oncol.* 34, 4102-4109 (2016).
3. Hegde, P. S., Karanikas, V. & Evers, S. The where, the when, and the how of immune monitoring for cancer immunotherapies in the era of checkpoint inhibition. *Clin. Cancer Res.* 22, 1865-1874 (2016).
4. Rosenberg, J. E. *et al.* Atezolizumab in patients with locally advanced and metastatic urothelial carcinoma who have progressed following treatment with platinum-based chemotherapy: a single-arm, multicentre, phase 2 trial. *Lancet* 387, 1909-1920 (2016).
5. Chen, P. L. *et al.* Analysis of immune signatures in longitudinal tumor samples yields insight into biomarkers of response and mechanisms of resistance to immune checkpoint blockade. *Cancer Discov.* 6, 827-837 (2016).
6. Ansell, S. M. *et al.* PD-1 blockade with nivolumab in relapsed or refractory Hodgkin's lymphoma. *N. Engl. J. Med.* 372, 311-319 (2015).
7. Dong, Z. Y. *et al.* Potential predictive value of TP53 and KRAS mutation status for response to PD-1 blockade immunotherapy in lung adenocarcinoma. *Clin. Cancer Res.* 23, 3012-3024 (2016).
8. Fehrenbacher, L. *et al.* Atezolizumab versus docetaxel for patients with previously treated non-small-cell lung cancer (POPLAR): a multicentre, open-label, phase 2 randomised controlled trial. *Lancet* 387, 1837-1846 (2016).
9. Kowanz, M. *et al.* Tumor mutation load assessed by FoundationOne (FM1) is associated with improved efficacy of atezolizumab (atezo) in patients with advanced NSCLC. *Ann. Oncol.* 27, 15-42 (2016).
10. Van Allen, E. M. *et al.* Genomic correlates of response to CTLA-4 blockade in metastatic melanoma. *Science* 350, 207-211 (2015).
11. Kim, J. M. & Chen, D. S. Immune escape to PD-L1/PD-1 blockade: seven steps to success (or failure). *Ann. Oncol.* 27, 1492-1504 (2016).
12. Heskamp, S. *et al.* Noninvasive imaging of tumor PD-L1 expression using radiolabeled anti-PD-L1 antibodies. *Cancer Res.* 75, 2928-2936 (2015).
13. Chatterjee, S. *et al.* A humanized antibody for imaging immune checkpoint ligand PD-L1 expression in tumors. *Oncotarget* 7, 10215-10227 (2016).
14. Rehman, J. A. *et al.* Quantitative and pathologist-read comparison of the heterogeneity of programmed death-ligand 1 (PD-L1) expression in non-small cell lung cancer. *Mod. Pathol.* 30, 340-349 (2017).
15. Smith, J. *et al.* Quantitative and qualitative characterization of two PD-L1 clones: SP263 and E1L3N. *Diagn. Pathol.* 11, 44 (2016).
16. McLaughlin, J. *et al.* Quantitative assessment of the heterogeneity of PD-L1 expression in non-small-cell lung cancer. *JAMA Oncol.* 2, 46-54 (2016).
17. Scheel, A. H. *et al.* Harmonized PD-L1 immunohistochemistry for pulmonary squamous-cell and adenocarcinomas. *Mod. Pathol.* 29, 1165-1172 (2016).
18. Madore, J. *et al.* PD-L1 expression in melanoma shows marked heterogeneity within and between patients: implications for anti-PD-1/PD-L1 clinical trials. *Pigment Cell. Melanoma Res.* 28, 245-253 (2015).
19. Sanmamed, M. F. & Chen, L. Inducible expression of B7-H1 (PD-L1) and its selective role in tumor site immune modulation. *Cancer J.* 20, 256-261 (2014).
20. Gniadek, T. J. *et al.* Heterogeneous expression of PD-L1 in pulmonary squamous cell carcinoma and adenocarcinoma: implications for assessment by small biopsy. *Mod. Pathol.* 30, 530-538 (2017).
21. McDermott, D. F. *et al.* Atezolizumab, an anti-programmed death-ligand 1 antibody, in metastatic renal cell carcinoma: Long-term safety, clinical activity, and immune correlates from a phase Ia study. *J. Clin. Oncol.* 34, 833-842 (2016).
22. Herbst, R. S. *et al.* Predictive correlates of response to the anti-PD-L1 antibody MPDL3280A in cancer patients. *Nature* 515, 563-567 (2014).

23. Dijkers, E. C. *et al.* Biodistribution of  $^{89}\text{Zr}$ -trastuzumab and PET imaging of HER2-positive lesions in patients with metastatic breast cancer. *Clin. Pharmacol. Ther.* 87, 586-592 (2010).
24. Gaykema, S. B. *et al.*  $^{89}\text{Zr}$ -trastuzumab and  $^{89}\text{Zr}$ -bevacizumab PET to evaluate the effect of the HSP90 inhibitor NVP-AUY922 in metastatic breast cancer patients. *Clin. Cancer Res.* 20, 3945-3954 (2014).
25. Lamberts, T. E. *et al.* ImmunoPET with anti-mesothelin antibody in patients with pancreatic and ovarian cancer before anti-mesothelin antibody-drug conjugate treatment. *Clin. Cancer Res.* 22, 1642-1652 (2016).
26. den Hollander, M. W. *et al.* TGF- $\beta$  antibody uptake in recurrent high-grade glioma imaged with  $^{89}\text{Zr}$ -fresolimumab PET. *J. Nucl. Med.* 56, 1310-1314 (2015).
27. Ogembo, J. G. *et al.* SIRP $\alpha$  and FHOD1 are unique markers of littoral cells, a recently evolved major cell population of red pulp of human spleen. *J. Immunol.* 188, 4496-4505 (2012).
28. Fullerton, J. N. & Gilroy, D. W. Resolution of inflammation: a new therapeutic frontier. *Nat. Rev. Drug Discov.* 15, 551-567 (2016).
29. Johnson, D. B., Rioth, M. J. & Horn, L. Immune checkpoint inhibitors in NSCLC. *Curr. Treat. Options Oncol.* 15, 658-669 (2014).
30. Powles, T. *et al.* MPDL3280A (anti-PD-L1) treatment leads to clinical activity in metastatic bladder cancer. *Nature* 515, 558-562 (2014).
31. Petrylak, D. P. *et al.* Atezolizumab (MPDL3280A) monotherapy for patients with metastatic urothelial cancer: long-term outcomes from a phase 1 study. *JAMA Oncol.* 4, 537-544 (2018).
32. Emens, L. *et al.* Inhibition of PD-L1 by MPDL3280A leads to clinical activity in patients with metastatic triple-negative breast cancer (TNBC). *Cancer Res.* 75, (suppl 15, abstr 2859) (2015).

## METHODS

### Patient population

Patients eligible for the study had histologically or cytologically documented locally advanced or metastatic bladder cancer, NSCLC, or TNBC. They were eligible for at least second-line systemic therapy, or, in case of bladder cancer and NSCLC, showed disease progression during or within 6 months of completing platinum-based adjuvant/neoadjuvant chemotherapy. Other eligibility criteria included measurability according to RECIST 1.1<sup>33</sup>, presence of a tumor lesion from which a biopsy could safely be obtained, age  $\geq$  18 years, written informed consent, Eastern Cooperative Oncology Group performance status of 0-1, and adequate hematologic and end-organ function. Exclusion criteria were central nervous system disease, leptomeningeal disease, uncontrolled tumor-related pain, effusion/ascites, hypercalcemia, hypoalbuminemia, HIV infection, active tuberculosis, hepatitis B or C infections, current or recent severe infections, other significant concomitant diseases including autoimmune diseases, recent treatment with systemic immunosuppressive or immunostimulatory medication, and prior treatment with CD137 agonists or immune checkpoint inhibitors.

The imaging and treatment studies were performed in compliance with all relevant ethical regulations. Both studies were approved by the Medical Ethical Committee of the University Medical Center Groningen (UMCG) and the Central Committee on Research Involving Human Subjects, and registered individually (ClinicalTrials.gov Identifiers NCT02453984 and NCT02478099). All patients provided written informed consent.

### Study design

This single-center, open-label, imaging study was performed together with a companion atezolizumab treatment study at the UMCG, the Netherlands.

Patients received 10 mg unlabeled atezolizumab followed by 37 MBq (1 mCi) zirconium-89 (<sup>89</sup>Zr)-atezolizumab (~ 1 mg antibody) intravenously. Previous pharmacokinetic studies showed that atezolizumab has dose-dependent kinetics.<sup>22, 34</sup> Therefore, to reduce fast atezolizumab clearance, the additional unlabeled protein dose was added. In the first cohort of patients, <sup>89</sup>Zr-atezolizumab injection was followed by four PET scans at 1 h and at 2, 4 and 7 days postinjection ( $\pm$  1 day). In the subsequent cohort, imaging was performed using the optimal schedule determined in the first cohort of patients. We considered the unlabeled antibody dose to be sufficient when the circulating amount of radioactivity on day 4 after <sup>89</sup>Zr-atezolizumab administration was comparable with other <sup>89</sup>Zr-monoclonal antibodies with well-known kinetics over time.<sup>23-26</sup> The optimal time point for PET scanning was determined by analyzing tumor tracer uptake and the available amount of radioactivity in the circulation.

After  $^{89}\text{Zr}$ -atezolizumab administration, patients were observed for at least 1 h for infusion-related reactions. All PET scans were performed in combination with a low-dose computerized tomography (CT) scan for attenuation correction and anatomic reference with a Biograph mCT 64-slice PET/CT camera or a Biograph mCT 40-slice PET/CT camera (both Siemens). Within 7 days of the last PET scan, a tumor biopsy was obtained, after which 1,200 mg i.v. atezolizumab monotherapy was administered on a three-weekly schedule. Diagnostic CT scans were performed at baseline within 14 days before tracer injection and every 6 weeks ( $\pm 3$  days) after the start of atezolizumab treatment, or if clinically indicated.

### $^{89}\text{Zr}$ -atezolizumab production and *in vivo* stability

$^{89}\text{Zr}$ -atezolizumab was produced at the UMCG according to good manufacturing practice guidelines, as described earlier.<sup>35,36</sup> Quality control methods and manufacturing processes were validated before the start of clinical manufacturing. Stability testing was performed on both the conjugated intermediate and the  $^{89}\text{Zr}$ -atezolizumab drug product. Release testing included size-exclusion high-performance liquid chromatography analysis for protein concentration and presence of aggregates, radiochemical purity testing, and an immunoreactivity assay to determine specific binding to PD-L1.  $^{89}\text{Zr}$ -atezolizumab was produced with a specific activity of 37 MBq/mg, a radiochemical yield of  $> 60\%$ , and a radiochemical purity of  $> 95\%$ . The immunoreactivity of  $^{89}\text{Zr}$ -atezolizumab was determined in a competitive binding assay with unlabeled atezolizumab as described earlier.<sup>37</sup> PD-L1 extracellular domain was used as a target. Unlabeled atezolizumab was added in a logarithmic concentration range of 0.5 ng/mL – 2 mg/mL, while  $^{89}\text{Zr}$ -atezolizumab was added with a fixed concentration of 1,000 ng/mL. The acceptance limit for immunoreactivity was  $> 70\%$ .

To determine the stability of  $^{89}\text{Zr}$ -atezolizumab *in vivo*, a small subset of patients' serum samples obtained 2, 4 and 7 days postinjection were analyzed by sodium dodecyl sulfate polyacrylamide gel electrophoresis followed by phosphor imaging analysis. The fractions of bound  $^{89}\text{Zr}$ -atezolizumab and free  $^{89}\text{Zr}$  were calculated as a percentage of total radioactivity detected.  $^{89}\text{Zr}$ -atezolizumab stored in saline at 2-8°C served as positive control.

### $^{89}\text{Zr}$ -atezolizumab PET

PET acquisition was dependent on the moment of scanning: 1 h after tracer injection a total body scan with up to 15 bed positions and 1.5 min per bed position was performed. At 2 and 4 days postinjection, head to upper thigh was scanned in up to 9 bed positions with 5 min per bed position and the legs in up to 6 bed positions with 2 min per bed position. For the first four subjects, on day 7 the head to upper thigh images were performed with up to 9 bed positions with 10 min per bed position and the legs in up to 6 bed positions with 4 min per bed

position. To account for the lower count rate at day 7 and to increase image quality, subsequent patients were imaged with up to 8 bed positions with 15 min per bed position. All PET images were reconstructed using the reconstruction algorithm recommended for multicenter <sup>89</sup>Zr-monooclonal antibody PET scan trials.<sup>38</sup>

PET image analysis was performed with the Accurate tool for volume-of-interest (VOI)-based lesion and background analysis.<sup>39</sup> Spherical VOIs with predefined sizes were drawn in the thoracic aorta, subcutaneous tissue, liver, spleen, kidney, intestine, lung, brain, bone marrow and bone cortex, and muscle to assess <sup>89</sup>Zr-atezolizumab normal organ distribution. Tumor lesions were delineated manually or with the help of automated delineation algorithms based on the baseline diagnostic CT scan. To account for partial volume effects, for all statistical analyses only non-irradiated tumor lesions larger than 2.0 cm were selected.

SUVs were calculated using the amount of injected activity, body weight and the amount of radioactivity within a VOI. We report the SUVmax for tumor lesions and the SUVmean for normal organ tracer uptake.

In addition to VOI-based analysis, tracer uptake in non-malignant lymph nodes and the tonsils was compared qualitatively with surrounding tissue uptake and with tracer uptake in the healthy liver. The lymph nodes were defined as non-malignant based on the diagnostic baseline CT scan by a dedicated radiologist, and tracer uptake was scored together with a dedicated nuclear medicine physician.

## Safety assessment

Assessment of adverse events was performed at each clinical visit and National Cancer Institute, Common Terminology Criteria for Adverse Events version 4.0 were used.<sup>40</sup>

## Pharmacokinetic assessments

Blood samples were collected for determination of tracer amount in the PBMC fraction and atezolizumab serum concentration before tracer injection, 1 h postinjection, and 2, 4 and 7 days postinjection.

Whole blood samples were collected in ethylenediaminetetraacetic acid blood tubes (BD) and fractionated into red blood compartment, plasma, and PBMC compartment by Ficoll-Paque Plus separation (GE Healthcare Life Sciences). Activity in different fractions was measured in a calibrated well-type LKB 1282 Compugamma system (LKB Wallac).

Atezolizumab serum concentration was measured by an indirect sandwich enzyme-linked immunosorbent assay (ELISA, performed by ICON Laboratory Services, Inc.). Values below the lower limit of quantification (60 ng/mL;  $n = 1$ ) were substituted by half this lower limit (that is, 30 ng/mL) before further data analysis.

### Atezolizumab internalization *in vitro*

Internalization of  $^{89}\text{Zr}$ -atezolizumab was determined in the human lung mucoepidermoid pulmonary H292 and the bronchioalveolar H358 tumor cell lines (American Type Culture Collection, NCIH292 and NCIH358, respectively).  $^{89}\text{Zr}$ -atezolizumab (50 ng) was added to  $1 \times 10^6$  cells and incubated for 1 h on ice. Thereafter, cells were washed with ice-cold phosphate-buffered saline containing 1% human serum albumin (Sanquin), and the total amount of bound activity was measured in a  $\gamma$ -counter. Next, cells were incubated for 1, 2 and 4 h at  $37^\circ\text{C}$  to allow internalization and at  $4^\circ\text{C}$  to serve as a control. After incubation, cells were washed with acidic buffer, 0.05 M glycine (Merck), 0.1 M NaCl (Merck) at pH 2.8, to remove the membrane-bound fraction. The amount of internalized activity was measured in a  $\gamma$ -counter. Internalized activity as a percentage of the total bound activity was determined. The mean standard deviation of three wells ( $n = 3$ ) was calculated using Graphpad Prism 5.0.

The assay described above, with up to 2 h incubation time, was also performed with PBMCs ( $5 \times 10^6$  cells) freshly isolated from buffy coat pooled from healthy volunteers, as well as T cells ( $5 \times 10^6$  cells) isolated from PBMCs expanded with recombinant human interleukin-2 (100 U/mL, Novartis Pharma B.V.), anti-CD3 (0.5  $\mu\text{g}/\text{mL}$ , R&D Systems) and anti-CD28 (2  $\mu\text{g}/\text{mL}$ , R&D Systems) for 3 days. Percentage of internalization was calculated as mean standard deviation of two wells ( $n = 2$ ) using Graphpad Prism 5.0.

The internalization rate was estimated by saturating the cell surface with  $^{89}\text{Zr}$ -atezolizumab at time zero and measuring the fraction of radioactivity that could no longer be displaced from the cell surface after incubation.

### Tumor biopsies and normal lymph node and spleen tissue

PD-L1 expression was assessed centrally (HistoGeneX) in post-tracer tumor biopsies using the SP142 and the SP263 IHC assays (Ventana Medical Systems) according to manufacturer staining and scoring protocols. PD-L1 staining on tumor cells (TC) and on tumor-infiltrating immune cells (IC) was evaluated. With the SP142 assays, tumors were scored as negative (IC0 or TC0: staining on  $< 1\%$  of IC or TC, respectively; IHC score 0) or positive (IC1/2/3 or TC1/2/3: staining on  $\geq 1\%$  of IC or TC; IHC score 1/2/3 depending on the highest staining for either IC or TC). With the SP263 assay, tumors were considered PD-L1-positive when the membrane of  $\geq 25\%$  of tumor cells stained for PD-L1 at any intensity.

Infiltration and localization of CD8-positive T cells was assessed using the clone C8/144B (Dako) to characterize histopathologically pre-existing immunity of these tumors. Tumors were classified as immunological deserts if intra-tumoral stroma areas or intra-epithelial areas contained either no or few CD8<sup>+</sup> T cells, inflamed if  $\geq 5\%$  of the intra-epithelial area was covered by CD8<sup>+</sup> T cells of intermediate density, or heterogeneous in case of any CD8 coverage in between.

Lymph node and spleen tissue, originating from spare healthy tissue not obtained from the study population, was also stained for PD-L1 and CD8 as described above to correlate with <sup>89</sup>Zr-atezolizumab uptake in these tissues.

To reveal tracer distribution at the microscopic level, formalin-fixed tumor sections (10 μM) of post-tracer tumor biopsies of two patients were exposed to a phosphor imaging screen for 72 h, and were then scanned with a Cyclone phosphor imager. Subsequent sections of the same tumor tissue were stained for hematoxylin and eosin, PD-L1 and CD8.

RNA from post-tracer tumor biopsies was isolated for gene expression analysis by TruSeq RNA Access RNA-seq (Q2Labsolutions).

PD-L1 IHC results were related to tumor SUVmax and clinical efficacy. Histopathological immune phenotypes and RNA expression levels (in reads per kilobase per million, RPKM) of interferon γ, chemokine ligand 9, granzyme B, CD8, and PD-L1, including combined T effector signature, were related to tumor SUVmax in an exploratory manner.

## Data analysis

Results presented here had a clinical cutoff date of 1 June 2018.

### *Pharmacokinetic analyses and biodistribution*

We evaluated the changes in atezolizumab concentration with time postinjection using linear mixed effect models taking clustering within patients, and if applicable within tumors, into account as random effects, and with days postinjection as fixed effect. Atezolizumab concentration was analyzed as measured by ELISA in serum, and by PET using the following parameters: the <sup>89</sup>Zr-atezolizumab SUVmean in healthy tissues, the <sup>89</sup>Zr-atezolizumab SUVmax in tumor lesions, and the tumor-to-background ratio (<sup>89</sup>Zr-atezolizumab tumor SUVmax divided by background SUVmean). We only evaluated tumor-to-background ratio changes in time for all tumors combined (compared with blood), and for lung and bone metastases (compared with healthy lung and bone marrow, respectively), as other tumor sites had too few data points for meaningful evaluation. Similarly, we only evaluated SUVmax changes over time according to tumor type for NSCLC and bladder cancer patients, as all TNBC patients underwent only two PET scans.

ELISA, SUVmax, and tumor-to-background values were natural log-transformed before analysis to improve model fit, as these data were substantially right-skewed. Using back-transformation, results of such models consequently yield estimates of geometric mean values of the response variable, and model coefficients can be expressed as the percentage change in the response variable per unit increase in the explanatory variable. We analyzed time postinjection as a categorical variable, resulting in estimates of the (geometric) mean atezolizumab concentration

per day, as well as continuously, resulting in time-concentration curves. To assess potential non-linear relationships between time since tracer injection and the various tracer concentration measures, we evaluated time in days without transformation (linear), and also by adding a natural logarithmic (log-linear) or a quadratic term (parabolic curve) for time to the models. We then used the Akaike Information Criterion of each model to select the best representation of the data. The relationship between tumor SUVmax values at day 4 and day 7 was also assessed with a mixed effect model, and by estimating the Pearson's correlation coefficient extended to clustered data, following natural log-transformation of both variables to obtain approximate normal distributions. We evaluated the correlation between ELISA-derived atezolizumab concentration (ng/mL, corrected for hematocrit) and PET derived atezolizumab concentration (ng/mL) in a similar way. The PET-derived atezolizumab concentration was interpolated by multiplying the SUVmean of the aorta with the injected total antibody mass averaged for body weight.

### ***Tumor tracer uptake across and within patients***

These analyses were based solely on day 7 postinjection tracer uptake measurements, as SUVmax of day 4 and day 7 were highly correlated. We first estimated the geometric mean SUVmax across all tumors taking between-patient heterogeneity into account using an intercept-only linear mixed effect model with patient as random effect, and natural log-transformed SUVmax as response variable. Then, to provide insight in the heterogeneity of  $^{89}\text{Zr}$ -atezolizumab uptake, we plotted the SUVmax of each tumor lesion, grouped per tumor type and ordered by increasing geometric mean SUVmax per patient, also visualizing tumor size and site, and with blood pool background uptake (SUVmean) as a reference. To further assess the within-patient heterogeneity in tracer uptake for patients with at least one tumor site, we assessed the relative difference per patient between the tumor sites with highest versus lowest uptake, as well as the coefficient of variation (that is, the standard deviation divided by the mean SUVmax of all tumor sites per patient after natural log-transformation, expressed as a percentage). We used linear mixed effect models with patient as a random effect to evaluate whether the geometric mean SUVmax differed according to tumor organ site and according to the primary tumor type, separately.

### ***Tumor tracer uptake compared with biopsy-derived molecular analyses***

First we evaluated the agreement between the SP142 and SP263 IHC analysis of PD-L1 expression in tumor biopsies by constructing confusion matrices (overall and according to tumor type) and by estimating kappa statistics.

Next, we assessed the association between SP142, SP263, and immune phenotype levels with day 7 postinjection  $^{89}\text{Zr}$ -atezolizumab SUVmax of the same lesions using independent samples *t*-tests and ordinary linear regression to test for a trend in increasing tracer uptake with increasing SP142 IHC levels (that is, fitted as a continuous variable coded 0, 1, or 2). These

analyses were conducted after natural log-transformation of SUVmax, thus yielding estimates of geometric means following back-transformation of the results.

We also compared the relationship between RNA sequencing-derived estimates of CD8, granzyme B, interferon  $\gamma$ , and chemokine ligand 9 gene-expression levels, as well as a combined 'T effector signature' (that is, the per biopsy average of the previous individual gene-expression levels) with day 7 postinjection <sup>89</sup>Zr-atezolizumab SUVmax. For this, RNA-sequencing data (in reads per kilobase per million) and SUVmax were natural log-transformed to achieve approximate normality before analysis by linear regression and before estimating the Pearson's and Spearman's correlation coefficients (the latter to also include a more robust correlation measure in view of the small number of data points (< 30) for these analyses).

### ***Clinical outcome***

Clinical outcome was evaluated in several ways. At a patient level, we evaluated the best-achieved RECIST response category, the best percentage change in sum of largest diameters (SLD) of target lesions, and the PFS and OS. We first used general descriptive methods to summarize clinical outcome including a swimmers plot, the median time of follow-up (assessed in patients still without progression at data cutoff), and the median time to progression. Next, we assessed the relationship between <sup>89</sup>Zr-atezolizumab SUVmax at day 7 and clinical outcome. For these analyses, SUVmax was first natural log-transformed and the results are thus reported as geometric means, or percentage changes in the average SUVmax. We specifically decided to summarize <sup>89</sup>Zr-atezolizumab uptake per patient as geometric mean SUVmax beforehand, and refrained from evaluating different <sup>89</sup>Zr-atezolizumab uptake features per patient to prevent overoptimistic results due to evaluating many features in a small dataset.

The relationship between best RECIST response categories and tumor lesion SUVmax was assessed by a linear-mixed model accounting for within-patient clustering by a random intercept, and by evaluating best RECIST response both categorically and continuously (that is, as a 0, 1, 2, 3 variable). When modeled continuously to test for a trend, we evaluated not only a linear fit, but also the addition of a natural logarithmic or a quadratic term, and used the Akaike information criterion to select the best representation of the data. The relationship between per patient geometric mean SUVmax and change over time in SLD was visualized by a spaghetti plot, whereas tracer uptake in relation to best percentage change in SLD of target lesions was visualized using a waterfall plot and further analyzed by linear regression and estimating the Pearson's correlation coefficient. The relationship between per patient geometric mean SUVmax and PFS and OS was explored by Kaplan-Meier survival plots, binning patients in a below-median and above-median geometric mean SUVmax group, and testing for survival differences using the log-rank test. We further quantified the relationship between these high and low tracer uptake patient groups by fitting Cox regression models (with Firth's

penalization to account for small sample bias) yielding hazard ratios for progressive disease and/or death. We decided a priori to bin patients at the median to achieve two equally sized groups to compare, and we refrained from exploring other/optimal thresholds in tracer uptake as the small dataset precluded meaningful threshold finding. In addition to binning, we also evaluated the relationship between PFS and OS and geometric mean SUVmax per patient continuously, again using Firth's penalized Cox regression models, and expressing the results per standard deviation change in SUVmax (assuming a log-linear relationship as the dataset was deemed too small to properly evaluate departure from linearity).

To evaluate to what extent observed relationships between tracer uptake and clinical outcome could be explained by differences between patients in tumor types and tumor load, we also adjusted for these variables by including them in the various regression and mixed regression models (tumor type categorically, tumor load – the number of tumor lesions with SUVmax data per patient – linearly). As the number of events for the survival analyses was rather small to estimate robust effects of these potential confounders together with tracer uptake in one model, we alternatively also adjusted the relationship between tracer uptake and PFS and OS by means of an inverse probability weighting (IPW) procedure based on propensity scores<sup>41</sup>, which may be statistically more efficient in small datasets. In this two-step procedure, first the predicted probability (that is, the propensity score) of belonging to the below- or above-median geometric mean SUVmax group was estimated by a logistic regression model containing the potential confounders, resulting in a weight for each patient by taking the reciprocal of this probability (that is, the IPW); in the second step, a regular Cox regression model for PFS or OS was used with only tracer uptake group as the explanatory variable while weighting patients by their IPW, thereby adjusting the association between tracer uptake and PFS or OS for the potential confounders. We performed these survival analyses in the entire study group and separately in a subgroup while excluding the breast cancer cases. This is because these cases all belonged to the below-median SUVmax group, thus prohibiting adequate adjustment for this tumor type due to collinearity. We checked whether IPW adjustment was adequate by assessing the C index of the propensity model refitted using its own weights (values close to 0.5 indicating perfect adjustment), and by comparing the confounder distribution between the groups with low and high tracer uptake following IPW.

We evaluated the ability of per patient geometric mean <sup>89</sup>Zr-atezolizumab SUVmax to discriminate between patients with complete or partial response versus stable or progressive disease as best response by estimating the area under the receiver operating characteristics curve. The C index was used to assess the ability to discriminate between patients with short and long (progression-free) survival. An area under the curve or C index of 1.0 indicates perfect discrimination and 0.5 indicates a worthless test. For these analyses, per patient geometric mean <sup>89</sup>Zr-atezolizumab SUVmax was evaluated continuously instead of binned at the median.

Similarly to the above, we also assessed the relationship between IHC-based PD-L1 expression by SP263 and SP142 antibodies and clinical outcome. As these tests were analyzed dichotomously (that is, positive or negative), their relationship with best RECIST response category was tested by the Fisher's exact test, and their relationship was tested with best percentage change in SLD by independent samples *t*-tests.

At a lesion level, we used spaghetti plots to visualize the relationship between day 7 <sup>89</sup>Zr-atezolizumab SUVmax and tumor size change during treatment. We then modeled the tumor size change during treatment as a function of baseline SUVmax using a linear mixed effect model with per-lesion percentage change in size at the various follow-up moments as response variable, time since start treatment and SUVmax as explanatory variables, and patient- and lesion-level random intercepts. Both time and SUVmax were natural log-transformed in these analyses, and a fixed effect intercept was omitted to force the regression lines through the origin (that is, a percentage change in size of 0 at time 0). We used an interaction term between time and SUVmax to test whether the change in lesion size during treatment depended on baseline SUVmax.

### ***Statistical inference***

All reported *P*-values are two-sided with a threshold for statistical significance of 5%, and estimates and measures of association are reported with 95% confidence intervals. We did not account for multiple testing due to the exploratory nature of this study, and further studies are thus needed for confirmation of the results. Analyses were performed using R software version 3.2.1 for Macintosh, specifically using the *lmer* function (libraries *lme4* version 1.1-11 and *lmerTest* version 2.0-20) for mixed effect models; the *cohen.kappa* function (library *psych* version 1.4.8) for estimating kappa statistics; the *roc* function (library *pROC* version 1.8) for estimating areas under the curves; the *survfit*, *survdiff* and *coxph* functions (library *survival* version 2.38-3) for Kaplan-Meier, log-rank, Cox regression analyses and estimating *C* indexes; and the *coxphf* function (library *coxphf* version 1.1.1) for Cox regression analyses with Firth's penalization.

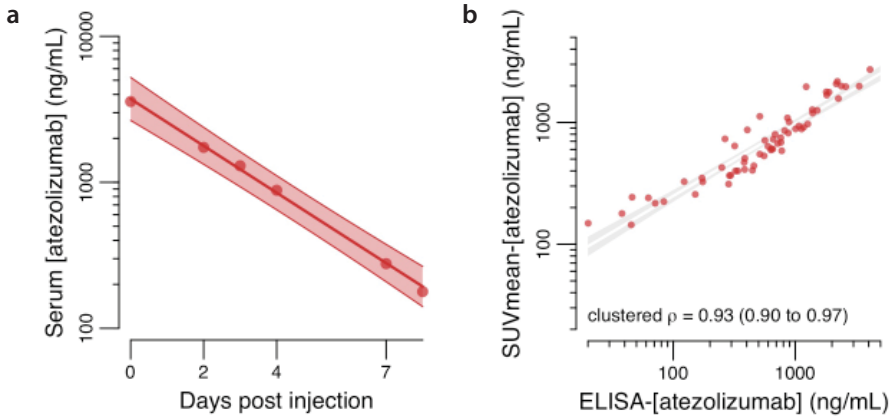
For regression analyses, we used Wald-based tests, for instance to compare different levels of a categorical variable (for example, specific tumor organ sites and primary tumor types), or likelihood-ratio-based tests to globally test the contribution of a categorical variable or test for interactions. Wald-based *P*-values of mixed effect model coefficients and 95% confidence intervals were based on Satterthwaite approximations to degrees of freedom under restricted maximum likelihood. Likelihood-ratio based *P*-values of mixed effect models were obtained under maximum likelihood.

*P*-values and 95% confidence intervals for the IPW-adjusted survival analyses were based on 4,000-fold bootstrap resampling, repeating the full two-step analysis approach within each bootstrap, and using the bootstrap percentile method for inference.

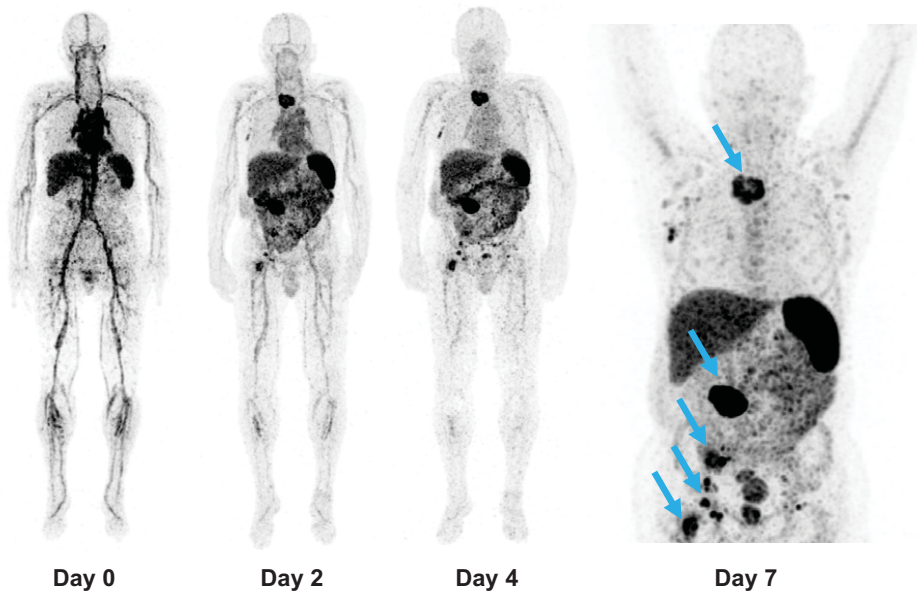
## METHODS-ONLY REFERENCES

33. Eisenhauer, E. A. *et al.* New response evaluation criteria in solid tumours: revised RECIST guideline (version 1.1). *Eur. J. Cancer* 45, 228-247 (2009).
34. Lamberts, L. E. *et al.* Antibody positron emission tomography imaging in anticancer drug development. *J. Clin. Oncol.* 33, 1491-1504 (2015).
35. Verel, I. *et al.* <sup>89</sup>Zr immuno-PET: comprehensive procedures for the production of <sup>89</sup>Zr-labeled monoclonal antibodies. *J. Nucl. Med.* 44, 1271-1281 (2003).
36. Terwisscha van Scheltinga, A. G. *et al.* ImmunoPET and biodistribution with human epidermal growth factor receptor 3 targeting antibody <sup>89</sup>Zr-RG7116. *MAbs* 6, 1051-1058 (2014).
37. Oude Munnink, T. H. *et al.* PET with the <sup>89</sup>Zr-labeled transforming growth factor-beta antibody fresolimumab in tumor models. *J. Nucl. Med.* 52, 2001-2008 (2011).
38. Makris, N. E. *et al.* Multicenter harmonization of <sup>89</sup>Zr PET/CT performance. *J. Nucl. Med.* 55, 264-267 (2014).
39. Frings, V. *et al.* Repeatability of metabolically active tumor volume measurements with FDG PET/CT in advanced gastrointestinal malignancies: a multicenter study. *Radiology* 273, 539-548 (2014).
40. National Cancer Institute. Common terminology criteria for adverse events v4.0. *NCI, NIH, DHHS.*, NIH publication # 09-7473. (2009).
41. Austin, P. C. & Stuart, E. A. Moving towards best practice when using inverse probability of treatment weighting (IPTW) using the propensity score to estimate causal treatment effects in observational studies. *Stat. Med.* 34, 3661-3679 (2015).

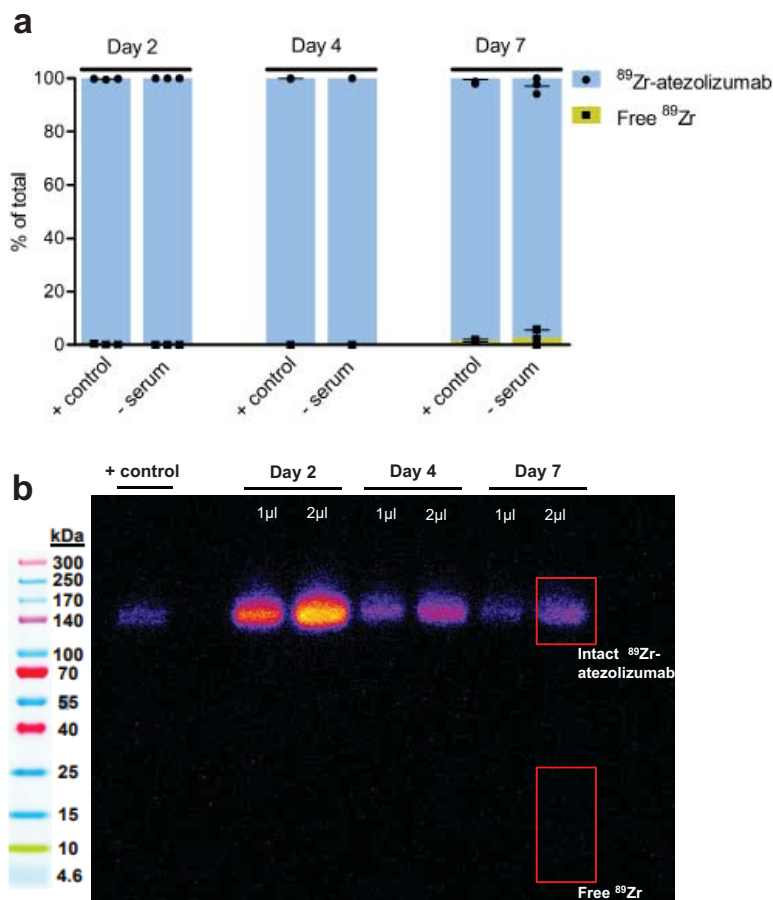
## SUPPLEMENTARY MATERIAL



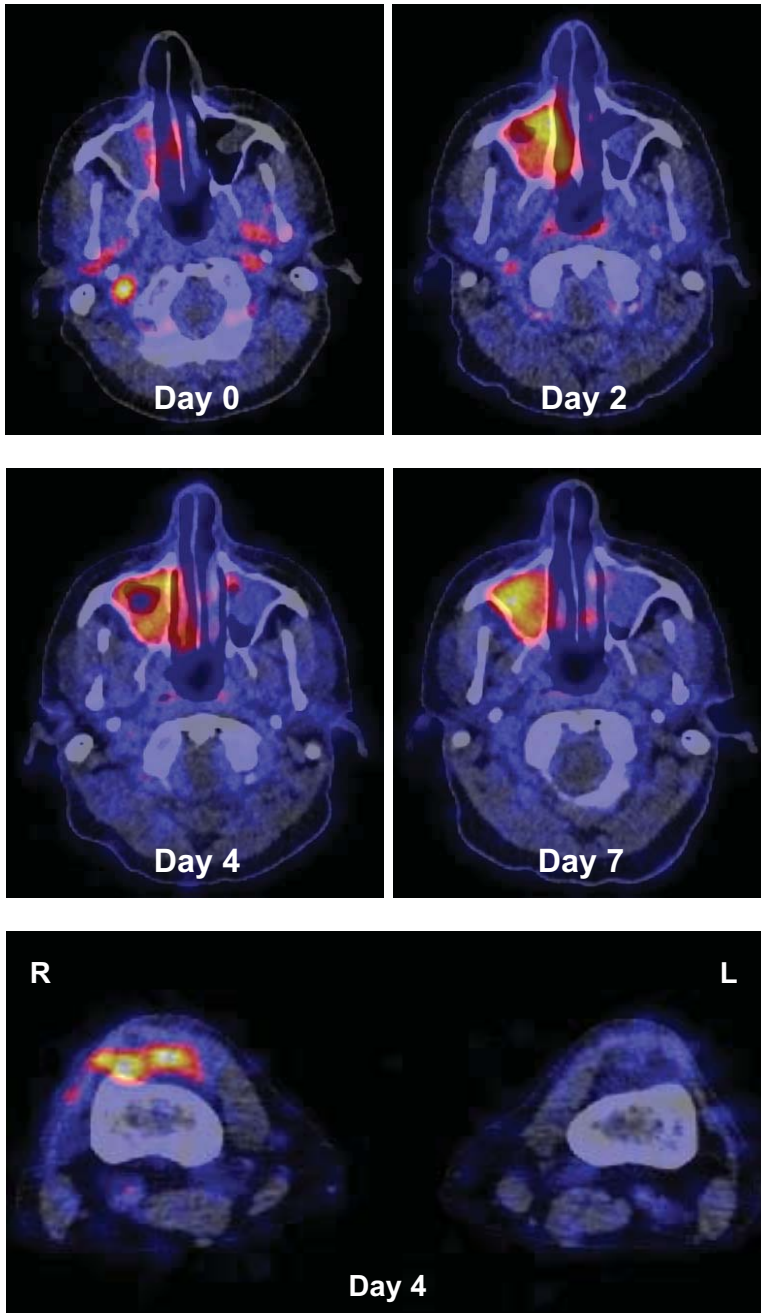
**Supplementary Figure 1** Atezolizumab pharmacokinetics. **(a)** Atezolizumab serum concentration (ng/mL) over time plotted as geometric means per time point, including fitted regression line with 95% CI based on a linear mixed effect model with 62 measurements from 22 patients. **(b)** Scatter plot of PET derived atezolizumab concentration and ELISA derived atezolizumab serum concentration (both ng/mL) and regression line with 95% CI based on a linear mixed effect model with 62 measurements from 22 patients;  $\rho$ : Pearson's correlation coefficient extended to clustered data with 95% CI.



**Supplementary Figure 2** <sup>89</sup>Zr-atezolizumab biodistribution. Representative PET images (maximum intensity projections) of a patient one hour post tracer injection, and at days 2, 4 and 7. Multiple bone lesions, malignant inguinal and mediastinal lymphadenopathy and a big abdominal wall metastasis are indicated with blue arrows on the last PET scan 7 days postinjection (PET scans were performed once per patient and time point).

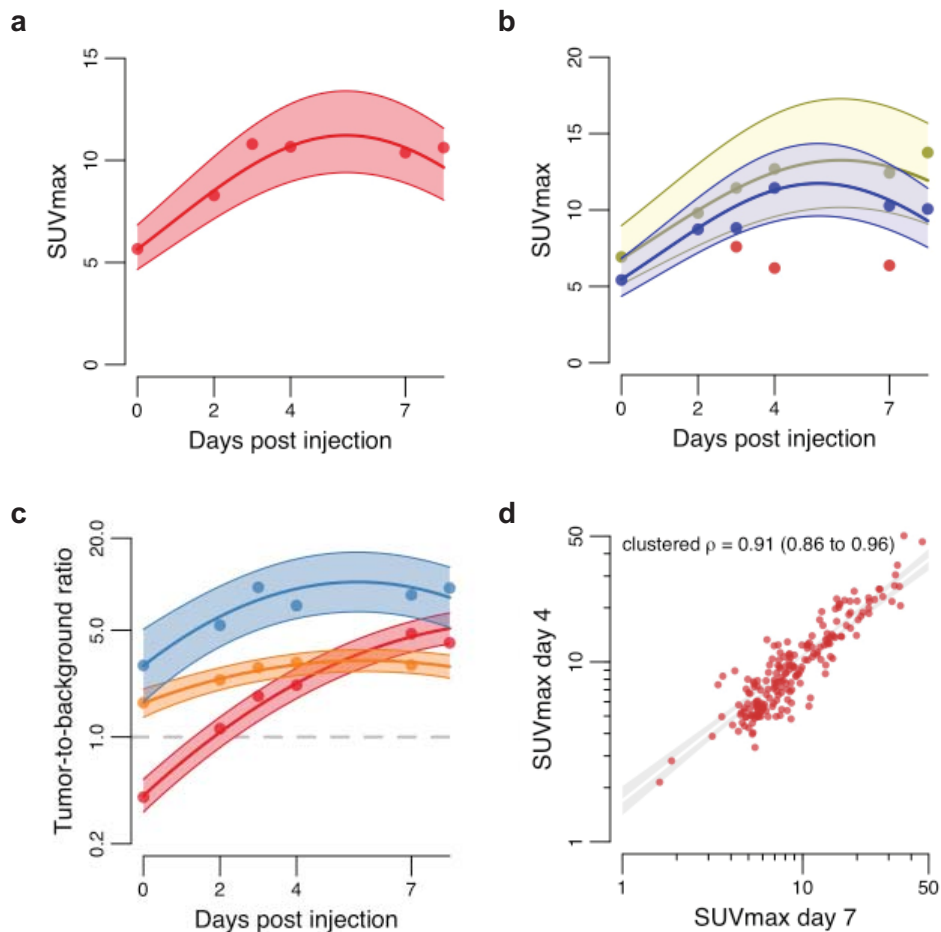


**Supplementary Figure 3** Intactness of  $^{89}\text{Zr}$ -atezolizumab over time. **(a)** Stability of  $^{89}\text{Zr}$ -atezolizumab determined by SDS-PAGE in patients' blood samples drawn 2, 4 and 7 days postinjection ( $n = 3$  biologically independent samples). Positive control (+ control) is  $^{89}\text{Zr}$ -atezolizumab stored at 2-8°C. Mean with error bars indicating standard deviation. **(b)** Representative example of an SDS-PAGE (SDS-PAGE was performed once per sample).

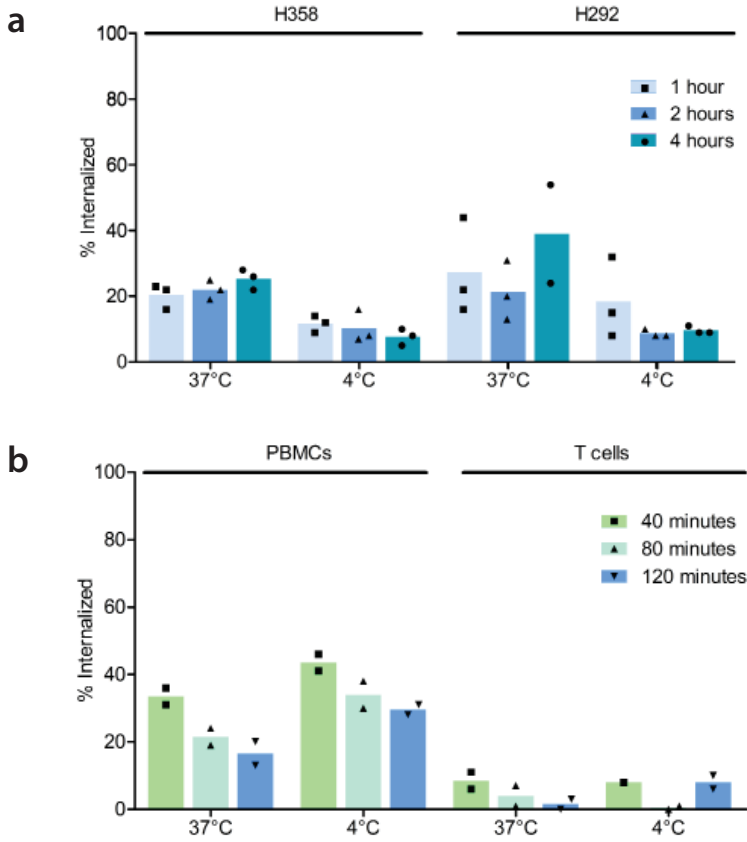


6

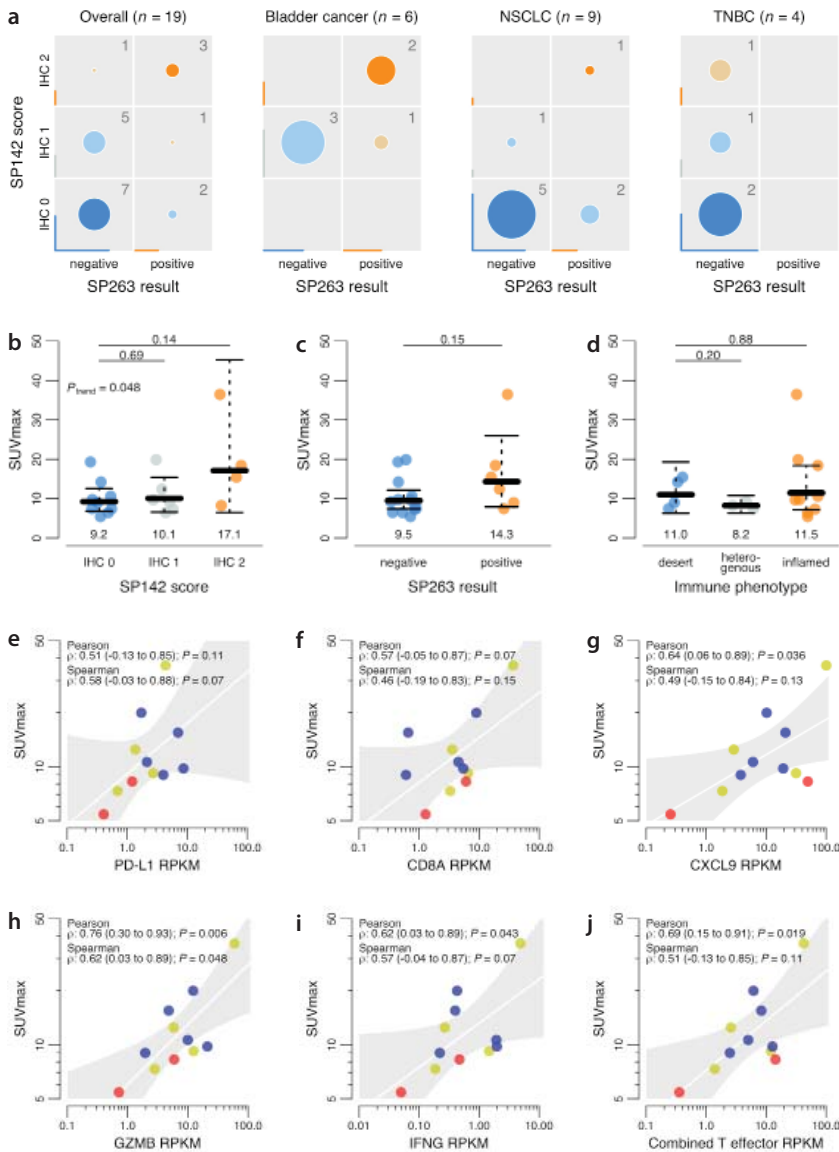
**Supplementary Figure 4** <sup>89</sup>Zr-atezolizumab uptake in sites of inflammation. Upper and middle panel show transversal PET/LD CT images of a patient with chronic sinusitis with increasing tracer uptake over time. Lower panel shows increased tracer uptake in a patient with bursitis of the right knee on day 4 after tracer injection (days 0 and 2 not scanned; knees were not in the field of view on day 7; PET scans were performed once per patient and time point).



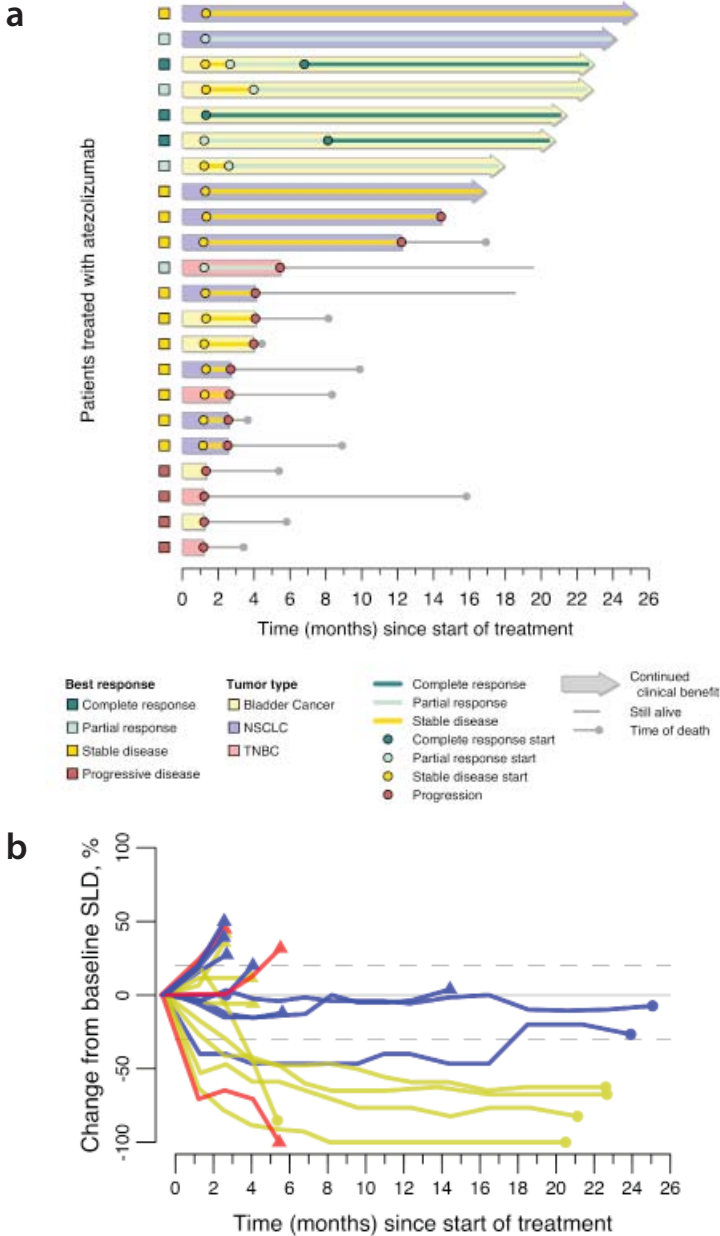
**Supplementary Figure 5**  $^{89}\text{Zr}$ -atezolizumab tumor uptake. **(a)** Relation between time post tracer injection and tumor SUVmax ( $n = 196$  in 22 patients) plotted as geometric mean per time point, including fitted regression line with 95% CI. **(b)** Relation between time post tracer injection and tumor SUVmax for bladder cancer (yellow,  $n = 85$  in 9 patients) and NSCLC (blue,  $n = 43$  in 9 patients) separately plotted as geometric mean per time point, including fitted regression line with 95% CI. For TNBC (red,  $n = 68$  in four patients) no time-activity curve was included as all four patients were only scanned at two time points, prohibiting curve-estimation. **(c)** Relation between time post tracer injection and tumor-to-background ratio of lung metastases (blue,  $n = 44$  in 10 patients) and bone metastases (orange,  $n = 62$  in 9 patients), as well as tumor-to-blood ratio (red,  $n = 196$  in 22 patients) plotted as geometric mean per time point, including fitted regression line with 95% CI. **(d)** Scatter plot of SUVmax day 4 and SUVmax day 7 and regression line with 95% CI based on a linear mixed effect model with 196 measurements from 22 patients;  $\rho$ : Pearson's correlation coefficient extended to clustered data with 95% CI.



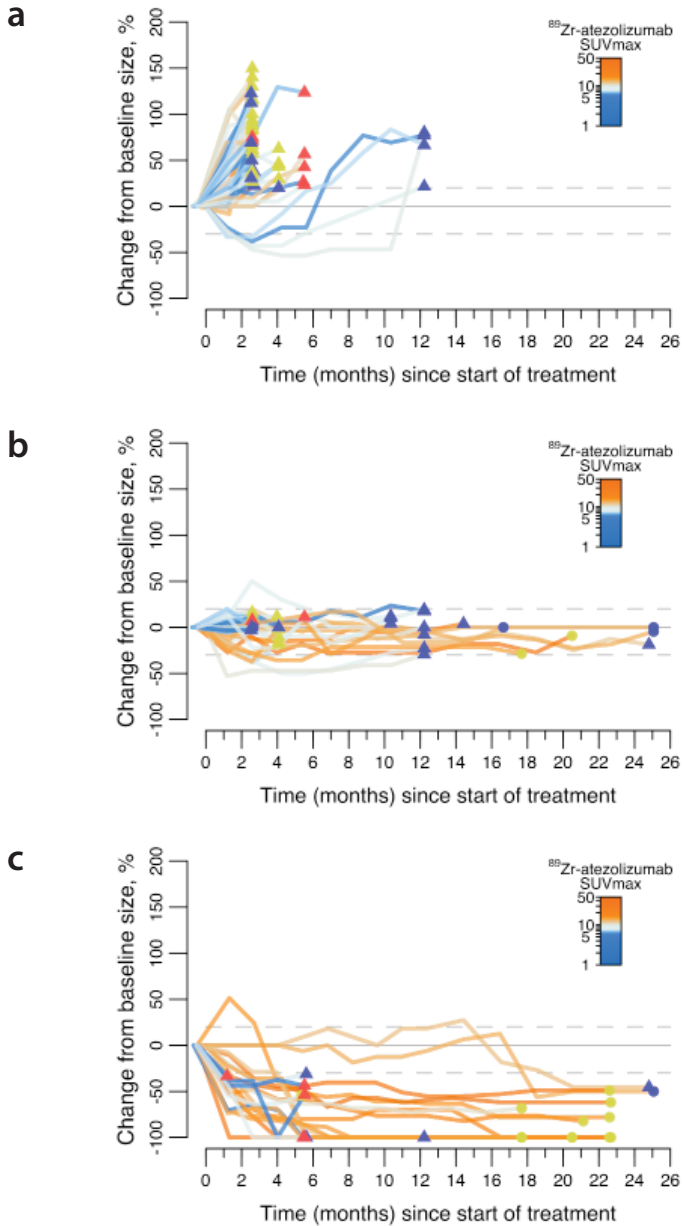
**Supplementary Figure 6** Internalization of <sup>89</sup>Zr-atezolizumab over time. **(a)** Internalization of <sup>89</sup>Zr-atezolizumab *in vitro* by H292 and H358 tumor cells (*n* = 3 replicate wells). **(b)** Internalization of <sup>89</sup>Zr-atezolizumab *in vitro* by human peripheral blood mononuclear cells (PBMCs) and T cells of healthy volunteers (*n* = 2 replicate wells).



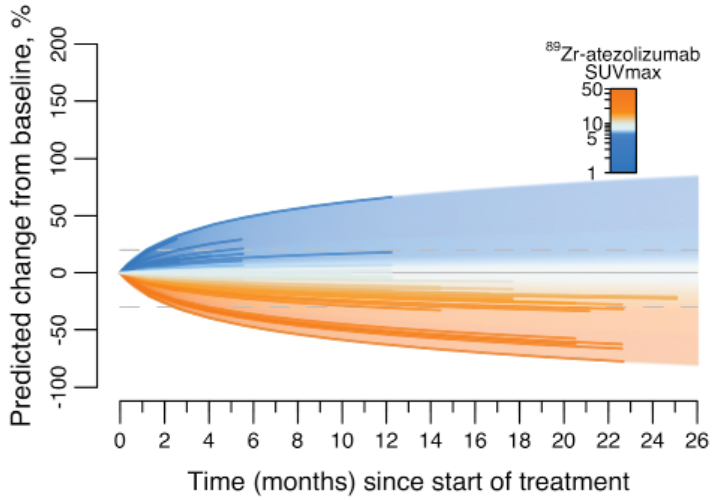
**Supplementary Figure 7** Relation of IHC, immune phenotypes, PD-L1 and T effector gene expression levels with  $^{89}\text{Zr}$ -atezolizumab tumor uptake. **(a)** Confusion matrix of the agreement in IHC results between the two tested PD-L1 antibodies, overall and according to cancer type (size of circles corresponds with the relative distribution in each panel; marginal horizontal and vertical lines show the distribution per antibody). **(b-c)** Relationship between PD-L1 IHC (**(b)** SP142, **(c)** SP263;  $n = 19$  biologically independent samples) or **(d)** immune phenotype based on IHC ( $n = 16$  biologically independent samples) of biopsied lesions and  $^{89}\text{Zr}$ -atezolizumab uptake on day 7 postinjection of the respective lesion. Data is summarized as geometric mean SUVmax with 95% CI as error bars; two-sided  $P$ -values shown on top are derived from independent-samples  $t$ -tests, and the  $p$  for trend by linear regression. **(e-j)** Pearson's and Spearman's rank correlation (95% CI) of PD-L1 **(e)** and gene expression levels of CD8 **(f)**, chemokine ligand 9 **(g)**, granzyme B **(h)**, interferon gamma **(i)** and combined T effector signature **(j)** with  $^{89}\text{Zr}$ -atezolizumab uptake of the biopsied lesion ( $n = 11$  biologically independent samples); RPKM, reads per kilobase per million; red, TNBC; blue, NSCLC; yellow, bladder cancer.



**Supplementary Figure 8** Response to atezolizumab monotherapy. **(a)** Swimmers plot of the 22 evaluable patients. **(b)** Change in baseline sum of diameters (SLD; longest for non-nodal lesions, short axis for nodal lesions) per patient over time with dashed gray reference lines at +20% and -30% change from baseline SLD. The circle or triangle at the end of the line represents ongoing tumor response or progressive disease, respectively, at the last available moment of information regarding SLD (not necessarily corresponding with actual PD date). Line color represents the tumor type (red, TNBC; blue, NSCLC; yellow, bladder cancer). At the data cut-off date of June 1 2018 seven patients were still in follow-up: four of them were still on treatment, two were discontinued from treatment after 2 years and have an ongoing response, and one patient discontinued treatment despite clinical benefit due to side effects.



**Supplementary Figure 9** Spaghetti plots at lesion level grouped for tumor response per lesion. Change in baseline diameter of single lesions (measured on CT; longest for non-nodal lesions, short axis for nodal lesions; diameter > 20 mm) over time ( $n = 651$  measurements from 107 metastases in 21 patients). Lines are color coded based on  $^{89}\text{Zr}$ -atezolizumab uptake (SUVmax). The circle or triangle at the end of the line represents ongoing tumor response or progressive disease, respectively, at the last available moment of patient based information regarding SLD, and the color represents the tumor type (red, TNBC; blue, NSCLC; yellow, bladder cancer). Lesions are grouped based on percent change in diameter from baseline compared to last measurement (**(a)**  $\geq 20\%$ ; **(b)**  $> -30\%$  and  $< 20\%$ ; **(c)**  $\leq -30\%$ ) with dashed gray reference lines at  $+20\%$  and  $-30\%$  change from baseline diameter.



**Supplementary Figure 10** Individual lesion's response to treatment. Graphical results of a linear mixed effect model showing the relation of percent change from baseline size over time and baseline SUVmax ( $n = 651$  measurements from 107 tumor lesions in 21 patients). The colored lines are predicted trajectories of actual lesions measured in the study for the duration of their actual observation, and the gradient filled area is a continuous representation of the model.

**Supplementary Table 1 Demographics and disease characteristics of evaluable patients (*n* = 22) at study entry**

	All <i>n</i> = 22	Geometric mean SUVmax below median <i>n</i> = 11	Geometric mean SUVmax above median <i>n</i> = 11
Median age, years (range)	62.5 (40-76)	60 (42-71)	63 (40-76)
Sex, <i>n</i> (%)			
Male	13 (59)	5 (45)	8 (73)
Female	9 (41)	6 (55)	3 (27)
Primary tumor, <i>n</i> (%)			
BC	9 (41)	3 (27)	6 (55)
TNBC	4 (18)	4 (36)	0 (0)
NSCLC	9 (41)	4 (36)	5 (46)
ECOG performance status, <i>n</i> (%)			
0	14 (64)	7 (64)	7 (64)
1	8 (36)	4 (36)	4 (36)
Number of metastases, <i>n</i>			
Median (min-max)	4 (1-50)	5 (2-50)	3 (1-24)
Mean (SD)	8.9 (11.9)	12.2 (15.1)	5.6 (6.7)
Number of previous systemic regimens in the locally advanced or metastatic setting, <i>n</i> (%)			
1	15 (68)		
2	6 (27)		
≥ 3	1 (5)		

BC, Bladder cancer. TNBC, Triple-negative breast cancer. NSCLC, Non-small cell lung cancer. ECOG, Eastern Cooperative Oncology Group. SUV, Standard uptake value.

**Supplementary Table 2 <sup>89</sup>Zr-atezolizumab and atezolizumab treatment-related adverse events in 22 evaluable patients**

Tracer*		No. (%) of events	
		Any grade	Grade 3**
Tracer*	Pruritus	1 (100)	-
Atezolizumab	Alanine aminotransferase increased	2 (2)	-
	Alkaline phosphatase increased	1 (1)	-
	Alopecia	1 (1)	-
	Aspartate aminotransferase increased	3 (3)	-
	Anorexia	1 (1)	-
	Arthralgia	3 (3)	-
	Chills	1 (1)	-
	Diarrhea	3 (3)	-
	Dizziness	1 (1)	-
	Dry eyes	1 (1)	-
	Dry mouth	1 (1)	-
	Dry skin	4 (5)	-
	Edema	3 (3)	-
	QT corrected interval prolonged	1 (1)	-
	Fatigue	4 (5)	-
	Flatulence	1 (1)	-
	Flu like symptoms	2 (2)	-
	Hyperthyroidism	4 (5)	-
	Hypothyroidism	2 (2)	-
	Gammaglutamyltransferase increased	9 (10)	-
	Infusion related reaction	4 (5)	1 (1)
	Insomnia	2 (2)	-
	Myalgia	4 (5)	-
	Nausea	1 (1)	-
	Pain in extremity	7 (8)	-
	Paresthesia	2 (2)	-
	Platelet count decreased	1 (1)	-
	Pneumonitis	1 (1)	-
	Pruritus	9 (10)	-
	Rash	7 (8)	-

AE, Adverse event. \* Tracer comprises <sup>89</sup>Zr-labeled and unlabeled atezolizumab. \*\* No grade 4 events were observed. No, number.

**Supplementary Table 3 Response rate per tumor type**

Tumor type (n)	CR (n)	PR (n)	SD (n)	PD (n)	ORR (%)
BC (9)	3	2	2	2	56
NSCLC (9)	0	1	8	0	11
TNBC (4)	0	1	1	2	25

BC, Bladder cancer. NSCLC, Non-small cell lung cancer. TNBC, Triple-negative breast cancer. CR, Complete response. PR, Partial response. SD, Stable disease. PD, Progressive disease. ORR, Objective response rate.

**Supplementary Table 4 Adjustment for tumor type and tumor load**

1. Results of linear mixed-models with random intercept per patient relating best RECIST response to SUVmax with various levels of adjustment ( $n = 22$  patients with 196 lesions):

Best RECIST response	Unadjusted			Adjusted for tumor type		
	% Difference in SUVmax	95% CI	<i>P</i>	% Difference in SUVmax	95% CI	<i>P</i>
PD	Reference	-	-	Reference	-	-
SD	41	-4 to 106	0.073	15	-26 to 79	0.49
PR	78	11 to 186	0.020	61	3 to 150	0.038
CR	235	98 to 467	0.00021	175	64 to 364	0.0013
Per category increase	45	24 to 69	2.24e <sup>-05</sup>	37	18 to 60	4.68e <sup>-05</sup>

Best RECIST response	Adjusted for tumor type and number of lesions			Adjusted for tumor type, number of lesions, lesion localization, VOI size		
	% Difference in SUVmax	95% CI	<i>P</i>	% Difference in SUVmax	95% CI	<i>P</i>
PD	Reference	-	-	Reference	-	-
SD	10	-33 to 81	0.68	3	-35 to 61	0.91
PR	53	-9 to 157	0.10	44	-10 to 130	0.12
CR	169	54 to 369	0.0025	110	26 to 249	0.0077
Per category increase	38	16 to 63	7.08e <sup>-05</sup>	28	10 to 50	0.00031

2. Results of relation between doubling in SUVmax and best percent change in SLD with various levels of adjustment by linear regression ( $n = 21$  patients):

Model	Estimate	95% CI	<i>P</i>
Unadjusted	-34	-61 to 9	0.010
Adjusted for tumor type	-41	-68 to -13	0.0060
Adjusted for tumor type and number of lesions	-41	-70 to -11	0.0096

Supplementary Table 4 continues on next page

**Supplementary Table 4 Continued**

3. Relation between SUVmax and PFS/OS (HR for above median SUVmax per patient and below median SUVmax) with various levels of adjustment:

	Small sample bias corrected Cox (Firth)					
	Unadjusted			Adjusted for tumor type and load		
	HR	95% CI	<i>P</i>	HR	95% CI	<i>P</i>
All patients ( <i>n</i> = 22)						
PFS	11.7	3.3 to 62.7	6.59e <sup>-09</sup>	10.0	2.2 to 62.4	0.0025
OS	6.3	1.8 to 33.4	0.0035	9.3	1.7 to 69.9	0.0084
Without TNBC ( <i>n</i> = 18)						
PFS	10.7	2.7 to 59.6	0.00055	12.6	2.7 to 79.7	0.00097
OS	7.5	1.9 to 41.7	0.0041	12.4	2.3 to 99.2	0.0029

	Regular Cox					
	Unadjusted			Adjusted for tumor type and load (IPW)*		
	HR	95% CI	<i>P</i>	HR	95% CI	<i>P</i>
All patients ( <i>n</i> = 22)						
PFS	14.2	4.5 to 45.7	< 0.001	14.7	4.4 to 45.7	< 0.001
OS	8.4	2.4 to 30.0	0.0015	8.5	1.9 to 33.5	0.0008
Without TNBC ( <i>n</i> = 18)						
PFS	13.2	4.1 to 40.9	< 0.001	13.9	3.9 to 41.3	< 0.001
OS	9.0	2.4 to 29.9	0.0030	9.2	1.6 to 33.5	0.020

\* Achieved balance assessed by post-IPW C-index (best 0.5; worst 1.0): All patients, tumor type and load adjustment: 0.60; No TNBC, tumor type and load adjustment: 0.50.

**Supplementary Table 5 Continuous analysis of relationship between <sup>89</sup>Zr-atezolizumab uptake and patient outcome**

	<sup>89</sup> Zr-atezolizumab uptake as geometric mean SUVmax	
	PFS	OS
HR*	6.6	4.0
95% CI	2.3-26.7	1.5-16.1
<i>P</i> **	0.000032	0.0018

PFS, progression free survival; OS, overall survival; HR, hazard ratio. \* HR per standard deviation decrease in the per patient geometric mean SUVmax. \*\* Likelihood ratio *P*.

**Supplementary Table 6 Discriminatory performance of <sup>89</sup>Zr-atezolizumab tumor uptake and PD-L1 IHC**

	geometric mean <sup>89</sup> Zr-atezolizumab uptake (n = 22)	IHC SP142 (n = 19)	IHC SP263 (n = 19)
AUC (95% CI)*	0.83 (0.55-1.00)	0.60 (0.35-0.85)	0.63 (0.39-0.88)
C-index PFS (95% CI)	0.86 (0.69-1.00)	0.55 (0.39-0.70)	0.60 (0.45-0.76)
C-index OS (95% CI)	0.80 (0.61-1.00)	0.55 (0.37-0.73)	0.65 (0.47-0.82)

AUC, area under the receiver operating characteristics curve; IHC, immunohistochemistry; PFS, progression free survival; OS, overall survival. \*Outcome defined as patients with and without CR/PR as best tumor response.





# Chapter 7

## **<sup>89</sup>Zr-trastuzumab PET supports clinical decision making in breast cancer patients, when HER2 status cannot be determined by standard work up**

---

Frederike Bensch<sup>1</sup>, Adrienne H. Brouwers<sup>2</sup>, Marjolijn N. Lub-de Hooge<sup>2,3</sup>, Johan R. de Jong<sup>3</sup>, Bert van der Vegt<sup>4</sup>, Stefan Sleijfer<sup>5</sup>, Elisabeth G.E. de Vries<sup>1</sup>, Carolien P. Schröder<sup>1</sup>

Departments of Medical Oncology<sup>1</sup>, Nuclear Medicine and Molecular Imaging<sup>2</sup>, Clinical Pharmacy and Pharmacology<sup>3</sup>, and Pathology and Medical Biology<sup>4</sup>, University of Groningen, University Medical Center Groningen, Groningen, the Netherlands and Department of Medical Oncology<sup>5</sup>, Erasmus MC Cancer Institute, Rotterdam, the Netherlands.

## ABSTRACT

**Background:** Up-to-date information on human epidermal growth factor receptor 2 (HER2) status in breast cancer (BC) is important, as expression can vary during the course of the disease, necessitating anti-HER2 therapy adjustments. Repeat biopsies, however, are not always possible. In this feasibility trial we assessed whether  $^{89}\text{Zr}$ -trastuzumab PET could support diagnostic understanding and aid clinical decision making, when HER2 status could not be determined by standard work up. Additionally, HER2 status on circulating tumor cells (CTCs) was assessed.

**Patients and methods:**  $^{89}\text{Zr}$ -trastuzumab PET was performed in patients if disease HER2 status remained unclear after standard work up (bone scan,  $^{18}\text{F}$ -FDG PET, CT and if feasible a biopsy). PET result and central pathologic revision of available tumor biopsies were reported to the referring physician. CTC HER2 status prior to PET was evaluated afterwards and therefore not reported. Diagnostic understanding and treatment decision questionnaires were completed by the referring physicians before, directly after and  $\geq 3$  months after  $^{89}\text{Zr}$ -trastuzumab PET.

**Results:** 20 patients were enrolled: 8 with 2 primary cancers (HER2-positive and HER2-negative BC or BC and non-BC), 7 with metastases inaccessible for biopsy, 4 with prior HER2-positive and -negative metastases and 1 with primary BC with equivocal HER2 status.  $^{89}\text{Zr}$ -trastuzumab PET was positive in 12 patients, negative in 7 and equivocal in 1 patient. In 15/20 patients,  $^{89}\text{Zr}$ -trastuzumab PET supported treatment decision. The scan altered treatment of 8 patients, increased physicians' confidence without affecting treatment in 10, and improved physicians' disease understanding in 18 patients. In 10/20 patients CTCs were detected; 6/10 showed HER2 expression. CTC HER2 status was not correlated to  $^{89}\text{Zr}$ -trastuzumab PET result or treatment decision.

**Conclusions:**  $^{89}\text{Zr}$ -trastuzumab PET supports clinical decision making when HER2 status cannot be determined by standard work up. The impact of CTC HER2 status needs to be further explored.

## INTRODUCTION

In metastatic breast cancer, treatment options are largely dependent upon the presence of the estrogen receptor, progesterone receptor and human epidermal growth factor receptor 2 (HER2), in addition to tumor load and location. The outcome of HER2 positive metastatic disease has fundamentally improved since the development of effective HER2 targeting agents such as trastuzumab, pertuzumab and trastuzumab-emtansine.<sup>1</sup> In this light, it is of particular interest that HER2 status can change during disease course, consequently necessitating anti-HER2 therapy adjustment. Furthermore, HER2 status discordancy between primary and residual or metastatic lesions, either HER2 loss or gain<sup>2</sup>, was related to shorter disease-free and overall patient survival in retrospective<sup>3,4</sup> and prospective analyses.<sup>5</sup> This discordancy, measured by immunohistochemistry (IHC) and/or in situ hybridization (ISH) techniques, ranged between 0-33%.<sup>2,3,6-14</sup> Moreover, HER2 expression can be heterogeneous within the same tumor.<sup>6,15,16</sup> Therefore, temporal and spatial heterogeneity may fundamentally affect HER2 status and therefore treatment response. Based on this data, clinical guidelines encourage repeat biopsies during the course of the disease. However, due to technical or patient related factors tumor lesions are not always (safely) accessible, leaving the clinician with a dilemma with regard to the disease's HER2 status.

HER2 imaging using <sup>89</sup>Zr-trastuzumab positron emission tomography (PET) could be a strategy to noninvasively assess HER2 expression in tumor lesions throughout the whole body.<sup>17,18</sup> It might, therefore, become a valuable tool to guide clinical decision making in metastatic breast cancer patients, who – despite extensive work-up – pose a clinical dilemma.<sup>19,20</sup> Characterization of circulating tumor cells (CTCs) might be another patient-friendly method to assess HER2 status on metastatic cells.<sup>21</sup> Since CTCs are likely shed from different tumor sites – metastases and the primary tumor, if still present – they might reflect both HER2 status and tumor heterogeneity. Consequently, the aim of this clinical feasibility trial was to assess whether <sup>89</sup>Zr-trastuzumab PET supports clinical decision making in patients suspected of metastatic or locally recurrent HER2-positive breast cancer, presenting with a dilemma defined as failure of the standard work-up to evaluate the present HER2 status of their disease. In addition, HER2 status of CTCs was assessed and correlated to treatment decision and <sup>89</sup>Zr-trastuzumab PET result.

## PATIENTS AND METHODS

### Patient population

This prospective single-center clinical trial protocol was approved by the medical ethics committee of the University Medical Center Groningen (UMCG; ClinicalTrials.gov identifier NCT01832051). All patients provided written informed consent.

Patients with suspected metastatic disease or local recurrence of HER2-positive breast cancer with a clinical dilemma defined as failure of standard work-up to evaluate the HER2 status were eligible. HER2-positivity, reported in the patient's history, was defined positive with an IHC of score 3+ or IHC of score 2+ followed by ISH showing HER2 amplification according to the American Society of Clinical Oncology guidelines.<sup>22</sup> Standard imaging work-up preferably consisted of a computed tomography (CT) of the chest and abdomen, a bone scintigraphy and a fluorine-18-fluorodeoxyglucose (<sup>18</sup>F-FDG) PET scan, accompanied by a metastasis biopsy, if feasible. Other eligibility criteria included age  $\geq$  18 years and Eastern Cooperative Oncology Group performance status of 0-2. Patients with a history of allergic reactions to immunoglobulins and pregnant or lactating women, as well as patients with any inabilities not allowing compliance with the study procedures, were excluded.

### **<sup>89</sup>Zr-trastuzumab PET scan**

Clinical grade <sup>89</sup>Zr-trastuzumab was produced at the UMCG as described previously.<sup>17</sup> Patients received 37 MBq ( $\pm$  10%;  $\sim$  1 mCi) <sup>89</sup>Zr-trastuzumab intravenously supplemented with unlabeled antibody to a total amount of 50 mg trastuzumab. Four days postinjection, head to upper thigh was scanned in up to 9 bed positions with 5 minutes/bed position in combination with a low dose CT scan for attenuation correction and anatomic reference with a Biograph mCT 64-slice PET/CT camera (Siemens). PET scans were reconstructed and visually analyzed by one dedicated nuclear medicine physician. The <sup>89</sup>Zr-trastuzumab PET scan was considered positive, when in comparison to the <sup>18</sup>F-FDG PET and in conjunction with conventional imaging (e.g. contrast enhanced CT scan, bone scan or MRI in case of brain metastases) the entire tumor load or a dominant part of the tumor load showed <sup>89</sup>Zr-trastuzumab tumor uptake.<sup>23</sup> <sup>89</sup>Zr-trastuzumab tumor uptake was considered substantial when tumor tracer uptake in visceral lesions (excluding brain) was at least comparable to or higher than liver background or in case of brain metastases when <sup>89</sup>Zr-trastuzumab uptake was exceeding brain background uptake allowing clear identification of the metastasis. Interpretation of <sup>89</sup>Zr-trastuzumab uptake in bone lesions was assessed in relation with visceral metastases.

Retrospectively, PET images were reconstructed using the harmonized reconstruction algorithm recommended for multicenter <sup>89</sup>Zr-mAb PET scan trials<sup>24</sup> and all tumor lesions on the conventional imaging were recorded, including measurability according to RECIST 1.1<sup>25</sup> and prior radiation therapy. Tumor lesions with a diameter of  $>$  15 mm on contrast enhanced CT scan were quantified, when tumor tracer uptake was considered not to be influenced by surrounding tissue and when a lesion was not irradiated  $\leq$  6 months of the <sup>89</sup>Zr-trastuzumab PET scan. With the AMIDE (A Medical Image Data Examiner) software (version 0.9.3,<sup>26</sup>) radioactivity was quantified in manually drawn volumes of interest around tumor lesions and several

background organs, and standardized uptake values (SUV) were calculated. We report SUVmax for tumor lesions and SUVmean for normal organ tracer uptake.

### **Clinical value**

To assess the influence of the  $^{89}\text{Zr}$ -trastuzumab PET scan on treatment decision, referring physicians completed earlier validated questionnaires before, directly after and > 3 months after the  $^{89}\text{Zr}$ -trastuzumab PET scan.<sup>27</sup> Information on the patient's history, which dilemma incited the referral for  $^{89}\text{Zr}$ -trastuzumab PET, as well as the intended treatment were assessed with the first questionnaire. In the second questionnaire, completed after receiving the scan result, the treating physician was asked to give the final diagnosis, the chosen treatment strategy and information on potential additional tests planned. With the last questionnaire referring physicians were asked to rate the contribution of the  $^{89}\text{Zr}$ -trastuzumab PET scan to their diagnostic understanding of the patient's disease and the choice of therapy using a 5-point scale (Supplementary Table 1). All questionnaires were checked for internal consistency.

### **Archival tumor samples**

Available archival tumor samples from the primary tumor site(s) or metastases were centrally revised and IHC (SP3; rabbit monoclonal antibody; NeoMarkers, Lab Vision Corp., Thermo Fisher Scientific, Fremont, California, USA), and in case of an IHC 2+ score ISH (PathVysion HER2/neu DNA probe kit, Vysis, Abbott Molecular, Des Plaines, IL) were repeated. HER2 positivity was defined as IHC 3+, or IHC 2+ with a positive ISH (HER2:CEP17 ratio  $\geq 2.0$  or an average of  $\geq 6.0$  HER2 copies per nucleus;<sup>22</sup>).

### **Circulating tumor cell analysis**

Before tracer injection, blood for CTC enumeration and CTC HER2 expression analysis was collected. Samples were transported to the laboratory of Clinical Tumor Immunology, Erasmus MC Cancer Institute, Rotterdam, the Netherlands, for analysis. One CellSave tube was used to obtain an EpCAM-based CTC count from 7.5 mL blood using the Epithelial Cell Kit (Janssen Diagnostics LLC, Raritan, NJ, USA) on CellSearch System according to manufacturer's instructions. CTCs were further characterized for HER2 expression within the Cell-Search system by a FITC-labeled anti-HER2 antibody as described by the manufacturer (CellSearch tumor phenotyping reagent HER2/neu; Janssen Diagnostics LLC). HER2 immunofluorescence staining intensity of 3+ and 2+ were scored as HER2-positive as described earlier.<sup>28</sup> CTC HER2 status was evaluated after inclusion of all patients and was not reported to the referring physician.

## Statistical analysis

Statistical analyses were performed using SPSS Version 23. To assess relation between CTC result and  $^{89}\text{Zr}$ -trastuzumab scan result or chosen treatment strategy, Spearman correlation was used.  $P \leq 0.05$  was considered to be a significant difference. Data are presented as mean  $\pm$  standard deviation (SD), unless otherwise stated.

## RESULTS

### Patient characteristics

Twenty patients were enrolled between July 2013 and June 2015 from all over the Netherlands and the Northern border area of Germany, with a median distance to our center of 125 km (range 20-247, Table 1). The  $^{89}\text{Zr}$ -trastuzumab PET scan was requested by the referring physicians (all: medical oncologists) due to following reasons (Supplementary Table 2): i) To differentiate between metastases of two primary cancers, either two primary breast cancers (one HER2-positive and the other HER2-negative), or a HER2-positive breast cancer and a second primary cancer from another origin ( $n = 8$ ), ii) to assess HER2 status of a single lesion inaccessible for biopsy, or in case of multiple lesions inability to perform repeat biopsies ( $n = 7$ ), iii) to assess HER2 expression of metastatic breast cancer with known heterogeneous HER2 status over time ( $n = 4$ ), and iv) to evaluate HER2 expression in metastatic breast cancer with prior equivocal histopathological result (HER2 IHC score 2+, ISH result: average 4.23 HER2 gene copies/nucleus,  $n = 1$ ).

**Table 1 Patient characteristics**

Characteristic	All patients ( $n = 20$ )
Median age, y (range)	56 (37-71)
Median travel distance to facility with $^{89}\text{Zr}$ -trastuzumab PET, km (range)	125 (20-247)
Sex	
Male	0
Female	20
Prior lines of anti-HER2 therapy	
0	4
1	9
2	2
> 3	5
Reported main clinical dilemma	
Two primary cancers	8
Unfeasibility of (repeated) biopsy	7
Heterogeneous HER2 status over time	4
Equivocal histopathological workup	1

### **<sup>89</sup>Zr-trastuzumab PET**

Highest normal organ <sup>89</sup>Zr-trastuzumab uptake was observed in the liver, followed by the kidney, intestine (= feces), blood pool and the spleen the lowest in subcutaneous tissue and the brain (Supplementary Fig. 1).

At visual assessment, <sup>89</sup>Zr-trastuzumab tumor uptake was considered positive in 12 patients, negative in seven patients and equivocal in one patient (Fig. 1 and Supplementary Table 2).

Retrospectively, a total of 404 tumor lesions were delineated on <sup>89</sup>Zr-trastuzumab PET after primary visual assessment of which 264 (65%) were considered evaluable. In two patients, none of the known metastases appeared on <sup>89</sup>Zr-trastuzumab PET and their scans, therefore, were considered negative. In the remaining 18 patients a median of 9 lesions (range 1-69) was evaluable. Heterogeneity of tumor tracer uptake was observed within patients, with a maximal 8-fold difference within one patient. Also, tumor tracer uptake varied greatly between patients, with a maximal 13-fold difference (data not shown).

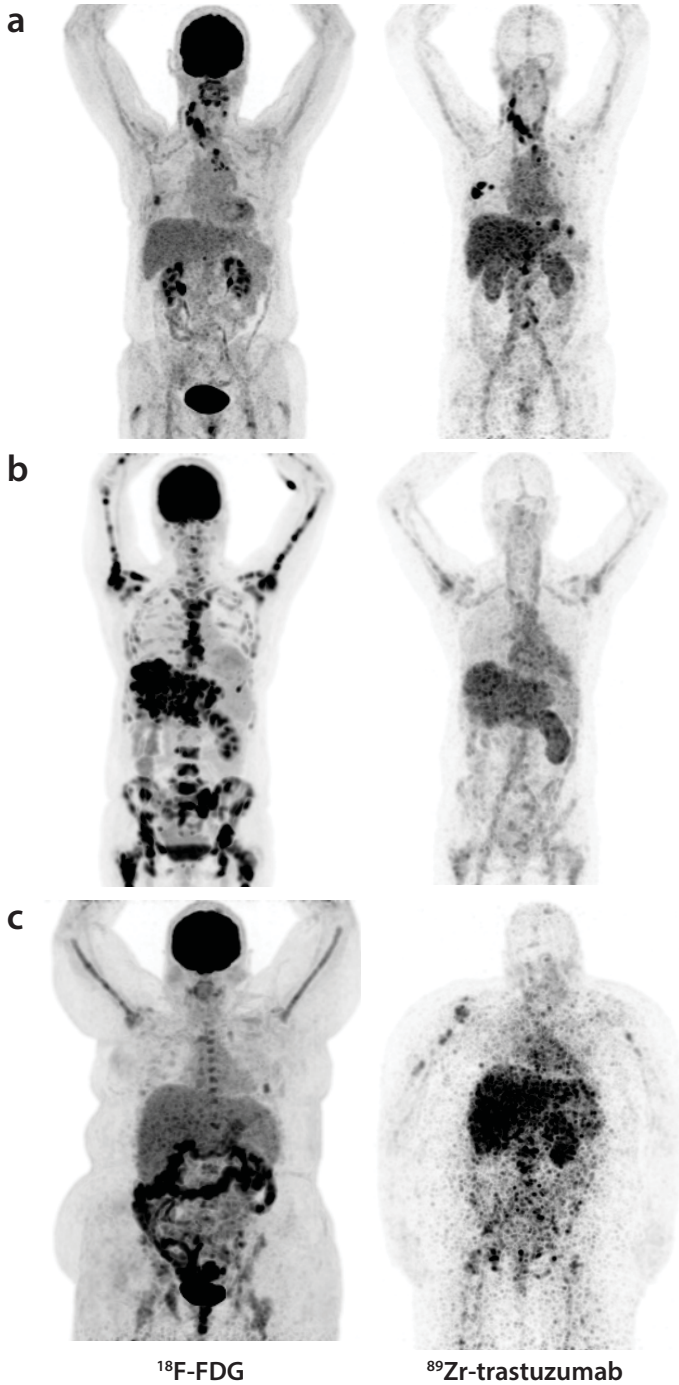
### **HER2 status in tumor biopsies in comparison to <sup>89</sup>Zr-trastuzumab PET**

For central revision a total of 42 tumor samples of 20 patients were available (primary  $n = 18$ , secondary  $n = 10$ , metastasis  $n = 14$ ). One patient, who had reported HER2-positive disease, was diagnosed with heterogeneous disease after central pathology revision (Table 2). Furthermore, two out of ten patients with a reported combination of HER2-positive and HER2-negative disease and the one patient with the equivocal histopathological result were diagnosed with HER2-negative disease after central revision.

The <sup>89</sup>Zr-trastuzumab PET scan was positive in seven out of eight patients with a previously HER2 positive primary tumor, and in five out of nine patients with a previous combination of HER2-positive and HER2-negative disease according to available tumor tissue (Table 2).

### **Clinical value of <sup>89</sup>Zr-trastuzumab PET**

The work-up including <sup>89</sup>Zr-trastuzumab PET scan improved the treating physician's understanding of the patient's disease in 18 (90%) patients (Fig. 2). The confidence over the (unaltered) treatment choice was improved in ten patients (50%), and in eight patients (40%) the treatment was changed. Five patients were started on anti-HER2 treatment and three patients did not receive HER2-targeting agents as consequence of the <sup>89</sup>Zr-trastuzumab scan (Table 3). In one patient the scan did not influence the understanding and/or treatment choice, and one physician of a patient with osteosarcoma and simultaneous HER2-positive breast cancer, rated choice of treatment based on the <sup>89</sup>Zr-trastuzumab PET as non-beneficial for the patient, although the scan improved her understanding of the disease.

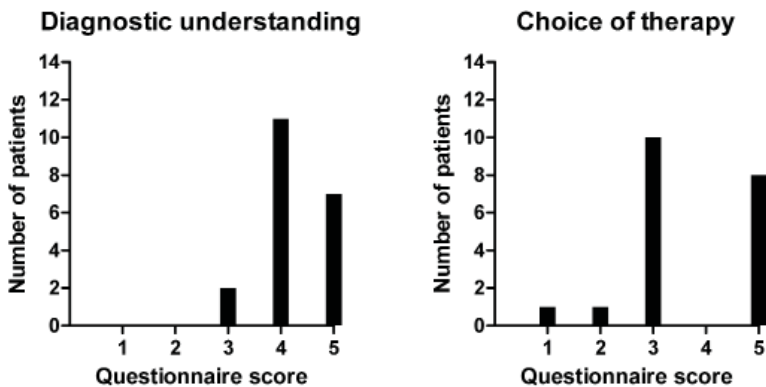


**Figure 1**  $^{18}\text{F}$ -FDG (left) and  $^{89}\text{Zr}$ -trastuzumab PET scans (right) of 3 patients: Example of a patient with a  $^{89}\text{Zr}$ -trastuzumab PET scan considered HER2-positive (a), a  $^{89}\text{Zr}$ -trastuzumab PET scan considered HER2-negative (b) and a  $^{89}\text{Zr}$ -trastuzumab PET scan considered equivocal (c).

**Table 2** Reported HER2 status in biopsies of primary tumors and metastases vs. result of central pathology revision, and  $^{89}\text{Zr}$ -trastuzumab PET result

Patient	Reported HER2 status	HER2 status after central revision	$^{89}\text{Zr}$ -trastuzumab PET result
1	HER2+ and HER2-	HER2+ and HER2-	Positive
2	HER2+	HER2+	Positive
3	HER2+ and HER2-	HER2- <sup>a</sup>	Negative
4	HER2+ and HER2-	HER2+ and HER2-	Positive
5	HER2+	HER2+	Negative <sup>b</sup>
6	HER2+	HER2+	Positive
7	HER2+ and HER2-	HER2+ and HER2-	Equivocal
8	HER2+	HER2+	Positive
9	HER2+ and HER2-	HER2+ and HER2-	Negative
10	HER2+	HER2+	Positive
11	HER2+ and HER2-	HER2+ and HER2-	Positive
12	HER2+ and HER2-	HER2+ and HER2-	Negative
13	HER2+ and HER2-	HER2+ and HER2-	Positive
14	HER2+ and HER2-	HER2- <sup>a</sup>	Negative
15	HER2+	HER2+	Positive
16	HER2+	HER2+	Positive
17	HER2+ and HER2-	HER2+ and HER2-	Negative
18	equivocal	HER2-	Negative
19	HER2+	HER2+ and HER2- <sup>a</sup>	Positive
20	HER2+	HER2+	Positive

<sup>a</sup> Initial HER2 IHC interpretation of primary tumor biopsy false positive. <sup>b</sup> Leptomeningeal metastases visualized on MRI where not visible on  $^{89}\text{Zr}$ -trastuzumab PET either due to negative HER2 status or due to their size below the detection limit.

**Figure 2** Contribution of the  $^{89}\text{Zr}$ -trastuzumab PET scan to the treating physicians diagnostic understanding (left) and choice of therapy (right) using a 5-point scale

**Table 3 Treatment decision before and after  $^{89}\text{Zr}$ -trastuzumab PET**

Treatment planned before $^{89}\text{Zr}$ -trastuzumab PET	Treatment given after $^{89}\text{Zr}$ -trastuzumab PET		
	Anti-HER2 ( $\pm$ chemo)	No anti-HER2 (other systemic treatment)	No systemic treatment
Anti-HER2 ( $\pm$ chemo)	5	2	0
No anti-HER2 (other systemic treatment)	2	4	0
No systemic treatment	1	0	3
Unsure on systemic treatment choice/dependent on additional test	2	1	0

### CTC HER2 status

CTCs were found in half of the patient population (median number of CTCs/7.5 mL = 6.5, range 1-99). In six of them, HER2-positive CTCs were found and three of the six patients also had a positive  $^{89}\text{Zr}$ -trastuzumab PET scan (Supplementary Table 3). Two out of the six patients, both with positive  $^{89}\text{Zr}$ -trastuzumab PET, received anti-HER2 treatment subsequently. Overall, CTC result was not correlated to  $^{89}\text{Zr}$ -trastuzumab PET result or subsequent treatment decision (correlation with PET result:  $r = 0.074$ ,  $P = 0.84$ ; correlation with treatment decision:  $r = -0.37$ ,  $P = 0.92$ ).

## DISCUSSION

In this small prospective clinical feasibility trial we show for the first time that  $^{89}\text{Zr}$ -trastuzumab PET can support diagnostic understanding and clinical decision making when HER2 status of metastatic or locally recurrent breast cancer cannot be determined by standard work up.

The  $^{89}\text{Zr}$ -trastuzumab PET scan improved the physician's understanding of the patient's disease in the majority of patients and the treatment strategy was changed in 40% of the study population. Five patients received initially unplanned anti-HER2 therapy, whereas in three patients, intended anti-HER2 therapy was withheld. By doing this, the latter patients were possibly saved from toxicity of a potentially ineffective treatment. Moreover, the savings of treatment related costs outweigh scan related costs manifold. Thereby, distance to  $^{89}\text{Zr}$ -trastuzumab PET was no issue in our trial as patients were willing to travel up to almost 250 km (~150 miles), implying that such molecular scan techniques, although localized only in specialized centers, can be within reach of a vast majority of patients. Using additional molecular imaging in standard clinical care will increase radiation exposure. In case of a  $^{89}\text{Zr}$ -trastuzumab PET, this additional radiation exposure equals that of one diagnostic CT scan of the chest, abdomen and pelvis.<sup>29-32</sup> The balance between risks and benefits of any additional procedure should always be carefully

considered in any patient population. In this particular population, a diagnostic dilemma is known to negatively affect their survival if left unsolved. In light of the potentially helpful information gained by the scan and also considering the incurable nature of their disease, we think that the benefits of a  $^{89}\text{Zr}$ -trastuzumab PET outweigh the risks in this particular patient population. Therefore, we consider this scan as suitable for clinical practice.

CTC analysis in metastatic breast cancer has shown to be a strong prognostic factor.<sup>33-36</sup> Since CTCs probably originate from different tumor sites, they might also provide a comprehensive view of tumor characteristics like HER2 status, including tumor heterogeneity. In our trial, CTCs were only detected in half of the patients, which corresponds with the earlier reported CTC detection rate.<sup>36</sup> The impact of CTC HER2 status on clinical decision making is unclear from the present study, as the result was not reported to the referring physician. Therefore this will have to be further explored. However, central pathology revision including renewed HER2 staining, and subsequent comparison of primary tumor and metastases biopsies, did deliver new insights in HER2 status in three out of twenty patients in this study. Therefore this could be worth considering in the standard setting.

Validation of molecular scan techniques is still an ongoing process. Clinical utility of  $^{89}\text{Zr}$ -trastuzumab PET, especially the relation of scan results with treatment response and survival data in recently diagnosed metastatic breast cancer patients is currently assessed in a prospective, multicenter observational cohort study conducted in the Netherlands (ClinicalTrials.gov Identifier: NCT01957332). In this trial, intra-patient heterogeneity of tumor tracer uptake will also further be evaluated, as so far the clinical implication of the observed heterogeneity is unclear. The trial, furthermore, supports validation and standardization of interpretation of this PET imaging technique, which is instrumental for potential further wider application as possible biomarker for treatment response in the future. Additionally, the impact of CTC enumeration and characterization for HER2 and its relation with  $^{89}\text{Zr}$ -trastuzumab PET is further explored in the mentioned trial. However, the present study already establishes  $^{89}\text{Zr}$ -trastuzumab PET as a diagnostic tool to help the treating physician in clinical decision making, in this niche population of patients with an otherwise undetermined HER2 status of their disease.

## Acknowledgments

We thank Linda Pot and Rianne Bakker for technical support for the labeling.

**Funding:** This work was financially supported by an unrestricted research grant from the Dutch A Sister's Hope foundation provided to. C. P. Schröder.

## Compliance with ethical standards

**Conflict of interest:** E.G.E. de Vries received research support from Hoffmann-La Roche and Genentech (payment to the institution). All other authors declared no competing interests.

**Research involving human participants:** All procedures performed in studies involving human participants were in accordance with the ethical standards of the institutional and/or national research committee and with the 1964 Helsinki declaration and its later amendments or comparable ethical standards.

**Informed consent:** Informed consent was obtained from all individual participants included in the study.

## REFERENCES

1. Thomas, A., Khan, S., Lynch, C. & Schroeder, M. Survival by HER2 receptor status in stage IV breast cancer: SEER 2010-2012. *J. Clin. Oncol.* 35, suppl, abstr 1032 (2017).
2. Lower, E. E., Glass, E., Blau, R. & Harman, S. HER2/neu expression in primary and metastatic breast cancer. *Breast Cancer Res. Treat.* 113, 301-306 (2009).
3. Niikura, N. *et al.* Loss of human epidermal growth factor receptor 2 (HER2) expression in metastatic sites of HER2-overexpressing primary breast tumors. *J. Clin. Oncol.* 30, 593-599 (2012).
4. Mittendorf, E. A. *et al.* Loss of HER2 amplification following trastuzumab-based neoadjuvant systemic therapy and survival outcomes. *Clin. Cancer Res.* 15, 7381-7388 (2009).
5. Lindstrom, L. S. *et al.* Clinically used breast cancer markers such as estrogen receptor, progesterone receptor, and human epidermal growth factor receptor 2 are unstable throughout tumor progression. *J. Clin. Oncol.* 30, 2601-2608 (2012).
6. Masood, S. & Bui, M. M. Assessment of HER2/neu overexpression in primary breast cancers and their metastatic lesions: an immunohistochemical study. *Ann. Clin. Lab. Sci.* 30, 259-265 (2000).
7. Gancberg, D. *et al.* Comparison of HER-2 status between primary breast cancer and corresponding distant metastatic sites. *Ann. Oncol.* 13, 1036-1043 (2002).
8. Regitnig, P., Schippinger, W., Lindbauer, M., Samonigg, H. & Lax, S. F. Change of HER2/neu status in a subset of distant metastases from breast carcinomas. *J. Pathol.* 203, 918-926 (2004).
9. Zidan, J. *et al.* Comparison of HER2 overexpression in primary breast cancer and metastatic sites and its effect on biological targeting therapy of metastatic disease. *Br. J. Cancer* 93, 552-556 (2005).
10. Vincent-Salomon, A. *et al.* HER2 status in patients with breast carcinoma is not modified selectively by preoperative chemotherapy and is stable during the metastatic process. *Cancer* 94, 2169-2173 (2002).
11. Tanner, M., Jarvinen, P. & Isola, J. Amplification of HER2/neu and topoisomerase IIa in primary and metastatic breast cancer. *Cancer Res.* 61, 5345-5348 (2001).
12. Santinelli, A., Pisa, E., Stramazotti, D. & Fabris, G. HER2 status discrepancy between primary breast cancer and metastatic sites. Impact on target therapy. *Int. J. Cancer* 122, 999-1004 (2008).
13. Gong, Y., Booser, D. J. & Sneige, N. Comparison of HER2 status determined by fluorescence in situ hybridization in primary and metastatic breast carcinoma. *Cancer* 103, 1763-1769 (2005).
14. Curigliano, G. *et al.* Should liver metastases of breast cancer be biopsied to improve treatment choice? *Ann. Oncol.* 22, 2227-2233 (2011).
15. Wu, J. M., Halushka, M. K. & Argani, P. Intratumoral heterogeneity of HER-2 gene amplification and protein overexpression in breast cancer. *Hum. Pathol.* 41, 914-917 (2010).
16. Hanna, W., Nofech-Mozes, S. & Kahn, H. J. Intratumoral heterogeneity of HER2/neu in breast cancer—a rare event. *Breast J.* 13, 122-129 (2007).
17. Dijkers, E. C. *et al.* Development and characterization of clinical-grade <sup>89</sup>Zr-trastuzumab for HER2/neu immunoPET imaging. *J. Nucl. Med.* 50, 974-981 (2009).
18. Ulaner, G. A. *et al.* Detection of HER2-positive metastases in patients with HER2-negative primary breast cancer using <sup>89</sup>Zr-trastuzumab PET/CT. *J. Nucl. Med.* 57, 1523-1528 (2016).
19. Gaykema, S. B. *et al.* Zirconium-89-trastuzumab positron emission tomography as a tool to solve a clinical dilemma in a patient with breast cancer. *J. Clin. Oncol.* 30, e74-5 (2012).
20. Bensch, F., van Rooijen, J. M., Schroder, C. P. & Reyners, A. K. A 21-year-old patient with a HER2-positive colorectal cancer. *Gastroenterology* 148, 20-21 (2015).
21. Onstenk, W., Gratama, J. W., Foekens, J. A. & Sleijfer, S. Towards a personalized breast cancer treatment approach guided by circulating tumor cell (CTC) characteristics. *Cancer Treat. Rev.* 39, 691-700 (2013).
22. Wolff, A. C. *et al.* Recommendations for human epidermal growth factor receptor 2 testing in breast cancer: American Society of Clinical Oncology/College of American Pathologists clinical practice guideline update. *J. Clin. Oncol.* 31, 3997-4013 (2013).

23. Gebhart, G. *et al.* Molecular imaging as a tool to investigate heterogeneity of advanced HER2-positive breast cancer and to predict patient outcome under trastuzumab emtansine (T-DM1): the ZEPHIR Trial. *Ann Oncol.* 27, 619-624 (2016).
24. Makris, N. E. *et al.* Multicenter harmonization of  $^{89}\text{Zr}$  PET/CT performance. *J. Nucl. Med.* 55, 264-267 (2014).
25. Eisenhauer, E. A. *et al.* New response evaluation criteria in solid tumours: revised RECIST guideline (version 1.1). *Eur. J. Cancer* 45, 228-247 (2009).
26. Loening, A. M. & Gambhir, S. S. AMIDE: a free software tool for multimodality medical image analysis. *Mol. Imaging.* 2, 131-137 (2003).
27. Herder, G. J. *et al.* Prospective use of serial questionnaires to evaluate the therapeutic efficacy of  $^{18}\text{F}$ -fluorodeoxyglucose positron emission tomography in suspected lung cancer. *Thorax* 58, 47-51 (2003).
28. Riethdorf, S. *et al.* Detection and HER2 expression of circulating tumor cells: prospective monitoring in breast cancer patients treated in the neoadjuvant GeparQuattro trial. *Clin. Cancer Res.* 16, 2634-2645 (2010).
29. Borjesson, P. K. *et al.* Radiation dosimetry of  $^{89}\text{Zr}$ -labeled chimeric monoclonal antibody U36 as used for immuno-PET in head and neck cancer patients. *J. Nucl. Med.* 50, 1828-1836 (2009).
30. Makris, N. E. *et al.* PET/CT-derived whole-body and bone marrow dosimetry of  $^{89}\text{Zr}$ -cetuximab. *J. Nucl. Med.* 56, 249-254 (2015).
31. McCollough, C. H., Bushberg, J. T., Fletcher, J. G. & Eckel, L. J. Answers to common questions about the use and safety of CT scans. *Mayo Clin. Proc.* 90, 1380-1392 (2015).
32. Eschner, W., Schmidt, M., Dietlein, M. & Schicha, H. PROLARA: prognosis-based lifetime attributable risk approximation for cancer from diagnostic radiation exposure. *Eur. J. Nucl. Med. Mol. Imaging* 37, 131-135 (2010).
33. Budd, G. T. *et al.* Circulating tumor cells versus imaging-predicting overall survival in metastatic breast cancer. *Clin. Cancer Res.* 12, 6403-6409 (2006).
34. Cristofanilli, M. *et al.* Circulating tumor cells, disease progression, and survival in metastatic breast cancer. *N. Engl. J. Med.* 351, 781-791 (2004).
35. Plaks, V., Koopman, C. D. & Werb, Z. Cancer. Circulating tumor cells. *Science* 341, 1186-1188 (2013).
36. Bidard, F. C. *et al.* Clinical validity of circulating tumour cells in patients with metastatic breast cancer: a pooled analysis of individual patient data. *Lancet Oncol.* 15, 406-414 (2014).

## SUPPLEMENTARY MATERIAL

**Supplementary Table 1 Questionnaire assessing clinical value of  $^{89}\text{Zr}$ -trastuzumab PET**

Diagnostic understanding	
1	$^{89}\text{Zr}$ -trastuzumab PET confused my understanding of this patient's disease and led to investigations I would not otherwise have done.
2	$^{89}\text{Zr}$ -trastuzumab PET confused my understanding of this patient's disease but did not lead to any additional investigations.
3	$^{89}\text{Zr}$ -trastuzumab PET had little or no effect on my understanding of this patient's disease.
4	$^{89}\text{Zr}$ -trastuzumab PET provided information which substantially improved my understanding of this patient's disease.
5	My understanding of this patient's disease depended upon diagnostic information provided only by $^{89}\text{Zr}$ -trastuzumab PET (unavailable from any other non-surgical procedure).
Choice of therapy	
1	$^{89}\text{Zr}$ -trastuzumab PET led me to choose therapy which in retrospect was not in the best interests of the patient.
2	$^{89}\text{Zr}$ -trastuzumab PET was of no influence in my choice of therapy.
3	$^{89}\text{Zr}$ -trastuzumab PET did not alter my choice of therapy but did increase my confidence in the choice.
4	$^{89}\text{Zr}$ -trastuzumab PET contributed to a change in my chosen therapy but other factors (other imaging tests, other diagnostic tests, changes in patient status) were equally or more important.
5	$^{89}\text{Zr}$ -trastuzumab PET was very important compared with other factors in leading to a beneficial change in therapy.

Supplementary Table 2 Details on the clinical dilemma and the results per scan modality per patient

Patient	Dilemma category	Description of dilemma	Bone scan	CT scan	<sup>18</sup> F-FDG PET-positive lesions	<sup>89</sup> Zr-trastuzumab PET interpretation
1	Heterogeneous HER2 status over time	HER2+ primary breast cancer and HER2- metastasis during course of disease	Two bone metastases (femur)	Peritonitis carcinomatosa, soft tissue metastases chest and back	Peritonitis carcinomatosa, multiple malignant lymph nodes (axillary, mediastinal), soft tissue metastases chest and back including subcutaneous lesions, four bone metastases (femur and rib), suspicious uptake intrapulmonary	Dominant part of tumor load shows <sup>89</sup> Zr-trastuzumab uptake exceeding healthy liver background → scan considered positive
2	Evaluation of HER2 status	Doubtful whether continuation of anti-HER2 therapy is indicated in patient with treatment induced cardiac toxicity	No bone metastases	Multiple lymph nodes (cervical, mediastinal), inhomogeneous thyroid gland, multiple skin metastases	Multiple lymph nodes (cervical, mediastinal, abdominal), multiple skin metastases, mammary lesion, right thyroid gland	Entire tumor load shows <sup>89</sup> Zr-trastuzumab uptake exceeding healthy liver background → scan considered positive
3	Heterogeneous HER2 status over time	HER2+ primary breast cancer and HER2- metastasis during course of disease	Multiple bone metastases (skull, sternum, clavicle, pelvic bone, femur, spine, ribs)	Multiple liver metastases, multiple bone metastases	Multiple bone metastases (skull, sternum, clavicle, pelvic bone, femur, spine, ribs), multiple liver metastases, multiple lymph nodes (cervical, mediastinal, iliacal)	Only slight <sup>89</sup> Zr-trastuzumab uptake in all for metastases suspicious lesions, uptake less than healthy liver background → scan considered negative
4	Heterogeneous HER2 status during time	HER2- primary breast cancer and HER2+ metastasis during course of disease	No bone metastases	Multiple lymph nodes (cervical, mediastinal, axillary), multiple lung metastases, two liver metastases	Multiple lymph nodes (cervical, mediastinal, axillary, abdominal), multiple lung metastases, two liver metastases, single bone metastasis	<sup>89</sup> Zr-trastuzumab uptake in cervical lymph node and liver metastases exceeds healthy liver background, remainder lesions only slight tracer uptake → scan considered positive
5	Evaluation of HER2 status	Leptomeningeal metastases visualized on MRI <sup>a</sup> ; biopsy not possible	No bone metastases	No suspicious lesions	No suspicious lesions	No focal <sup>89</sup> Zr-trastuzumab uptake → scan considered negative

6	Two primary tumors	Differentiation between lesions of HER2+ breast cancer and malignant lymphoma	Single bone metastasis (scapula)	Multiple liver metastases	Diffuse liver metastases, diffuse <sup>18</sup> F-FDG uptake in bone marrow	Entire tumor load shows <sup>89</sup> Zr-trastuzumab uptake exceeding healthy liver background ➔ scan considered positive
7	Two primary tumors	HER2+ primary breast cancer and HER2- secondary breast cancer	Multiple bone metastases (diffuse in whole skeleton)	Multiple bone metastases, suspicious lesion adrenal gland and single lung nodule	No clear evidence of bone metastases, lesion in adrenal gland or lung, only diffuse <sup>18</sup> F-FDG uptake	Diffuse <sup>89</sup> Zr-trastuzumab uptake in suspicious bone and visceral lesions, uptake less than healthy liver background ➔ scan considered equivocal
8	Evaluation of HER2 status	Doubtful whether continuation of anti-HER2 therapy is indicated after years of treatment and progression of disease	Multiple bone metastases (spine, ribs, humerus, scapula, pelvic bone, femur)	Multiple bone metastases (spine, ribs, humerus, scapula, pelvic bone, femur)	Multiple bone metastases (spine, ribs, humerus, scapula, pelvic bone, femur), multiple brain metastases	Dominant part of tumor load shows <sup>89</sup> Zr-trastuzumab uptake exceeding healthy liver background ➔ scan considered positive
9	Two primary tumors	HER2+ primary breast cancer, HER2- breast cancer metastases and thyroid cancer	Multiple bone metastases (ribs)	Multiple bone metastases (ribs)	Multiple bone metastases (ribs)	Only slight <sup>89</sup> Zr-trastuzumab uptake in all for metastases suspicious lesions, uptake less than healthy liver background ➔ scan considered negative
10	Evaluation of HER2 status	Discrepant response to anti-HER2 therapy, doubtful whether continuation of anti-HER2 therapy is indicated	Single bone metastasis (spine)	Single bone metastasis (spine)	NA	Bone metastasis shows <sup>89</sup> Zr-trastuzumab uptake exceeding healthy liver background ➔ scan considered positive
11	Two primary tumors	HER2- primary breast cancer and HER2+ secondary breast cancer	NA	Multiple lymph nodes (cervical, mediastinal)	Multiple lymph nodes (cervical, mediastinal)	Dominant part of tumor load shows <sup>89</sup> Zr-trastuzumab uptake exceeding healthy liver background ➔ scan considered positive

Supplementary Table 2 continues on next page.

Supplementary Table 2 Continued

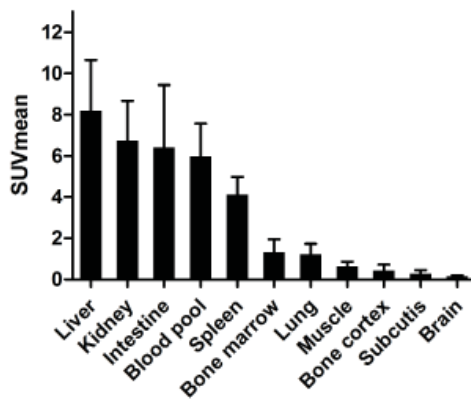
Patient	Dilemma category	Description of dilemma	Bone scan	CT scan	<sup>18</sup> F-FDG PET-positive lesions	<sup>89</sup> Zr-trastuzumab PET interpretation
12	Two primary tumors	HER2- primary breast cancer and HER2+ secondary breast cancer	Multiple bone metastases (pelvic bone, spine, scapula, femur)	Multiple bone metastases (pelvic bone, spine, scapula, femur), multiple liver metastases	Multiple bone metastases (pelvic bone, spine, scapula, femur), multiple liver metastases, multiple suspicious lymph nodes (axillary)	No focal <sup>89</sup> Zr-trastuzumab uptake → scan considered negative
13	Two primary tumors	HER2+ primary breast cancer and HER2- secondary breast cancer	No bone metastases	Lymph node (mediastinal) and single bone metastasis (sacrum)	Lymph node (mediastinal) and single bone metastasis (sacrum)	Entire tumor load shows <sup>89</sup> Zr-trastuzumab uptake exceeding healthy liver background → scan considered positive
14	Heterogeneous HER2 status over time	HER2+ primary breast cancer and HER2- metastasis during course of disease	Multiple bone metastases (sternum, pelvic bone)	Multiple bone metastases (sternum, pelvic bone), multiple lymph nodes (cervical, mediastinal), pleural metastases, multiple liver metastases	Multiple bone metastases (sternum, pelvic bone), multiple lymph nodes (cervical, mediastinal), pleural metastases, multiple liver metastases	Only slight <sup>89</sup> Zr-trastuzumab uptake in all for metastases suspicious lesions, uptake less than healthy liver background → scan considered negative
15	Evaluation of HER2 status	Suspicious lymph node, no biopsy possible	No bone metastases	Multiple lymph nodes (abdominal), multiple liver metastases	Multiple lymph nodes (abdominal), multiple liver metastases	Dominant part of tumor load shows <sup>89</sup> Zr-trastuzumab uptake exceeding healthy liver background → scan considered positive
16	Evaluation of HER2 status	Differentiation between radionecrosis and recurrent brain metastasis	No bone metastases	No suspicious lesions	Single brain metastasis	Brain metastasis shows <sup>89</sup> Zr-trastuzumab uptake exceeding healthy liver and brain background → scan considered positive

17	Two primary tumors	HER2- primary breast cancer and HER2+ secondary breast cancer	Diffuse uptake in multiple locations in the spine (differential diagnosis osteoporosis or metastases)	Suspicious bone lesions (spine, differential diagnosis osteoporosis or metastases)	Multiple lymph nodes (cervical, mediastinal), diffuse uptake in spinal lesions (differential diagnosis osteoporosis or metastases)	Only slight <sup>89</sup> Zr-trastuzumab uptake in all for metastases suspicious lesions, uptake less than healthy liver background → scan considered negative
18	Equivocal or ambiguous work-up	HER2 ISH equivocal	Multiple bone lesions (sternum, scapula, ribs, spine, pelvic bone, femur)	Mamma, multiple lymph nodes (axillary, mediastinal, abdominal), multiple bone lesions (sternum, scapula, ribs, spine, scapula, ribs, spine, pelvic bone, femur)	Mamma, multiple lymph nodes (axillary, mediastinal), multiple bone lesions (sternum, scapula, ribs, spine, pelvic bone, femur)	Only slight <sup>89</sup> Zr-trastuzumab uptake in all for metastases suspicious lesions, uptake less than healthy liver background → scan considered negative
19	Two primary tumors	HER2+ breast cancer and osteosarcoma	Single bone metastases (rib)	Subcutaneous thoracic lesion and single bone metastases (rib), single pleural lesion, multiple lymph nodes (parasternal)	Subcutaneous thoracic lesion and single bone metastases (rib), multiple lymph nodes (parasternal), single pleural lesion (suspicious for osteosarcoma)	Dominant part of tumor load shows <sup>89</sup> Zr-trastuzumab uptake exceeding healthy liver background, no to slight <sup>89</sup> Zr-trastuzumab uptake in pleural lesion → scan considered positive
20	Evaluation of HER2 status	Suspicious lung nodule, no biopsy possible	No bone metastases	Suspicious pulmonary lesions (differential diagnosis infiltrates, metastases), multiple bone lesions (spine, pelvic bone, ribs)	Two aspecific lesions mamma, multiple suspicious intrapulmonary lesions, single brain metastasis, single bone metastasis (pelvic bone)	Brain metastasis shows <sup>89</sup> Zr-trastuzumab uptake exceeding healthy liver and brain background, remaining lesions don't show evident <sup>89</sup> Zr-trastuzumab uptake → scan considered positive

<sup>a</sup> Three extra axial lesions visualized on MRI brain, differential diagnosis leptomeningeal metastases or meningioma. NA, not available.

**Supplementary Table 3 Results of <sup>89</sup>Zr-trastuzumab PET vs. CTC count and CTC HER2 status**

Patient	<sup>89</sup> Zr-trastuzumab PET result	CTC count (n)	HER2-positive CTCs (n)
1	Positive	8	0
2	Positive	5	3
3	Negative	70	0
4	Positive	0	-
5	Negative	0	-
6	Positive	99	94
7	Equivocal	0	-
8	Positive	5	5
9	Negative	21	1
10	Positive	0	-
11	Positive	0	-
12	Negative	13	2
13	Positive	0	-
14	Negative	1	1
15	Positive	1	0
16	Positive	0	-
17	Negative	0	-
18	Negative	0	-
19	Positive	1	0
20	Positive	0	-



**Supplementary Figure 1** Normal organ <sup>89</sup>Zr-trastuzumab distribution depicted as mean SUVmean (+ SD).



# Chapter 8

## Summary and future perspective

---

## SUMMARY

Over the last decades, drug development has improved survival in multiple cancer types. Especially with the arrival of agents targeting the immune system like immune checkpoint inhibitors, a new era of cancer treatment has begun in which even in case of metastatic disease complete responses over several years have been observed. Despite all achievements in the recent years, however, cancer remains a leading cause of death worldwide. Multiple cancer types do not or not sufficiently respond to currently available treatment. Non-response, thereby, is a multilayer problem including inherent resistance and tumor heterogeneity, as well as development of resistance originating from either the tumor cells themselves or the microenvironment during the course of disease. Furthermore, multiple drugs and/or combinations cannot be used broadly in the clinic despite potential potency due to major side effects. Obtaining detailed information on drug pharmacokinetics and pharmacodynamics already early in drug development, providing information on target heterogeneity and early response prediction in a patient friendly way, are major challenges in clinical research. One possible technique that could address these challenges might be molecular positron emission tomography (PET) imaging with radioactively labeled antibodies.

The aim of the research described in this thesis was to investigate the role of molecular imaging with different monoclonal antibodies in increasing knowledge of whole body pharmacokinetics and pharmacodynamics. Furthermore, we evaluated the contribution of molecular imaging to therapy decision making and to response prediction.

**Chapter 1** provides a general introduction of the topic and outlines the thesis. In **chapter 2**, we reviewed the literature on the potential role of molecular PET imaging in breast cancer as response evaluation of bone metastases, the most common site of metastases in this cancer type, is hampered since these lesions are not measurable according to the generally applied Response Evaluation Criteria in Solid Tumours (RECIST). Molecular imaging, in contrast, is not dependent on measurement of anatomical size changes, but can be used to assess status and changes of general tumor processes, such as glucose metabolism and DNA synthesis, and also more specific targets, like hormone receptors, growth factor receptors and targets in the tumor microenvironment before and during therapy. In breast cancer, especially  $^{89}\text{Zr}$ -trastuzumab PET, as measure for the human epidermal growth factor receptor 2 (HER2) and  $^{18}\text{F}$ -fluoroestradiol ( $^{18}\text{F}$ -FES) PET for evaluation of the estrogen receptor status seem to have the potential to aid treatment selection for the individual patient. Furthermore, serial imaging of general tumor processes with tracers such as  $^{18}\text{F}$ -fluorodeoxyglucose (FDG) may provide early prediction of anti-tumor efficacy. Future trials will need to specify uptake characteristics for different breast cancer subtypes, as well as for different chemotherapy and/or targeted therapy regimens, the optimal moment of scanning, the quantification method and validation of PET with conventional imaging.

Next to the HER2 protein, which is firmly established as important drugable target in breast cancer, the more recently identified HER3 protein is a potential target in multiple cancer types. In **chapter 3** we describe biodistribution and tumor uptake by serial imaging with the  $^{89}\text{Zr}$ -labeled therapeutic anti-HER3 antibody lumretuzumab before and during treatment in patients with advanced or metastatic HER3-positive solid tumors. Optimal PET conditions were found to be 4 and 7 days after administration of  $^{89}\text{Zr}$ -lumretuzumab with 100 mg unlabeled lumretuzumab. The highest tracer uptake was seen in the liver (mean standardized uptake value (SUVmean)  $6.4 \pm 1.1$  on day 4 after injection), followed by the circulation, the kidneys, spleen and intestine. Tracer uptake was much lower in brain, muscle, bone, abdominal cavity and lung (SUVmean of 0.2 to 0.9). Tumor SUVmax 4 days after tracer injection was  $3.4 (\pm 1.9)$ , ranging from 0.5 up to 8.9 with an up to 6-fold difference in mean tumor tracer uptake between patients. About 33% of tumor lesions with a diameter  $\geq 10$  mm were  $^{89}\text{Zr}$ -lumretuzumab PET-negative. Saturation analysis assessed in seven patients showed that 4 days after lumretuzumab administration, tumor uptake decreased by 11.9% ( $\pm 8.2$ ), 10.0% ( $\pm 16.5$ ) and 24.6% ( $\pm 20.9$ ) at pharmacodynamic-active doses of 400, 800 and 1600 mg, respectively, when compared to baseline. Membranous HER3 was completely downregulated in paired skin biopsies already at and above 400 mg lumretuzumab. In contrast to the phase I pharmacodynamic data, there was no clear evidence of tumor saturation by PET imaging as tumor uptake did not plateau with increasing doses. The latter might be explained by multiple factors: the signal visualized with PET is 1) a combination of membrane-bound activity and the intracellular fraction as the tracer is being internalized, 2) a function of time as after internalization the relatively long-living radionuclide  $^{89}\text{Zr}$  remains in tumor cells and PET images were performed serially over several days in contrast to a biopsy which reflects a single moment in time and 3) also influenced by factors such as enhanced permeability and retention effects in tumor lesions, and potentially unspecific tracer uptake e.g. due to the effect of Fc gamma receptor engagement within the tumor environment.

In **chapter 4**, we used  $^{89}\text{Zr}$ -fresolimumab to visualize the transforming growth factor- $\beta$  in recurrent high-grade glioma before treatment with the monoclonal antibody fresolimumab. On day 4 after tracer injection, normal brain tissue tracer uptake was low with an SUVmean of 0.3, ranging from 0.2 to 0.5, and mean tumor tracer uptake calculated as SUVmax was 4.6, ranging from 1.5 up to 13.9. Treatment with fresolimumab was generally well tolerated without infusion-related reactions and mainly low grade adverse events. Despite the good penetration capacity of the monoclonal antibody into the recurrent high-grade glioma lesions as visualized by PET imaging, no clinical benefit of single agent fresolimumab treatment was observed in this small and often extensively pretreated patient group in which only one dose of fresolimumab was tested.

Until now, imaging trials mainly focused on biodistribution analysis of single agents, disregarding comparison across different antibodies, which, however, might be of great value during drug development. Therefore, in **chapter 5**, we performed a comparative biodistribution

analysis of four  $^{89}\text{Zr}$ -labeled monoclonal antibodies previously explored in clinical studies based on the  $^{89}\text{Zr}$ -harmonization protocol and conducted according to our standardized delineation protocol for  $^{89}\text{Zr}$ -tracers.  $^{89}\text{Zr}$ -lumretuzumab (anti-HER3),  $^{89}\text{Zr}$ -MMOT0530A (anti-mesothelin),  $^{89}\text{Zr}$ -bevacizumab (anti-vascular endothelial growth factor) and  $^{89}\text{Zr}$ -trastuzumab (anti-HER2) showed a similar distribution pattern in healthy tissue. On day 4 after tracer injection, about one-third of the injected tracer dose was found in the circulation, up to 15% in the liver and only 4% in the spleen and kidney. Lower tracer concentrations were seen in bone marrow, lung, compact bone, muscle, fat and the brain. Despite low tracer accumulation per gram of tissue, large-volume tissues, especially fat, can influence overall distribution: On average, 5-7% of the injected tracer dose accumulated in fat, with a peak of 19% in a patient with morbid obesity. The similar biodistribution of the four antibodies is probably based on the similar molecular structure, binding characteristics and metabolic pathways. With this first comparative analysis we aimed to create a basis for a prospectively growing imaging data warehouse of antibody-based tracers. In the future, this warehouse will need to grow to increase its impact: especially with addition of tracers imaging the immune system, new molecules belonging to another IgG subclass and with different molecule size or structure such as bispecific antibodies.

In **chapter 6**, we describe the results from first-in-human imaging with  $^{89}\text{Zr}$ -labeled atezolizumab, an anti-programmed death-ligand 1 (PD-L1) antibody, and correlated uptake data with immunohistochemistry and RNA results from the tumor tissue samples and with treatment response. With 10 mg unlabeled antibody added, blood pool, and liver and kidney  $^{89}\text{Zr}$ -atezolizumab uptake on day 4 were comparable to day 4 results of earlier described  $^{89}\text{Zr}$ -antibody tracers. In contrast to earlier studied monoclonal antibody based tracers, we observed high and variable  $^{89}\text{Zr}$ -atezolizumab uptake in the spleen, non-malignant lymph nodes and sites of inflammation, which corresponds with local PD-L1 expression by CD8-positive T-cells and antigen presenting cells such as dendritic cells and macrophages. Tumor uptake was generally high, with a SUVmax up to 46, but heterogeneous within and between patients and tumor types. In our exploratory study, which did not include a large patient population and no immunohistochemically PD-L1 highly positive tumor biopsies, we observed that higher tracer uptake prior to atezolizumab treatment was related to better response, progression free and overall survival; more so than immunohistochemistry and RNA sequencing. Further development of this imaging biomarker for PD-L1 status, including expansion of the study population needs to take place to confirm these first results.

In **chapter 7**, we describe results of a trial in metastatic breast cancer patients presenting with a clinical dilemma defined as failure of the standard work-up to evaluate the present HER2 status. In this specific patient population we assessed the contribution of  $^{89}\text{Zr}$ -trastuzumab PET to disease understanding and clinical decision making. In 90% of the cases the physicians' disease understanding was increased by  $^{89}\text{Zr}$ -trastuzumab PET, in 50% of the patients the physicians'

confidence for the pre-planned treatment choice was increased without affecting the choice, and in 40% of the patients treatment was altered based on the  $^{89}\text{Zr}$ -trastuzumab PET result. As central pathology revision with renewed HER2 staining delivered new insights in three of 20 patients, implementation of this step in the standard setting might be worth considering. HER2 status of circulating tumor cells, detected in 50% of the study population, was not correlated to  $^{89}\text{Zr}$ -trastuzumab PET result or treatment decision.

## DISCUSSION AND FUTURE PERSPECTIVES

### Assessment of clinical utility of molecular imaging

To be able to implement molecular imaging in clinical practice, amongst others information on the predictive value of the tracer in comparison and/or in addition to the standard work-up, evaluation of efficacy and cost-effectiveness is needed. For molecular imaging in breast cancer, this information is becoming more and more available. In addition to already published molecular imaging trials in this cancer type, in **chapters 2 and 7** of this thesis we describe the potential role of molecular PET imaging in general, and the role of HER2 imaging in clinical decision making in a specific patient population presenting with a clinical dilemma with regard to their disease's HER2 status. Clinical utility is currently further assessed in the Dutch, prospective, multicenter IMPACT-metastatic breast cancer trial (ClinicalTrials.gov identifier NCT01957332) in which next to  $^{18}\text{F}$ -FDG, also estrogen receptor and HER2 imaging is investigated in a larger population of newly diagnosed metastatic breast cancer patients. In the future, preliminary findings of other targets evaluated in first-in-human imaging trials and (additional) information on clinical utility also in a variety of tumor types is necessary. Furthermore, molecular imaging findings will need to be (further) cross validated, on the one hand with current golden standard tumor biopsy based techniques such as immunohistochemistry, fluorescent in situ hybridization, in combination with RNA and/or DNA sequencing. On the other hand, molecular imaging should be compared with molecular techniques which also have the potential to capture whole body target status, such as circulating tumor cells or circulating tumor DNA. Finally, the use of molecular imaging as biomarker should be confirmed in larger patient populations, ideally as part of randomized controlled trials, which can only be realized when reliable automated delineation algorithms become available.

### Increase knowledge of target biodistribution by means of comparative analysis

In **chapters 3-6** we describe the biodistribution of newly developed tracers and results of the first comparative biodistribution analysis of four  $^{89}\text{Zr}$ -labeled monoclonal antibody tracers including establishment of a basis for a molecular imaging warehouse. Upscaling of imaging

trials in general is hampered by amongst others cost factors and radiation burden. In this light, collection of data in a warehouse, similar to meta-analyses in clinical intervention trials, could contribute to more firm evidence to support utility of molecular imaging in clinical practice. Also, knowledge of drug distribution, and establishment and fine tuning of standardized protocols could be increasingly being facilitated this way. An example of the usefulness of data sharing is provided by the RECIST criteria, which have been verified with a warehouse containing imaging and outcome data from numerous trials. As the scientific community in the recent years is more and more recognizing the strength of data sharing, this might be a hopeful approach also for molecular imaging. The impact of the findings based on the established molecular imaging warehouse can increase in the coming years, especially with expansion of the warehouse by adding tracers visualizing the immune system and new drug constructs with unknown biodistribution such as bispecific antibodies.

### Imaging of the immune system

Imaging of the checkpoint inhibitor atezolizumab and its favorable predictive capacity is described in **chapter 6**. In the extension phase of this imaging trial (ClinicalTrials.gov identifier NCT02453984) patients are imaged during atezolizumab treatment to assess influence of the treatment dose on healthy tissue and tumor tracer uptake. In the coming years, molecular imaging will further be used as a tool to assess the immune system and its various components. Already now, several trials are recruiting to evaluate uptake characteristics of other checkpoints and/or their inhibitors ( $^{89}\text{Zr}$ -CX-072 and  $^{18}\text{F}$ -BMS-986192 both targeting PD-L1;  $^{89}\text{Zr}$ -pembrolizumab and  $^{89}\text{Zr}$ -nivolumab both targeting PD-1). Also first tracers to visualize activated T-cells (e.g.  $^{99\text{m}}\text{Tc}$ -IL2 or  $^{18}\text{F}$ -IL2) or specific subgroups of T-cells (e.g. CD8 imaging) are in development; And for other immune cells like B-cells, macrophages and Natural Killer cells, and even components of the extracellular matrix, tracers are becoming available, too. In the evolving field of immunotherapy with new targets arising (e.g. OX40, LAG 3, TIM 3, GITR, CD137) and an increasing number of combination regimens for several cancer types, knowledge of dynamics of the players of the immune system and their interaction with the microenvironment, especially over time and in response to the various treatment options, will be a major issue. Not only combinations with other immune cell activating or checkpoint targeting drugs will be a main research focus, but also combination strategies thought to induce expression of a certain immune response related target, to act synergistically with immunotherapy or to support immune cell function, will further be assessed. Candidate targets of interest, thereby, are for example the transforming growth factor- $\beta$ , which can be produced by aggressive tumors in large amounts leading to local immune suppression via regulatory T cells and the vascular endothelial growth factor, which – when overproduced – leads to fast development

of leaky vessels in tumors possibly hampering immune cell trafficking to the tumor. Both, when blocked, could aid the mechanism of action of immunotherapies. Also, combination with certain chemotherapies or radiotherapy could support immunotherapy when administered concurrently or sequentially, as they increase presentation of tumor-associated antigens on antigen-presenting cells and stimulate T cell diversification. Molecular imaging by PET might play a role in this development with its capacity to obtain whole body information over time in a non-invasive manner. Thereby, next to understanding mechanisms of action, the ultimate research goal will remain on patient selection to further improve overall survival. Additionally, fluorescent molecular imaging might add to this by delivering more detailed information on the microscopic level. And finally, as the latter technique is not using radioactive probes but fluorescence, it could be used more repeatedly and not only in the field of oncology but also in immune mediated inflammatory diseases.

### **Assessment of heterogeneity and its clinical relevance**

As visualized in all imaging trials and described in performed molecular analyses within and outside of this thesis, target heterogeneity within tumor lesions and also over time has been recognized as important phenomenon in oncology. Heterogeneity exists across tumor types and subtypes; there is heterogeneity of tumor cell characteristics, as well as in the tumor (immune) microenvironment. Thereby, heterogeneity can be found at all levels of the cell machinery, *e.g.* at the protein level, the RNA or DNA level, and it can also be measured in the blood pool as circulating tumor cells or circulating cell free tumor DNA. In the coming years, we will continue describing this heterogeneity in various tumor types and changes throughout treatment by means of tissue-based molecular analyses methods including computational pathology, blood-based methods and non-invasive (molecular) imaging. We will, furthermore, need to continue adding clinical outcome data to assess which markers are relevant for clinical decision making and prognosis. Thereby, it will be of interest to assess whether single characteristics serve satisfactorily as biomarkers or whether – and if so, which clusters of characteristics are most informative, next to the question of tumor specificity. Depending on the prevalence of the targetable characteristic(s) per tumor type, it will not be possible to gather necessary clinical data in large randomized controlled trials. Smart basket trial designs will increasingly be necessary to define the clinical value of targeted therapies in various tumor types. Finally, to deal with all the data which can be obtained per patient and/or tumor (site) in combination with the already obtained knowledge about clinical outcome, we will need to develop software tools to help interpreting, combining and updating these data and support clinical decision making.

In conclusion, in this thesis we describe the role of molecular imaging to obtain deeper knowledge of pharmacokinetics and -dynamics of several monoclonal antibodies that are

in clinical development or already approved drugs for patient use. Furthermore, we show in modest size studies that molecular imaging may aid decision making and response prediction in specific patient populations, which, in the future might support patient selection to improve treatment outcome and survival.





# Chapter 9

**Nederlandse samenvatting  
(Dutch summary)**

---

In de laatste decennia is de prognose van vele soorten kanker verbeterd, mede door de ontwikkeling van nieuwe, specifiek op de tumor en diens eigenschappen gerichte geneesmiddelen. Vooral door de ontwikkeling van immunotherapie is een nieuw tijdperk in de antikankerbehandeling aangebroken, waarbij ook langdurige antitumoreffecten in patiënten op kunnen treden. Het is al langer bekend dat tumorcellen het immuunsysteem kunnen remmen waardoor zij hierdoor niet kunnen worden aangevallen en opgeruimd. Met de nieuw ontwikkelde immunotherapie worden echter de afweercellen weer geactiveerd, waardoor deze de tumorcellen kunnen herkennen en vernietigen. Helaas blijft kanker een van de meest belangrijke doodsoorzaken wereldwijd, ondanks alle vooruitgang in de behandeling. Er blijken namelijk ook een groot aantal tumoren niet of onvoldoende op de huidige beschikbare geneesmiddelen te reageren. Hierbij spelen meerdere factoren een rol, zoals bijvoorbeeld bestaande of verworven resistentie tegen de behandeling, en heterogeniteit van eigenschappen van de tumorcellen zelf of van omliggende cellen en weefsel. Het is daarom belangrijk om reeds vroeg in de ontwikkeling gedetailleerde informatie over het nieuwe geneesmiddel te verkrijgen. Bijvoorbeeld de verdeling van het medicament in het hele lichaam en in de tumor inclusief de effecten hiervan, ook wel farmacokinetiek en farmacodynamiek genaamd. Ook is de heterogeniteit van tumoreigenschappen waartegen medicijnen gericht kunnen worden belangrijk. Verder is het van groot belang om een patiëntvriendelijke techniek te hebben die kan helpen om te voorspellen welke patiënten baat kunnen hebben bij de behandeling, bij voorkeur al vooraf of in een vroeg stadium daarvan. Eén mogelijke techniek die gebruikt kan worden om deze vragen te onderzoeken, is moleculaire beeldvorming middels positronemissie tomografie (PET) met radioactief gemarkeerde antilichamen.

Het doel van het onderzoek beschreven in dit proefschrift was dan ook de rol van moleculaire beeldvorming met verschillende antilichamen te bestuderen om meer gedetailleerde informatie over de farmacokinetiek en farmacodynamiek van deze antilichamen te verkrijgen. Daarnaast hebben wij onderzocht of moleculaire beeldvorming iets kan bijdragen aan klinische besluitvorming en het voorspellen van de reactie van de tumor op de behandeling.

In **hoofdstuk 1** wordt een korte inleiding gegeven en worden de verschillende hoofdstukken geïntroduceerd. In dit proefschrift worden onderzoeken beschreven waarbij gebruik is gemaakt van PET-scans met zirconium-89 ( $^{89}\text{Zr}$ ) gelabelde antilichamen, ook wel tracers genoemd. In de hoofdstukken 3, 4, 6 en 7 is deze techniek gebruikt om de farmacokinetiek en farmacodynamiek van nieuwe antikankermedicijnen te beoordelen. In hoofdstuk 5 werden PET-scans van vier eerder onderzochte geneesmiddelen opnieuw geanalyseerd om naar overeenkomsten en verschillen in de farmacokinetiek te kunnen kijken. Uiteindelijk zijn deze gegevens te gebruiken als basis voor een steeds groeiend 'warenhuis'.

In **hoofdstuk 2** geven wij een overzicht van de literatuur over de rol van moleculaire beeldvorming middels PET bij patiënten met borstkanker. Deze techniek is bij borstkanker mogelijk

van toegevoegde waarde omdat men hiermee tumorprocessen zoals glucosemetabolisme, maar ook tumoreigenschappen zoals hormoon- of groeifactorreceptoren en eigenschappen van de tumoromgeving kan afbeelden. Door voorafgaand aan de behandeling en tijdens of nadien scans te maken, kunnen de veranderingen van deze eigenschappen in de tijd beoordeeld worden. Bij borstkanker is de aanwezigheid van de humane epidermale groeifactorreceptor 2 (HER2) en de oestrogeenreceptor (ER) op de tumor van belang omdat de patiënt bij aanwezigheid van deze eigenschappen specifieke behandelingen kan krijgen. Met PET-scans kan de aanwezigheid van HER2 na toediening van  $^{89}\text{Zr}$ -trastuzumab, als ook de aanwezigheid van ER na toediening van  $^{18}\text{F}$ -fluoroestradiol ( $^{18}\text{F}$ -FES) beoordeeld worden. Beide tracers kunnen mogelijk helpen bij de selectie van patiënten, en ook bij het vroegtijdig beoordelen van de reactie van een tumor op een behandeling. Er zijn echter nog aanvullende studies nodig om de exacte beoordelingscriteria per borstkankersubtype en per geneesmiddel(groep) vast te leggen. Daarnaast moet ook nog onderzocht worden wat het optimale scan moment is en hoe de scan zich verhoudt tot de huidige standaard beeldvorming voor het beoordelen van respons.

Naast HER2 werd recent HER3 geïdentificeerd als potentieel tumor kenmerk waartegen medicijnen gericht kunnen worden. Een nieuw ontwikkeld antilichaam tegen HER3, lumretuzumab, werd door ons gelabeld met  $^{89}\text{Zr}$  en in **hoofdstuk 3** beoordeeld met een PET studie. Het resultaat van de scan was het meest optimaal na injectie van het  $^{89}\text{Zr}$ -gelabeld lumretuzumab in combinatie met 100 mg ongelabeld lumretuzumab met PET-scans op dag 4 en 7 na injectie. Het antilichaam werd vooral opgenomen in de lever (gemiddelde gestandaardiseerde opname waarde (SUVmean)  $6,4 \pm 1,1$  op dag 4 na injectie), gevolgd door de bloedsomloop, nieren, milt en darmen. De opname van het antilichaam was veel lager in het brein, de spieren, botten, buikholte en longen (SUVmean tussen 0,2 en 0,9). De maximale tumoropname (SUVmax) op dag 4 was  $3,4 (\pm 1,9)$ , met een spreiding van 0,5 tot maximaal 8,9, en er was een maximaal 6 maal verschil in de gemiddelde tumoropname per patiënt. Ongeveer een derde van alle tumorlaesies met een diameter gelijk of groter dan 10 mm was  $^{89}\text{Zr}$ -lumretuzumab negatief. De tumoropname bleek na toediening van 400, 800 of 1600 mg lumretuzumab te dalen met respectievelijk 11,9% ( $\pm 8,2$ ), 10,0% ( $\pm 16,5$ ) en 24,6% ( $\pm 20,9$ ) vergeleken met de uitgangswaarde. Bij de analyse van huidbiopten die voorafgaand aan behandeling en na de eerste toediening lumretuzumab waren afgenomen bleek het membraangebonden HER3 volledig verdwenen te zijn vanaf een dosis van 400 mg en hoger. In tegenstelling tot de eerder beschreven fase I farmacokinetische data en de geanalyseerde huidbiopten, toonde de PET analyse geen tumorsaturatie. Dit zou verklaard kunnen worden door meerdere factoren: 1. Het PET signaal is een combinatie van membraangebonden HER3 en een intracellulaire fractie, aangezien het gelabelde antilichaam na binding aan de cel, in de cel wordt opgenomen; 2. Het PET signaal is afhankelijk van de tijd: het gelabelde antilichaam wordt namelijk intracellulair opgenomen en het relatief langlevende radionuclide  $^{89}\text{Zr}$  verblijft ook na afbreken van het

antilichaam in de cel. In tegenstelling tot een biopt, wat een momentopname is, toont het PET beeld informatie van meerdere dagen; en 3. Het PET signaal wordt niet alleen bepaald door de HER3-specifieke opname, maar ook door eigenschappen van het tumorweefsel zelf zoals verhoogde permeabiliteit van de in de tumor liggende vaten en retentie van de tracer met als gevolg mogelijk aspecifieke opname.

In **hoofdstuk 4** werd  $^{89}\text{Zr}$ -fresolimumab, een antilichaam tegen het groei-eiwit TGF- $\beta$ , in recidiverende hooggradige gliomen met PET gevisualiseerd voor de start van de behandeling met fresolimumab. Vier dagen na tracerinjectie was de gemiddelde maximale tumoropname 4,6 (spreiding 1,5 tot 13,9), met een lage traceropname in het omliggende hersenweefsel met een SUVmean van 0,3 (spreiding 0,2 tot 0,5). Na de PET-scan werd de patiënt behandeld met fresolimumab, wat goed werd verdragen en voornamelijk slechts milde bijwerkingen veroorzaakte. Ondanks het feit dat het antilichaam de bloed-hersenbarrière goed kon passeren en in de tumor kon ophopen, wat zichtbaar was op de PET-scan, sloeg de behandeling met fresolimumab niet aan bij deze al uitgebreid behandelde groep patiënten.

Tot op heden concentreerde de meerderheid van studies met gelabelde antilichamen zich enkel op de beschrijving van de biodistributie van een specifiek antilichaam, zonder de uitkomsten te vergelijken met antilichamen gericht tegen andere tumorkenmerken. De vergelijking van verschillende antilichamen en hun gedrag in het menselijke lichaam zou echter van toegevoegde waarde kunnen zijn tijdens geneesmiddelenontwikkeling. In de studie die in **hoofdstuk 5** beschreven wordt, hebben wij daarom PET-scan data van vier eerder onderzochte  $^{89}\text{Zr}$ -gelabelde antilichamen opnieuw geanalyseerd. Deze analyse werd gebaseerd op het recent verschenen protocol over harmonisatie van studies met  $^{89}\text{Zr}$ -gelabelde tracers en uitgevoerd naar aanleiding van ons standaardprotocol voor analyse van  $^{89}\text{Zr}$ -gelabelde tracers.  $^{89}\text{Zr}$ -lumretuzumab (antilichaam tegen HER3),  $^{89}\text{Zr}$ -MMOT0530A (antilichaam tegen mesotheline),  $^{89}\text{Zr}$ -bevacizumab (antilichaam tegen de groeifactor VEGF) en  $^{89}\text{Zr}$ -trastuzumab (antilichaam tegen HER2) lieten een vergelijkbare distributie in normaal weefsel zien. Op dag 4 na tracerinjectie bleek ongeveer een derde van de geïnjecteerde tracerdosis nog in het bloed te zitten, 15% in de lever en 4% in de milt en de nieren. Daarentegen waren de tracerconcentraties in het beenmerg, de longen, de botten, de spieren, het vetweefsel en het brein laag. Ondanks deze lage traceraccumulatie per gram weefsel, kan de verdeling in het lichaam wel sterk beïnvloed worden door weefsels die in grote hoeveelheid in het lichaam voorkomen: Gemiddeld accumuleerde 5-7% van de geïnjecteerde tracerdosis in het vetweefsel, wat opliep tot 19% bij een patiënt met morbide obesitas. De vier onderzochte antilichamen tonen dus een vergelijkbare biodistributie, waarschijnlijk door de vergelijkbare moleculaire structuur, antilichaambinding en manier van werken in de cel. Wij willen deze eerste vergelijkende analyse gebruiken als basis voor een groeiend 'warenhuis' van moleculaire beeldvorming middels PET. Dit 'warenhuis' van gegevens kan in de komende jaren verder uitgebreid worden met tracers die het immuunsysteem afbeelden, maar ook met

moleculen die bij een andere klasse antilichaam horen (IgG 1-4), of een andere grootte of structuur hebben dan de hier geanalyseerde antilichamen.

In **hoofdstuk 6** worden de resultaten beschreven die verkregen zijn met <sup>89</sup>Zr-atezolizumab, een tracer die voor het eerst in mensen werd gebruikt. Atezolizumab is een antilichaam gericht tegen PD-L1, wat een belangrijk schakelpunt is in het immuunsysteem dat door de tumor wordt uitgezet. PD-L1 komt tot expressie op tumor cellen en op cellen van het immuunsysteem. Door behandeling met atezolizumab wordt het eigen immuunsysteem weer geactiveerd waardoor deze tegen de tumorcellen kan vechten. In de beschreven studie hebben wij de tumoropname van <sup>89</sup>Zr-atezolizumab in patiënten met blaaskanker, longkanker en borstkanker gerelateerd aan tumorweefsel analyses (immunohistochemische kleuringen), analyses van de ribonucleïnezuur (RNA) van de tumor en aan de behandeluitkomsten. Na injectie van het gelabelde antilichaam in combinatie met 10 mg ongelabeld antilichaam was de gemeten hoeveelheid tracer in de bloedsomloop, lever en nieren 4 dagen na tracersinjectie vergelijkbaar met de opname van eerder beschreven <sup>89</sup>Zr-antilichaamtracers. In tegenstelling tot andere antilichamen zagen wij met <sup>89</sup>Zr-atezolizumab echter zeer hoge en variabele opname in de milt, in normale lymfeklieren en op plaatsen van lokale ontsteking. Deze locaties komen overeen met plaatsen met lokaal verhoogde PD-L1 expressie door verschillende cellen van het immuunsysteem. De opname van de tracer in de tumor was over het algemeen hoog met een SUVmax tot 46, maar ook heterogeen in en tussen patiënten en tumortypes. In deze eerste studie, met een beperkt aantal patiënten die geen tumoren hadden met zeer hoge PD-L1 expressie, bleek hoge traceropname in de tumor voorspellend te zijn voor respons op de behandeling en overleving. De PET resultaten konden de reactie op de behandeling zelfs beter voorspellen dan de huidige standaard PD-L1 expressie zoals gemeten met immunohistochemie en het tumor RNA. In het vervolg zal PET met <sup>89</sup>Zr-atezolizumab verder ontwikkeld en onderzocht moeten worden, en moeten de resultaten van deze hier gepresenteerde studie in een groter aantal patiënten bevestigd worden.

Tenslotte wordt in **hoofdstuk 7** een studie beschreven die is uitgevoerd bij patiënten met gemetastaseerde borstkanker waarbij er sprake is van een klinisch dilemma omtrent de HER2 status van de tumor. In deze specifieke patiëntenpopulatie hebben wij onderzocht of een <sup>89</sup>Zr-trastuzumab PET-scan de behandelend oncoloog kan helpen om de ziekte van de patiënt beter te begrijpen en bij de behandelkeuze. Het bleek dat de behandelend oncoloog in 90% van de gevallen een beter beeld van de ziekte kreeg door het maken van de <sup>89</sup>Zr-trastuzumab PET-scan. Verder voelde 50% van de behandelend oncologen zich gesteund in hun behandelkeuze door de scan, en in 40% van de gevallen werd de behandeling zelfs aangepast naar aanleiding van de PET-scan. Tevens leverde pathologische revisie van het oude bewaarde tumormateriaal in drie van 20 patiënten nieuwe inzichten op. Het lijkt daarom zinvol ook dit altijd te doen in het diagnostisch proces van patiënten met onbegrepen ontwikkeling van hun ziekte. Bepaling van de HER2 expressie van vrij in het bloed circulerende kankercellen (die maar bij 50% van

de patiënten in het bloed aangetroffen werden), was niet gerelateerd aan de scan resultaten of de behandelbeslissing.

Samenvattend wordt in dit proefschrift de rol van moleculaire beeldvorming middels PET beschreven om een beter inzicht te krijgen in de farmacokinetiek en farmacodynamiek van meerdere antilichamen die reeds in klinische ontwikkeling zijn of al geregistreerd zijn voor de behandeling van patiënten met kanker. Daarnaast laten wij in studies met een beperkt aantal patiënten zien dat moleculaire beeldvorming klinische besluitvorming kan ondersteunen, en kan helpen bij het voorspellen of een patiënt wel of geen baat bij de behandeling heeft. In de toekomst zou deze techniek de selectie van patiënten kunnen ondersteunen en daardoor mogelijk behandeluitkomsten en uiteindelijk overleving verbeteren.





# Chapter 10

**Deutsche Zusammenfassung  
(German summary)**

---

In den letzten Jahrzehnten wurde das Gesamtüberleben von Krebspatienten durch die Entwicklung von neuen Behandlungsmethoden drastisch verbessert. Vor allem durch Arzneistoffe, die am Immunsystem angreifen, den sogenannten Immun-Checkpoint-Inhibitoren, wurde eine neue Ära in der Krebsbehandlung eingeläutet. Trotz dieser Errungenschaft bleibt Krebs aber immer noch eine der führenden Todesursachen weltweit. Viele Krebsarten reagieren nicht oder nur ungenügend auf die heute verfügbaren Behandlungen. Die Gründe hierfür sind multifaktoriell: Tumoren können resistent gegen bestimmte Medikamente sein, oder sie entwickeln Resistenzen im Verlauf der Behandlung. Mittlerweile weiß man zudem, dass Tumorgewebe heterogen ist und Resistenzen nicht nur von den Tumorzellen ausgehen, sondern auch von der Tumorumgebung. Außerdem können viele entwickelte Arzneimittel nicht uneingeschränkt appliziert oder kombiniert werden aufgrund potenziell lebensbedrohlicher Neben- oder Wechselwirkungen. Darum ist es wichtig schon frühzeitig in der Entwicklung neuer Medikamente detaillierte Informationen über die Verteilung eines Medikamentes im Körper (Pharmakokinetik) und dessen Auswirkungen (Pharmakodynamik) zu versammeln. Thema der heutigen Forschung ist die Beschreibung der Position des Zielmoleküls, sowie die Veränderung seiner Expression. Des Weiteren liegen Effektivität des Arzneimittels und Patientenfreundlichkeit im Fokus.

Eine Technik, die zur Beantwortung einiger dieser Fragen eingesetzt werden kann, ist die Positronen-Emissions-Tomographie (PET) mit radioaktiv markierten Antikörpern.

Das Ziel dieser Dissertation war es die Rolle der molekularen Bildgebung mit verschiedenen Antikörpern zu untersuchen um mehr Informationen über deren Pharmakokinetik und -dynamik zu erhalten. Es wurde außerdem beurteilt, ob molekulare Bildgebung bei Therapieentscheidungen helfen und die Effektivität von zielgerichteten Krebsbehandlungen vorhersagen kann.

In **Kapitel 1** werden nach einer kurzen Einleitung alle folgenden Kapitel introduziert. In den beschriebenen Studien wurde den Patienten Zirkonium-89 ( $^{89}\text{Zr}$ ) markierte Antikörper, sogenannte Tracer, injiziert und wurden anschließend PET-Scans durchgeführt. In Kapitel 3, 4, 6 und 7 wurde diese Technik verwendet um die Pharmakokinetik und -dynamik von neuen Krebsmedikamenten zu beurteilen. In Kapitel 5 wurden PET-Scans von bereits untersuchten Arzneimitteln nochmals analysiert mit dem Ziel Gemeinsamkeiten und Unterschiede zu beschreiben.

**Kapitel 2** beinhaltet eine Literaturübersicht über die Rolle von molekularer Bildgebung mittels PET bei Patienten mit Brustkrebs. Der Einsatz dieser Technik kann bei Brustkrebs vorteilhaft sein, da neben dem Glukosemetabolismus, auch Tumoreigenschaften wie zum Beispiel der humane epidermale Wachstumsfaktorrezeptor 2 (HER2) und der Östrogenrezeptor (ER), und auch Eigenschaften der Tumorumgebung abgebildet werden können. Serielle PET-Scans von Patienten erlauben obendrein die Beurteilung dieser Tumoreigenschaften im zeitlichen Verlauf. Auf diese Weise kann patientenfreundlich ermittelt werden ob ein Patient mit hormonaler Therapie und/oder gegen HER2 gerichtete Therapie behandelt werden sollte. Bevor  $^{89}\text{Zr}$ -trastuzumab (HER2) und

$^{18}\text{F}$ -fluoroestradiol ( $^{18}\text{F}$ -FES; ER) als Tracer im klinischen Alltag eingesetzt werden können, müssen jedoch noch zusätzliche Studien durchgeführt werden um genaue Beurteilungskriterien für den jeweiligen Brustkrebssubtyp und der jeweiligen Arzneimittel(gruppe) festzulegen. Außerdem muss beurteilt werden wann genau im diagnostischen Prozess diese Scans vorteilhaft sind und wie ihre diagnostische Spezifität und Sensitivität im Vergleich zum Goldstandard, der Biopsie, sind.

Neben HER2 wurde jüngst auch HER3 als potentieller Angriffspunkt von neuen Krebsmedikamenten identifiziert. Wir haben einen dieser neuen Antikörper gegen HER3, Lumretuzumab, mit  $^{89}\text{Zr}$  radioaktiv markiert und in einer PET-Scan Studie beurteilt (**Kapitel 3**). Die besten Bilder erhielten wir nach der Injektion von  $^{89}\text{Zr}$ -Lumretuzumab zusammen mit 100 mg unmarkiertem Antikörper vier und sieben Tage nach der Injektion. Der Antikörper akkumulierte am stärksten in der Leber (gemittelter standardisierter Aufnahmewert, SUVmean,  $6,4 \pm 1,1$  vier Tage nach der Injektion), gefolgt von der Blutbahn, den Nieren, der Milz und dem Darm. Im Gehirn, den Muskeln, Knochen, der Bauchhöhle und den Lungen sammelte sich der Antikörper in nur geringen Mengen an (SUVmean zwischen 0,2 bis 0,9). Die gemittelte maximale Tumortraceraufnahme (SUVmax) vier Tage nach der Injektion war  $3,4 (\pm 1,9)$ , mit einer Streuung von 0,5 bis maximal 8,9 und einem maximal 6-fachen Unterschied in der Tumoraufnahme zwischen Patienten. Ungefähr ein Drittel aller Metastasen größer oder gleich 10 mm war  $^{89}\text{Zr}$ -Lumretuzumab negativ. Nach der Injektion von 400, 800 oder 1600 mg unmarkiertem Lumretuzumab nahm die Tumoraufnahme mit  $11,9 (\pm 8,2)$ ,  $10,0\% (\pm 16,5)$  und  $24,6\% (\pm 20,9)$  im Gegensatz zum Ausgangswert ab. Die Analyse von Hautbiopsien, die vor und nach der ersten Behandlung mit Lumretuzumab abgenommen wurden, zeigte, dass das membrangebundene HER3 ab einer Dosis von größer oder gleich 400 mg Lumretuzumab vollständig unterdrückt wurde. Im Gegensatz zu diesen Daten und Daten aus früheren Phase-1 Studien, wurde in unserer PET-Studie keine vollständige Tumorsättigung beobachtet. Verschiedene Gründe könnten eine Erklärung für das beobachtete Phänomen bieten: 1. Das PET-Signal ist eine Kombination von Signalen, nämlich vom membrangebundenen HER3 und der intrazellulären Fraktion, da der Tracer nach der Bindung an die Zelle nach intrazellulär aufgenommen wird. 2. Das PET-Signal ist abhängig von der Zeit: Das Radionuklid  $^{89}\text{Zr}$  verbleibt nach der intrazellulären Aufnahme und dem Abbau vom Antikörper unbeschadet in der Zelle. Im Gegensatz zu einer Biopsie, welche eine Momentaufnahme darstellt, ist das PET-Signal somit eine Summe von Radioaktivität, die sich über mehrere Tage angesammelt hat. Zu guter Letzt wird das PET-Signal nicht nur durch die HER3-spezifische Bindung generiert. Auch Eigenschaften des Tumorgewebes, wie zum Beispiel erhöhte Permeabilität der den Tumor umgebenden Gefäße und Retention des Tracers im Tumorgewebe tragen als unspezifische Komponenten zum PET-Signal bei.

In **Kapitel 4** wird  $^{89}\text{Zr}$ -Fresolimumab, ein Antikörper gegen das Wachstumsprotein TGF- $\beta$ , in rezidivierten hochgradigen Gliomen vor der Behandlung mit Fresolimumab mittels PET

visualisiert. Vier Tage nach der Tracerinjektion war die mittlere maximale Tumortraceraufnahme 4,6 (Streuung 1,5 bis 13,9) mit einer niedrigeren Traceraufnahme im umliegenden Gewebe (SUVmean 0,3, Streuung 0,2 bis 0,5). Nach der PET-Serie wurden die Patienten mit Fresolimumab behandelt. Die Behandlung wurde im Allgemeinen gut vertragen und verursachte nur milde Nebenwirkungen. Obwohl der Antikörper die Blut-Hirn-Schranke gut passieren und im Tumorgewebe akkumulieren konnte, was auf den PET-Scans zu sehen ist, war die Behandlung in dieser schwer vorbehandelten Patientengruppe nicht effektiv.

Die meisten PET-Studien konzentrieren sich auf die Beschreibung der Pharmakokinetik von einem einzigen radioaktiv markiertem Antikörper, ohne diesen mit anderen Antikörpern zu vergleichen. Der Vergleich von verschiedenen Antikörpern und ihrem Verhalten im menschlichen Körper könnte aber möglicherweise wertvolle Informationen liefern im Bezug auf die Entwicklung neuer Arzneimittel. In der Studie, die in **Kapitel 5** beschrieben wird, haben wir darum PET-Scan Daten von vier  $^{89}\text{Zr}$ -markierten Antikörpern erneut analysiert. Der Ausgangspunkt unserer Analyse war das kürzlich erschienen Protokoll zur Harmonisierung von PET-Scanstudien und die Ausführung wurde auf unser Standardprotokoll für  $^{89}\text{Zr}$ -markierte Tracer basiert.  $^{89}\text{Zr}$ -Lumretuzumab (Antikörper gegen HER3),  $^{89}\text{Zr}$ -MMOT0530A (Antikörper gegen Mesothelin),  $^{89}\text{Zr}$ -Bevacizumab (Antikörper gegen den Wachstumsfaktor VEGF) und  $^{89}\text{Zr}$ -Trastuzumab (Antikörper gegen HER2) verteilen sich ähnlich im menschlichen Körper. Vier Tage nach der Tracerinjektion war etwa ein Drittel der injizierten Dosis im Blut, 15% waren in der Leber und 4% in der Milz und den Nieren. Im Gegensatz dazu waren die Tracerkonzentrationen im Knochenmark, den Lungen, dem kompakten Knochen, den Muskeln, dem Fett und dem Gehirn niedrig. Trotz der geringen Tracerkonzentration pro Gramm Gewebe kann die Verteilung des Tracers im Körper stark durch Gewebe, die in großen Mengen vorkommen, beeinflusst werden: Im Schnitt akkumulierten 5-7% der injizierten Tracerdosis im Fettgewebe. Bei einer Patientin mit morbidem Adipositas waren es jedoch 19%. Die ähnliche Verteilung der vier Antikörper beruht wahrscheinlich auf der ähnlichen molekularen Struktur, der vergleichbaren Antikörperbindung und dem ähnlichen Wirkprinzip in der Zelle. Die Daten dieser ersten Vergleichsstudie formen die Basis eines wachsenden „Warenhauses“ voller pharmakokinetischer Daten von verschiedenen radioaktiv markierten Antikörpern. Das „Warenhaus“ wird in den kommenden Jahren wachsen durch Analyse von Tracern, die das Immunsystem abbilden, aber auch Molekülen, die zu einer anderen Antikörperklasse (IgG 1-4) gehören oder eine andere Größe oder Struktur haben.

In **Kapitel 6** wird molekulare Bildgebung mit  $^{89}\text{Zr}$ -Atezolizumab, einem Tracer, der zum ersten Mal in Menschen angewendet wird, beschrieben. Atezolizumab ist ein Antikörper gegen PD-L1, einem wichtigen Kontrollpunkt im Immunsystem. Durch Aktivierung von PD-L1 wird der Tumor nicht mehr vom Immunsystem erkannt und kann dadurch ungestört wachsen. PD-L1 kommt auf Tumorzellen und auch auf Zellen des Immunsystems vor. Durch die Behandlung mit Atezolizumab wird das körpereigene Immunsystem wieder aktiviert, sodass

es den Krebs angreifen kann. In der beschriebenen Studie wurde die Tumoraufnahme von  $^{89}\text{Zr}$ -Atezolizumab bei Patienten mit Blasenkrebs, Lungenkrebs und Brustkrebs korreliert mit der PD-L1 Immunhistochemie, der RNA-Analyse und der Effektivität der Behandlung. Nach der Injektion von  $^{89}\text{Zr}$ -Atezolizumab in Kombination mit 10 mg unmarkiertem Antikörper war die Traceraufnahme im Blut, der Leber und den Nieren vergleichbar mit der Aufnahme anderer  $^{89}\text{Zr}$ -Antikörpertracer. Im Gegensatz zu den anderen Antikörpern akkumulierte  $^{89}\text{Zr}$ -Atezolizumab stark in der Milz, in verschiedenen Lymphknotenstationen und an Orten an denen vermehrt PD-L1 exprimierende Zellen des Immunsystems zu finden sind. Die Tumortraceraufnahme war im Allgemeinen sehr hoch mit einem SUVmax bis zu 46, aber auch heterogen zwischen Patienten und Tumortypen. In dieser Studie, mit einer begrenzten Anzahl Patienten und ohne Tumoren mit sehr hoher PD-L1 Expression, war eine hohe Traceraufnahme prädiktiv für die Effektivität der Behandlung und das progressionsfreie Überleben. Der PET-Scan konnte die Reaktion auf die Behandlung sogar besser vorhersagen als die Immunhistochemie oder die RNA-Analyse. In kommenden Studien müssen diese Resultate in einer größeren Patientenpopulation bestätigt werden.

Zuletzt wird in **Kapitel 7** eine Studie an Patienten mit metastasiertem HER2-positiven Brustkrebs und einem klinischen Dilemma in Bezug auf den HER2-Status ihrer Erkrankung beschrieben. In dieser spezifischen Patientenpopulation haben wir untersucht ob ein  $^{89}\text{Zr}$ -Trastuzumab-PET-Scan dem behandelnden Onkologen helfen kann, die Erkrankung seines Patienten besser zu verstehen, und ob die Behandlungsentscheidung unterstützt werden kann. In 90% der Fälle bekamen die behandelnden Ärzte durch den PET-Scan eine bessere Einsicht in die Erkrankung ihres Patienten. Fünfzig Prozent der behandelnden Onkologen fühlte sich in ihrer Behandlungsentscheidung bestätigt, und in 40% wurde die Behandlung angepasst in der Folge des PET-Scans. Die erneute, zentrale pathologische Beurteilung von altem Tumormaterial lieferte bei 3/20 Patienten neue Informationen. Es empfiehlt sich daher diesen Schritt in den diagnostischen Prozess von Patienten mit einem solchen klinischen Dilemma aufzunehmen. Die Beurteilung der HER2 Expression auf frei im Blut zirkulierenden Tumorzellen, die bei nur 50% der Patienten vorkommen, korrelierte nicht mit dem PET-Scan Ergebnis oder der Therapieentscheidung.

In dieser Dissertation wurde die Rolle von molekularer Bildgebung mittels PET in der Onkologie beschrieben. Diese Technik wurde benutzt um mehr Informationen über die Pharmakokinetik und Pharmakodynamik von neuen Antikörpern zu bekommen. In klinischen Studien mit einer begrenzten Anzahl Patienten wurde gezeigt, dass molekulare Bildgebung bei klinischen Entscheidungen helfen kann und einen prädiktiven Wert hat. In der Zukunft kann diese Technik möglicherweise bei der Selektion von Patienten helfen und dadurch die Effektivität von Behandlungen und schlussendlich das Gesamtüberleben von Patienten verbessern.



## **Curriculum vitae**

### **Publications**

---

## **CURRICULUM VITAE**

Frederike Bensch was born August 26, 1985 in Hagenow, Germany. After graduating from the Christian-Ludwig-Liscow Gymnasium in Wittenburg in 2005, Frederike moved to Heidelberg and later to Mannheim to study Medicine at the University of Heidelberg. She did her final internships at the Departments of Internal Medicine, Pulmonology and Hepato-Pancreatico-Biliary Surgery and Liver Transplantation at the University Medical Center Groningen (the Netherlands) and at the Department of Pathology at the University Medical Center Mannheim.

Frederike discovered her interest in research already in Mannheim where she was enrolled in the Junior Scientific Master Class research program for medical students. She studied multidrug transporters in thymomas and thymic carcinomas at the Department of Pathology in the group of Professor A. Marx and Professor P. Ströbel in Mannheim and at the Department of Cell Biology, in the membrane cell biology group led by Dr. J.W. Kok at the University of Groningen. This research resulted in a doctorate degree in Medicine (Dr. med.).

After finishing her study in November 2011, she moved to the Netherlands to embark on her PhD-project as research physician and PhD student in the group of Professor E.G.E. de Vries and Dr. C.P. Schröder at the Department of Medical Oncology, University Medical Center Groningen. During this research period Frederike was involved in multiple translational research projects, co-supervised several medical, veterinary medicine and technical medicine students, presented her work at multiple (inter)national meetings and congresses, and received a personal Dutch Cancer Society Fellowship Grant. The latter allowed her to spend almost 5 years in research, which resulted in this thesis.

Since January 2017, Frederike is working at the Department of Internal Medicine at the Martini Hospital as part of her training to become a pulmonologist.

With the intention to further expand her knowledge and skills, Frederike is planning a research visit at the Cancer Research UK Institute, Cambridge University, under supervision of Professor C. Caldas in the beginning of 2019. Her research plan was awarded with the Pieter de Mulder Award of the Dutch Medical Oncology Association and she received additional funding from the Louise Rottinghuis Foundation.

## PUBLICATIONS

1. Bensch F, van Kruchten M, Lamberts LE, Schröder CP, Hospers GA, Brouwers AH, van Vugt MA, de Vries EG. Molecular imaging for monitoring treatment response in breast cancer patients. *Eur. J. Pharmacol.* 717, 2-11 (2013).
2. Kol A, Terwisscha van Scheltinga AGT, Timmer-Bosscha H, Lamberts LE, Bensch F, de Vries EGE, Schröder CP. HER3, serious partner in crime: therapeutic approaches and potential biomarkers for effect of HER3-targeting. *Pharmacol. Ther.* 143, 1-11 (2014).
3. De Vries EGE, van der Graaf WTA, Verheul HMW, Schröder CP, Menke CW, Boven E, Hoekstra O, Huisman M, van Herpen C, Desar I, Oyen W, Boerman O, Visser E, de Geus-Oei L-F, Brouwers AH, Glaudemans AWJM, de Jong JR, de Vries EFJ, Bensch F. Towards patient tailored cancer treatment supported by molecular imaging. IMPACT: IMaging PATients for Cancer drug selectiOn – Metastatic Breast Cancer (IMPACT-MBC). *Tijdschrift voor Nucleaire Geneeskunde* 36, 1221-1223 (2014).
4. Bensch F, van Rooijen JM, Schröder CP, Reyners AK. A 21-year-old patient with a HER2-positive colorectal cancer. *Gastroenterology* 148, 20-21 (2015).
5. De Vries EGE, van der Graaf WTA, Verheul HMW, Schröder CP, Menke CW, van Herpen CML, Brouwers A, Glaudemans AWJM, Hoekstra OS, Oyen W, Bensch F, van Es SC, van Helden EJ, Boon E. IMPACT: Op weg naar een gepersonaliseerde anti-kankerbehandeling met behulp van moleculaire beeldvorming. Drie lopende studies voor mamma-, colorectaal- en niercelcarcinoom. *Nederlands Tijdschrift voor Oncologie* 12, 114-120 (2015).
6. Den Hollander MW, Bensch F, Glaudemans AW, Oude Munnink TH, Enting RH, den Dunnen WF, Heesters MA, Kruyt FA, Lub-de Hooge MN, de Groot JC, Pearlberg J, Gietema JA, de Vries EG, Walenkamp AM. TGF- $\beta$  antibody uptake in recurrent high-grade glioma imaged with  $^{89}\text{Zr}$ -fresolimumab PET. *J. Nucl. Med.* 56, 1310-1314 (2015).
7. Lamberts LE, Menke-van der Houven van Oordt CW, ter Weele EJ, Bensch F, Smeenk MM, Voortman J, Hoekstra OS, Williams SP, Fine BM, Maslyar D, De Jong JR, Gietema JA, Schröder CP, Bongaerts AHH, Lub-de Hooge MN, Verheul HMW, Sanabria S, Glaudemans AJWM, De Vries EGE. ImmunoPET with anti-mesothelin antibody in patients with pancreatic and ovarian cancer before anti-mesothelin antibody-drug conjugate treatment. *Clin. Cancer Res.* 22, 1642-1652 (2016).
8. Bensch F, Lamberts LE, Smeenk MM, Jorritsma-Smit A, Lub-de Hooge MN, Terwisscha van Scheltinga AGT, de Jong JR, Gietema JA, Schröder CP, Thomas M, Jacob W, Abiraj K, Adessi C, Meneses-Lorente G, James I, Weisser M, Brouwers AH, de Vries EGE.  $^{89}\text{Zr}$ -lumretuzumab PET imaging before and during HER3 antibody lumretuzumab treatment in patients with solid tumors. *Clin. Cancer Res.* 23, 6128-6137 (2017).

9. Bensch F, Smeenk MM, van Es SC, de Jong JR, Schröder CP, Oosting SF, Lub-de Hooge MN, Menke-van der Houven van Oordt CW, Brouwers AH, Boellaard R, de Vries EGE. Comparative biodistribution analysis across four different <sup>89</sup>Zr-monoclonal antibody tracers—The first step towards an imaging warehouse. *Theranostics* 8, 4295-4304 (2018).
10. Bensch F, Brouwers AH, Lub-de Hooge MN, de Jong JR, van der Vegt B, Sleijfer S, de Vries EGE, Schröder CP. <sup>89</sup>Zr-trastuzumab PET supports clinical decision making in breast cancer patients, when HER2 status cannot be determined by standard work up. *Eur. J. Nucl. Med. Mol. Imaging* 45, 2300-2306 (2018).
11. Bensch F, van der Veen EL, Lub-de Hooge MN, Jorritsma-Smit A, Boellaard R, Kok IC, Oosting SF, Schröder CP, Hiltermann TJN, van der Wekken AJ, Groen HJM, Kwee TC, Elias SG, Gietema JA, Sanabria Bohorquez S, de Crespigny A, Williams SP, Mancao C, Brouwers AH, Fine BM, de Vries EGE. Clinical <sup>89</sup>Zr-atezolizumab imaging as a potential PD-L1 biomarker in cancer patients. *Nat. Med.* 24, 1852–1858 (2018).
12. Van der Veen EL, Bensch F, Glaudemans AWJM, Lub-de Hooge MN, de Vries EGE. Molecular imaging to enlighten cancer immunotherapies and underlying involved processes. *Cancer Treat. Rev.* 70, 232-244 (2018).





## **Dankwoord (Acknowledgments)**

---

Gedurende mijn onderzoeksjaren, die uiteindelijk resulteerden in dit proefschrift, heb ik de mogelijkheid gekregen om veel te leren van verschillende mensen met diverse achtergronden. Ik ben iedereen zeer erkentelijk voor alle tijd en kennis die men mij heeft geschonken. Er zijn een aantal collega's en vrienden die ik specifiek wil noemen en bedanken.

Alvorens ik daaraan begin, wil ik graag alle patiënten en hun familie bedanken die deel hebben genomen aan een van de klinische studies die ik heb mogen begeleiden. Zonder hun inzet waren de studies en uiteindelijk het tot stand komen van dit proefschrift niet mogelijk geweest.

Allereerst wil ik graag mijn promotor prof. dr. E.G.E. de Vries en mijn copromotor dr. C.P. Schröder bedanken.

Beste Liesbeth, via Wouter Nagengast kwam ik bij jou terecht voor een kennismakingsgesprek. Ik weet nog, dat ik al tijdens mijn online zoektocht, voorafgaand aan onze eerste afspraak onder de indruk was van jouw ervaring en kennis en kunde in de onderzoeksweld. Sindsdien hebben vele afspraken plaatsgevonden en ik word nog steeds niet teleurgesteld, want elke keer valt er iets nieuws te leren. Ik ben dankbaar dat jij mij een deel van de onwijs leuke en onzettend grote onderzoeksweld hebt laten zien, voor het vertrouwen dat jij mij hebt gegeven bij het uitvoeren van de verschillende studies en de ontzettend goede, doelgerichte, inspirerende, enthousiaste begeleiding die ik tijdens mijn promotietraject heb mogen ontvangen.

Beste Carolien, niet alleen bij het schrijven van wetenschappelijke stukken maar ook in het dagelijks leven heb ik veel van jou en jouw goed en politiek correct taalgebruik en taalgevoel geleerd. Ik blijf mij erover verwonderen hoe jij een stuk kan herschrijven zodat het nog mooier en duidelijker wordt. Ondanks alle drukte tijdens gewone werkdagen kon ik altijd binnenstappen en vragen of problemen met jou bespreken. Jouw enthousiasme maar ook jouw reële kijk op ons werk als artsen en onderzoekers zal ik me altijd blijven herinneren.

Graag wil ik de leden van de leescommissie prof. dr. H.W. Nijman, prof. dr. G.M. van Dam en prof. dr. O. Boerman bedanken voor de beoordeling van mijn proefschrift.

De KWF Kankerbestrijding wil ik graag bedanken voor hun financiële steun voor het uitvoeren van een deel van het onderzoek.

Zonder alle ondersteuning binnen de afdeling Medische Oncologie, administratief, logistiek, of gewoon vanwege de gezelligheid, waren al de studies niet zo soepel gelopen, daarom dank aan Gretha, Bianca, Hilda, Hetty, Coby, Greetje, Arja, Gerrie, Gerry, Hendrique, Laura en alle polimedewerkers. Aan de stafleden en fellows mijn dank voor de supervisie en alle feedback omtrent het onderzoek.

Imaging studies zijn alleen mogelijk door multidisciplinaire samenwerking. Zonder de farmaceuten geen tracer, zonder de scanner en alle kunde hieromheen geen beelden en interpretatie. Ik wil daarom graag alle betrokken collega's van de apotheek en de nucleaire geneeskunde bedanken, in het bijzonder Marjolijn, Hendrikus, Annelies, Elly, Stijn, Martin, Anton,

Linda, Rianne en Silke, Adrienne, Andor, Johan (de Jong), Ronald, Eelco, Paul, Johan (Wiegers), Hans en uiteraard de planners van de nucleaire.

Eveneens wil ik graag alle collega's van buiten het UMCG voor de leuke en leerzame samenwerking in het kader van de IMPACT-studies bedanken.

Gedurende de imagingstudie met <sup>89</sup>Zr-atezolizumab mocht ik nauw samenwerken met de collega's van de longenoncologie. Na een warm welkom was het alsof we al jaren samen hebben gewerkt, daarom ook jullie, Harry, Jeroen, Anthonie en Lucie, bedankt. Ik verheug me op de opleidingstijd bij jullie en alle collega's van de afdeling Longgeneeskunde.

Hartelijk dank ook aan alle coauteurs voor hun kennis en inzet bij het tot stand komen van de stukken. Sjoerd, dank voor jouw statistische expertise en mooie grafieken!

Mede-strijders van Y3 en U4, bedankt! Wat een gezelligheid bij vlees en bier en op alle weekenden en uitjes, in het bijzonder Titia, Niek, Martine, Hink, Rob, Michel, Sietske, Hilde, Sophie, Kees, Clarieke, Suzanne, Bertha, Sjoukje, Grytsje, Danielle, Elmiere, Majory, Jolien, Lars, Thijs, Kirsten, Iris, Pieter, Maaïke, Tjaart en Lotte. Dank aan de nieuwe generatie onderzoekers voor het gedoogbeleid op beide kamers.

Liebe Mutti und lieber Papa, danke für alle Möglichkeiten und euer Vertrauen bei allem was ich mache. Liebe Franzi, trotz aller Unterschiede ist es schön dich als meine Schwester zu haben, die mich bei allem unterstützt.

Lieve schoonfamilie, bedankt voor alle oppasuren en de gezelligheid tijdens etentjes, uitjes en vakanties tussen al het harde werk.

Lieve Hjalmar, dank voor jouw liefde en steun, en de praktische oplossingen om bergen van imaging data snel te sorteren. Lene en Finn, ik hou van jullie.

